



HAL
open science

Implementation of a clinical dosimetry workflow to perform personalized dosimetry for internal radiotherapy

Alex Vergara Gil

► **To cite this version:**

Alex Vergara Gil. Implementation of a clinical dosimetry workflow to perform personalized dosimetry for internal radiotherapy. Medical Imaging. Université Paul Sabatier - Toulouse III, 2022. English. NNT : 2022TOU30170 . tel-04008274

HAL Id: tel-04008274

<https://theses.hal.science/tel-04008274v1>

Submitted on 28 Feb 2023

HAL is a multi-disciplinary open access archive for the deposit and dissemination of scientific research documents, whether they are published or not. The documents may come from teaching and research institutions in France or abroad, or from public or private research centers.

L'archive ouverte pluridisciplinaire **HAL**, est destinée au dépôt et à la diffusion de documents scientifiques de niveau recherche, publiés ou non, émanant des établissements d'enseignement et de recherche français ou étrangers, des laboratoires publics ou privés.



THÈSE

En vue de l'obtention du

DOCTORAT DE L'UNIVERSITÉ DE TOULOUSE

Délivré par : *l'Université Toulouse 3 Paul Sabatier*

Présentée et soutenue le *03/10/2022* par :

Alex Vergara Gil

Implementation of a clinical dosimetry workflow to perform
personalized dosimetry for internal radiotherapy

JURY

PIERRE PAYOUX	Professeur, Université Toulouse 3 Paul Sabatier	Examineur
LUC SIMON	Docteur, Institut Universitaire de Cancer de Toulouse	Examineur
LUDOVIC FERRER	Docteur, Institut de Cancérologie de l'Ouest (Angers/Nantes)	Examineur
LYDIA STRIGARI	Directrice de Recherche, Université de Bologne	Rapporteuse
ELIF HINDIÉ	Professeur, Université de Bordeaux	Rapporteur

École doctorale :

*GEETS - Génie Electrique Electronique, Télécommunications et Santé :
du système au nanosystème*

Spécialité :

Radio-physique et Imagerie Médicale

Unité de Recherche :

Centre de Recherche en Cancérologie de Toulouse (INSERM UMR 1037)

Directeur de Thèse :

Manuel Bardiès

Rapporteurs :

Lydia Strigari et Elif Hindié



THÈSE

**En vue de l'obtention du
DOCTORAT DE L'UNIVERSITÉ DE TOULOUSE
Délivré par l'Université Toulouse 3 - Paul Sabatier**

**Présentée et soutenue par
Alex VERGARA GIL**

Le 3 octobre 2022

**Mise en uvre d'un flux de travail de dosimétrie clinique pour
réaliser une dosimétrie personnalisée pour la radiothérapie
interne vectorisée**

Ecole doctorale : **GEETS - Génie Electrique Electronique, Télécommunications et
Santé : du système au nanosystème**

Spécialité : **Radiophysique et Imagerie Médicales**

Unité de recherche :
CRCT - Centre de Recherche en Cancérologie de Toulouse

Thèse dirigée par
Manuel BARDIES

Jury

Mme Lydia STRIGARI, Rapporteur
M. Elif HINDIE, Rapporteur
M. Pierre PAYOUX, Examineur
M. Luc SIMON, Examineur
M. Ludovic FERRER, Examineur
M. Manuel BARDIES, Directeur de thèse

Résumé — La médecine nucléaire est une spécialité médicale qui étudie la physiologie des organes et le métabolisme de divers types de tumeurs. La médecine nucléaire utilise des produits pharmaceutiques liés à un isotope radioactif. La radiothérapie interne vectorisée (RIV) est une spécialité de la médecine nucléaire où le vecteur est dirigé vers des cibles, généralement des tumeurs, et où l'action des rayonnements ionisants vise à détruire les tumeurs. Le suivi et l'optimisation de la RMT nécessitent l'évaluation de l'irradiation délivrée au patient (dosimétrie).

Il y a un manque de standardisation en dosimétrie interne. Cette thèse propose une approche standardisée avec des flux de travail descriptifs pour la dosimétrie clinique. Un logiciel appelé OpenDose3D, basé sur 3D-Slicer en tant que module open source mettant en œuvre les flux de travail proposés, est développé, validé et mis à la disposition du public. Le module a été utilisé en recherche clinique dans le projet MEDIRAD.

Mots clés : Dosimétrie interne, workflows cliniques, 3D-Slicer.

Abstract — Nuclear medicine is a medical specialty that studies the physiology of organs and the metabolism of various types of tumors. Nuclear medicine uses pharmaceuticals bound to a radioactive isotope. Molecular radiotherapy (MRT) is a specialty of nuclear medicine where the vector is directed to targets, usually tumors, and the action of ionizing radiation is aimed at destroying tumors. The follow-up and optimization of MRT requires the evaluation of the irradiation delivered to the patient (dosimetry).

There is a lack of standardization in internal dosimetry. This thesis provides a standardized approach with descriptive clinical dosimetry workflows. A software named OpenDose3D, based in 3D-Slicer and implementing the proposed workflows was developed, validated and was made publicly available as an open source module. The module was used in clinical research within the MEDIRAD project.

Keywords: Internal dosimetry, Clinical dosimetry workflows, 3D-Slicer.

Centre de Recherches de Cancérologie de Toulouse
UMR 1037, INSERM
Ecole Doctorale GEET
Université Toulouse III, Paul Sabatier
31000 Toulouse, France

Acknowledgements

As any other PhD thesis, mine contains a lot of work that was done with the help of numerous people that contributed one way or another. The list is very large in my case as it involved several stages of support, guidance, experimentation, redaction and revision. I wrote these acknowledgements in English as everyone present in this list speaks different languages and I have to select a common one for all of them.

I will start thanking my beautiful wife **Yaniela Marrero**. She is actually the biggest support I have in my life, making my enthusiasm never fade, even in the worst situations. Thanks for filling my life with purpose and joy. Thanks for giving me my two kids, for whom I live.

I am enormously thankful to **Professor Manuel Bardiès** from CRCT, INSERM Toulouse, France (and currently at IRCM, ICM Montpellier). Who believed in me at the moment of hiring me to fill a position in his team to take care of the Medirad Project, which will be described in this dissertation. Thanks for your support to start a PhD and for showing me it was possible to do it together with the job I was hired for. Thanks for refining my point of views, making them more fitted to the real world problems we were trying to solve. I had the pleasure to be involved in a very dynamic team, that contributed to my professional formation with the exchange of ideas to solve everyone's problems as team problems.

I am greatly thankful to **Professor Leonel Torres Aroche**, which started me in the medical physics field. Thanks to him, I gained love for this profession and could see it as a way of life. I shall also thank to all the team in the CIC in Havana for all the clinical experience. Thanks also to **Marco Coca** and **Carlos Calderón** for their support.

Thanks to the Medirad team, specially to **Glenn Flux**, **Francesca Leek** and **Jan Taprogge** from NHS Royal Marsden for their support and guidance.

Special thanks to **Erick Mora Ramírez**, who was really helpful during my integration in Prof Bardiès team. He taught me how to sort all the administrative problems and how to be both worker and student at the same time.

Thanks to my colleagues at CRCT Team 15: **Gunjan Kayal**, **Maxime Chauvin**, **Juan Camilo Ocampo**, **Naomi Clayton**, **Ana Rita Barbeiro** and **Jonathan Tranel** for all the time together brainstorming and for all the stimulating discussions. Specially to Gunjan and Maxime for the last stage of the team 15, helping me to solve last minutes issues and problems. Thanks also to **Quan Gan**, a good master's student that help me a lot to solve a big technical problem during my work related to the comparison of different softwares.

Huge thanks to **Janick Rüegger** for the help in the initial stages of OpenDose3D. His work was critical to set up most of the main aspects of this work, the graphical conception, the test suite and the modularization of the code. Thanks also to **Thiago Lima** for supporting

Janick's work and for all the revisions and discussions.

Huge thanks to **José Alejandro Fragoso** for the help in the maintenance of OpenDose3D, specially for the bug tracking and solving.

Thanks to all the Italian colleagues, specially to **Profesor Massimiliano Pacilio** for his huge support to my work since the very start. Thanks to **Alessia Milano** and **Enrico Fabrizi** for the validation of the Monte Carlo scripts. Also thanks to **Marta Cremonesi**, **Francesca Botta** and **Andrea Mairani** for the common work publishing some of my work.

Huge thanks to **Daniele Pistone**, and **Professor Ernesto Amato** for using OpenDose3D in their job, contributing significantly to the independent validation. Thanks to Daniele for all the bug tracking, really helpful to solve non-trivial issues.

I had the opportunity to participate in the coordinated research project initiated by the IAEA titled Dosimetry in Molecular Radiotherapy for Personalized Patient Treatments. My sincere thanks go to all the members of this project for their support and encouragement. Especially to the organizers **Gian Luca Poli** at start and **Peter Knoll** at the end.

Thanks to **Michael Ljungberg** for allowing us to write a chapter on Patient-specific Dosimetry Calculations in his Handbook of Nuclear Medicine and Molecular Imaging for Physicists.

Thanks to **Michael Lassman** for allowing us to write a chapter on Absorbed dose calculation in his book Dosimetry for Radiopharmaceutical Therapy.

Finally, I would like to thanks to my parents for all their love and sacrifice allowing me to focus on studying and preparing my future; to my brother, for standing next to me in the rough parts of my life; and to my parents-in-law for all their support.

Alex Vergara Gil

Lille, October 2022

Contents

Acronyms	ix
Introduction générale	1
General Introduction	5
1 Theoretical framework	9
1.1 General background	9
1.2 Pharmacokinetics	13
1.3 Dosimetry in internal radiotherapy	15
1.4 Medical Images	25
1.5 Absorbed dose calculation algorithms	33
1.6 Conclusions	38
2 Clinical Dosimetry Workflows	41
2.1 Introduction	41
2.2 Clinical Dosimetry workflows	43
2.3 The European Project MEDIRAD (H2020)	48
2.4 The IRDBB database	50
2.5 Proposed CDW in MRT	53
2.6 Conclusion	61
3 Development of OpenDose3D	63
3.1 3D-Slicer	64
3.2 OpenDose3D module description	73
4 OpenDose3D module benchmarking	91

4.1	Evaluation of the generated kernels for convolution	91
4.2	Benchmarking of the Monte Carlo implementation	98
4.3	Comparison against commercial software	102
4.4	Absorbed dose rate algorithm comparison	115
4.5	Conclusions	127
5	Implementation of patient specific clinical dosimetry	129
5.1	Dosimetry for IUCT	130
5.2	Dosimetry for RMH	140
5.3	Dosimetry for UKW	150
5.4	Discussion	164
	Conclusion (FR)	167
	Conclusion (EN)	171
	Bibliography	175
	Appendix A Appendix to Chapter 2	185
A.1	DICOM header data required for CDW	185
	Appendix B Appendix to Chapter 3	189
B.1	Required DICOM fields	189
	Appendix C Appendix to Chapter 5	191
C.1	RMH data tables	191
C.2	IUCT data tables	198
C.3	UKW data tables	205
	Appendix D Scientific Production	213
D.1	Original papers	213

<i>CONTENTS</i>	vii
D.2 Abstracts	213
D.3 Books	214
D.4 International conferences	214
List of Figures	217
List of Tables	223

Acronyms

ADR	<i>Absorbed Dose Rate</i>	NTCP	<i>Normal Tissue Complications Probability</i>
CDW	<i>Clinical Dosimetry Workflow</i>	PET	<i>Positron Emission Tomography</i>
CI/CD	<i>continuous integration and continuous delivery</i>	PSF	<i>Point spread function</i>
CT	<i>Computed Tomography</i>	PVE	<i>Partial volume effect</i>
DICOM	<i>Digital Imaging and Communications in Medicine</i>	RLP	<i>radio-labeled pharmaceutical</i>
EDW	<i>Electron density relative to water</i>	ROI	<i>Region of interest</i>
FFT	<i>Fast Fourier Transform</i>	SAF	<i>Specific absorbed fraction</i>
FOV	<i>Field of View</i>	SIRT	<i>Selective Internal Radiotherapy</i>
DPK	<i>Dose Point Kernel</i>	SPECT	<i>Single Photon Emission Computed Tomography</i>
ICRP	<i>International Commission on Radiological Protection</i>	TCP	<i>Tumor Control Probability</i>
ICRU	<i>International Committee for Radiological Units</i>	TAC	<i>Time Activity curve</i>
LED	<i>Local Energy Deposition</i>	TIAC	<i>Time integrated activity coefficient</i>
MC	<i>Monte Carlo</i>	VDK	<i>Voxel Dose Kernel</i>
MIRD	<i>Committee on Medical Internal Radiation Dose</i>	VOI	<i>Volume of interest</i>
MRT	<i>Molecular Radiotherapy</i>	WB	<i>Whole Body</i>

Introduction générale

La médecine nucléaire est une spécialité médicale chargée d'étudier la physiologie des organes et le métabolisme de divers types de tumeurs. La médecine nucléaire utilise des produits pharmaceutiques liés à un isotope radioactif. Ces produits sont imagés par des systèmes hybrides de tomographie d'émission de positrons (TEP) ou tomographie d'émission monophotonique (TEMP) associés à la tomodensitométrie (TDM), ce qui permet la réalisation d'une imagerie anatomique et fonctionnelle. La radiothérapie interne vectorisée (RIV) est une spécialité de la médecine nucléaire où le vecteur est dirigé vers des cibles généralement tumorales, et où l'action des radiations ionisantes a pour but de détruire les tumeurs. Le suivi et l'optimisation de la RIV passe par l'évaluation des irradiations délivrées au patient (dosimétrie).

Dans ce contexte, notre équipe développe des outils permettant la réalisation de dosimétries cliniques en RIV. L'objectif de la dosimétrie clinique est de déterminer la dose absorbée par le patient, tant pour les tumeurs que pour les organes/tissus normaux (critiques), afin d'obtenir la réponse clinique souhaitée. Dans ce contexte, plusieurs flux de travail cliniques ont été proposés dans la littérature. Cependant, ils se concentrent principalement sur certaines étapes du flux de travail clinique, ils manquent de clarté dans la définition des détails, ils ne sont pas assez précis et ils ne sont pas standardisés.

L'objectif principal de cette thèse de doctorat est de proposer un flux de travail dosimétrique, en décrivant tous les détails à partir de la calibration, et en passant par toutes les étapes l'acquisition de l'image du patient, le traitement des données et les algorithmes détaillés de calcul de la dose absorbée.

Dans le chapitre 1, les principes fondamentaux de la dosimétrie clinique sont présentés avec un compendium bibliographique dédié contenant des informations pertinentes sur l'état actuel et les problèmes non résolus de la dosimétrie clinique. Un contexte général sur la radiothérapie décrivant les principales procédures mises en œuvre dans les cliniques est introduit avec une courte liste des radionucléides les plus pertinents utilisés pour la radiothérapie interne ainsi que les produits pharmaceutiques les plus pertinents. Ensuite, une description de la pharmacocinétique et de la façon de la mesurer. Le processus de dosimétrie en radiothérapie interne est décrit avec les différentes alternatives actuellement disponibles dans la littérature. Les techniques d'imagerie médicale et de la manière d'obtenir des images calibrées du patient, tant anatomiques que fonctionnelles, sont énumérées avec un résumé des techniques de traitement d'images (reconstruction et correction). Une compilation bibliographique sur les procédures de calcul de la dose absorbée est présentée.

Dans le chapitre 2, différents flux de travail de dosimétrie clinique sont présentés, avec quelques exemples de mise en œuvre dans des postes de travail de dosimétrie clinique. Nous décrivons aussi le projet européen MEDIRAD (H2020) : notre rôle consiste à réaliser la dosimétrie clinique dans le cadre d'un essai clinique. Nous proposons deux flux de travail de dosimétrie clinique, qui diffèrent en fonction de la manière dont les variables dépendantes du temps sont traitées, c'est-à-dire si l'intégration temporelle est effectuée sur l'activité ou les

débits de dose absorbés :

Le flux de travail d'intégration des activités : Il s'agit du flux de travail classique, où l'activité intégrée dans le temps est évaluée en premier. Il met d'abord en œuvre l'intégration temporelle de l'activité présente dans les volumes d'intérêt (VOI). Le calcul dosimétrique est ensuite effectué avec une certaine hypothèse préétablie, comme le dépôt local d'énergie (DLE) à l'échelle du VOI, bien que d'autres hypothèses soient également utilisées dans la pratique.

Le flux de travail d'intégration du débit de dose absorbée : Il met en œuvre le calcul des débits de dose absorbée à l'échelle du voxel pour chaque temps d'acquisition. Différents algorithmes de calcul sont envisagés : le dépôt local d'énergie (DLE), la convolution homogène par FFT et la simulation Monte Carlo (MC). Ensuite, l'intégration temporelle est réalisée sur les débits de dose absorbée moyens définis pour chaque VOI, et à chaque temps, pour obtenir la dose absorbée finale par organe. Ce flux de travail permet de prendre en compte les variations de volume, de forme et de masse des organes au cours du traitement. Il fournit également le débit de dose absorbée qui est un paramètre conditionnant l'effet biologique des rayonnements en RIV.

L'intégration temporelle a été développée, dans les deux cas, comme un outil d'ajustement pharmacocinétique qui produit un tableau des activités cumulées ou des doses absorbées.

Enfin, nous aurons une discussion sur les caractéristiques souhaitables d'un ensemble de dosimétrie.

Dans le chapitre 3, un module open source nommé OpenDose3D (OD3D), qui effectue la dosimétrie au niveau des organes des patients subissant une RIV, est présenté comme une preuve de concept du flux de travail dosimétrique clinique proposé. OD3D a été développé selon la philosophie du logiciel libre afin de promouvoir une approche académique unique. En ce sens, il n'y aura plus besoin de développements individuels dans chaque laboratoire, car le logiciel est non seulement accessible mais aussi modifiable par des propositions à l'équipe de direction. OD3D est créé comme un module python de 3D-Slicer.

3D-Slicer est un système complet d'importation et de manipulation d'images médicales, qui accepte des images hybrides PET/CT ou SPECT/CT reconstruites, acquises à différents moments après l'administration. 3D-Slicer comprend déjà certaines fonctionnalités nécessaires à la dosimétrie clinique, comme le recalage et la segmentation d'images. Il permet également la création de flux de travail, sous forme de scripts, pour développer de nouvelles fonctionnalités.

Le module OD3D met en œuvre différentes étapes telles que la normalisation DICOM, le rééchantillonnage CT et le redimensionnement SPECT/CT pour obtenir les cartes de densité et d'activité 3D. Les volumes d'intérêt (VOI) peuvent être segmentés manuellement par l'utilisateur à l'aide du module spécifique 3D-Slicer. Le recalage des images acquises à différents moments est effectué automatiquement à l'aide du module Elastix de 3D-Slicer (recalage CT-CT). À l'exception de la segmentation VOI/organe pendant le processus dosimétrique, toutes

les étapes de calcul ont été entièrement automatisées.

Le module est disponible en tant que module officiel de 3D-Slicer, ce qui permet son installation via le gestionnaire d'extensions. Le code source a été mis à disposition sur internet avec un manuel utilisateur et un manuel développeur.

Dans le chapitre 4, une comparaison complète d'OD3D est présentée. Pour garantir la qualité du développement, une méthode d'intégration continue et de livraison continue (CI/CD) a été mise en œuvre sous la forme d'une suite de tests. Les mises à jour successives sont garanties pour préserver la fonctionnalité des flux de travail définis sur la base des tests effectués. Si un test échoue, la mise à niveau est rejetée.

OD3D vise à être accepté par la communauté comme une solution standard valide. Pour cela, chaque section du logiciel doit être testée et validée par rapport à d'autres solutions acceptées. Chaque étape de la mise en œuvre du flux de travail est testée par comparaison avec un logiciel établi (universitaire ou commercial).

On a utilisé deux stations commerciales pour effectuer toutes les étapes du flux de travail de dosimétrie sur un patient test et on a comparé les résultats avec OD3D. Une comparaison des algorithmes de segmentation, de la mesure de l'activité et du processus d'intégration temporelle est aussi effectuée.

Enfin, une comparaison des différents algorithmes de débit de dose absorbée inclus dans OD3D est réalisée et présentée.

Dans le chapitre 5, nous décrivons une mise en œuvre clinique de l'ensemble des travaux (flux de travail + OD3D) dans le cadre du projet MEDIRAD. OD3D pour produire des données de dosimétrie clinique pour 71 patients dans trois centres cliniques.

Enfin, une conclusion générale est présentée, avec les questions qui restent en suspens et les perspectives de travaux futurs.

General Introduction

Nuclear medicine is a medical specialty that studies the physiology of organs and the metabolism of various types of tumors. Nuclear medicine uses pharmaceuticals bound to a radioactive isotope. These products are imaged by hybrid positron emission tomography (PET) or single photon emission computed tomography (SPECT) systems combined with computed tomography (CT), allowing for anatomical and functional imaging. Molecular radiotherapy (MRT) is a specialty of nuclear medicine where the vector is directed to targets, usually tumors, and the action of ionizing radiation aims at destroying tumors. The follow-up and optimization of MRT requires the evaluation of the irradiation delivered to the patient (dosimetry). In this context, we have developed tools designed for clinical dosimetry in MRT.

The aim of clinical dosimetry is the determination of the absorbed dose within the patient, both for tumors and normal (critical) organs/tissues, in order to get the desired clinical response. In this context several clinical workflows has been proposed in the literature. However, these are mostly focused on some steps of the clinical workflow, they lack of clarity in the definition of the details, and they are not standardized.

The main objective of this doctoral thesis is to propose a standardized clinical dosimetric workflow, describing all the details starting from calibration, and passing through all steps such as patient image acquisition, data treatment, and detailed absorbed dose calculation algorithms.

chapter 1 presents of the fundamentals of clinical dosimetry with a dedicated bibliography compendium with relevant information presenting the current status and the unsolved problems of clinical dosimetry. A general background on radiotherapy describing the main procedures implemented in the clinics is introduced with a short list of the most relevant radionuclides used for internal radiotherapy is presented together with the most relevant pharmaceuticals. Following, a description of the pharmacokinetics and how to determine it, is presented. The dosimetry process in internal radiotherapy is presented with the different alternatives currently available in literature. A presentation of medical imaging techniques and how to obtain calibrated images from the patient, both anatomical and functional, is presented with a summary of image processing techniques (reconstruction and correction). A bibliographic compilation on the procedures to calculate the absorbed dose is presented.

chapter 2 presents different clinical dosimetry workflows, with some examples of implementation in clinical dosimetry workstations. The European project MEDIRAD (H2020) is introduced. Our role within MEDIRAD consisted in performing clinical dosimetry in a clinical trial study. We propose two clinical dosimetry workflows, which differ according to the way time-dependent variables are processed, i.e. whether the time integration is performed on the activity or on absorbed dose rates:

The activity integration workflow: This is the conventional workflow, where the time-integrated activity is assessed first. It initially implements the time integration of activity present in the volumes of interest (VOI). The dosimetric calculation is then performed with some pre-established assumption, like local energy deposition (LED) at the VOI scale, although other assumptions are also used in practice.

The absorbed dose rate integration workflow: It implements the calculation of absorbed dose rates at the voxel scale for each acquisition time. Different computational algorithms are considered: local energy deposition (LED), homogeneous convolution using FFT and Monte Carlo (MC) simulation. Then, the temporal integration is performed on average absorbed dose rates defined for each VOI, and at each time, to obtain the final absorbed dose per organ. This workflow allows taking into account the variations in volume, shape and mass of the organs during the treatment. It also provides the absorbed dose rate which is a parameter conditioning the biological effect of radiation in MRT.

Time integration was developed in both cases as a pharmacokinetic fitting tool, which produces a table of cumulative activities or absorbed doses.

Finally, a discussion of the desirable features of a dosimetry package is presented.

chapter 3 presents an open source module named OpenDose3D (OD3D), which performs dosimetry at the organ level of patients undergoing molecular radiotherapy, as a proof of concept of the proposed clinical dosimetric workflows. OD3D was developed under the open source philosophy to promote academic approaches and sustainability of the developments. In this sense the software is not only accessible to all, but also modifiable through proposals to the management team. OD3D was created as a 3D-Slicer python module.

The OD3D module implements different steps such as DICOM normalization, CT resampling and SPECT/CT resizing to obtain the 3D density and activity maps. The volumes of interest (VOI) can be manually segmented by the user using specific 3D-Slicer modules. The registration of images acquired at different times is performed automatically using the Elastix module of 3D-Slicer (CT-CT registration). Except for the VOI/organ segmentation during the dosimetric process, all calculation steps are fully automated.

The module is available as an official module of 3D-Slicer, which allows its installation via the extension manager. The source code was made available on internet with a user manual and a developer manual.

chapter 4 presents a full benchmarking of OD3D. To guarantee the quality of the development, a continuous integration and continuous delivery (CI/CD) method was implemented in the form of a test suite. The successive upgrades are guaranteed to preserve the functionality of the defined workflows based on the performed tests. If a test fails, then the upgrade is rejected.

OD3D is aimed to be accepted by the community as a valid standard solution. For this, every section of the software has to be tested and validated against other accepted solutions.

Each step in the workflow implementation is tested by comparison against an established software (either academic or commercial).

We used two commercial software to perform all steps in the dosimetry workflow on a test patient, and we compared the results against OD3D. A comparison in segmentation algorithms, activity measurement and time integration process was also made.

Finally, a comparison of the different absorbed dose rate algorithms included in OD3D is presented with a comparison between them.

chapter 5 presents a clinical implementation of the whole work (workflows + OD3D) as part of the MEDIRAD project. OD3D was utilized to produce clinical dosimetry data for 71 patients in three clinical centers.

Finally, a general conclusion is presented, with questions that are still pending and perspectives for future work.

Theoretical framework

Contents

1.1	General background	9
1.1.1	Brachytherapy	11
1.1.2	Selective internal radiotherapy (SIRT)	11
1.1.3	Molecular radiotherapy (MRT)	11
1.2	Pharmacokinetics	13
1.3	Dosimetry in internal radiotherapy	15
1.3.1	MIRD formalism to calculate the absorbed dose	18
1.3.2	Model based dosimetry	19
1.3.3	Patient Specific dosimetry	24
1.4	Medical Images	25
1.4.1	Computed Tomography	25
1.4.2	Single Photon Emission Tomography	26
1.4.3	Positron Emission Tomography	27
1.4.4	Image reconstruction	28
1.4.5	Image corrections	30
1.4.6	System Calibration	31
1.5	Absorbed dose calculation algorithms	33
1.5.1	Local Energy Deposition	34
1.5.2	Convolution	35
1.5.3	Monte Carlo	38
1.6	Conclusions	38

1.1 General background

According to the French National Institute of Cancer (INCa), cancer is the main cause of premature death in France since 2004. This can be appreciated in Figure 1.1. The main therapies to fight cancer nowadays are the surgical procedures, the chemotherapy and the external and internal radiotherapy. Not all these therapies have the same efficacy against all

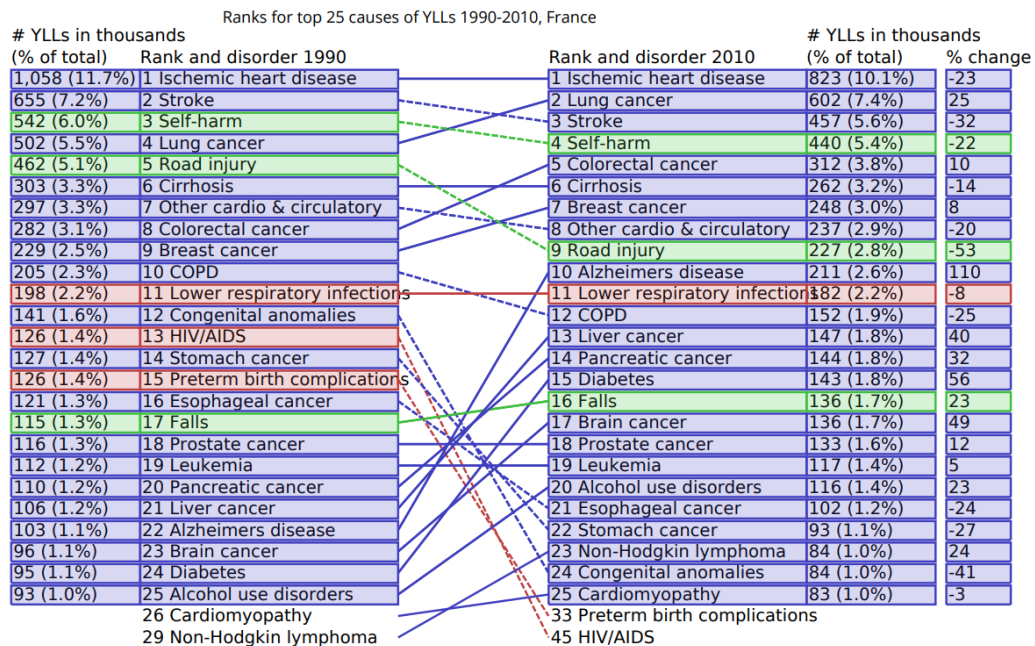


Figure 1.1: Change in the top 25 causes of years of life lost (YLL) due to premature mortality in France from 1990 to 2010. http://www.healthdata.org/sites/default/files/files/country_profiles/GBD/ihme_gbd_country_report_france.pdf

cancers, since the disease can have very different behaviors such as rapid evolution, metastatic processes or just resistance to therapeutic procedures.

Radiotherapy consists in the use of ionizing radiation, which provokes damage at cellular level, specially in the DNA where it can destroy some critical bonds and eventually induce cell death.

External radiotherapy makes use of ionizing beams (X-Rays, γ -rays, electrons, protons, etc.) produced by some external equipment. This is by far the most used approach for radiotherapy. It works for identified targets that are the majority of cases, but in the case of diffused or non-visible targets, it is impossible to apply it without increasing the risk of normal tissue complications in the patient. A more comprehensive background for external radiotherapy can be found in [HILL 2014].

Internal radiotherapy is generally utilized where external radiotherapy can't be applied. It can be used either as main therapy, or concomitant/sequential to external radiotherapy. It can be subdivided in three procedures: brachytherapy, selective internal radiotherapy (SIRT), and molecular radiotherapy (MRT). A more comprehensive background for internal radiotherapy can be found in [STELSON 1995].

1.1.1 Brachytherapy

Brachytherapy is an internal radiotherapy procedure that consists in the introduction of sealed radioactive material inside or very close to solid tumors. The common isotopes used are ^{137}Cs , ^{60}Co , ^{137}Cs and ^{192}Ir . These isotopes have a wide range of physical properties like different emitted particle type, energy and range. The usual procedure is the use of some guide (catheters, etc.) to place the source in the desired position, then a device exposes the isotope during the desired time. Another possibility is the use of permanent implants using grains (i.e. ^{192}Ir for prostate implants).

Brachytherapy can be used on well identified, accessible tumors, it is usually not suitable for multiple tumors. A comprehensive background for brachytherapy can be found in [MARWAHA 2013].

The main advantage compared to the other procedures, is the limitation of the irradiation of surrounding healthy tissues, which allows a better control in the therapy effects. The main disadvantage is the requirement of a very invasive procedure to place the source directly inside the patient.

1.1.2 Selective internal radiotherapy (SIRT)

Selective internal radiotherapy (SIRT) is an internal radiotherapy procedure that consists in the administration of sealed sources of minuscule dimensions through arteries irrigating tumors. The main example is the liver radio-embolization using ^{90}Y micro-spheres [WOLLNER 1988; PÖPPERL 2005].

The main advantage is the selective targeting of unresectable tumors, destroying them with short ranged radiation, with minimal effect on healthy tissue. The disadvantage is that it is restricted to tumors that are irrigated by unique arteries.

1.1.3 Molecular radiotherapy (MRT)

Molecular Radiotherapy (MRT) is an internal radiotherapy procedure that consists in the administration of radio-labeled pharmaceuticals (radiopharmaceuticals). The pharmaceuticals used are in general molecules (peptides, immuno-conjugates, etc.), which are modified with a radionuclide trap (chelator) in which an isotope (metallic) can be incorporated [IAEA 2015]. The objective is to have a selective molecule that targets cellular receptors or participates in cellular metabolism, transporting the isotope only to the desired cells. The targets can be the different parts of the cell: nuclei, membrane, etc. A comprehensive background for MRT can be found in [BUSCOMBE 2012].

The main advantage compared to the other procedures, is a selective destruction of cells. The radiopharmaceuticals are usually administered in a systemic way, and therefore the

biodistribution and pharmacokinetics should ensure that no detriment is caused to healthy tissues.

The main disadvantages are the search for the right molecule that generates really expensive treatments compared to other internal radiotherapy procedures. However, as shown in some studies¹, the cost of chemotherapy treatments can be in average 58% higher than the cost of nuclear medicine treatments (including MRT).

In France, the molecules and isotopes allowed for MRT purposes are listed in the law (L 511-1 of French public health code). The isotopes used (^{131}I , ^{177}Lu , ^{90}Y) are mostly β^- -emitters, although a more recent approved treatment like XOFIGOTM uses ^{223}Ra , an α -emitter [HÖLLRIEGL 2021].

1.1.3.1 Isotope ^{131}I

^{131}I was the first ever used radioisotope in MRT [HERTZ 1946] as a form of NaI. It is used for the treatment of thyroid cancer and hyperthyroidism thanks to its natural affinity for iodine. Nowadays, by the use of other transport vectors, its use was extended to other types of cancers as neuroblastomas [GARAVENTA 1991; SCHMIDT 2016] and non-small cell lung cancer [YANG 2018].

^{131}I ($T_{1/2} = 8.02$ days) is a beta emitter (average kinetic energy of electrons emitted 192 keV) but it is also a high energy gamma emitter 364 keV (81.5%) [ECKERMAN 2008]. This makes this isotope to have effects in both penetrating and non-penetrating radiation range.

1.1.3.2 Isotope ^{177}Lu

^{177}Lu ($T_{1/2} = 6.65$ days) was initially used as a colloidal form for interstitial injection with the objective of peritumoral lymph nodules sterilization [KYKER 1956]. Nowadays, the applications of ^{177}Lu are extended to the peptide receptors radiotherapy (PRRT) [KWEKKEBOOM 2005], with ^{177}Lu -DOTATATE and other analogue peptides (DOTATOC, DOTANOC, etc.) in patients with endocrine gastro-entero-pancreatic tumors.

^{177}Lu is mainly a beta emitter with an average kinetic energy for the emitted electron of 149 keV [ECKERMAN 2008]. But it also has two gamma emissions with energies of 113 keV (6.23%) and 208 keV (10.4%) that are suitable for imaging.

¹Nomaswazi Cordelia Gabela, Comparison of the Costs of Treating Prostate Cancer with Standard Chemotherapy Regimens versus Targeted Nuclear Medicines, MSc dissertation, South Africa 2020, available at: https://ukzn-dspace.ukzn.ac.za/bitstream/handle/10413/19006/Gabela_Nomaswazi_Cordelia_2020.pdf

1.1.3.3 Isotope ^{90}Y

^{90}Y ($T_{1/2} = 64.2$ h) was used initially in SIRT for the radio-embolization of hepatic carcinomas with the development of micro-spheres made of glass [WOLLNER 1988] or resin [PÖPPERL 2005]. But it has also been introduced to MRT for the treatment of non Hodgkin Lymphoma [WISEMAN 2000] and neuroendocrine tumors [BUSCOMBE 2012].

^{90}Y is a pure beta emitter (no gamma), with an average kinetic energy of electrons emitted of 932 keV [ECKERMAN 2008]. Imaging can be made using the bremsstrahlung for SPECT cameras [KIM 2011]. Using PET cameras is also possible because of a minor decay branch to the 0^+ first excited state of zirconium-90 followed by $\beta^-\beta^+$ internal pair production at a very low branching ratio of $(31.9 \pm 0.5) \times 10^{-6}$ [KAO 2013].

1.2 Pharmacokinetics

In dependence of the procedure, the isotope used is either placed inside the patient with a sealed source (brachytherapy), administered in static containers (brachytherapy grains placed directly or SIRT spheres injected by trans-arterial embolization), administered as a radiopharmaceutical by intravenous injection (MRT) or ingested as a chemical form in a compressed pill (MRT).

In the case of brachytherapy and SIRT, the source activity is well known as it can be measured directly before the procedure. Moreover, once placed, the sources don't change in position or in time. For MRT, the source is distributed inside the patient and its activity concentration highly depends on metabolic processes. In this case the activity concentration do vary in position and in time.

Pharmacokinetics is the characteristic interactions of a drug and the body in terms of its absorption, distribution, metabolism, and excretion [GARATTINI 2007]. In the case of radiopharmaceuticals, it can be measured in time using radiation detectors [ICRP30 1979] or specifically using the medical images [ICRP68 1994].

Measuring the amounts or the concentrations of drugs in blood, urine or other fluids, tissues or organs at different times after the administration, much information can be obtained on drug absorption and on the passage of drug molecules between blood and tissues and finally on the drug elimination [URSO 2002].

Figure 1.2 show the typical pharmacokinetics of a radiopharmaceutical inside a typical organ. It can be split in two main processes: uptake and washout. During uptake process the radiopharmaceutical is incorporated in the organ, and then it is excreted after the metabolic process (washout). Since these two process occur at different speed, there is one phase where uptake is predominant and a second phase where washout is predominant.

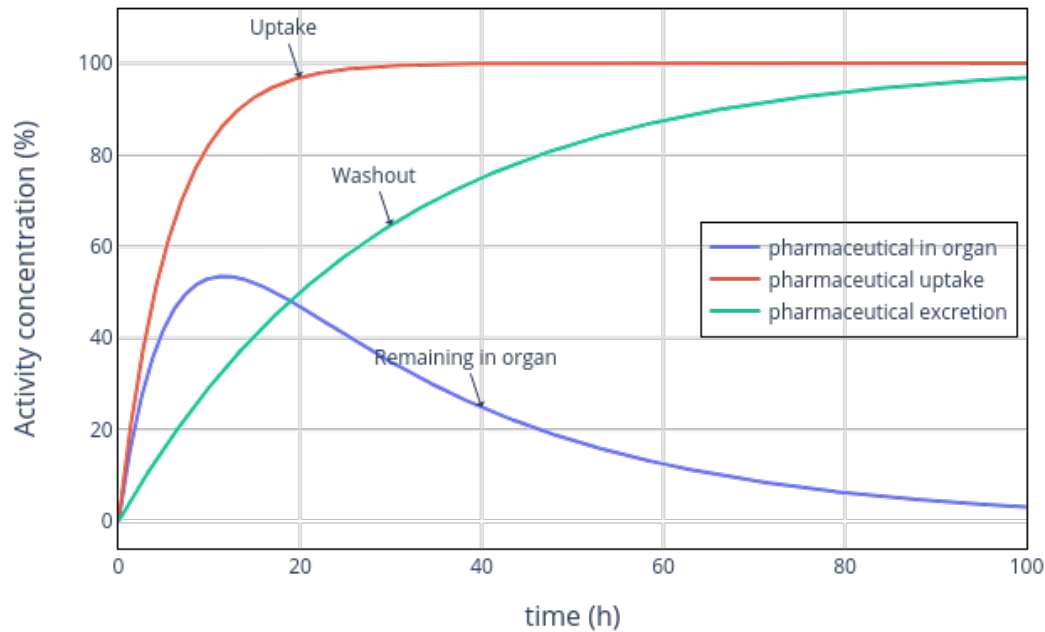


Figure 1.2: Typical processes in the pharmacokinetics of a radiopharmaceutical inside an organ: Uptake and washout

The main characteristics of the PK curve are [URSO 2002]:

- peak concentrations (C_{max})
- peak time (T_{max})
- terminal half-life ($T_{1/2}$)
- area under the curve (AUC)

Figure 1.3 show where to find the main characteristics of the PK curve. In the case of $T_{1/2}$, it has to be extracted from the last section of the curve (tail), where there is no longer an influence of the uptake, and the curve can be approximated to a mono exponential.

A typical PK estimation has to deal with time sampling of the measurements. In the case of internal radiotherapy, this time sampling is the acquisition time points.

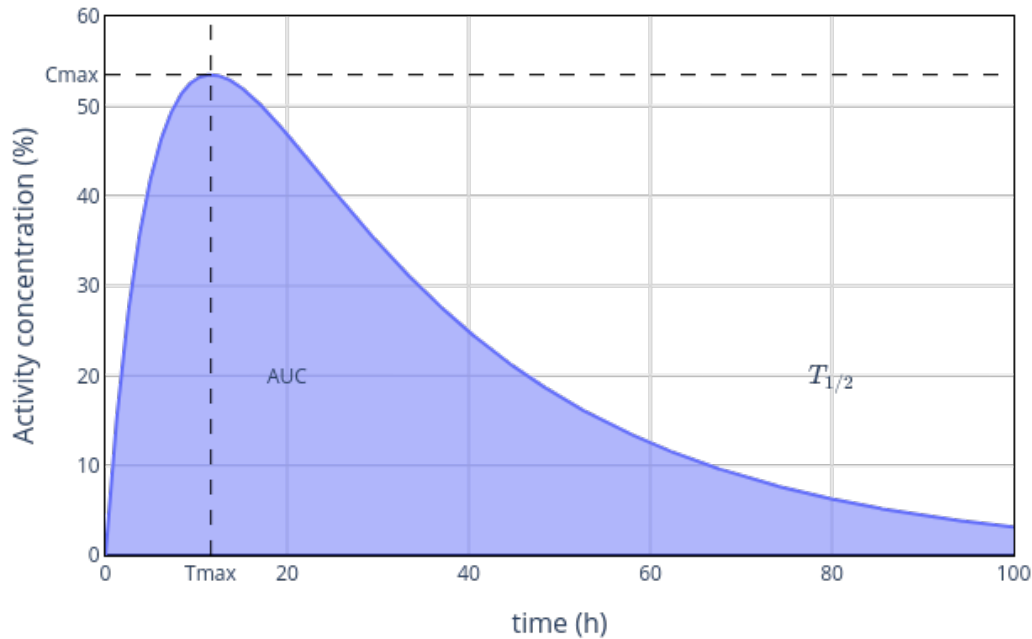


Figure 1.3: Main characteristics of the PK curve: (T_{max}, C_{max}) is the coordinate of the peak, AUC is the area under the curve that obtained by integration to infinity, and $T_{1/2}$ is the terminal half-life obtained by assuming mono exponential behavior of the tail.

1.3 Dosimetry in internal radiotherapy

Dosimetry is the determination and measurement of the amount or dosage of radiation absorbed by a substance or living organism by means of a dosimeter. In radiotherapy in general the magnitude used is the absorbed dose (D). The absorbed dose [$\text{Gy} = \text{J}\cdot\text{kg}^{-1}$] is defined by the International Committee for Radiological Units (ICRU) as the energy deposited (E) in a certain mass (m) of material [ICRU REPORT 10A 1962], Equation 1.1. The absorbed dose rate (\dot{D}) is defined as the differential in time of the absorbed dose, Equation 1.2.

$$D = \frac{E}{m} \quad (1.1)$$

$$\dot{D} = \frac{dD}{dt} = \frac{dE}{mdt} \quad (1.2)$$

The International Commission on Radiological Protection (ICRP) initially defined the "maximum permissible radiation dose per organ", that was tabulated for the main body organs and intended only for radiation protection [ICRP2 1959], and therefore did not consider the situation of radiotherapy. This list was extended [ICRP10 1968] to include the metabolic processes of radionuclides inside the human body. However, these data were tabulated for healthy adults with the purpose of radiation safety, and the pharmacokinetics may be radically different in particular diseases for non-healthy patients. Also, these data have not contained information regarding the distribution of radionuclides in pregnant women, fetuses or children [ICRP17 1969]. In the [ICRP60 1990], the radiation dose was finally renamed absorbed dose.

In February 1968, the Committee on Medical Internal Radiation Dose (MIRD) issued their first three pamphlets. Pamphlet No 1 [LOEVINGER 1976] defined the formalism to calculate the radiation dose (posteriorly named absorbed dose in subsequent revisions). Some definitions and units differed from the ICRP nomenclature but the mathematical formalism, and the simplified procedure to calculate the absorbed dose were an outstanding addition to the tabular data from ICRP.

The energy deposition ratio ($\frac{dE}{dt}$) depends on the characteristics of the media (density and composition), the radionuclide emission spectra and the activity. The activity can be measured using functional images. The mass can be measured using anatomical images. Therefore, an integration over time using the pharmacokinetic data is possible to calculate the absorbed dose.

In 1968 the MIRD defined the residence time τ [s] as the normalization of the time-integrated activity respect to the administered activity A_0 [Bq] [LOEVINGER 1976], this was renamed as the time integrated activity coefficient (TIAC) [BOLCH 2009], and represents an easy way to tabulate the pharmacokinetics:

$$\tau(r_S, T_D) = \frac{\tilde{A}(r_S, T_D)}{A_0} \quad (1.3)$$

Where $\tilde{A}(r_S, T_D) = \int_0^{T_D} A(r_S, t) dt$ [Bq·s] is the time-integrated activity (or total number of nuclear transformations) in source tissue r_S over integration period T_D .

The pharmacokinetics is then the main variable taken into account when estimating an administration to get a response to the treatment [SAWIN 1997]. The level of radioactivity administered is primarily fixed, sometimes adjusted by body weight, body surface area, or clinical factors. Prescription levels for different treatments are commonly determined empirically, using similar approaches as for chemotherapy [STOKKE 2017].

Dosimetry is a means to get an objective picture of the delivered irradiation, but is useful if it is correlated to the effect, in order to allow therapy optimization. This is difficult to get as it is basically not studied. [STRIGARI 2014] reports examples where the absorbed dose effect relationships (ADER) in MRT were observed. The efficacy of radiotherapy is bounded with the biological effect that it provokes not only in the tumor but also in the normal tissue.

In external radiotherapy the measure of the efficacy of the treatment is defined as the Tumor Control Probability (TCP) and the Normal Tissue Complications Probability (NTCP) [WARKENTIN 2004]. These two magnitudes are defined in base of the absorbed dose to the tissue (D), the type of radiation, the cellular radiosensitivity (α and β parameters are tissue-specific constants that represent the survival curves of cells [WESSELS 2008]) among other variables.

During internal irradiation in nuclear medicine in contrast to external irradiation the cells and organs are continuously irradiated over a longer period with a permanently changing dose rate. This might modify the impact of the ionizing radiation although the same absorbed dose is delivered. Because of the continuous irradiation in nuclear medicine, the repair of cell damage is already taking place during therapy. Therefore, new magnitudes must be defined.

[FOWLER 1960; FOWLER 1963] defines the Biologically Effective Dose (BED) in function of the absorbed dose as:

$$BED(D(r_T)) = D(r_T) \cdot RE(D(r_T)) \quad (1.4)$$

Where $D(r_T)$ is the absorbed dose in the target region and $RE(D(r_T))$ is the relative effectiveness defined as:

$$RE(D(r_T)) = 1 + \frac{G}{\alpha/\beta} \cdot D(r_T) \quad (1.5)$$

Where α and β parameters are the same as for external radiotherapy and the factor G is expressed as:

$$G = \frac{\lambda}{\lambda + \mu} \quad (1.6)$$

Where $\lambda = \ln 2/T_{1/2}$ is the decay constant of the radionuclide and μ is the sub-lethal damage recovery constant (assuming an exponential repair rate). This way, G is defined in terms of sub-lethal damage taking place during therapy.

Finally, the cell surviving fraction (F_S) is expressed in terms of the BED as:

$$F_S = \exp(-\alpha \cdot BED(D(r_T))) \quad (1.7)$$

1.3.1 MIRD formalism to calculate the absorbed dose

The MIRD Pamphlet 21 [BOLCH 2009] was proposed for the standardization of the nomenclature used in dosimetric calculations between MIRD and ICRP. The MIRD formalism proposes some basic magnitudes.

- The absorbed fraction $\phi(r_T \leftarrow r_S, E_i, t)$, defined as fraction of radiation energy E_i emitted within the source tissue r_S at time t that is absorbed in the target tissue r_T .
- The specific absorbed fraction (SAF) $\Phi(r_T \leftarrow r_S, E_i, t) = M^{-1}(r_T, t) \cdot \phi(r_T \leftarrow r_S, E_i, t)$ is defined as the ratio of the absorbed fraction and the target mass.
- The mean energy of the i^{th} transition per nuclear transformation is defined as $\Delta_i = E_i \cdot Y_i$ for the general case. But for β^- particles it is defined as the mean kinetic energy per disintegration of the emission spectrum $\Delta_i^{e^-} = E_{kinetic}^{e^-}$.

The S factor [$\text{Gy} \cdot \text{Bq}^{-1} \cdot \text{s}^{-1}$] is then defined as:

$$S(r_T \leftarrow r_S, t) = \sum_i \Delta_i \cdot \Phi(r_T \leftarrow r_S, E_i, t) \quad (1.8)$$

This is the radionuclide and geometry specific quantity representing the mean absorbed dose rate to target tissue r_T at time t after administration per unit activity present in source tissue r_S . The value of S, tabulated for reference dosimetry, is based on pre-constructed whole-body models representing reference individuals of a given sex, age, total body mass, and standard height.

The absorbed dose rate (ADR) in [$\text{Gy} \cdot \text{s}^{-1}$] for a target tissue r_T can be expressed as:

$$\dot{D}(r_T, t) = \sum_{r_S} A(r_S, t) \cdot S(r_T \leftarrow r_S, t) \quad (1.9)$$

Where $A(r_S, t)$ [Bq] is the time-dependent activity of the radiopharmaceutical in source tissue r_S .

The mean absorbed dose $D(r_T, T_D)$ to target tissue r_T over a defined integration period T_D after administration of the radioactive material to the subject is given as:

$$D(r_T, T_D) = \int_0^{T_D} \dot{D}(r_T, t) dt = \sum_{r_S} \int_0^{T_D} A(r_S, t) \cdot S(r_T \leftarrow r_S, t) dt \quad (1.10)$$

In some situations where the time dependence of S can be neglected, the Equation 1.10 may be reduced to the following time-independent form:

$$D(r_T, T_D) = \sum_{r_S} \tilde{A}(r_S, T_D) \cdot S(r_T \leftarrow r_S) = A_0 \sum_{r_S} \tau(r_S, T_D) \cdot S(r_T \leftarrow r_S) \quad (1.11)$$

That is expressed in terms of the time integrated activity coefficient $\tau(r_S, T_D)$.

1.3.2 Model based dosimetry

In reference dosimetry, the absorbed dose can be calculated using S-values from a reference model. This type of dosimetry is implemented for new radiopharmaceuticals during the course of their development. Reference dosimetry is meant to document the irradiation delivered by standard procedures. Reference models are used to allow the comparison between different radiopharmaceuticals. Keeping the dosimetric model constant allows for a fair comparison of the dosimetric properties of different radiopharmaceuticals [MORA 2019].

Standardized model are derived from population studies to simulate the human body. The initial models, like that defined in [ICRP23 1975], were used to calculate dosimetric factors in the subsequent publications [ICRP30 1979; ICRP68 1994] by using local energy deposition (using $\phi(r_T \leftarrow r_S, E_i, t) = \delta_S^T$) of charged particles.

The reference models can be classified accordingly to geometry definition.

Mathematical models: approximates every organ and the whole body to a set of geometrical shapes. The main purpose is to be able to use analytical or Monte Carlo methods to calculate the organ S factors directly in the model. The Oak Ridge National Laboratory (ORNL), proposed their first "reference man" models in 1960 [ICRP2 1959], improving it later as a hermaphrodite adult [ICRP23 1975], and extended posteriorly to represent several age models [CRISTY 1987]. These models were also used by [ICRP30 1979; ICRP68 1994] to estimate organ to organ dosimetric factors. Figure 1.4 show the ORNL age-specific models.

Voxelized models: are a 3D distribution of voxels representing several quantities (material, composition, density, organ or tissue). Initial models like the Zubal [ZUBAL 2000] have been used extensively. [ICRP110 2009] presented a reference adult male and female. [ICRP133 2016] used these models to publish SAF values for mono-energetic sources. A larger work,

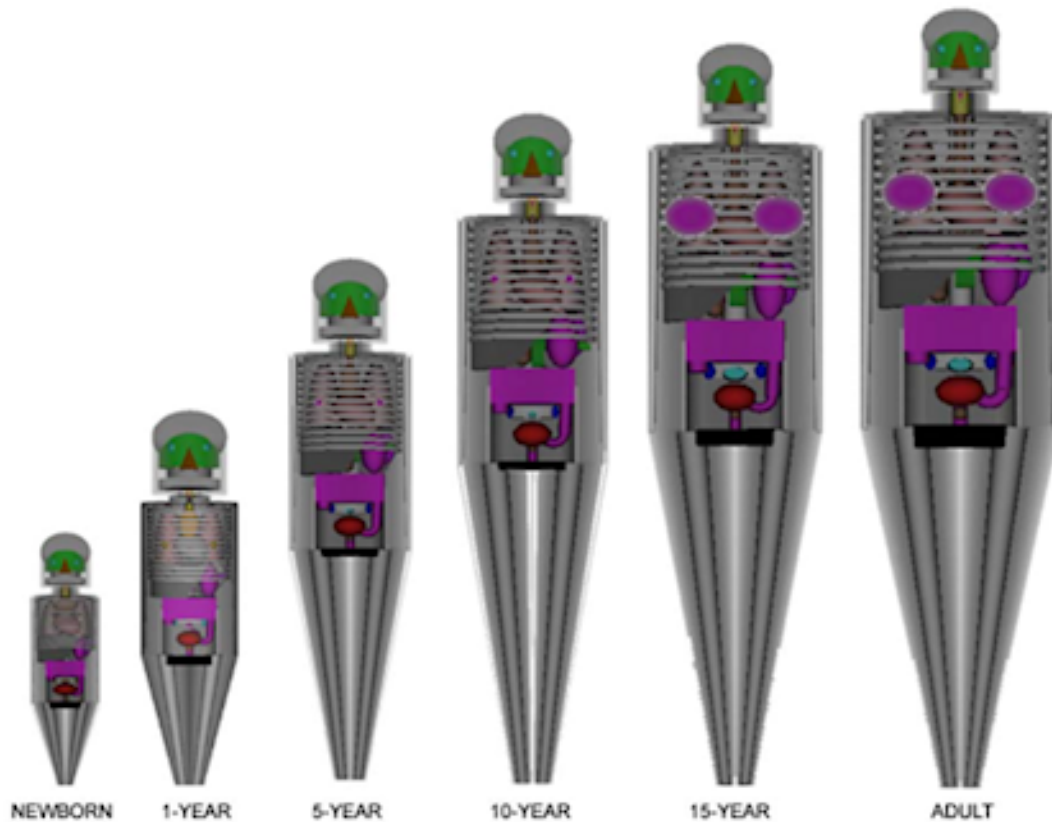


Figure 1.4: ORNL's age-specific mathematical anthropomorphic models.

similar to ICRP133, was made by OpenDose project [CHAUVIN 2020], including several independent teams and several calculation software to create a reference SAF database freely available. Figure 1.5 show the ICRP 110 voxelized models.

Hybrid mathematical models: these are mathematical models but using non-uniform rational B-spline (NURBS) meshes to represent each organ in the anatomical model. The main advantages are the possibility to deform each organ independently to adapt to specific situations and to have various spatial sampling that is critical for thin or small structures like eyes or organ walls. [ICRP145 2020] presented mesh based models of the same reference models defined in ICRP 110. Figure 1.6 show the ICRP 145 mesh based models.

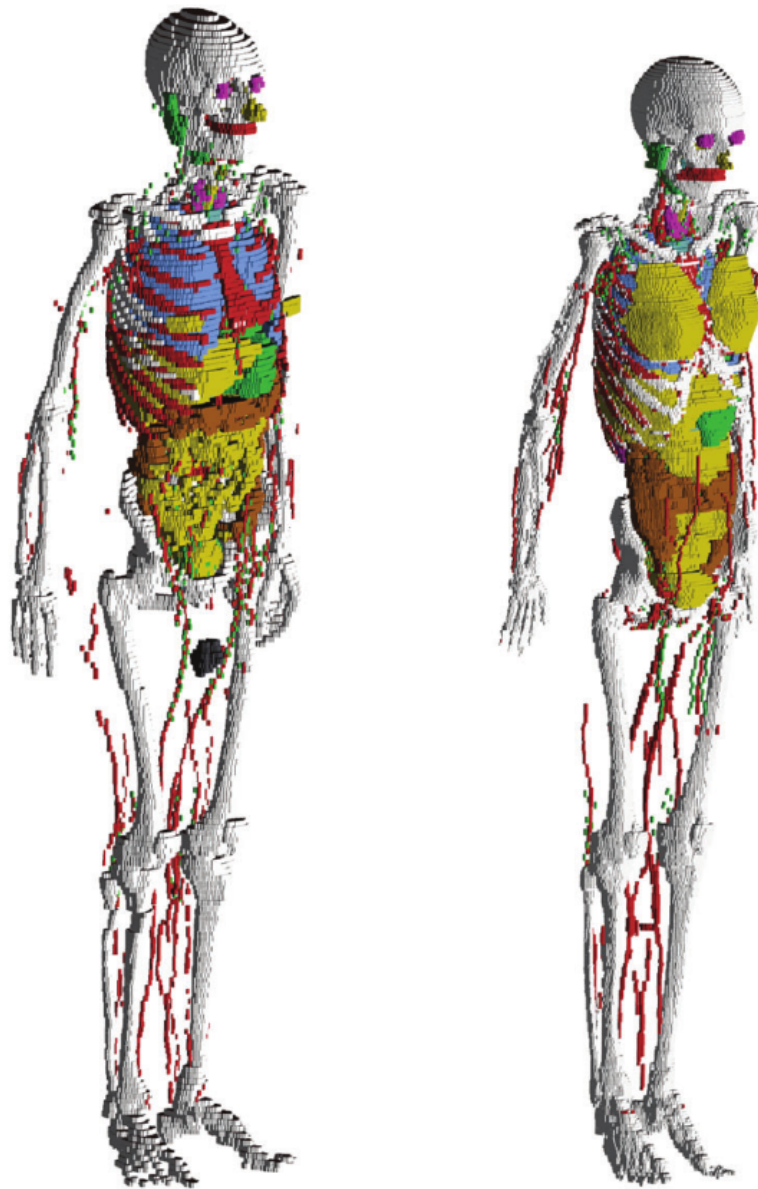


Figure 1.5: ICRP 110 voxelized models.

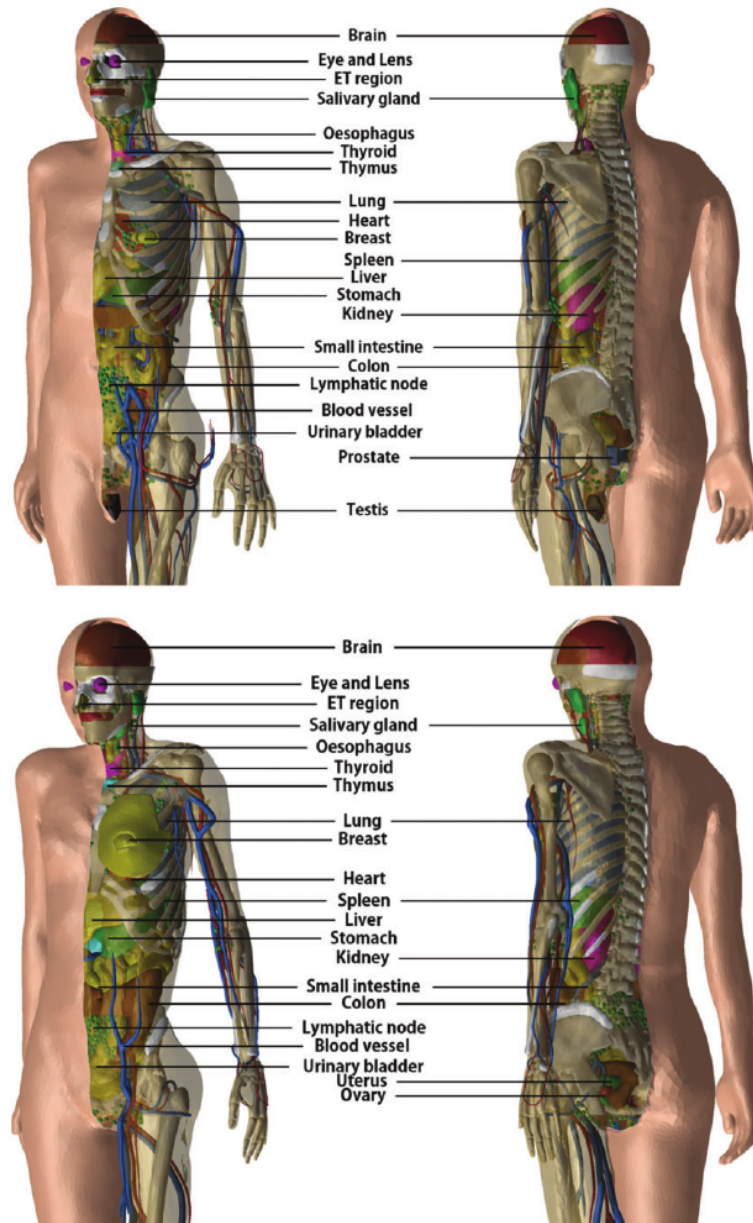


Figure 1.6: ICRP 145 mesh models.

As seen in Equation 1.10, the S values for different combination of sources and targets need to be used to derive the absorbed dose delivered. The S-values for the reference models are usually included inside some dosimetric solutions, which can perform the required calculations.

MIRDOSE: First published by [STABIN 1996], proposed a series of mathematical models to implement the absorbed dose calculations. While MIRDOSE 1 was an internal academic software, MIRDOSE 2 was released in 1987 for IBM compatible computers and included about 60 radionuclides and the mathematical models from the Cristy-Eckerman series [CRISTY 1987; STABIN 2004]. MIRDOSE 2 was widely distributed and used in the nuclear medicine community. MIRDOSE 3 was released in 1994 with more than 200 radionuclides and 10 models, with an added series representing the pregnant (3, 6, 9 month gestation time) and non-pregnant woman. Version 3 also includes a model for calculating self absorbed dose to small, unit-density spheres (such as tumors) and a much-improved and more detailed bone and bone marrow model. This software was discontinued [RIDIC 2000] per request of the FDA with concerns about its use as a medical device.

OLINDA/EXM: This software was created as a replacement for MIRDOSE, taking into account all the FDA recommendations [STABIN 2005]. It makes use of updated mathematical models and the principle is the same as MIRDOSE for calculating the S-values. These are used then to estimate the absorbed doses using user supplied residence times. The version 2.0 is included in the workstation Hermes [STABIN 2018] and includes new human NURBS models and nuclides.

MIRDCALC: The MIRDCalc internal dose calculation software has been developed as a community tool for calculating organ-level radiopharmaceutical dosimetry. The software enables biodistribution-to-dosimetry calculations using the MIRDC schema and incorporates calculation-specific details for 333 isotopes ([ICRP107 2008]) and a family of 12 ICRP reference phantoms (Male and Female; ages 0, 1, 5, 10, 15, Adult) with 81 source organs/regions and 43 target organ/regions and up to 5 spherical tumors [KESNER 2018].

IDAC 2.1: Available as both a software and a web application [ANDERSSON 2017], was developed based on the ICRP-specific absorbed fractions and computational framework of internal dose assessment given for reference adults in [ICRP110 2009; ICRP133 2016]. The program uses the radionuclide decay database of [ICRP107 2008] and considers 83 different source regions irradiating 47 target tissues, defining the effective dose as presented in [ICRP60 1990] and [ICRP103 2007] recommendations.

OpenDose Calculator: The OpenDose collaboration uses a collaborative approach to provide open access resources for nuclear medicine dosimetry [CHAUVIN 2020]. Utilizes the models provided by [ICRP110 2009] to compute the SAF, then internally computes the S values

for each of the 141 sources to all 172 targets. OpenDose brings together resources and expertise from 18 international teams to produce and compare traceable dosimetric data using 6 of the most popular Monte Carlo codes in radiation transport (EGSsrc/EGS++, FLUKA, GATE, Geant4, MCNP/MCNPX and PENELOPE). OpenDose Calculator [MCKAY 2018], is built as a Java application on top of the database of S values.

1.3.3 Patient Specific dosimetry

Model based dosimetry uses reference models to perform dosimetry [STABIN 2014]. But as there is a spread in the patients characteristics (sex, mass, metabolism, etc.), there is a need to include patient data in the dosimetry calculations in internal radiotherapy to account for patient variability.

However, for many years, model based dosimetry was the only possibility, due to the difficulty in implementing AD calculations from clinical images. With the introduction of the MIRD schema [LOEVINGER 1976], it was possible to get the AD directly from the pharmacokinetics, by using tables of S values calculated in models.

It is possible to perform a mass adjustment to the final estimations [PETOUSSI HENSS 2007]. Both OLINDA/EXM and IDAC2.1 are able to perform this correction, using measured masses for the desired regions. The correction for non-penetrating radiation is:

$$S(r_S \leftarrow r_S)^{patient} = S(r_S \leftarrow r_S)^{reference} \cdot \frac{m_S^{reference}}{m_S^{patient}} \quad (1.12)$$

and a second order correction for penetrating radiation is defined as:

$$S(r_S \leftarrow r_S)^{patient} = S(r_S \leftarrow r_S)^{reference} \cdot \left(\frac{m_S^{reference}}{m_S^{patient}} \right)^{2/3} \quad (1.13)$$

The correction for cross irradiation is usually considered as not necessary and by all means would be difficult to implement. [PETOUSSI HENSS 2007] mentioned that correction by mass is unnecessary even when the source and target are close to each other. Moreover, they concluded that another descriptor (related to geometry) for patient-specific scaling of reference S-values should be found.

The patient data obtained by some means of measurement, can be used partially or entirely in the dosimetry process. The most common data used is the mass as already described in this chapter. It is also possible to utilize the patient images acquired in the follow-up process, or scheduled to perform the dosimetry specifically in the patient treatment workflow.

Adjusting S values from a reference model to a given patient geometry is a fast way to personalize dosimetry. However, as some studies suggest [MARCATILI 2015], it does not take cross irradiation dosimetry into account. To account for all possible corrections, a full patient specific dosimetry is needed [STABIN 2019].

The evidence that patient specific dosimetry based on imaging yields better result in patient clinical outcome than model based dosimetry, has been reported by some authors [GARIN 2020].

1.4 Medical Images

To implement the clinical dosimetry based on imaging, the patient data in terms of activity distribution and density distribution must be measured by some means. In most cases, imaging equipment used in the hospitals will generate images objects (medical images), corresponding to volumetric data of some physical property (anatomical or functional) [BIDGOOD 1997].

The Digital Imaging and Communications in Medicine (DICOM) is the standard for the communication and management of medical imaging information and related data [GIBAUD 2008]. Among other things, DICOM defines format of objects for communicating images and image-related data.

As a result of imaging exam, imaging equipment generates DICOM files, where each file corresponds to one Instance, and is tagged with the information that allows to determine the Series, Study and Patient information to put it into the proper location in the hierarchy. There is a variety of DICOM objects defined by the standard. Most common object types are those that store the image volumes produced by the CT scanners. Those objects most often will have multiple files (instances) for each series. Image processing tasks most often are concerned with analyzing the image volume, which most often corresponds to a single Series. Figure 1.7 presents the hierarchy that the DICOM standard follows.

Examples of medical imaging procedures used are: Computed Tomography (CT) (anatomical image); Single Photon Emission Tomography (SPECT) (functional image); Positron Emission Tomography (PET) (functional image). With the combination of functional and anatomical images, it is possible to get the patient specific data (activity and density distributions) required to perform the dosimetry.

1.4.1 Computed Tomography

A CT scan or computed tomography scan (formerly known as computed axial tomography or CAT scan) is a medical imaging technique used in radiology to obtain detailed internal images of the body non-invasively for diagnostic purposes [FRIEDLAND 1996]. CT scanners use a rotating X-ray tube and a row of detectors placed in the gantry to measure X-ray

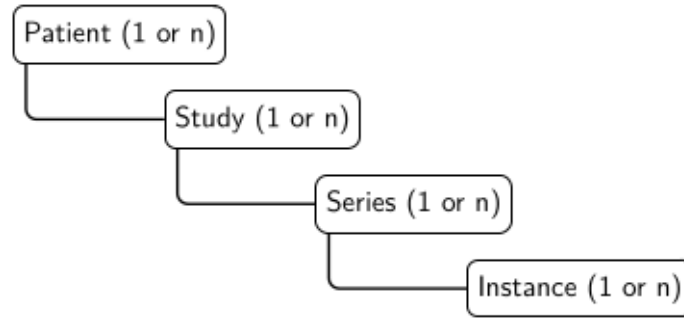


Figure 1.7: DICOM hierarchy: A DICOM folder contains 1 or several patients. A patient contains 1 or more studies that correspond to single imaging exam encounter. A study is made of 1 or more series that correspond to single image acquisitions, most often corresponding to a single image volume. A series consists of 1 or more instances with each instance corresponding to a single slice of the image

attenuation by different tissues inside the body. The multiple X-ray measurements taken from different angles are then processed on a computer using reconstruction algorithms to produce tomographic (cross-sectional) images (virtual "slices") of a body.

The result of a CT scan is a volume of voxels, a matrix array of physical properties, in this case relative attenuation. The relative attenuation is expressed with Hounsfield Units (HU) described by [HOUNSFIELD 1980].

$$HU = 1000 \cdot \frac{\mu_{tissue} - \mu_{water}}{\mu_{water} - \mu_{air}} \quad (1.14)$$

Where μ is the CT linear attenuation coefficient of the material. This equation for CT purposes is defined such as $HU_{air} = -1000$ and $HU_{water} = 0$ as arbitrary absolute values. This constrains allows rewriting Equation 1.14 as:

$$HU = 1000 \cdot (\mu_w^t - 1) \quad (1.15)$$

Where now μ_w^t is the electron density relative to water (EDW) of the tissue, and it is a dimensionless parameter.

1.4.2 Single Photon Emission Tomography

Hal Anger introduced the gamma camera as a novel detection technique able to visualize the activity distribution of an administered radionuclide or radiopharmaceutical [ANGER 1958].

The scintigraphy is a test in nuclear medicine, where gamma emitting radiopharmaceuticals are administered to a patient. The gamma rays escape from patient body and interacts with a scintillation crystal, after which detectors are placed to determinate the position of the interaction. A collimator is used to guarantee that detected photons came from a specific direction directly in front of the desired region. The discretization of the 2D space receives the name of pixel, and the dimensions of the image is named resolution. The image is then formed by storing the intensity of each pixel, which is related to the activity of the radiopharmaceutical. The set of collimator, crystal, detectors and image formation devices receives the name of gamma camera [ANGER 1958].

Single Photon Emission Tomography (SPECT) imaging is performed by using a gamma camera to acquire multiple 2-D images (also called projections), from multiple angles around the patient. Projections are acquired at defined points during the rotation, typically every 3 to 6 degrees. In most cases, a full 360-degree rotation is used to obtain an optimal reconstruction. The time taken to obtain each projection is also variable, but 15 s to 30 s is typical. This gives a total scan time of 20 min to 40 min.

Multi-headed gamma cameras can accelerate acquisition. For example, a dual-headed camera can be used with heads spaced 180 degrees apart, allowing two projections to be acquired simultaneously, with each head requiring 180 degrees of rotation, reducing total scan time by half with same setting as single head camera. Triple-head cameras with 120-degree spacing are also used.

A computer is then used to apply a tomographic reconstruction algorithm to the multiple projections, yielding a 3-D matrix oriented in the same reference frame than the patient. The individual matrix element values, named voxel, correspond to detections (counts) in the gamma camera and are proportional to the activity in the emission point. This data set may then be manipulated to show slices along any chosen axis of the body, similar to those obtained from other tomographic techniques, such as CT.

1.4.3 Positron Emission Tomography

Positron Emission Tomography (PET) is a functional imaging technique, similar to SPECT, that uses radiotracers to visualize and measure changes in metabolic processes, and in other physiological activities including blood flow, regional chemical composition, and absorption.

The difference to SPECT is that the radiotracers must be β^+ -emitters and that a coincidence detection process is added to measure only positron-electron annihilation [KHALIL 2011]. Different tracers are used for various imaging purposes, depending on the target process within the body. For example, ^{18}F -FDG is commonly used to detect cancer, $\text{Na } ^{18}\text{F}$ is widely used for detecting bone formation, and ^{15}O is sometimes used to measure blood flow.

The final image is a 3-D volume of voxels representing the coincidence events, that are proportional to the radiotracer concentration. Most recent PET scanners already make the conversion, reporting directly the radiotracer activity concentration.

1.4.4 Image reconstruction

Historically, image reconstruction was a clinical need for CT scans, and with the time it became also a need for other medical procedures like SPECT and PET [WILLEMINK 2018]. The problem is to build a 3D image, representing some physical quantity, starting from 2D projections.

Originally, CT images were reconstructed with an iterative method called algebraic reconstruction technique (ART) [GORDON 1970; FLEISCHMANN 2011]. Due to lack of computational power at the moment, this technique was quickly replaced by simple analytic methods such as filtered back projection (FBP). FBP was the method of choice for decades, until the first iterative reconstruction (IR) technique was clinically introduced in 2009 with the introduction of more powerful calculation hardware [STILLER 2018].

The back-projection is the technique in which an estimate of the original 3D matrix is made based on the available projections. Figure 1.8 show the steps of the back-projection technique.

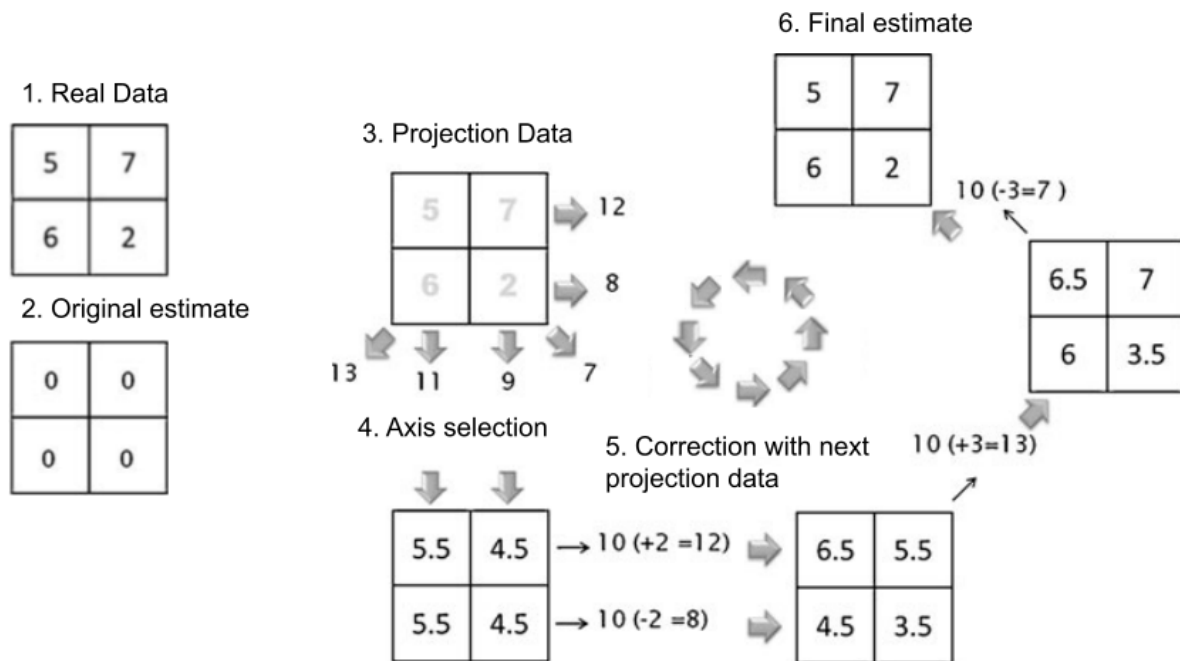


Figure 1.8: Back-projection technique. To calculate the four pixel values in the image from the measured ray sums, the original estimate starts with all pixel values at zero. Starting arbitrarily with the vertical rays, the ray sums in the estimated image are all zero, but the measured values are 11 and 9. These "errors" are divided equally between the two pixels along each ray (5.5 in the two left pixels, 4.5 in the two right pixels). Next, the horizontal ray sums in the estimated image (both 10) are compared with the measured values (12 and 8), and the resulting errors (+2 and -2) are added along the horizontal rays. Finally, the errors in the diagonal ray sums are all added in successive steps. In this simple case, the correct image is obtained in a single iteration, but typically, several iterations are required.

In the FBP, the projections are first convoluted with a filter or kernel, controlling the characteristics of reconstructed image data. The filter is necessary to compensate for the blurring resulting from nonuniform data sampling inherent to the CT acquisition process, and restores or enhances the edges of the structures of the imaged object.

The method of FBP is subject to several approximations regarding the CT data acquisition process. The approximations made in view of the CT imaging process, especially of noise free projection data not accounting for the variation of Poisson distributed photon count statistics, lead to a strong impact of image noise and the susceptibility to artifacts, e.g. caused by photon starvation of projections for CT acquisitions at low dose and in morbidly obese patients. Therefore, FBP does not offer much potential for radiation dose reduction, since reducing radiation dose results in increased image noise compromising diagnostic image quality [STILLER 2018].

To deal with the problems of FBP, the IR was reintroduced. An ideal IR method therefore consists of the following steps:

1. Based on an initial image estimate, derived from reconstruction using FBP, new projections are simulated by forward-projection (transition from image to projection space).
2. Comparing the new projections to the measured projections a correction term is calculated from their difference.
3. The current image estimate is updated by back-projection of the correction term (transition from projection to image space).
4. The process is repeated until some predefined criterion is met.

In the forward projection step, simulating projections of the current image data estimate requires a model of the imaging process. For CT, the model shall include the CT system optics as well as system statistic (radiation spectrum). For SPECT and PET, the model requires some way to deal with the radiation transport and will include the detector response characteristics.

Examples of iterative reconstruction methods are the Maximum Likelihood Expectation Maximization (MLEM), the Ordered Subset Expectation Maximization (OSEM) and the Model Based Iterative Reconstruction (MBIR). These algorithms differ only in how they implement the above steps. MLEM does a gradient based forward projection [LANGE 1987] in consecutive steps. OSEM does a calculation acceleration to the MLEM, although it has the same principle [HUDSON 1994]. A dedicated coincidence OSEM algorithm is available for PET reconstruction [LEVKOVILZ 2001]. MBIR is intended explicitly for CT [STILLER 2018].

Compared to FBP, the main strength of IR methods is an effective reduction of image noise and artifacts. Thereby, signal-to-noise (SNR) and contrast-to-noise (CNR) ratios increase, and visualization of low-contrast features is enhanced. For SPECT and PET, however, this is not enough, and further image corrections are needed.

1.4.5 Image corrections

Spatial resolution and detection sensitivity are two important performance characteristics that play an important role in molecular imaging research using SPECT and PET tracers. Although the clinical gamma camera can provide a tomographic resolution of about 10 mm, some preclinical SPECT scanners can provide a sub-millimeter spatial resolution pushing down to half millimeters. This situation is different in clinical and preclinical PET imaging where the spatial resolution of preclinical PET scanners is about 1.0 mm to 2.0 mm while that of clinical PET scanners lies in the range of 4.0 mm to 6.0 mm [KHALIL 2011].

Dedicated brain PET scanners, however, can achieve a slightly better spatial resolution (2.5 mm) in the central field of view. These resolution differences are mainly due to the fact that SPECT systems are not affected by some physical and fundamental limits that hinder the PET camera to reach sub-millimeter ranges, although some research groups were able to achieve a resolution of less than 1mm using fine segmented lutetium orthosilicate (LSO) crystal [KHALIL 2011].

Many factors serve to impact the final reconstructed images of data acquired from a PET scanner. These are crystal size, positron range, photon acollinearity, intercrystal interaction and scatter, depth of interaction and the reconstruction algorithm [SANCHEZ-CRESPO 2004]. The coincidence detection eliminates the need of the physical collimation used in SPECT, since the annihilation occurs in a very well-defined direction. The use of a time of flight detection from ultra rapid electronics, improve even more the spatial resolution.

SPECT degrading factors have been extensively studied in the literature [VAN GILS 2016] and, namely, include attenuation, scatter and resolution effects, in addition to motion artifacts. Apart from the later, most of these physical issues can be resolved in great part by the use of SPECT/CT systems [HWANG 2008]. With the use of the CT, the reconstruction algorithm can perform attenuation and scatter correction. More corrections can be made by simulating the detector/collimator response [IAEA 2009]. The final SPECT image still has a high uncertainty when converted to activity because of partial volume effects (PVE), dead time, detector response and septal penetration.

The attenuation correction is that part of the reconstruction process whereby those counts (events) assumed lost due to attenuation within the object are restored. This correction may be performed prior to, during or after the main reconstruction operation and usually requires knowledge of the distribution of attenuating tissue, for example, of the outside surface of the patient (the body contour) and not just of the distribution of the activity within the body.

The scatter correction is the process to eliminate the effects resulting from scattered photons registered within the photopeak window. Such a scatter correction may sometimes be performed by software alone, by collecting data from a different (lower) energy window or by use of asymmetric or multiple energy windows. Another possibility to do scatter correction is by performing a Monte Carlo simulation using the CT to get the scatter image; this is then subtracted from the respective projection during the reconstruction process.

The partial volume effect is the loss of signal (normally observed as a loss of contrast) that occurs when an object partially occupies the sensitive volume of an imaging instrument (usually in space, but also in time), i.e. slice thickness effects and the point spread function (PSF) effects. Movement effects are also included. PVE causes an apparent loss of contrast of small objects. This effect will depend not only on the size of the objects but to some extent on the shape of the object.

1.4.6 System Calibration

The calibration is the process of checking a measuring instrument to see if it is accurate. In the case of medical imaging, our measuring instruments are the CT and the PET/SPECT scanners.

The CT calibration is commonly made using phantoms with density inserts. Scanner specific parameters, like the kVp, beam quality, beam hardening, filter and reconstruction algorithm used, can affect the CT number in Hounsfield unit (HU) of each voxel as defined by [HOUNSFIELD 1980].

Figure 1.9 show a typical calibration phantom with inserted rods of known electron density relative to water (EDW).

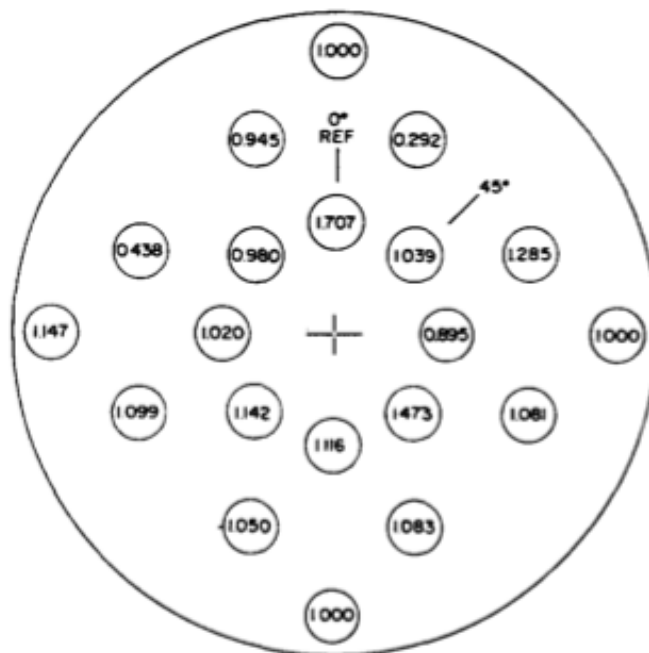


Figure 1.9: A 33 cm diameter electron density calibration phantom. The numbers represent EDW for each rod. Manufactured by RMI and explained in detail by [CONSTANTINO 1992].

The inserted rods also have known density values, allowing to calculate the HU to density calibration curve.

A descriptive explanation on how to perform SPECT quality controls can be found at IAEA Human Health website, where the IAEA-NMQC toolkit is located [INTERNATIONAL ATOMIC ENERGY AGENCY 2018]. In this site there are a series of resources such as the IAEA Human Health Series 6 book [IAEA 2009], a series of online education courses (videos) on practical procedures for performing SPECT quality controls, and the IAEA-NMQC plugin for ImageJ, that allows to process the images obtained and report the required camera parameters. One of the quality controls described is the SPECT calibration, which reports the camera coefficient (sensitivity) that has to be controlled in time.

The SPECT sensitivity is defined as number of counts detected for some known activity in a standard phantom. A known activity concentration is placed into a specified phantom, normally a uniform cylinder. The phantom is filled with a known activity that is diluted in water to fill the entire volume. Then the phantom is leaved for some time (usually 6 hours) for homogenization process. Finally, a SPECT image is acquired and post-processed [IAEA 2009].

The image post-processing includes a reconstruction of the acquired SPECT projections to generate a 3D image. During this process some corrections must be applied by the use of CT (attenuation), using multiple acquisition windows (scatter) and by the use of detector characteristics (partial volume effect).

The final image obtained after reconstruction process is used to calculate the sensitivity. The result is normally expressed as counts detected per second per unit of activity concentration.

$$S \left[\frac{\text{counts}}{\text{MBq}\cdot\text{s}} \right] = \frac{C[\text{counts}]}{A[\text{MBq}] \cdot T_{cal}[\text{s}]} \quad (1.16)$$

Where $C[\text{counts}]$ is the total counts measured in the whole FOV of the image, $A[\text{MBq}]$ is the activity corrected by decay in MBq, and T_{cal} is the acquisition time of the calibration image in seconds. Usually C is corrected for background as:

$$C[\text{counts}] = V_t \cdot \left(\frac{C_{in}}{V_{in}} - \frac{C_{out}}{V_{out}} \right) \quad (1.17)$$

Where V_t is the real tank volume, V_{in} is the volume of the segmented region inside the tank A_{in} , V_{out} is the volume of a segmented region outside the tank A_{out} but still inside the FOV, C_{in} is the measured counts in A_{in} , and C_{out} is the measured counts in A_{out} .

The correction for decay of the activity is done in three steps: correction for syringe retention, correction for decay during homogenization process, and correction for decay during acquisition. The final value is:

$$A[\text{MBq}] = (A_{full} - A_{empty}) \cdot e^{-\lambda \cdot T_{decay}} \cdot \frac{1 - e^{-\lambda \cdot T_{cal}}}{\lambda \cdot T_{cal}} \quad (1.18)$$

Where A_{full} is the measurement of the syringe with full volume of the radionuclide, A_{empty} is the empty syringe measurement, $\lambda = \ln 2 \cdot T_{1/2}^{-1}$ is the radionuclide decay coefficient, $T_{1/2}$ is the radionuclide half life, and T_{decay} is the time during homogenization process.

Finally, any SPECT image acquired under the exact same protocol can be converted to activity map using a voxel by voxel operation of:

$$A_{voxel}[\text{MBq}] = C_{voxel}[\text{counts}] \cdot S^{-1} \left[\frac{\text{counts}}{\text{MBq} \cdot \text{s}} \right] \cdot T_{SPECT}^{-1}[\text{s}] \quad (1.19)$$

Where $T_{SPECT}[\text{s}]$ is the SPECT acquisition time in seconds. The measurement of this time must follow exactly the calibration procedure: if the acquisition is made using more than one head, then the number of heads shall be used (multiplied) in both T_{cal} and T_{SPECT} .

It must be said that if the SPECT does not follow exactly the same acquisition protocol than the calibration acquisition, then the sensitivity factor is a priori not valid for Equation 1.19. This restriction applies to the entire process including the reconstruction and all corrections that are made.

1.5 Absorbed dose calculation algorithms

SPECT/PET imaging can be used for activity determination, cumulative activity can be derived using PK estimations to be used in model-based dosimetry (using S values). CT imaging can be used to get anatomical data (density map, attenuation map) to perform corrections on the SPECT imaging (attenuation, scatter) and to estimate the organ/VOI mass in order to mass-adjust the S values from the models [BOLCH 1999].

To perform patient specific image-based dosimetry, images are used to define the geometry for radiation transport and absorption algorithm implementation. The absorbed dose calculation can be made in several scales such as voxel, combination of voxels (VOI) or entire organs. There are different algorithms to calculate the absorbed dose depending on the radiation type, the scale of the VOI involved and the characteristics of the media contained by the VOI.

1.5.1 Local Energy Deposition

The local energy deposition is an analytical method based on the assumption that all the kinetic energy of the charged particles emitted is absorbed locally in the same volume of the source. The simplicity of this assumption makes the calculation algorithm really fast.

The mean free path length of charged particles involved in nuclear medicine procedures is often less than one centimeter in water. The resolution of SPECT images is usually over a centimeter [KHALIL 2011], with resolution recovery techniques applied this resolution can be reduced to barely less than a centimeter. However, the voxel size of SPECT images are around 4.0 mm. For all these reasons, the kinetic energy deposition of the charged particles cannot be discriminated by the SPECT images and the deposition is made the inner vicinity of each emitting voxel. This allows calculating the absorbed dose using the MIRD formalism at voxel level [BOLCH 1999], where the emitting region has an absorbed fraction of $\phi(r_S \leftarrow r_S) = 1$.

$$D(r_T) = \frac{E_{kinetic}^{e-}}{m_{voxel}} \quad (1.20)$$

Where $E_{kinetic}^{e-}$ is the average kinetic energy per disintegration in [J] of electron spectra emitted by the isotope contained in the voxel and m_{voxel} is the voxel mass in [kg].

To calculate the absorbed dose rate (\dot{D}) in every voxel, given a density map $\rho_{i,j,k}$ in [$\text{kg}\cdot\text{m}^{-3}$] and an activity map $A_{i,j,k}$ in [Bq], the Equation 1.21 can be used. Both the activity map and the density map must have the exact same resolution.

$$\dot{D}_{i,j,k} = \frac{A_{i,j,k} \cdot E_{kinetic}^{e-}}{\rho_{i,j,k} \cdot V_{voxel}} \quad (1.21)$$

Where V_{voxel} is the volume of the voxels in [m^3].

To calculate the absorbed dose rate in a VOI or an organ, the procedure is similar.

$$\dot{D}_{organ} = \frac{E_{kinetic}^{e-}}{m_{organ}} \cdot \sum_{i,j,k} A_{i,j,k} \quad (1.22)$$

Where the sum covers all voxels belonging to the organ.

1.5.2 Convolution

Considering the medium as homogeneous, and taking into account the fact that the emission is isotropic, a response function in spherical coordinates can be defined as the dose-point kernel (DPK). The dose-point kernel represents the spherically symmetrical absorbed dose rate distribution due to a point source of activity at the center of a sphere [GIAP 1995].

$$DPK(r) = \frac{dE}{\rho \cdot 4\pi r^2 dr} \quad (1.23)$$

Where dE is the energy deposited per disintegration in the volume $dV(r) = 4\pi r^2 dr$. This is usually expressed with the linear energy transfer (J) as $J(r) = \frac{dE}{dr} = \rho \cdot 4\pi r^2 \cdot DPK(r)$.

The DPK is pre-calculated in water for several isotopes, this is a time-consuming process through Monte Carlo simulation (MC). It is also possible to pre-calculate it in other media, but generally it is possible to use other materials using the correction formalism proposed by [CROSS 1992] as shown in Equation 1.24. This formalism avoids new calculations for every material.

$$DPK(r) = \eta_w^3 \cdot \left(\frac{\rho}{\rho_w}\right)^2 \cdot DPK_w(\eta_w \cdot r) \quad (1.24)$$

Where DPK_w is the pre-calculated DPK in water, ρ is the density of the new material and η_w is the relative attenuation of the material respect to water.

The direct convolution of the activity map using the DPK as a response function was the first approximation used to perform the dosimetry [BERGER 1978]. The Equation 1.9 can be rewritten for a voxelized geometry in terms of a convolution as:

$$\dot{D}_{i,j,k}(t) = \sum_{m,n,o} A_{m,n,o}(t) \cdot S_{i,j,k \leftarrow m,n,o}(t) = \mathbb{A} \times \mathbb{S} \quad (1.25)$$

The operation is made as matrix convolution, and it is a very time-consuming operation. But it can be improved by performing the convolution in Fourier space. The dose-point kernel in spherical coordinates must be converted into rectangular coordinates in order to use the 3D FFT operation. This 3D rectangular matrix must be the same size and represent the same physical voxel as the activity matrix.

This method presents conceptual errors that are really gross in the close vicinity of each voxel: the Fourier convolution in this case acts as if all the activity of each voxel were

concentrated in its center, and the remaining of the voxel contains no activity. It is specially critical for self-absorbed dose. In Table 1 of MIRD 17 [BOLCH 1999], a relative difference of 60% is observed between point source and volumetric source respect to the same self volumetric target. To solve this issue, the MIRD 17 proposes to convert the DPK to voxel dose kernel map:

$$VDK(O \leftarrow A) = \iint DPK(R_{O \leftarrow A}) dV_A dV_O \quad (1.26)$$

Where the contribution of voxel A in voxel O is integrated over both volumes. With this definition it is now possible to write:

$$\dot{D}(i, j, k) = (\mathbb{A} \times \mathbb{VDK})(i, j, k) \quad (1.27)$$

Where both, \mathbb{A} and \mathbb{VDK} , are now matrix with same voxel size. The convolution can be made in matrix mode or using discrete Fourier convolution.

Another possibility to calculate the VDK matrix, is with direct MC, which may provide more realistic results. Using the MC, some authors like [LANCONELLI 2003] provided a database of pre-calculated VDK for selected voxel sizes, materials and isotopes. This approach is very time-consuming and not practical to implement as new voxel sizes and new isotopes appear frequently, having to recalculate everything every time.

Finally, it is also possible to generate the VDK from pre-calculated DPK [FRANQUIZ 2003], this allows to add new isotopes, materials, and voxel sizes on demand.

1.5.2.1 Generation of VDK from the DPK

The method used to derive VDK, starting with pre-calculated DPK, is described by [FRANQUIZ 2003]. It consists in a multidimensional Volume to Volume integral, performed using Monte Carlo integration of the DPK function, from voxel O to voxel A. O refers to the voxel in the origin of coordinates and A refers to any target voxel with coordinates (x, y, z) including O itself. Therefore, Equation 1.26 is transformed into Equation 1.28:

$$VDK(O \rightarrow A) = \sum_O \sum_A \frac{DPK(R_{O \rightarrow A})}{N} \quad (1.28)$$

Where the sum occur in randomly selected points inside the voxels A and O, N is the number of pair points simulated and $R_{O \leftarrow A}$ is the distance between a pair of the selected

random points from A and O respectively. As with any Monte Carlo algorithm, the more points are simulated, the more accurate is the result because of the Central Limit Theorem [DAVIDSON 1994]. Figure 1.10 presents the graphic interpretation of this procedure.

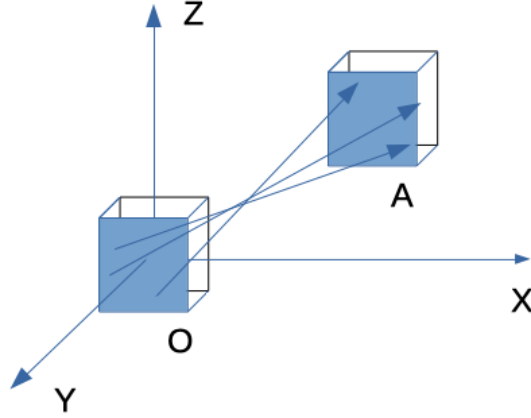


Figure 1.10: Integration of DPK over two voxels [FRANQUIZ 2003]

1.5.2.2 Using homogeneous VDK in heterogeneous geometries

In the common practice the absorbed dose calculation is performed in a non-homogeneous density map. For some large organs, like the brain and the liver, the deviation ($\delta = \frac{stddev}{mean}$) in the density can be neglected as it rounds the 2%. However, in the general case, this deviation is big enough to have an impact in the ADR calculation. To solve this issue some density correction solutions can be implemented.

Pre-density correction uses VDK different from water to perform the convolution. Using Equation 1.28 with the DPK calculated by Equation 1.24, it is possible to correct for density in large homogeneous organs.

Post-density correction uses VDK in water to perform the convolution and then divides voxel wise by the density map expressed in $[g \cdot cm^{-3}]$.

$$\dot{D}_{corrected}(i, j, k) = \frac{\dot{D}_{water}(i, j, k)}{\rho(i, j, k)} \quad (1.29)$$

These methods keep the speed of homogeneous convolution adding just a matrix division. But they don't take into account the traversed path density. This can lead to errors within regions of the body associated with tissue-air or tissue-bone interfaces [BOLCH 1999]. Moreover, they require that the density map must have the exact same resolution as the activity

map, otherwise the voxel-wise division is just not possible.

1.5.3 Monte Carlo

The Monte Carlo method consists in the use of random numbers to solve a variety of problems in several areas of interest. Monte Carlo simulations (MC) are a well-established method for studying physical processes in medical physics [SARRUT 2014]. There are several MC codes already available: Geant4 [AGOSTINELLI 2003; ALLISON 2006; ALLISON 2016], EGSnrc [KAWRAKOW 2020], FLUKA [FERRARI 2005], Gate [JAN 2004], MCNP [GOORLEY 2012].

The software GATE, based on the GEANT4 library from CERN, was specially designed to solve medical physics problems. GATE is an open-source MC toolkit for simulating imaging, radiotherapy (RT) and dosimetry applications in a user-friendly environment, which is well validated and widely accepted by the scientific community. In RT applications, during treatment planning, it is essential to accurately assess the deposited energy and the absorbed dose per tissue/organ of interest, as well as the local statistical uncertainty. Several types of realistic dosimetric applications are described including: molecular imaging, radio-immunotherapy, radiotherapy and brachytherapy.

MC simulations to solve dosimetry problems in medical physics are considered the gold-standard [AGOSTINELLI 2003; JAN 2004].

To perform the MC simulation for internal dosimetry using GATE, the density map and the activity map must be given. It is possible to extract the density map from the anatomical CT image. In the same way, the activity map can be extracted from the functional image either SPECT or PET. The Monte Carlo method runs in the CT resolution as it records simulated interactions with matter. In order to avoid the oversampling of the activity map due to difference in resolution with the density map, it is highly recommended having the same resolution in both the activity map and the density map. Although it is not mandatory in this case.

1.6 Conclusions

The internal radiotherapy procedures need to implement the clinical dosimetry process. In this chapter we have presented an overview of the basic elements that conform the clinical dosimetry.

Pharmacokinetics shows to be difficult to measure, but with the introduction of imaging methods it is possible to measure directly the variation of the activity concentration in time.

The clinical dosimetry can be subdivided in two main processes based on the initial data and assumptions. Model based dosimetry assumes a standard model for the conversion of activity to absorbed dose. Patient specific dosimetry uses patient images to get the initial

data (activity and density).

The conversion of activity to absorbed dose can be made with different approaches: local energy deposition, convolution and Monte Carlo.

The current status of the clinical dosimetry needs to be discussed and how it is implemented in the practice.

Clinical Dosimetry Workflows

Contents

2.1	Introduction	41
2.2	Clinical Dosimetry workflows	43
2.2.1	Academic solutions	44
2.2.2	Commercial workstations	46
2.3	The European Project MEDIRAD (H2020)	48
2.4	The IRDBB database	50
2.5	Proposed CDW in MRT	53
2.5.1	Calibration workflow	54
2.5.2	Absorbed dose via activity integration workflow	56
2.5.3	Absorbed dose via absorbed dose rate integration workflow	59
2.5.4	Desirable features of a dosimetry package	61
2.6	Conclusion	61

2.1 Introduction

In previous chapter, we presented MRT and the basics of radiopharmaceutical dosimetry. Clinical dosimetry is difficult to implement.

With the introduction of SPECT imaging [ANGER 1958], it is possible to measure directly the activity of the radiopharmaceutical inside the patient. Therefore, patient specific measurements for pharmacokinetic are possible.

For radiotherapy modalities such as external radiotherapy or brachytherapy, it would not be acceptable to treat patients without an accurate therapy planning, including determination of the absorbed doses delivered to target tissues and to organs at risk. For MRT, however, personalized dosimetry-based treatments have been the slowest to develop among the existing radiotherapy modalities [GLEISNER 2017].

The Council Directive (2013/59/Euratom) mandates the use of dosimetry-based treatment planning and verification of the absorbed doses delivered. In Chapter VII, Medical Exposures, Article 56, Optimization, it is stated that:

- For all medical exposure of patients for radiotherapeutic purposes, exposures of target volumes shall be individually planned, and their delivery appropriately verified taking into account that doses to non-target volumes and tissues shall be as low as reasonably achievable and consistent with the intended radiotherapeutic purpose of the exposure.

According to the same Directive (Chapter II, Definitions, Article 4, Definitions):

- radiotherapeutic means pertaining to radiotherapy, including nuclear medicine for therapeutic purposes.

With this Directive, the dosimetry process should be an integral part of the patient treatment in MRT.

However, for decades, there were few available dosimetric solutions and most were model based calculations (sometimes integrating patient specific corrections).

More recent developments attempted to integrate the AD calculations inside the patient data processing. With the increase of calculation power, and the decrease in workstation prices, patient-specific dosimetry became a real possibility, with academic and even commercial software. These solutions may implement some relevant steps in the patient data processing workflow.

The main problems of all these solutions are the lack of standardization in the data processing workflow, the non-traceability and the non-reproducibility of the individual steps in the calculation.

- The non standardization of calibration and acquisition protocols between vendors. This leads to non standardized data (extra coefficients, missing data fields, etc.).
- There are also intermediary results that can't be stored as data in the DICOM standard since there is no definition for them (non-traceability). This leads to vendor-specific solutions that cant talk with others, thereby limiting the possibility to benchmark.
- In order to check the results from one software there is little possibility to use another solution: If the individual steps are not recorded, any intermediary data may be lost. If they are recorded, they are stored in a proprietary format that can't be read by other software. Even using the same software, it may be difficult to reproduce entirely a calculation as sometimes critical intermediary data needs to be recalculated. (non-reproducibility)

Another problem is the non standardization of acquisition workflows between hospitals. This depends on the local situation (human resources and expertise, available technologies) including the ethics committees, all factors that eventually condition the acquisition/processing protocol. Some workflows are planar (Whole body scan, multiple time points), SPECT/CT

single time point, hybrid (a combination between planar and single SPECT/CT) and multiple time points SPECT/CT.

An optimal software solution would be one that implements a full workflow, adapted to each case. Currently, the usual procedure is to use a commercial or an academic software, combined with a set of tools to manipulate the data.

2.2 Clinical Dosimetry workflows

The clinical dosimetric workflow (CDW) is related to the phases associated to treat all medical images and data in a multi SPECT/CT or PET/CT scenario, in which the aim is to calculate the absorbed dose for specific organs/tissues. Usually this CDW is associated to a particular formalism, like the MIRD, in which data are acquired and processed. But, its broader than the dosimetry formalism as it defines a full chain from acquisitions to results, and not only the calculation steps. Figure 2.1 presents one example of clinical dosimetry workflow given in [BARDIÈS 2021].

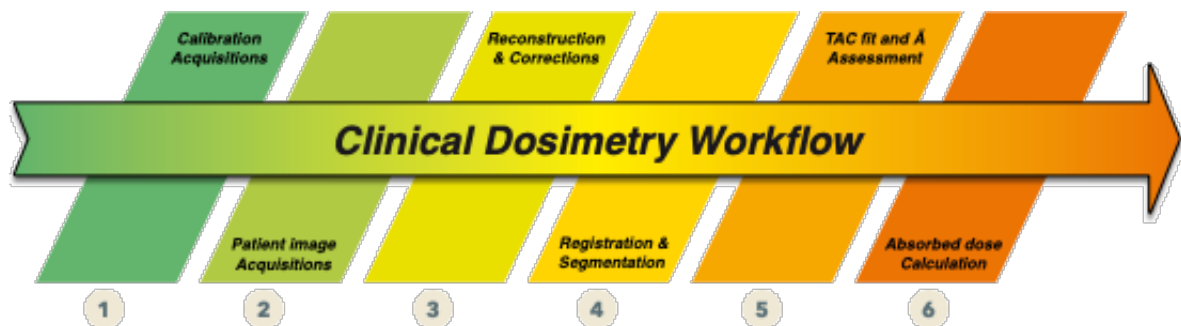


Figure 2.1: Simplified clinical dosimetric workflow, created by Manuel Bardiès [BARDIÈS 2021].

The different steps to process the patient data to perform the dosimetry are:

1. Image acquisition for calibration: In principle this acquisition should be done using the same protocol used for patient imaging. Normally a test-object (also called phantom) is used for that purpose. The objective is to calculate the calibration factor, which is going to relate the number of counts within the image with the quantified activity per voxel.
2. Patient image acquisition: This image covers one or several sections of the patient body, where critical organs and/or tumors are present. Depending on the dosimetric protocol, several sections can be obtained for the same time point measurement. In addition, usually several times point measurements are needed.
3. Reconstructions and corrections: In a 3D scenario when reconstructions are performed, corrections are also implemented; hence, counts per voxel are going to be generated.

Using the calibration factor, activity per voxel can be determined instead of counts per voxel, if it's necessary. It needs to be stated that a real quantitative reconstruction, taking into account all possible corrections, can only be made by the vendor acquisition software. Every reconstruction made in a generic workstation is subject to approximations, and the uncertainty associated to these may not justify its use.

4. Registration and segmentation: Due to several patient image acquisition, a registration process is necessary to create a reference space among all data sets, some software use Whole FOV registration; few use organ-based registration. Normally one data set is used to be the reference against the other data sets, to match/fit two images. Segmentation is a procedure in which a ROI or VOI is generated with the aim to be characterized the bio-kinetics.
5. TAC and TIAC assessment: Having the same reference for all the time points and ROI/VOI segmented, generating time-activity curves for each structure is performed to calculate the TIA as it is expressed in Equation 1.11. There are several options to integrate these curves.
6. Absorbed dose calculation: There are several ways to calculate absorbed doses as seen in previous chapter. These include local energy deposition, convolution, and Monte Carlo. Tabular approaches using precomputed dosimetric values (S factors) can also be implemented, where the S values are computed using one of the algorithms presented above. All these possibilities will produce different types of outputs, average absorbed dose, absorbed dose maps and voxel-based absorbed dose in which absorbed dose volume histogram can be generated. Knowing radiobiological information, some other parameters can be estimated.

There are software created for commercial reasons, and it is also a practice to have home-made solutions in academic or hospital institutions. Every software must implement one or more steps in the dosimetry workflow, but not necessarily all of them, and not in that order. Existing solutions usually do not implement all CDW steps. Therefore, there is a need for a broader description of a general CDW that covers all possible cases, to derive which variables are necessary in each step.

We are going to present different academic and commercial software proposed in the literature, in order to analyze how they implement clinical dosimetry workflow.

2.2.1 Academic solutions

Home-made, academic software, are made routinely in each department to cover research in situations of new radiopharmaceuticals and new protocols. Since there is no clear definition on the CDW, each academic software is made differently, and are intended only to solve a very specific problem. That's why they are also not standardized. Moreover, most of them are not available outside their home institution, so they can't be evaluated or benchmarked against other solutions.

Some solutions, mentioned in chapter 1, are used exclusively for AD calculations. We will review their current status and the CDW steps they implement.

MIRDOSE: is no longer available, it was discontinued per request of the FDA [STABIN 1996].

OLINDA/EXM: its version 1 implemented the pharmacokinetics and the AD calculation step using the MIRD schema [STABIN 2005]. Version 1 was discontinued and is no longer available. Starting from version 2, it was moved into a commercial station, but keeping the same steps of the CDW as before [STABIN 2018].

MIRDCALC: is a more recent MSEXCEL-based software that implements the MIRD schema. It implements the pharmacokinetics and the AD calculation [KESNER 2018].

IDAC 2.1: implements the pharmacokinetics and the AD calculation using the MIRD schema [ANDERSSON 2017].

OpenDose Calculator: implements the pharmacokinetics and the AD calculation using the MIRD schema [MCKAY 2018].

As we can see, none of these available academic solutions implements more than the AD calculation or the pharmacokinetics. Other relevant academic software are:

RMH DoDose: Not available for the community, developed in the Royal Marsden Hospital [ABREU 2021b]. Implements patient image loading, image processing, pharmacokinetics, AD calculation and data reporting.

3DID, 3DRD: Not available for the community, developed by [SONG 2006]. Is a set of different software, each implementing a different step in the CDW. 3D-ID converts the CT and SPECT images into MCNP data. 3D-RD performs the MCNP output processing. The pharmacokinetics in planar images is performed manually in a third party software. Therefore, this system does not qualify as a software package.

ULMDOS: Available per user request to authors, developed by [GLATTING 2005]. Implements the pharmacokinetics using planar images.

NUKDOS: Available per user request to authors, is a more complete software implementing the MIRD schema from image processing, pharmacokinetics, AD calculation, and reporting

[KLETTING 2015]. It includes the software NUKFIT as a module similar to ULMDOS but generalizing also to 3D images.

LundADose: Available per user request to authors, is a complete software implementing a home-made CDW based on the MIRD schema. Implements from image reconstruction, image processing, pharmacokinetics, AD calculation, and reporting [SJOGREEN GLEISNER 2005]. It includes modules for 2D and 3D image processing and an integrated Monte Carlo code. This system allows for flexibility in the steps for CDW.

All these solutions are implementing the MIRD schema. Still, there is a need for a standardized approach, available for the community as open source resources (protocols, databases, software).

2.2.2 Commercial workstations

Examples of available commercial workstations implementing some steps in the CDW are Hermes Hybrid Dosimetry Module™, Dosisoft Planet® Dose, SurePlan™ MRT from MIM, and QDose™ from ABX-CRO advanced pharmaceutical services Forschungsgesellschaft mbH. Some of these workstations were studied by [MORA 2019]. The CDW implemented in commercial workstation was also presented more recently by [DELLA GALA 2021].

The following is a compilation of the implementation of the CDW for MRT in the mentioned workstations. All these stations are medical devices (CE marking or FDA approval) and can be used in a clinical context.

Hermes Dosimetry: In the case of the Hermes workstation, reconstruction can be performed with HybridRecon. This workstation also contains the Dosimetric Module (HDM), which has been used with ^{177}Lu -DOTATATE patient data [HIPPELÄINEN 2016]. Patient data can be used under different scenarios, for example, either a minimum of 3 serial Anterior-Posterior WB; or 3 serial Anterior-Posterior WB and one SPECT (or SPECT/CT study) or 3 serial SPECT (or SPECT/CT studies). The proposed calibration method is based on a uniformly filled cylindrical phantom. HDM requires a calibration factor in $\text{MBq}\cdot\text{counts}^{-1}$ obtained from SPECT/CT acquisitions. Time-fitting can be done using mono-exponential or bi-exponential approaches. By knowing the injected activity and injection time, the residence times can be estimated in HDM and its results can be exported to OLINDA/EXM V2.0 [STABIN 2012] that is included in the workstation. A second possibility is to use its incorporated HIRD approach, a semi-MC method assuming electrons to absorb locally and accelerated MC simulations for photons [HIPPELÄINEN 2017].

Planet Dose from DOSISOFT: works only with SPECT/CT reconstructed images and no calibration method is suggested by this company, also operates on Linux (CentOS7-64bits).

The calibration factor can be expressed in units of $\text{Bq}\cdot\text{counts}^{-1}$, but other options are available. Planet Dose allows the usage of different calibration factors, thus, the user can vary acquisition time. The reconstruction is not available, so it expects data already reconstructed and corrected. Time-fitting can be done by different approaches, for instance, using the trapezoidal method, mono-exponential, bi- or tri-exponentials. Planet Dose can estimate the mean absorbed dose by convolution [DIEUDONNÉ 2010; DIEUDONNÉ 2011; DIEUDONNÉ 2013] and assuming local energy deposition [PASCIAK 2014]. This software has been used for other applications, for instance in PET/CT for radiotherapy purposes [DESBORDES 2014; DESBORDES 2017; VERA 2013] and in the treatment of liver cancers with ^{90}Y microspheres [GARDIN 2017].

SurePlan™ MRT from MIM: is a software application that can be installed either in Windows or macOS environments. An extra module of MRT performs image reconstruction of imported raw data under the same platform. MRT works using different workflows, allowing the user to work with 3D or hybrid datasets. The calibration method is similar to that of HERMES. The calibration factor can be expressed in different units depending on user needs, in this case $\text{MBq}\cdot\text{counts}^{-1}$. Manual and automatic registration (rigid or elastic) and segmentation can be performed using different tools. Time-fitting can be done using different approaches: trapezoidal (including tail extrapolation), mono-exponential or bi-exponential fit, and there is an automatic option to choose the best fitting option per VOI. MRT also allows voxel-based TAC fitting and integration. MRT estimates mean absorbed dose in VOI (also generating a DVH) by convolution of DVK. Fitting/integration results and DVH can be obtained at the voxel level.

QDose® from ABX-CRO: integrates all dosimetry steps from image data import and processing to analysis and reporting. No reconstruction module is available, so it expects data reconstructed and corrected. QDOSE features a comprehensive range of workflows, running in parallel, including planar (2D), hybrid (2.5D) and volumetric (3D) dosimetry as well as a dedicated SIRT dosimetry module in one package. Absorbed dose calculations are performed according to the MIRD pamphlet No. 16, by using IDAC-Dose calculation software (ICRP 110) or by using the ICRP Specific absorbed fractions (ICRP 133).

In summary, Hermes and MIM are able to perform image reconstruction. QDose proposes only model-based dosimetry at the organ level. Planet Dose, Hermes and MIM could estimate the mean absorbed dose considering both organ-based and voxel-based approaches, and it is observed that they propose new variants, in addition to the workflow described, to calculate the absorbed dose. The new variants include the voxel-based activity integration in time, and in the case of Planet Dose, the VOI based absorbed dose rate integration in time.

To get the certification as a medical device (CE or FDA), a software must comply with very specific requirements. The CE mark confirms that the medical device meets certain "essential requirements" of the European General Medical Devices Directive (i.e. that it is fit and safe for the intended purpose). It also shows that the medical device can be freely

marketed anywhere in the EEA without further control.

In the certification process, there is no mention of the protocol or standard to be followed, and new protocols are explicitly not being covered. This leads to a variety of clinical protocols that makes the dosimetry clinical workflow as a non standardized procedure. Figure 2.2 presents the comparison of the CDW implementation by different commercial workstations, some of them already described here. We can appreciate the variety of implementations that often omits some steps, and sometimes invert the order of some processes.

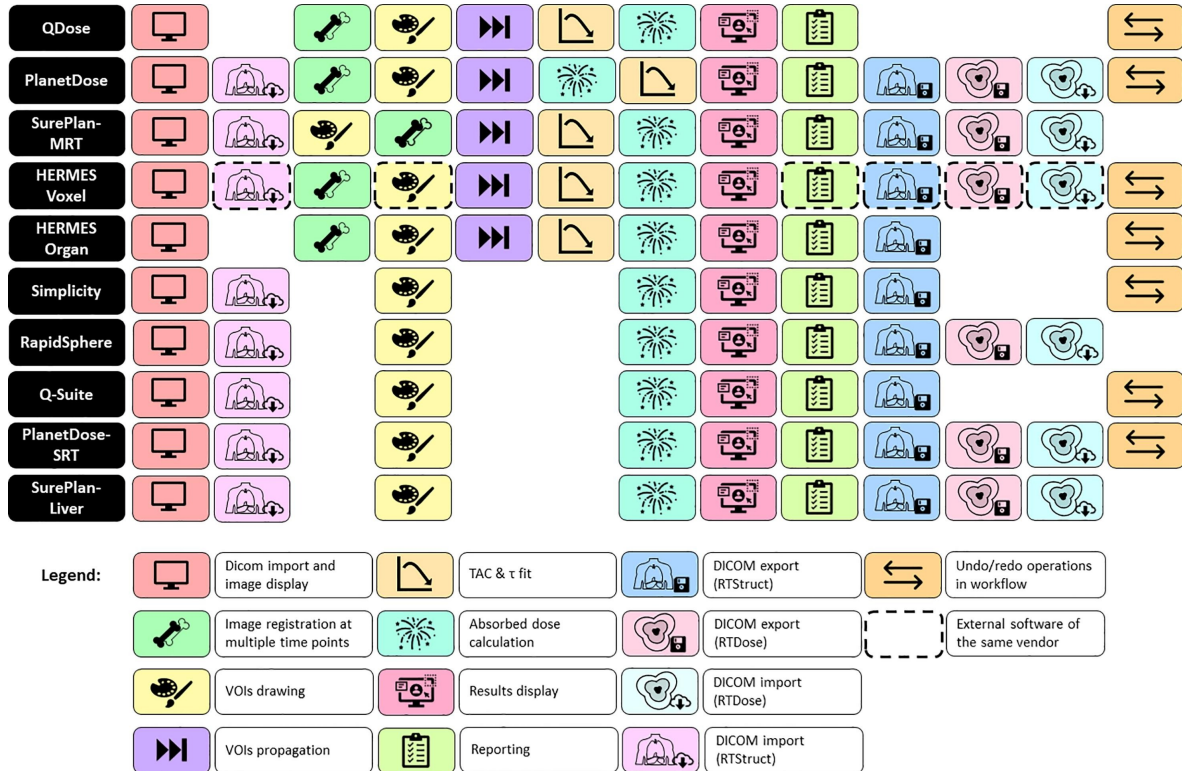


Figure 2.2: Commercial workstation comparison, how they implement the CDW steps and in which order [DELLA GALA 2021].

There is a need for a standardization of the CDW. This includes a homogenization of acquisition protocols, a description of the initial data needed to perform all steps. Moreover, there should be a process that includes all possible data workflows and all the details in every process.

2.3 The European Project MEDIRAD (H2020)

The European project MEDIRAD (H2020), supported by the European scientific societies of radiology, nuclear medicine, radioprotection and radiotherapy, is a 4-year project aimed at enhancing the scientific bases and clinical practice of radiation protection in the medical field. MEDIRAD addresses the need to better understand and evaluate the health effects

of low-dose ionising radiation exposure from diagnostic and therapeutic imaging and from off-target effects in radiotherapy.

The MEDIRAD project consists of six interdependent work packages, each of which contains tasks and deliverables vital to the project's success.

Work package 1 (WP1) Took care of the general project management and administration of the MEDIRAD Project. It liaises with the European Commission (EC), facilitate effective information exchange within the consortium, address contractual and reporting requirements, and coordinate the project governance.

Work package 2 (WP2) Developed novel methodologies to reduce patient and staff irradiation and potential radiation-related risks of cancer and non-cancer outcomes from chest imaging while maintaining or improving diagnostic information from existing and emerging techniques. In WP2, an integrated imaging and dose biobank (IRDBB) was developed to address research needs [GIBAUD 2020], initially in a context of radiology.

Work package 3 (WP3) Performed a clinical trial and implements the tools necessary to establish, for the first time in a multicenter setting, the range of absorbed doses delivered to healthy organs undergoing thyroid ablation and the threshold absorbed dose required for a successful thyroid ablation. This enables patient specific treatment planning that minimizes risk to the patient while ensuring a successful outcome and will facilitate development of a large scale epidemiological study of the effect of low absorbed doses from irradiation of normal organs with internal sources of radionuclides.

Work package 4 (WP4) Integrated clinical epidemiology, radiobiology, and modelling approaches to gain more insight into the mechanisms leading to radiation-induced cardiotoxicity in breast cancer patients and to develop and validate classical Normal Tissue Complication Probability and mechanistic models to relate low to moderate doses to the heart to a variety of biological, subclinical and clinical endpoints. WP4 aimed to contribute to more accurate risk estimations for early and late radiation-induced cardiovascular biological and clinical events and thus provide potential targets for primary and secondary prevention.

Work package 5 (WP5) Improved the direct estimation of cancer risk following low doses of ionizing radiation from CT scanning in childhood and adolescence and to study the role of factors - including age and genetic and epigenetic variants which may modify this risk.

Work package 6 (WP6) Formulated science-based policy recommendations for the effective protection of patients, medical workers and the public to decision-makers and practition-

ers. WP6 organized a web-based consultation of a wide range of stakeholders and disseminates the MEDIRAD results to broader communities interested in radiation protection.

We were associated in the MEDIRAD WP3, that involved patient-specific dosimetry for therapeutic uses of ^{131}I in the treatment of thyroid remnants. In this project, the dosimetry for different clinical centers had to be performed.

In WP3, data was collected from 100 patients with thyroid cancer treated with ^{131}I post-thyroidectomy, enrolled in 4 European clinical departments: Toulouse (IUCT-O), Sutton (RMH), Würzburg (UKW) and Marburg (UKM) [LEEK 2019]. Due to a variety of reasons, each center designed its own clinical protocol, therefore no acquisition standardization was possible. We were asked to perform the patient dosimetry. Therefore, we proposed the creation of a software module developed and validated implementing the various acquisition workflows, and also to perform the clinical dosimetry using our software.

2.4 The IRDBB database

In WP2, a computer system called Image and Radiation Dose BioBank (IRDBB), designed to manage image and dosimetric data in an integrated way, was developed [GIBAUD 2020]. Even though we had no initial role in WP2, we proposed to perform a specific study of available/desirable CDW to be used. This allowed in-depth analysis of the CDW, and the identification of the variables that need to be stored in the database.

This semantic database was implemented as a Resource Description Framework (RDF) graph aligned onto an application ontology called *OntoMEDIRAD*, that specifies the semantics of any information within this database. The main components of the database were the same blocks of the proposed CDW. The choice of an ontology-based approach aims eventually at facilitating the access to MEDIRAD research data to a wide community of researchers interested in low dose research, e.g. via federated systems.

The overall IRDBB system was a platform designed [GIBAUD 2020]:

1. to support the importation of research data sent by the MEDIRAD users, see Figure 2.3
2. to store this data, see Figure 2.4
3. to provide tools enabling MEDIRAD users to query and retrieve this data, see Figure 2.5.

Basically, two kinds of data were involved: image data and dosimetric data. Image data were images corresponding to the exposure to ionizing radiation, e.g. chest computed tomography (CT) images, or images acquired as part of a diagnostic procedure. Although this was the original plan, it resulted impossible to get the approval from the ethics committee. Therefore, images belonging to a targeted radiotherapy procedure selected in the MEDIRAD WP3, namely ^{131}I treatment of differentiated thyroid cancer were used instead.

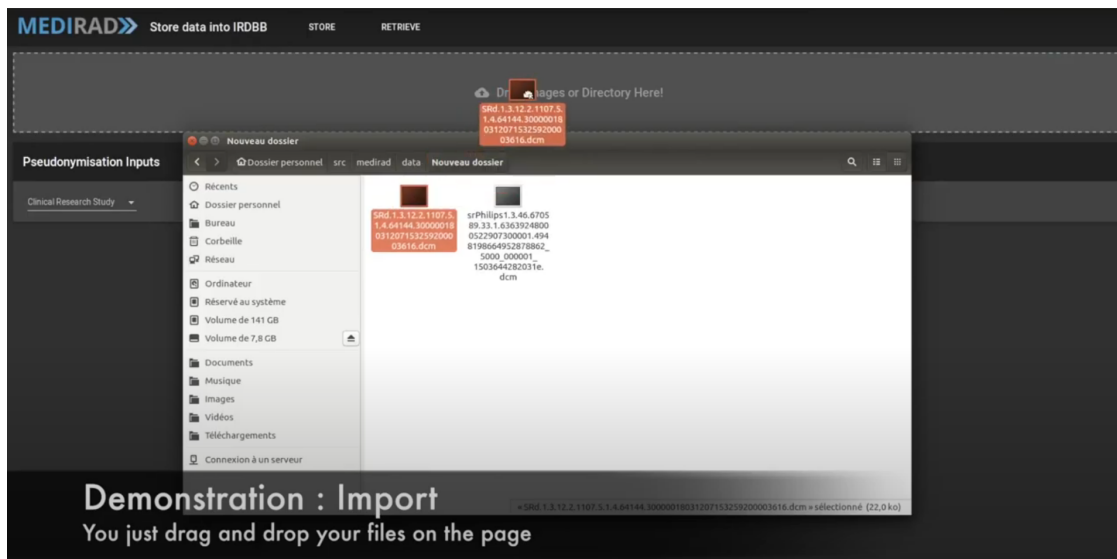


Figure 2.3: IRDBB import demonstration

The latter procedure requires performing several nuclear medicine (NM) explorations for locating precisely the distribution of the radiopharmaceutical in the body over time, a prerequisite for the calculation of absorbed doses to organs. Dosimetric data can be provided in various ways, either produced by imaging devices such as CT Radiation Dose Structured Reports (CT SR), or as results of calculations made by MEDIRAD researchers using advanced dosimetry methods. The data can be represented either in DICOM format or in some other non-DICOM format.

The advantages of the IRDBB database, are the definition of the parameters to consider/store to allow dosimetry traceability, storage of all the intermediate data for reproducibility, and the implementation of a standardized data storage that includes DICOM and non-DICOM data. All these parameters and data were defined as part of this work.

In the case of DICOM data, the system stores all the original DICOM files for referencing. The non-DICOM data includes all calculation tables with descriptors and results tables (as csv files); also all the intermediate data including transformations maps (linear or b-spline as h5 files to preserve structure), calculated images (activity maps, density maps, absorbed dose rate maps stored as nrrd image format to preserve orientation and structure identifiers) and the segmentation data (as nrrd segmentation format to preserve the contours). The storage of non-DICOM files is not possible with currently available DICOM storage solutions.

In order to fill the dosimetric data, a software solution need to be created that performs the data manipulation (dosimetry report) and packaging (xml package). This software must follow the predefined CDW and export the relevant data to integrate in the IRDBB. From this necessity, we needed to create our own proof of concept software, implementing all these requirements. The predefined CDW shared by both IRDBB and our proposed software is described below.

Internal AET: DCM4CHEE

Accession number: Issuer of accession number

Referring physician name: Modality

Study Date / Time: Study date from: Study date to: Study time from: Study time to:

Study ID	Study Instance UID	Study Date	Study	R. Physician's Name	Accession Number	Modalities	Study Description	#S	#I
Siemens CT	21006317	UNKNOWN	1953-07-24	M					
1. CEM1000073284522	1.2.250.1.74.20180312170000.10...	2018-03-12	14:43:51		CEM1000073284522	SR	(Avec inject.) Scanner cranie	1	1
2. TEST CRANE RANDO	12345678	1999-08-08	08:48:27	O					
8356	1.3.46.67059.33.1.63639247425...	2017-08-25	08:48:27			SR	CRANE STANDARD	1	1

Demonstration : Storage
Now all our files are on the storage (DCM4CHEE)

Figure 2.4: IRDBB storage demonstration

MEDIRAD Store data into IRDBB STORE RETRIEVE

Retrieve data

DICOM data Non DICOM data

Request description: List of CT radiation SR, cumulated doses and scope of accumulation

Send Request

RDF Response

Report	Dose	Value	Unit	Scopedaccumul
Computed_Tomography_X-Ray_088d5ef6-09e6-4c6b-b2f6-0a7968020d13	CT_Dose_Length_Product_Total_15bc611f-c832-4640-a176-cf638f2e743b	802.9	milligray_centimeter	Imaging_study_15e79fd9-adff-4a59-a0a7-317a5885edec
Computed_Tomography_X-Ray_0ad63f60-c8be-448c-8277-5d50296e11ad	CT_Dose_Length_Product_Total_150ab848-1e51-404c-9368-433e5cc9843c	1820.65	milligray_centimeter	Imaging_study_94364c70-20c2-45a3-9295-797abf745b2

Demonstration : Querying
Example : list all Accumulated Doses and Scope of Accumulation

Reproducir (k)

Figure 2.5: IRDBB querying demonstration

2.5 Proposed clinical dosimetry workflows in molecular radiotherapy

The common approach for CDW, and how the different clinical stations implement it, has been presented. It was observed that the common approach does not cover all situations and fell short in describing the details on how to do individual steps, how the data shall flow, and what are the relevant data to have to begin with.

As a part of MEDIRAD WP2, a more descriptive CDW was proposed, explaining all the details of each step. A workflow by time-integrating the absorbed dose rates in organs was also introduced as described in Equation 1.10. The additional path can now intrinsically consider the time-dependence of the VOI characteristics (mass, volume, shape) that were only approximated at best in the MIRN formalism as described in subsection 1.3.1. This second workflow is already present in some commercial software like Planet Dose and MIM. Therefore, a more generic graph, covering both situations needs to be presented.

Figure 2.6 shows the proposed CDW, where each box represents a process and each arrow represents data flow; each process requires data input and produces data output. The data produced in one process can be the input of the next. This same definition is followed by all graphs in this work.

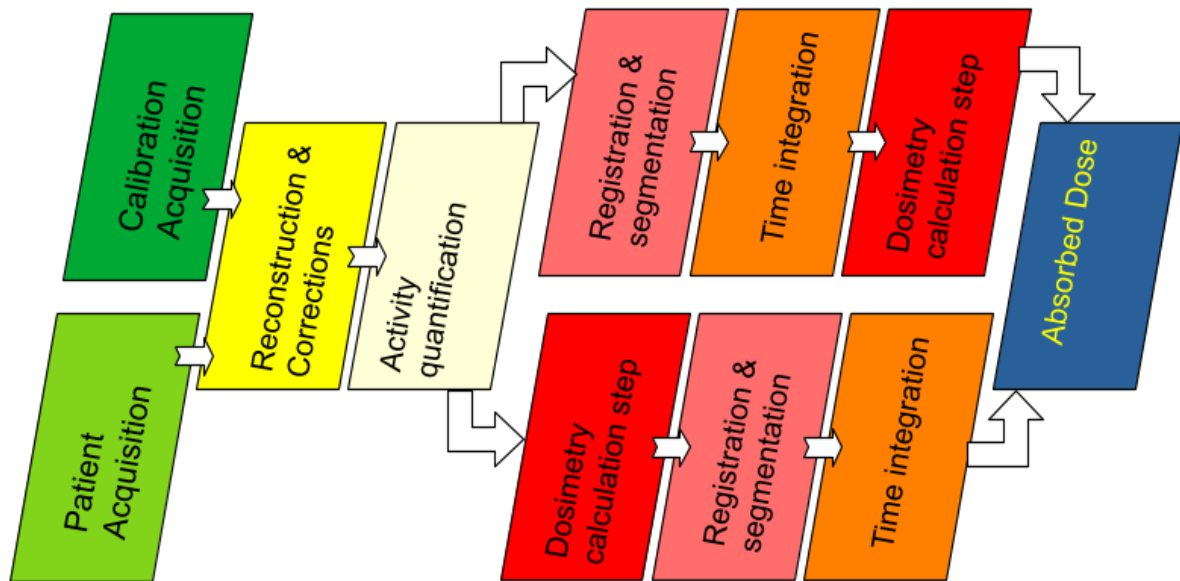


Figure 2.6: Proposed clinical dosimetric workflow.

More detailed explanations are needed in order to implement this workflow into practice. Specifically, we need to elaborate in each specific process and detail the specific data flow for each alternative path. Detailed workflows for calibration, activity integration path and absorbed dose integration path are presented following.

2.5.1 Calibration workflow

The first process in the workflow is the calibration that is displayed in Figure 2.7.

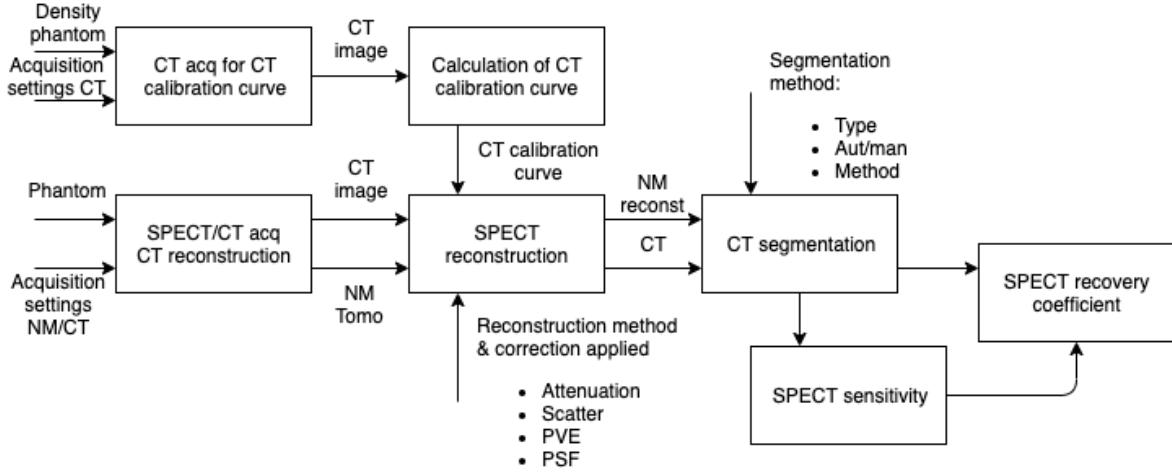


Figure 2.7: Calibration process workflow

This workflow is divided in two processes: CT calibration (calibration of CT response to reference density objects) and SPECT/CT system calibration.

2.5.1.1 CT calibration

The CT image of the calibration phantom is acquired using default system protocols (the same used for patient acquisition). The reconstruction shall include all corrections applied to patient image reconstruction and whenever possible is recommended to use the MBIR technique.

Using the studies of [SCHNEIDER 1996] on this phantom, we obtain Equation 2.1 to calculate the density ρ [g·cm⁻³] of the material starting with calibrated CT images. Figure 2.8 show the default calibration curve. On site studies were performed to assess the accuracy of this curve for the installed CT equipment.

$$\rho = \begin{cases} 6.128 \times 10^{-4} & \text{for } HU < -1000 \\ 9.991 \times 10^{-4} \cdot HU + 1.000 & \text{for } HU \in [-1000, -741) \\ 1.026 \times 10^{-3} \cdot HU + 1.020 & \text{for } HU \in [-741, -70) \\ 9.083 \times 10^{-4} \cdot HU + 1.012 & \text{for } HU \in [-70, 98) \\ 5.108 \times 10^{-4} \cdot HU + 1.051 & \text{for } HU \in [98, 260) \\ 6.625 \times 10^{-4} \cdot HU + 1.011 & \text{for } HU \in [260, 3071] \\ 3.047 & \text{for } HU > 3071 \end{cases} \quad (2.1)$$

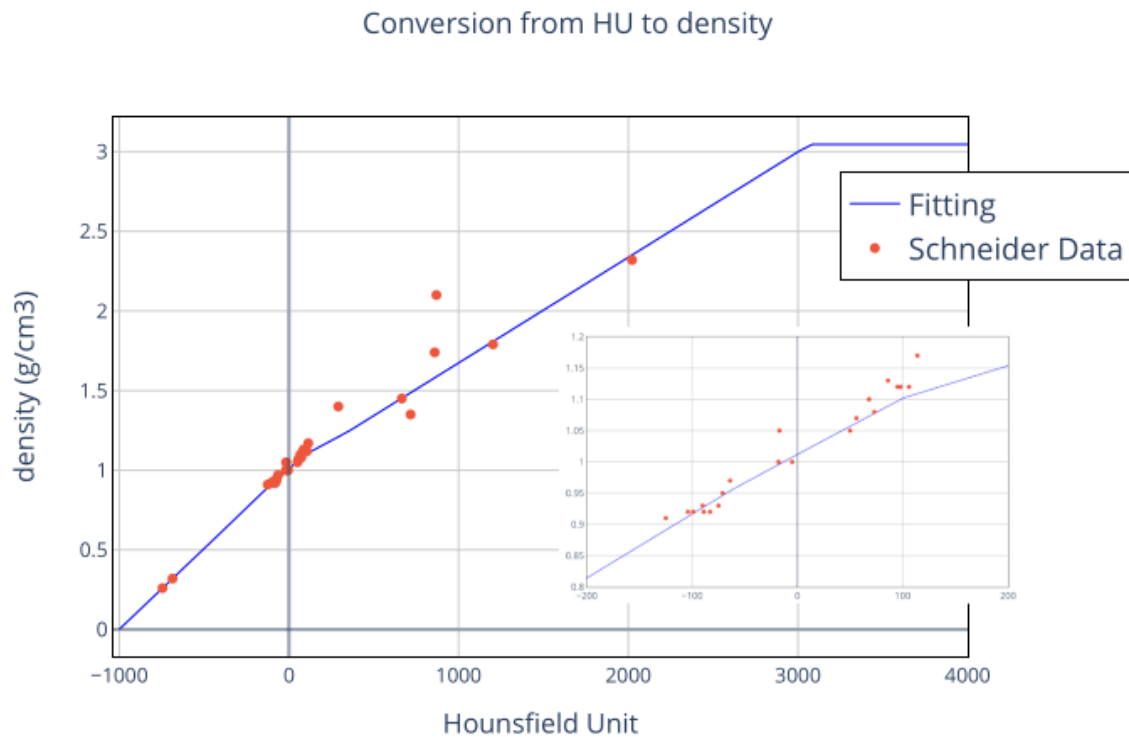


Figure 2.8: Hounsfield Units to density calibration curve using data from [SCHNEIDER 1996].

2.5.1.2 SPECT/CT system calibration

Once the CT is calibrated, giving HU values as direct response and with validated calibration curve, the next step is to calibrate the entire SPECT/CT system. This is subdivided into system alignment and SPECT calibration.

The SPECT images of a predefined phantom (recommended the Jaszczak¹) are acquired using the exact same protocol as for patient acquisitions.

For hybrid systems, alignment may be an issue [MATSUNARI 1998]. Fortunately, modern systems can perform automatic alignment included in the fusion process. For reconstruction, the aligned CT image is used for attenuation correction. Scatter correction is also recommended, but it depends on the capabilities of the acquisition system. Detector response correction must be applied in all cases.

Once the SPECT is reconstructed, the sensitivity factor is calculated Equation 1.16 using a homogeneous section with known volume and activity concentration. The calibration curve is calculated using hot inserts with known activity.

¹Jaszczak phantom patent: <https://worldwide.espacenet.com/patent/search/family/023486432/publication/US4499375A?q=pn%3DUS4499375>

If the patient SPECT acquisition is made following this same procedure then it can be converted to activity by using the sensitivity factor.

2.5.2 Absorbed dose via activity integration workflow

The proposed workflow to obtain the absorbed dose per organ via activity per organ integration is shown in Figure 2.9. This is just a variation of Figure 2.6 with just the activity integration branch.

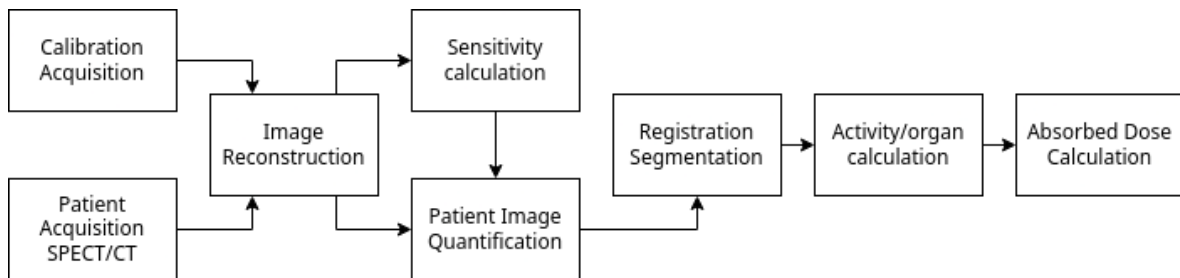


Figure 2.9: Activity integration workflow

To be able to implement this workflow, a more detailed description is needed. Without displaying the calibration steps, as they are already described in subsection 2.5.1, the workflow is presented in Figure 2.10.

As mentioned, the patient acquisition must be done with the same acquisition protocol used for the system calibration, including the reconstruction process and all corrections that are implemented. The workflow expects to have as input a set of multi time point quantitative SPECT/CT images, preferably in DICOM format as the acquisition details are included in the headers and can be imported automatically. In this process the CT is resampled to SPECT resolution for further calculations. The output of this process are converted images: the CT is converted to density using Equation 2.1, and the SPECT is converted to activity map using the sensitivity factor, Equation 1.19.

The image processing process consists of a series of sub-steps:

- **Registration:** In this step all images are translated to a reference coordinate system. Usually the reference is taken as one of the CT images, but this can also be an external CT. This process can have also a deformation step to handle for patient motion and organ displacements. Alternatively, the same transformation tensors (deformation maps) can be inverted to generate a map to each time point coordinate system.
- **VOI segmentation:** In this step all volumes of interest (VOI) are defined.
- **VOI Propagation:** The system must be able to redefine the same VOI in each time point.

The following process is the VOI activity determination. It requires the quantified activity map and a segmentation as input. This process produces a table of activity per VOI at each time point. The procedure is just to sum all the activity defined by the voxels that are contained in a specified VOI in a certain time point. In this process it is also possible to export in the same table the VOI mass per time point, as it is required by some absorbed dose calculation methods.

The next process is the time activity curve fit. It uses a pharmacokinetic assessment for the time integration. The input is the activity per VOI per time point table, the fitting method and the assumptions made for the incorporation and tail sections. The output of this step is the table of time integrated activity, or alternatively the time integrated activity coefficient (TIAC).

The final process is the absorbed dose calculation per VOI using Equation 1.11. The required S values can be assumed to be local deposition or can be extracted from a model based approach. As input are required the VOI definitions matching to the specified model data. Finally, a report is created with the following data:

- Activity maps (DICOM)
- Density maps (DICOM)
- VOI definitions in common reference (RTSTRUCT)
- Activity per VOI per time point (Table)
- VOI mass per time point (Table)
- Absorbed dose per VOI (Table)

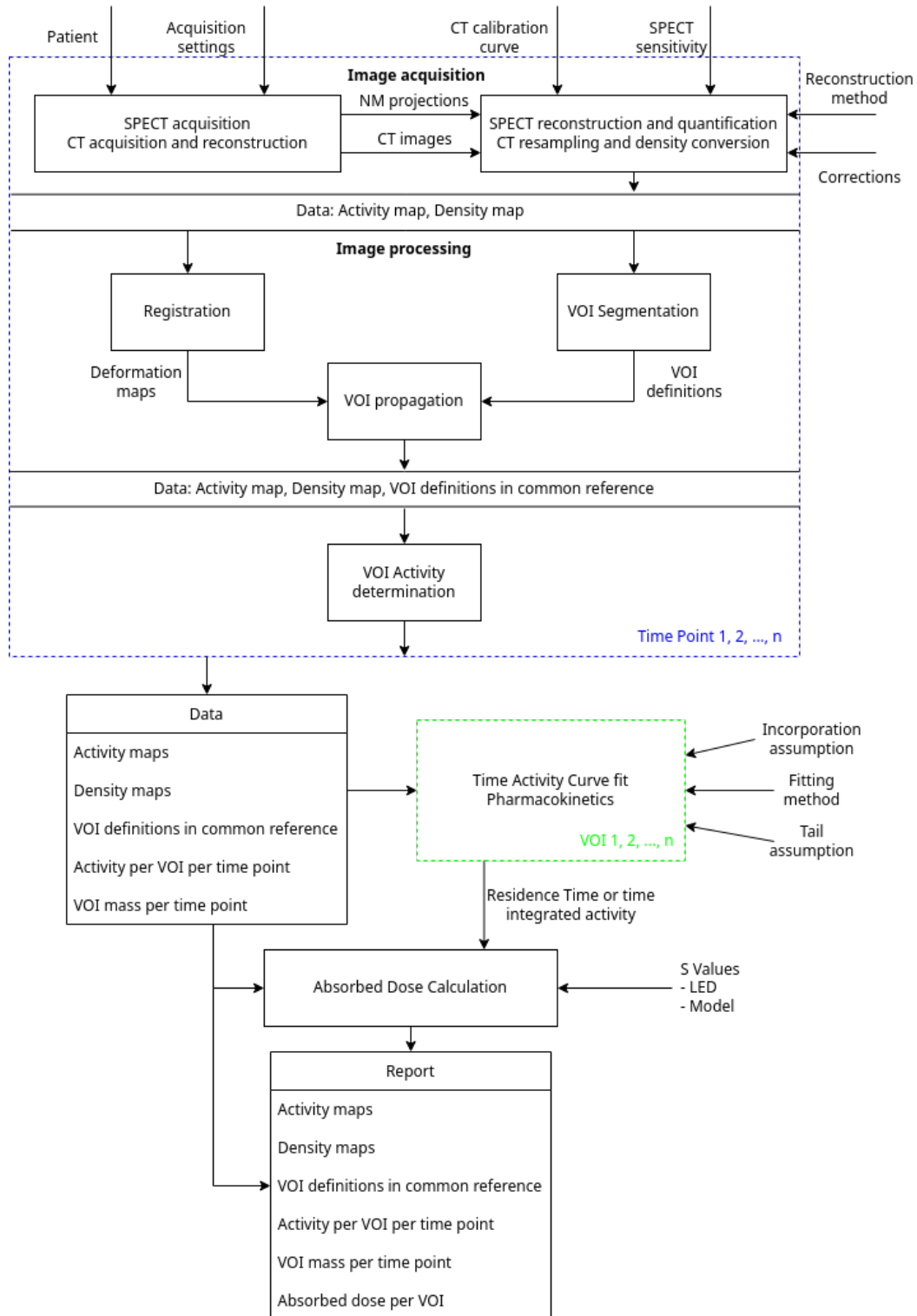


Figure 2.10: Activity integration workflow, full details. The blue dotted box means repeated in every time point, the green dotted box means repeated in every VOI.

2.5.3 Absorbed dose via absorbed dose rate integration workflow

The proposed workflow to obtain the absorbed dose per organ via absorbed dose rate per organ integration is shown in Figure 2.11. This is just a variation of Figure 2.6 with just the ADR integration branch. As can be noticed, this workflow shares several steps with the activity integration workflow: calibration, patient acquisition, reconstruction, registration, and segmentation. The differences are more detailed in Figure 2.12 with a full detailed workflow description.

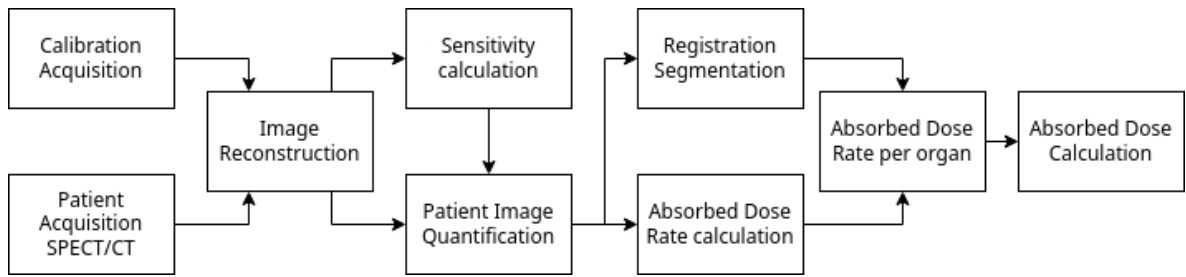


Figure 2.11: ADR integration workflow

The main difference is that now the absorbed dose rate is calculated in each time point and Equation 1.9 is used instead. Since now the activity values are used as a voxel map, more options are available for the ADR estimation. Now it is possible to use voxel-based Monte Carlo simulations (MC) or convolution approaches. Furthermore, since the VOI mass per time point is used, the time-dependence of mass is intrinsically considered by this workflow.

After the calculation of the ADR voxel map, the ADR per VOI is calculated using Equation 2.2.

$$\dot{D}_{VOI} = \frac{\sum_{i,j,k} \dot{D}_{i,j,k} \cdot m_{i,j,k}}{m_{VOI}} \quad (2.2)$$

Where $m_{i,j,k} = \rho_{i,j,k} \cdot V_{voxel}$ is the voxel mass and $m_{VOI} = \sum_{i,j,k} m_{i,j,k}$ is the VOI mass.

The output of this step is a table of ADR per VOI per time point. This is used for time integration in the same way as described in previous chapter and resumed in Figure 3.16.

The output of the time integration of ADR is directly the Absorbed Dose. Therefore, this is the last calculation step.

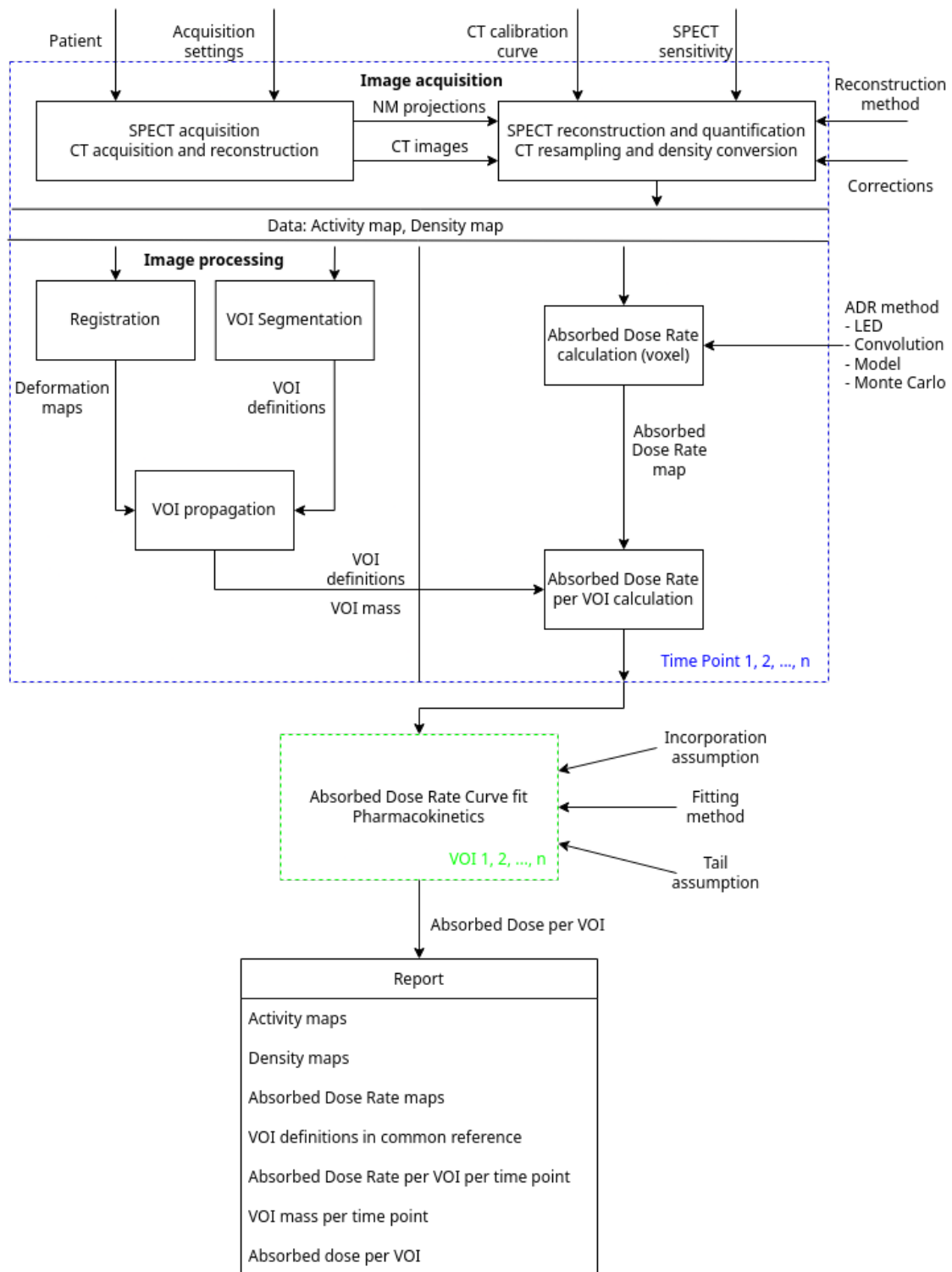


Figure 2.12: ADR integration workflow, full details. The blue dotted box means repeated in every time point, the green dotted box means repeated in every VOI.

Finally, a report is created with the following data:

- Activity maps (DICOM)
- Density maps (DICOM)
- Absorbed Dose Rate maps (DICOM)
- VOI definitions in common reference (RTSTRUCT)
- Absorbed Dose Rate per VOI per time point (Table)
- VOI mass per time point (Table)
- Absorbed dose per VOI (Table)

2.5.4 Desirable features of a dosimetry package

In order to implement these workflows in practice, a dosimetry package should include:

- Different options for each step: This should allow flexibility for each case, adapting to each input data. It also allows for different order in the required steps of the CDW.
- I/O (DICOM RT): The solution should implement a full DICOM management, including extraction of relevant data. section A.1 presents the DICOM header data required to fulfill a CDW.
- Possibility to save intermediary results: This is critical for reproducibility as the calculations became traceable.
- Implementation of calibration workflows: Most software solutions omit this critical step, leading to possible errors in the quantification.
- Reporting: The software solution should create a series of reports depending on the information level desired.

2.6 Conclusion

There are several software that implement different parts of the CDW. Some of them only focus on the AD calculation, while others are more complete but still lack some needed functionalities. The different software implement different CDW, there is no standardization with different software implementing either the activity integration workflow or the absorbed dose rate integration workflow. This lack of standardization also leads to different acquisition protocols. Moreover, since there is no consensus, some systems don't even include the calibration procedure in their workflow. We conclude that there is a need for a standardized CDW that

includes all aspects with detailed description. The CDW proposed in this chapter are aimed to solve this problematic.

For the MEDIRAD project, we decided to develop a solution that integrates all possible acquisition protocols under a common CDW. Available software solutions do not address this problem. Moreover, the need of reproducibility and traceability in the data processing automatically excludes some of the most used available solutions. Therefore, we conclude that there is a need for a home-made solution that will implement some (not necessarily all) of the desirable features identified in this chapter. The solution will also be able to connect to the data management solutions developed inside MEDIRAD, like the IRDBB database.

Development of a clinical research tool implementing the proposed clinical dosimetry workflows

Contents

3.1	3D-Slicer	64
3.1.1	DICOM Manager	65
3.1.2	Volume Resampling	66
3.1.3	Volume Registration	68
3.1.4	Segmentation	71
3.2	OpenDose3D module description	73
3.2.1	File standardization	77
3.2.2	Activity and density maps creation	80
3.2.3	Absorbed dose rate algorithms	80
3.2.4	Time Data Extraction	84
3.2.5	Time Integration	86
3.2.6	Reporting	89

In last chapter we decided to develop a solution that integrates all possible acquisition protocols under a common CDW. We have named it OpenDose3D (OD3D) since it was originally conceived to be part of the OpenDose Collaboration [CHAUVIN 2020] as the patient specific dosimetry module.

OD3D was developed as a python module of 3D-Slicer. It started as an absorbed dose calculator, but eventually it implemented all the steps defined for a clinical dosimetry workflow, except the reconstruction, thanks to the work done inside the MEDIRAD project.

To be able to talk about OD3D, first we need to define why do we choose 3D-Slicer as our main developing framework.

3.1 3D-Slicer

3D-Slicer is an open source software platform for medical image informatics [FEDOROV 2012], image processing, and three-dimensional visualization. Built over two decades through support from the National Institutes of Health of the United States and a worldwide developer community, Slicer brings free, powerful cross-platform processing tools to physicians, researchers, and the public in general.

The development of 3D-Slicer including its numerous modules, extensions, datasets, pull requests, patches, issues reports, suggestions is made possible by users, developers, contributors and commercial partners around the world.

3D-Slicer is:

- A software platform for the analysis (including registration and interactive segmentation) and visualization (including volume rendering) of medical images and for research in image guided therapy.
- A free, open source software available on multiple operating systems: Linux, macOS and Windows
- Extensible, with powerful plug-in capabilities for adding algorithms and applications.

Features include:

- Multi organ: from head to toe.
- Support for multi-modality imaging including, MRI, CT, US, nuclear medicine, and microscopy.
- Bidirectional interface for devices.

There is no restriction on use, but Slicer is not approved for clinical use and intended for research.

The most powerful Feature of 3D-Slicer is the plug-in capabilities, specially to add user made python interfaces and scripts. The Extension Wizard module creates a sample module with all requirements (Figure 3.1).

The newly created extension separates three main sections:

1. Graphic interface (GUI): Here all the graphic user interactions are defined: buttons, etc. Also, all required actions (functionalities) when using the graphic objects. In 3D-Slicer, the *pyqt* package for graphic interfaces it is used.

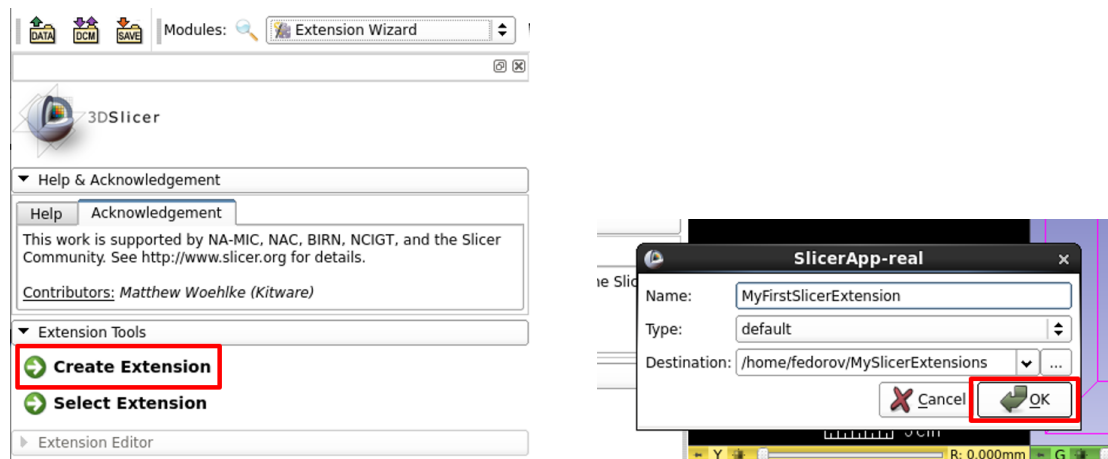


Figure 3.1: 3D-Slicer Extension Wizard

2. Logic: Here all actual logic is defined, it shall be created one function per desired action from the GUI.
3. Test: Every function in the Logic must be tested. A perfect test does not exist, but the more the tests cover the better it is to test the functionality of the logic.

Some functionalities desirable for a clinical dosimetry software are already available inside 3D-Slicer and therefore do not need to be re-developed. OD3D reutilizes some already existing modules, specifically DICOM import, data management, general registration, segment editor and transformations, through a specific API that exposes their logic to new python extensions.

In the next paragraphs, we will present the already existing modules that were recycled to design the clinical dosimetry software. We will also present the choices that were made when a given module proposed several options.

3.1.1 DICOM Manager

In order to get the patient images, commonly in DICOM format, a software needs to implement a DICOM Manager. The manager allows to load the relevant data into some specialized variables that contain not only the image, but also all the required descriptors.

3D-Slicer provides a DICOM database, an interactor and a series of plugins for dealing with different DICOM files. The user can import individual files, DICOM folders and full DICOM node queries from a remote server. Figure 3.2 shows the graphical interface of the 3D-Slicer DICOM module.

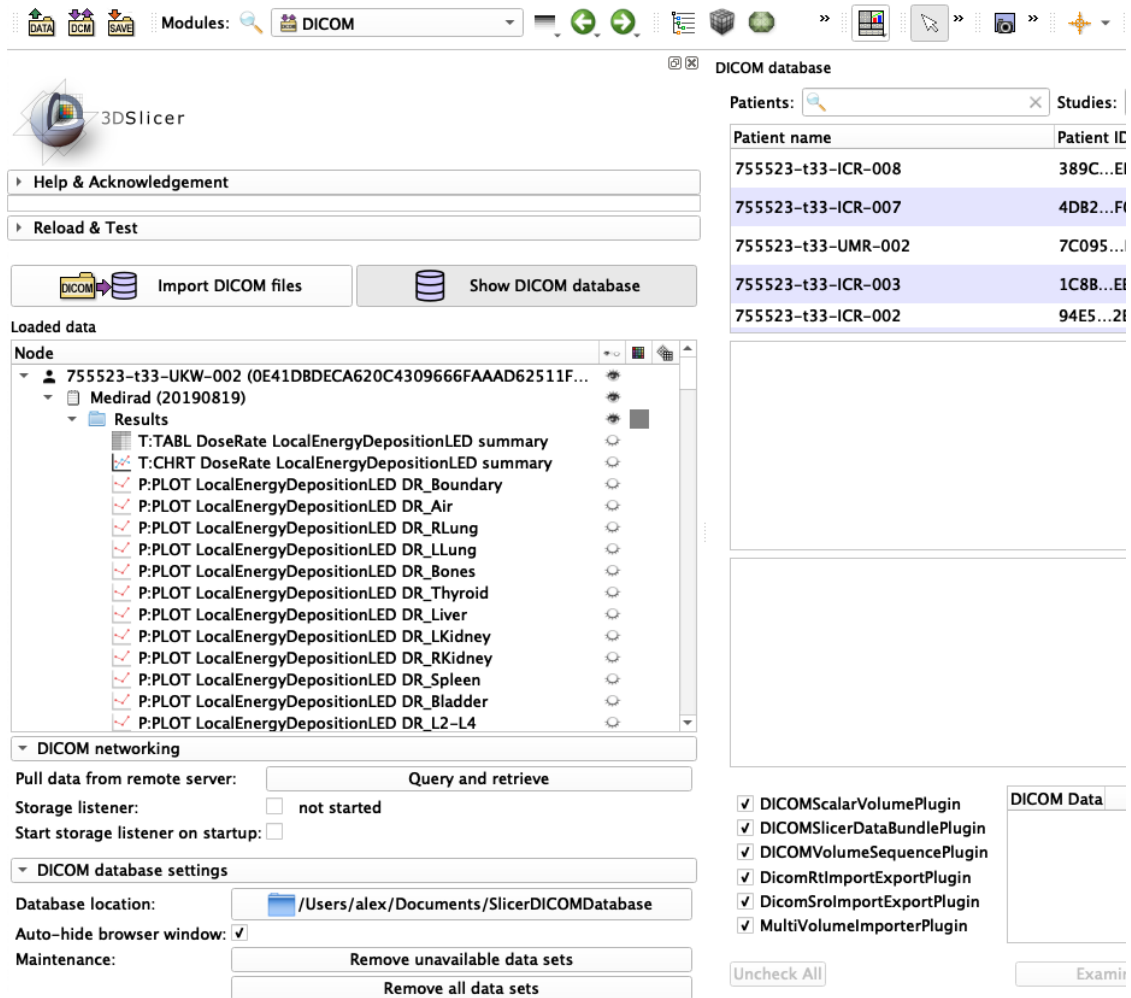


Figure 3.2: DICOM module of 3D-Slicer

3.1.2 Volume Resampling

In order to implement the absorbed dose calculation, we have seen that the density map and the activity map are required to have the exact same resolution. However, the CT and the PET/SPECT have intrinsic different resolutions. Therefore, a volume resampling is required. The resampling can be made to adopt the CT resolution by increasing SPECT resolution, however this creates artificial data increasing even more the overall uncertainty.

In this work we have decided to adopt SPECT resolution by decreasing CT resolution. This has been proven to not affect the dosimetry results compared to non resampled images using the Monte Carlo method [PISTONE 2021b]. However, the use of non resampled images creates absorbed dose artifacts due to the activity oversampling in the CT resolution.

Resampling is the action of building a new dataset (image, surface, fiducials etc.) from an existing one, but with a different orientation, resolution, field of view or aspect ratio. This

process uses a projection that can be made using interpolation or more advanced techniques using Fourier transformations.

3D-Slicer supports several resampling methods. But the one that preserves structure volumes is the windowed *sinc*-interpolation ($\text{sinc}(x) = \frac{\sin x}{x}$) [MEIJERING 1999]. The *sinc*-interpolation is defined as:

$$I(x, y, z) = \sum_{i=\lfloor x \rfloor + 1 - m}^{\lfloor x \rfloor + m} \sum_{j=\lfloor y \rfloor + 1 - n}^{\lfloor y \rfloor + n} \sum_{k=\lfloor z \rfloor + 1 - o}^{\lfloor z \rfloor + o} I(i, j, k) K(x - i) K(y - j) K(z - k) \quad (3.1)$$

Where $K(x)$ is the interpolation kernel. Several kernels are possible, however we need to preserve not only the volume but also the shape of our defined structures. Therefore, we have decided to use the Lanczos kernel to preserve the structure edges, which is defined by:

$$K(x) \Rightarrow L(x) = \begin{cases} 1 & \text{for } x = 0 \\ \frac{a \cdot \sin \pi x \cdot \sin \frac{\pi x}{a}}{\pi^2 x^2} & \text{if } x \neq 0 \text{ and } |x| \leq a \\ 0 & \text{for } |x| > a \end{cases} \quad (3.2)$$

Properties As long as the parameter a is a positive integer, the Lanczos kernel is continuous everywhere, and its derivative is defined and continuous everywhere (even at $x = \pm a$, where both *sinc* functions go to zero). Therefore, the reconstructed signal $S(x)$ too will be continuous, with continuous derivative. The Lanczos kernel is zero at every integer argument x , except at $x = 0$, where it has value 1. Therefore, the reconstructed signal exactly interpolates the given samples: we will have $S(x) = s_i$ for every integer argument $x = i$.

Advantages The theoretically optimal reconstruction filter for band-limited signals is the *sinc* filter, which has infinite support. The Lanczos filter is one of many practical (finitely supported) approximations of the *sinc* filter. Each interpolated value is the weighted sum of $2a$ consecutive input samples. Thus, by varying the $2a$ parameter one may trade computation speed for improved frequency response. The parameter also allows one to choose between a smoother interpolation or a preservation of sharp transients in the data. For image processing, the trade-off is between the reduction of aliasing artifacts and the preservation of sharp edges. Also, as with any such processing, there were no results for the borders of the image. Increasing the length of the kernel increases the cropping of the edges of the image.

Limitations Since the kernel assumes negative values for $a > 1$, the interpolated signal can be negative even if all samples were positive. More generally, the range of values of the interpolated signal may be wider than the range spanned by the discrete sample values. In

particular, there may be ringing artifacts just before and after abrupt changes in the sample values, which may lead to clipping artifacts. However, these effects were reduced compared to the (non-windowed) *sinc* filter [MELJERING 1999]. For $a = 2$ (a three-lobed kernel) the ringing is $< 1\%$.

All these procedures, and more interpolation procedures, were implemented in the *BRAINS-Resample* module from 3D-Slicer.

3.1.3 Volume Registration

Registration is the action of assigning a common reference frame for two images in a way that a reference set of structures were located in both images in the same position. The registration can be rigid with no deformation of the images, with linear deformation and with elastic deformation. A combination of rigid and linear deformation is commonly used in the general case, whereas the elastic registration is mainly used for anatomical images (CT and/or MR).

Figure 3.3 shows the graphical interface of the general registration module from 3D-Slicer. This module allows to create several transformation types, but it is mainly used to create linear transformations that include the rigid ones. The non-linear registration is only tested for brain and skull, and does not work well in other areas.

Figure 3.4 shows the graphical interface of the elastic registration module from 3D-Slicer. This module uses an external software (Elastix) that is bundled into the Slicer interface. Elastix was tested for general anatomical image registration (CT-CT and CT-MR) and is the recommended option in that situation.

The result of the registration process is a transformation that can be a matrix or a deformation (vectorial) field. This is applied to every volume in the respective time point. It can be noticed that in this work we avoid modifying the original volumes while registering, using only the transformation matrix applied to a certain volume.

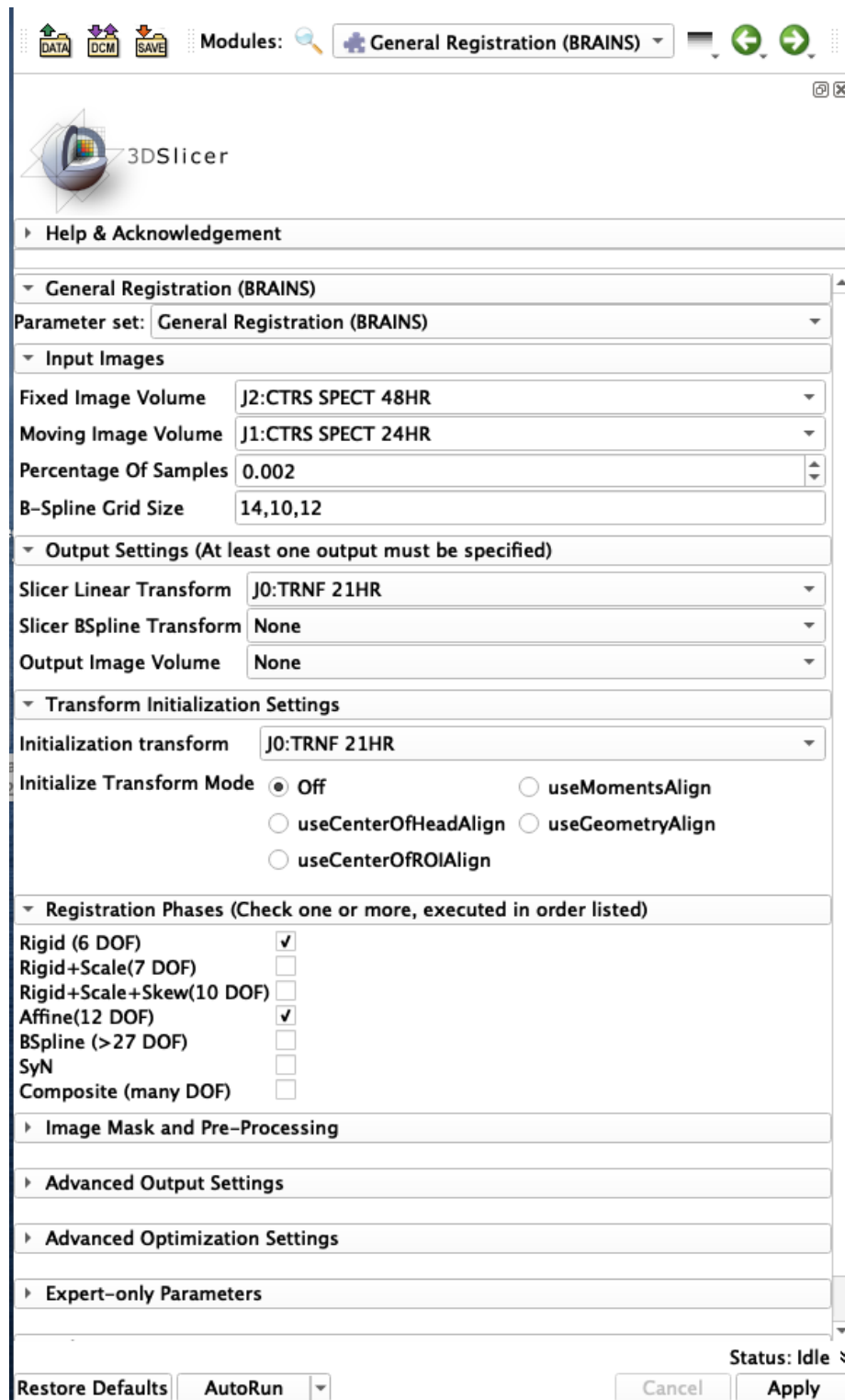


Figure 3.3: General Registration module of 3D-Slicer

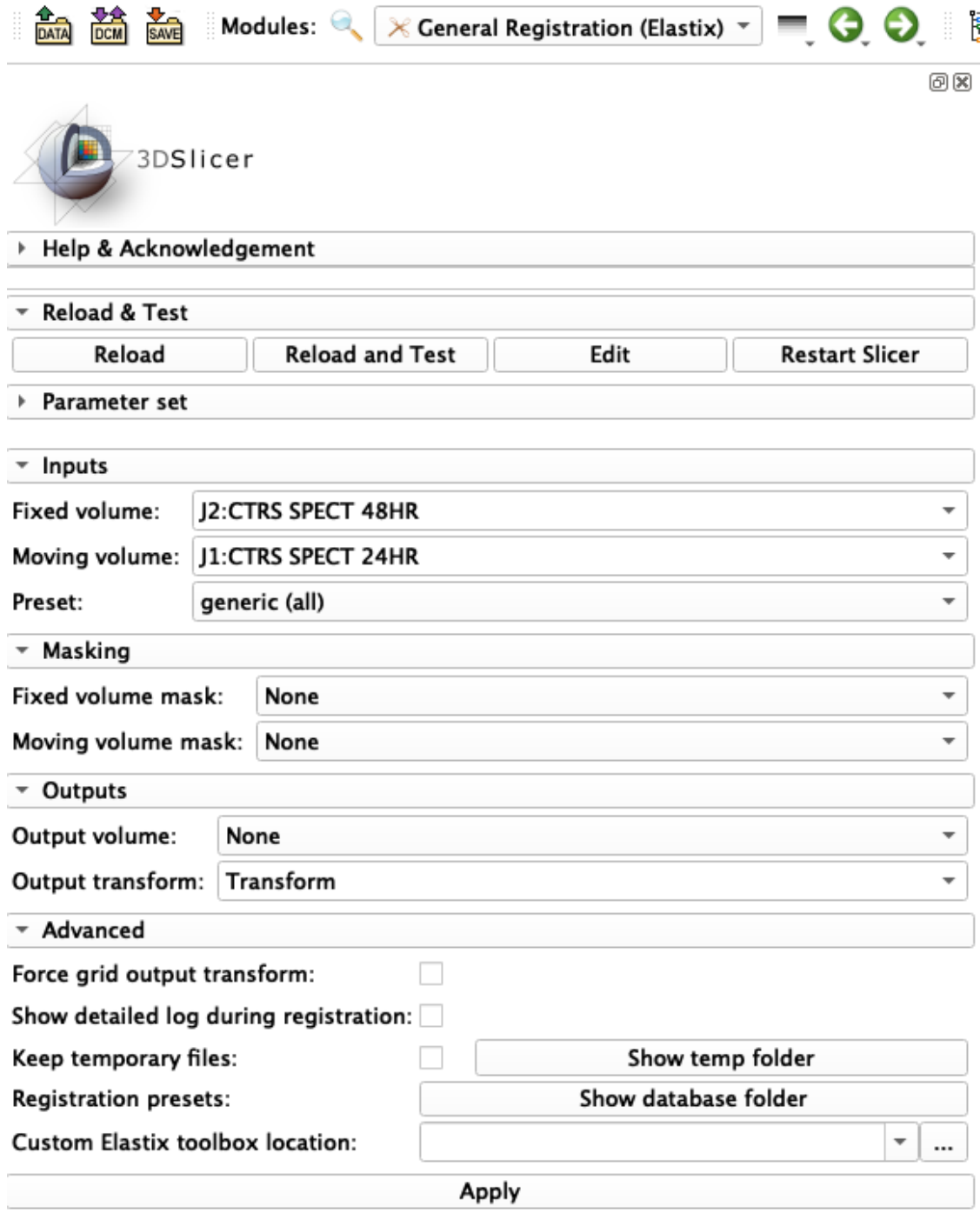


Figure 3.4: Elastic registration module of 3D-Slicer

3.1.4 Segmentation

Segmentation is the action of defining volumes of interest (VOI) in each desired image. The action is made by defining a group of voxels in an image to have a selected label, either by painting, thresholding or by using other more advanced tools. 3D-Slicer brings a full set of tools to perform advanced 3D segmentation, including painting with a 3D brush.

Usually, the commercial software bundle the segmented regions with the image used for segmentation. Therefore, it must be switched between anatomical mode and functional mode to perform a multimodal segmentation.

In 3D-Slicer however, the VOI is composed of segments that can be defined in different images. Therefore, the segmentation can be intrinsically multimodal.

Once the segments (VOI) have been defined, it is possible to review them, either by placing them over the CT image or by visualizing them in 3D view. Figure 3.5 shows the final result of a sample segmentation with several VOI. Figure 3.6 displays the Segment Editor module of 3D-Slicer.

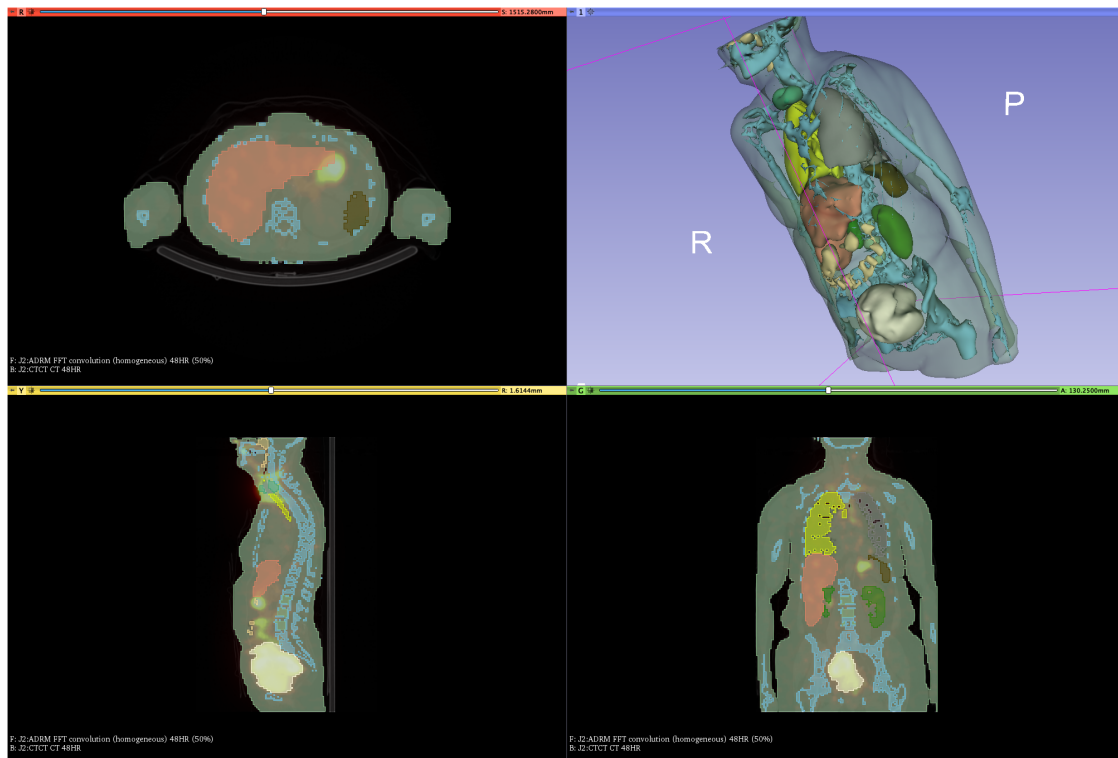


Figure 3.5: View of a sample segmentation



Figure 3.6: Segment Editor module of 3D-Slicer

3.2 OpenDose3D module description

As part of MEDIRAD WP3, a 3D-Slicer module was developed and named OpenDose3D (OD3D) [VERGARA GIL 2020]. The module has been also included into the OpenDose Project [CHAUVIN 2020] for dissemination in the medical physics community as a research tool.

OD3D was designed in a way that all steps are independent, reproducible and traceable. Intermediate steps are always stored and are dependent only on previous steps. The workflow must be completed starting from the step that was repeated/recalculated.

OD3D provides the possibility to perform the dosimetry of a molecular radiotherapy (MRT) treatment cycle with several time point CT and SPECT or PET acquisitions. It contains several utilities and follows starting from reconstructed images to the end of the clinical dosimetry workflows, allowing activity and absorbed dose rate integration. Figure 3.7 shows the graphical interface developed.

The decision of not implementing the reconstruction step is based in that most acquisition systems already implement it with all relevant corrections (vendor specific). Therefore, in our case there was not a practical need for that. Moreover, in order to implement the reconstruction, we need to replicate each camera geometry (several vendors, several models) to implement ourselves the corrections. This is also impractical for the present work.

In order to use reconstructed images we need to take into account that the calibration image must be reconstructed with the exact same protocol to have a valid sensitivity coefficient.

Following a description of the developed functionalities:

- Parameters panel allows entering common variables for the study, such as the SPECT sensitivity and the isotope.
- Preprocessing panel allows to prepare the essential objects for the calculation.
 - Rename files button allows to create the required variables, group the files by time point and rename all files using a convention.
 - Resample CTs button allows performing automatic CT volumes resampling using the procedures already available in slicer (using Lanczos interpolation)
 - Rescale button converts the CT Volumes into density using a well-established procedure and also converts the SPECT volumes to Activity map volumes.
- Registration panel allows to spatially register all volumes taking one of them as reference. It uses the registration methods available in slicer (rigid + elastic).
 - The user is expected to review the results in the transformation module, correct manually all broad deviations and repeat the registration.

- Each registration is applied to all volumes of a given time point. In the case of elastic registration, each VOI is registered independently.
- Repeating the execution after manually adjusting broad deviations refine the registration.
- Absorbed Dose Rate Calculation panel allows selecting among different procedures (local energy deposition, homogeneous FFT convolution, heterogeneous convolution and Monte Carlo simulation). This panel is not taken into account in the activity CDW.
 - The Activity threshold bar in the heterogeneous convolution is designed to remove Poisson noise influence in the calculations (increasing calculation speed). The recommended value of 5.0 % shall be accurate in most cases.
 - There is no activity threshold in any other procedure.
- Segmentation panel allows importing user defined segmentations.
 - The Propagate Segmentation button is completely optional to handle volume variations per time point.
 - If the original segmentation is propagated then the module will use the respective segmentation that will be placed in each time point folder.
 - The user can then refine the segmentations in each time point using the Segment Editor module.
- Segment Tables and Plots panel: if a segmentation is provided then it is possible to obtain segment statistics either from the activity maps or from the absorbed dose rate volumes.
 - Segment statistic tables are created in each time point for either activity map volumes or absorbed dose rate volumes.
 - The respective time plots are also calculated; at this point a common table is created for the following integration in time.
- Time Integration panel is the final output of the module. A table either based in activity map or absorbed dose rate statistics per segment is created by integration in time.
 - The extrapolation to zero allows selecting how to model early time-dependent phenomena, from injection to first acquisition (linear, constant, exponential).
 - The Integration Algorithm allows selecting the algorithm that will be used for the time integration from the first acquisition to the last acquisition (trapezoid, mono-exponential, bi-exponential, tri-exponential, auto-fit). The auto-fit option calculates a Bayesian inference coefficient (BIC) to determinate the best fit (the smallest BIC) among all provided functions for each VOI.
- Utilities panel allows performing optional tasks.
 - Clean Scene erases all non-conform Volumes and also erases all intermediate results.

- Settings panel allows handling optional functionalities

The source code was published in a public GitLab repository inside the OpenDose project at <http://gitlab.com/opendose/opendose3d>.

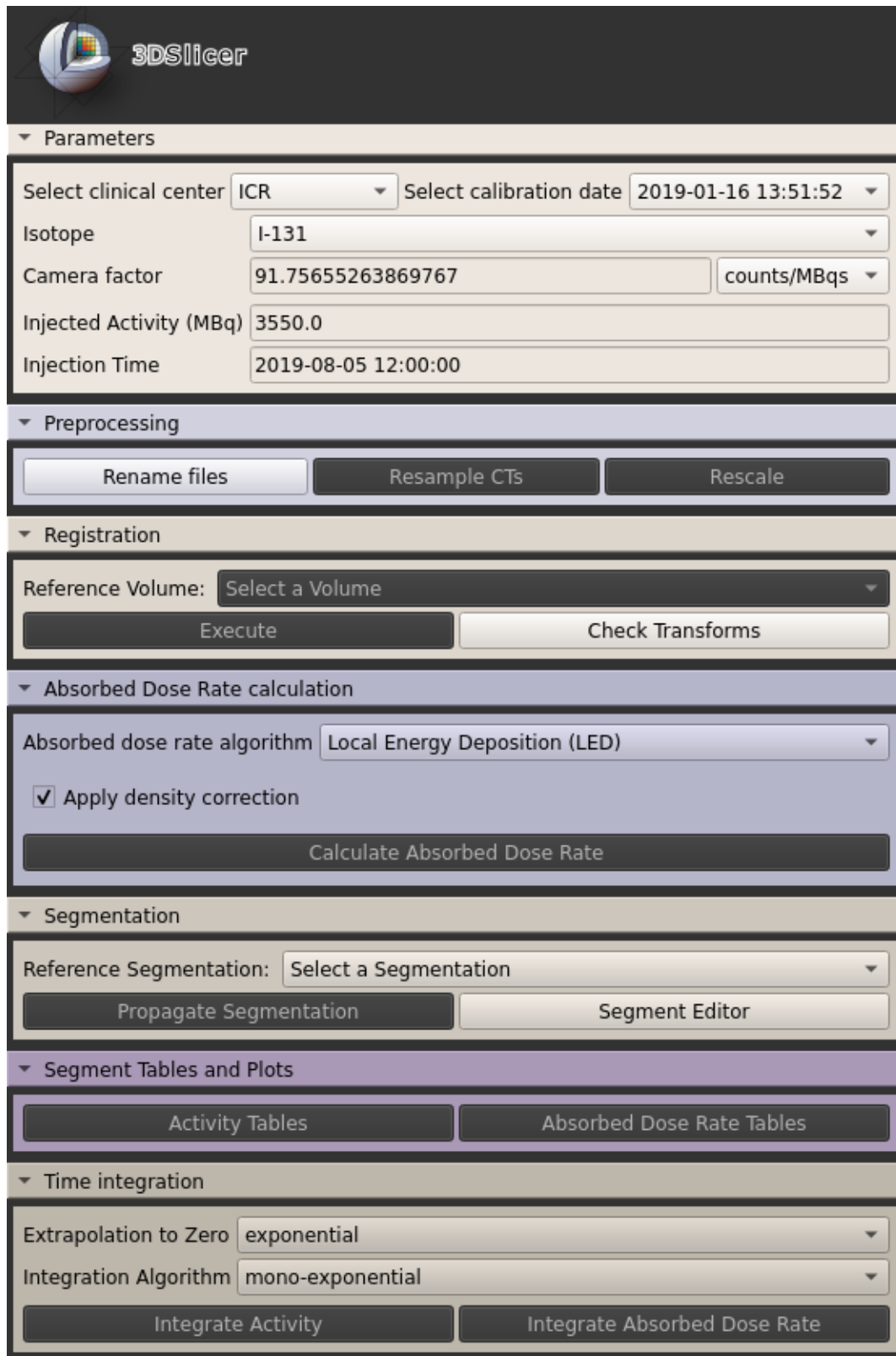


Figure 3.7: General overview of the OpenDose3D module

3.2.1 File standardization

In order to implement the workflows, it is necessary to add more functionalities to 3D-Slicer like file standardization. This is defined as grouping all DICOM files into a predefined data structure similar to the DICOM hierarchy in Figure 1.7. The proposed data hierarchy is implemented as shown in Figure 3.8.

In addition to naming and grouping, an extraction of relevant DICOM data is attempted to be extracted from the respective DICOM headers of provided images. Any missing data will result in an empty field that must be filled manually after standardization process, as any blank field will block the workflow. section B.1 shows the list of required DICOM fields.

To add the missing data fields is possible using the 3D-Slicer Data module shown in Figure 3.9. Inside there is a MRML node information table with the possibility to edit the missing data fields (Attribute value). Although it is possible to add/remove the attributes, it is not recommended as it will destroy the data requirements. Instead, this shall be used only for filling/editing the missing/wrong values.

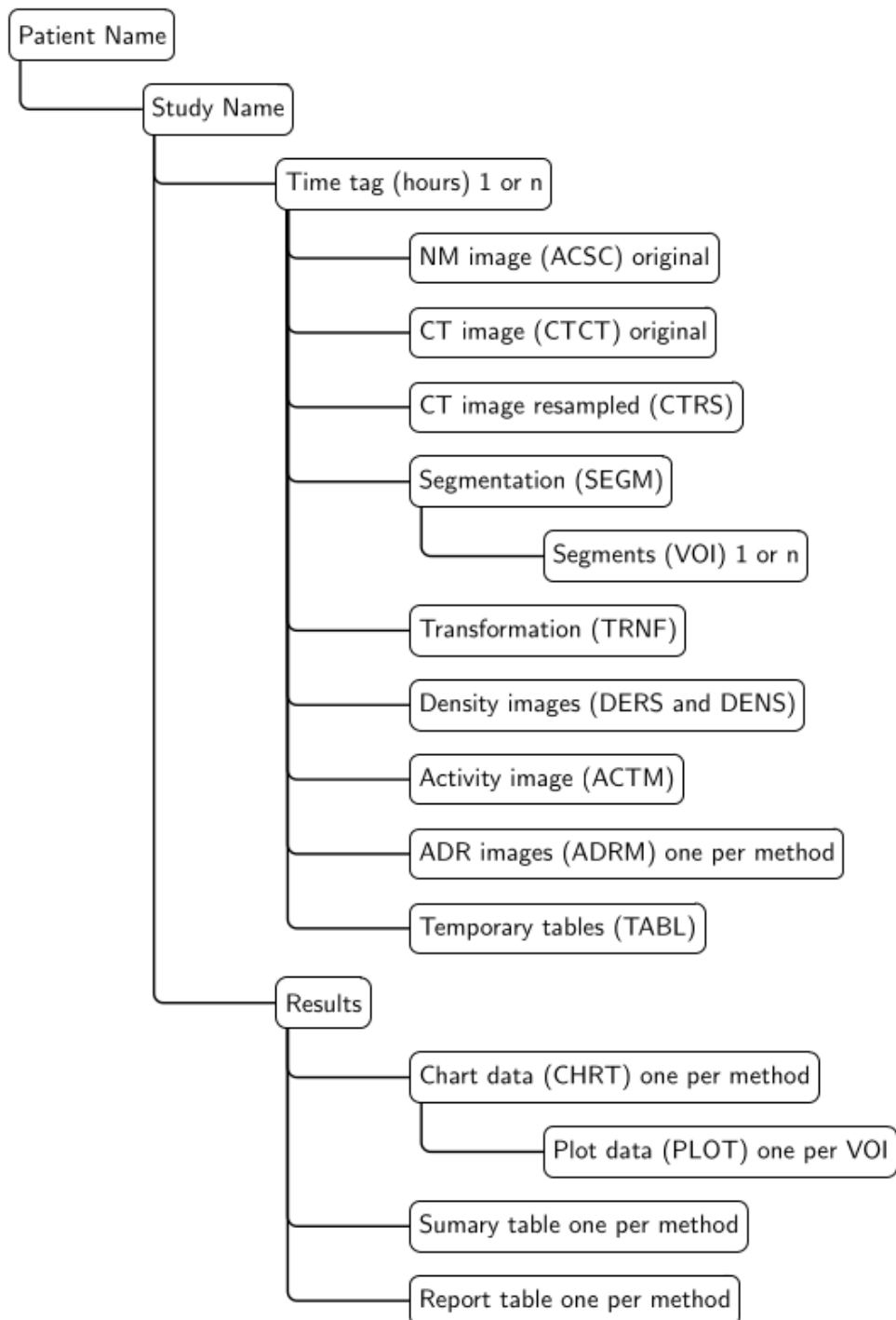


Figure 3.8: Data hierarchy: There is only one patient now for processing and one study corresponding to one administration. The time folders (1 or n) contains the respective images. Each image is now tagged with a unique identifier, more images will be added later during processing.

The screenshot displays the 3D-Slicer Data Module interface. At the top, there are three tabs: "Subject hierarchy", "Transform hierarchy", and "All nodes". The "Subject hierarchy" tab is active, showing a tree view of the data. The selected node is "J2:ACSC SPECT 48HR". Below the tree, there are checkboxes for "Show transforms" (checked) and "Show MRML ID's" (unchecked). A "Subject hierarchy item information" section is also visible.

Below the hierarchy, there is a "Filter:" input field and a section for "MRML node information". This section contains a table with the following data:

Attribute name	Attribute value
DICOM.Acquisition.Date	2019-08-21 12:22:09
DICOM.Acquisition.Duration	599.82
DICOM.Acquisition.Sensitivity	73.5
DICOM.Acquisition.SensitivityUnits	counts/MBqs
DICOM.Calibration.Duration	600
DICOM.Injection.Activity	3510.7894161381
DICOM.Injection.Date	2019-08-19 11:55:58
DICOM.Injection.Radiopharmaceutical	NaI
DICOM.Isotope	I-131
DICOM.Modality	NM
DICOM.PatientID	755523-t33-UKW-002
DICOM.PatientName	755523-t33-UKW-002
DICOM.SeriesInstanceUID	1.3.12.2.1107.5.6.1.1001.307201191...
DICOM.Study.Date	2020-01-23 12:46:06

At the bottom of the table, there are "Add" and "Remove" buttons.

Figure 3.9: 3D-Slicer Data Module. Adding/editing missing tags can be done under the MRML node information table

3.2.2 Activity and density maps creation

Once the data is standardized, it is time to proceed with the calculation of the activity and density maps. These are build as 3D-Slicer volumes.

Activity map The activity map is created for each time point with tag ACTM. The starting points were the NM calibration (sensitivity $S[\text{counts}\cdot\text{MBq}^{-1}\cdot\text{s}^{-1}]$, calibration acquisition time $t_{cal}[\text{s}]$) and the SPECT image (ACSC) in counts. Each voxel is calculated using Equation 1.19.

Density map The density map is created for each time point with two resolutions: density map at CT resolution (tag DENS) and density map at NM resolution (tag DERS). The DENS volume is created using the Schneider Equation 2.1 with the original CTCT volume. For the DERS volume, a resampled CT at NM resolution (tag CTRS) is build using the resampling procedures described. Finally, the Equation 2.1 can be used on the CTRS volume to produce the DERS volume.

3.2.3 Absorbed dose rate algorithms

The absorbed dose rate algorithms implemented in the module were local energy deposition, convolution homogeneous, convolution heterogeneous and Monte Carlo as described in section 1.5. Figure 3.10 show the graphical interface of the ADR algorithm selector.

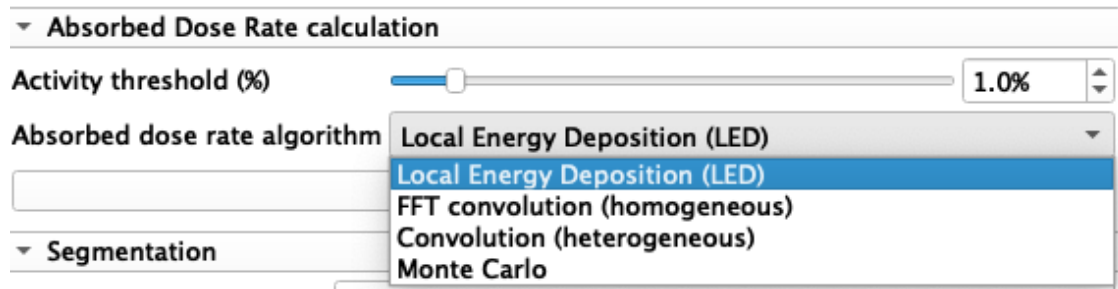


Figure 3.10: Implementation of the absorbed dose rate algorithm selector

3.2.3.1 Local energy deposition

Using the database from MIRD [ECKERMAN 2008], a python script was created to obtain the average kinetic energy of the electrons emitted. Table 3.1 shows the calculated energy for selected isotopes ^{177}Lu , ^{131}I and ^{90}Y .

This energy is used in Equation 1.21 for voxel calculations or in Equation 1.22 in VOI calculations. A density correction is made after the calculation by either selecting the desired

Radioisotope	^{177}Lu	^{131}I	^{90}Y
$E_{kinetic}^{e-}$ [keV]	148.23	191.97	931.81

Table 3.1: Average kinetic energy of emitted charged particles per disintegration for selected isotopes

material (water, soft tissue, cortical bone, lung or adipose) or by making a voxel wise division by the density map. Figure 3.11 shows the graphical interface in OD3D.

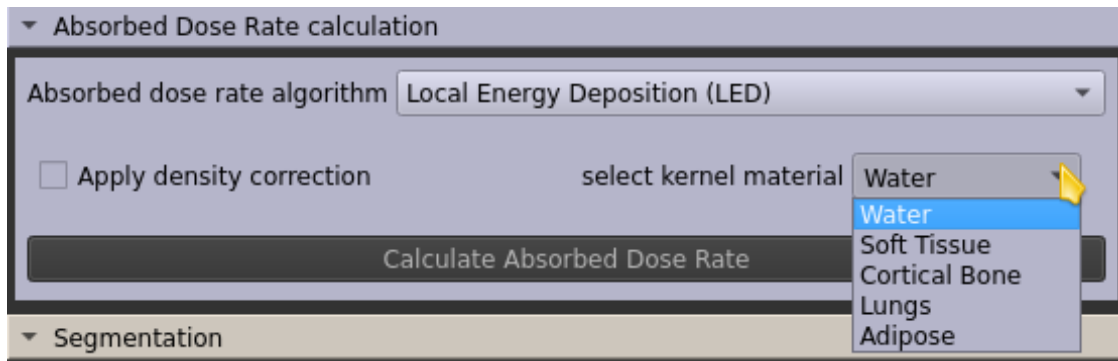


Figure 3.11: Implementation of the absorbed dose rate calculation by local energy deposition (LED)

3.2.3.2 Convolution

All convolution algorithms require a dose kernel to work described in subsection 1.5.2. These kernels were generated using dose point kernels obtained with GATE [SARRUT 2014] which were integrated in a voxel wise Monte Carlo Integration described in subsection 1.5.2.1 that has been proven to get very accurate results [PACILIO 2015]. The whole procedure was implemented in a python script.

Homogeneous Convolution The homogeneous convolution is implemented in OD3D using the package *scipy* that contains a multidimensional FFT convolution. Passing the activity map and the kernel with the same voxel sizes is enough to obtain the ADR map. The kernels are calculated for different materials (water, soft tissue, cortical bone, lung or adipose) and are available in the site <https://gitlab.com/opendose/opendosedvkdta>. The material can be selected in the module before performing the convolution.

Another possibility is to correct by using the density map making a voxel wise division. In this case a water kernel is used for the convolution and the density correction is performed after the convolution. For this the Apply density correction option must be marked.

Figure 3.12 show the graphical interface in OD3D.

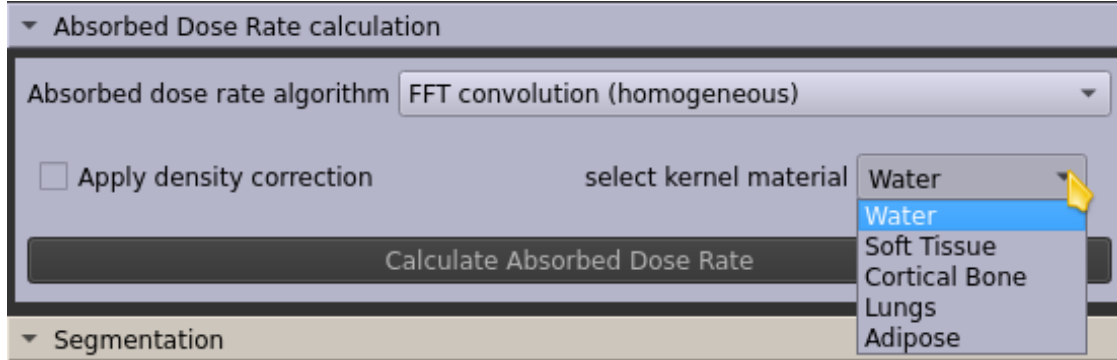


Figure 3.12: Implementation of the absorbed dose rate calculation by FFT homogeneous convolution (FFT)

Heterogeneous Convolution A fast-heterogeneous convolution algorithm (FHCA) was implemented in OD3D following Equation 3.3 and presented in EANM 2019 congress [VERGARA GIL 2019b]. The density correction is difficult to implement as it demands special care on the algorithmic procedure, otherwise, it will not be useful compared to alternate methods like Monte Carlo.

To start with, not all voxels have a usable value as they have no activity, or they have values of the order of the Poisson noise of the image. These voxels can be eliminated by thresholding.

The first approximation is the limit of the kernel, which is controlled by the user and can be assumed good enough after 5 times the electron maximum distance into the media to include all photon contribution. After this distance, the contribution decays exponentially, and is only relevant for non-source voxels. For the more energetic isotopes like ^{90}Y , this distance is around 10 mm. Therefore, a limit of 50 mm can be considered safe for most beta emitter isotopes.

For the average density, we made use of a vectorial grid, which quickly identifies voxels that belong to the line connecting the source and the target voxels. In this line, we plot 1000 samples in the density map and average them using fast *numpy* procedures.

The algorithm can be resumed by transforming Equation 1.25 into:

$$\dot{D}_{i,j,k}(t) = \sum_{m,n,o} A_{m,n,o}(t) \cdot \frac{S_{i,j,k \leftarrow m,n,o} \cdot \rho_w}{\bar{\rho}_{i,j,k \leftarrow m,n,o}(t)} \quad (3.3)$$

Where $\bar{\rho}_{i,j,k \leftarrow m,n,o}(t)$ is the average density in the linear path between voxel i, j, k and voxel m, n, o in the time t after the administration. The value of $S_{i,j,k \leftarrow m,n,o}$ is derived from the VDK using the relative positions of both voxels.

Finally, the entire procedure is vectorized and parallelized. The vectorization makes use

of fast vectorial procedures in *numpy* and the parallelization makes use of multi-threads to use several processors at once in the calculation. Figure 3.13 show the graphical interface in OD3D.

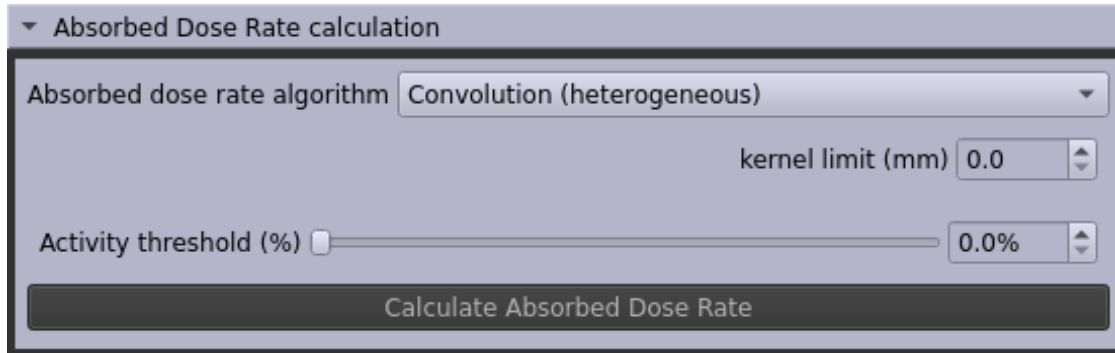


Figure 3.13: Implementation of the absorbed dose rate calculation by fast heterogeneous convolution algorithm (FHCA)

3.2.3.3 Monte Carlo

Using the software GATE [SARRUT 2014], it is possible to calculate the absorbed dose rates in each time point based on the density image and the activity map, that were calculated in previous steps.

Before the start of this work, a software named MCID was created [BOTTA 2012; BOTTA 2013] to generate the input files for Monte Carlo calculations. MCID would only run in Windows and could read DICOM, Interfile and ITK images. Originally implementing MCNP5 calculations, a new version running on top of GATE was created and validated [MILANO 2021]. This new version introduces also the ion source from GATE [VERGARA GIL 2019a].

The main problem of MCID was the maintainability, as it depended on close source system compilers and operating licenses. To avoid this and other issues, like the obsolete programming language (delphi) which has been discontinued, it was decided to reimplement the system in an open source system with modern scripting facilities. Hence, all the functionalities were translated to OD3D. But the essence, the template input files for GATE, were kept.

This template, previously used by MCID, is now filled by OD3D using patient specific data. Figure 3.14 show the graphical interface for Monte Carlo simulations in OD3D.

In the case of multiple time points an extra helper script is also created to run parallel simulations using GATE. Figure 3.15 show the structure of the files created for the input of GATE.

After running GATE, the patient folder will contain the raw absorbed dose images. The entire folder has to be imported back to OD3D to properly convert all volumes to proper units, since GATE images are expressed in $\text{Gy}\cdot\text{s}^{-1}$ and in OD3D they should be in $\text{mGy}\cdot\text{h}^{-1}$

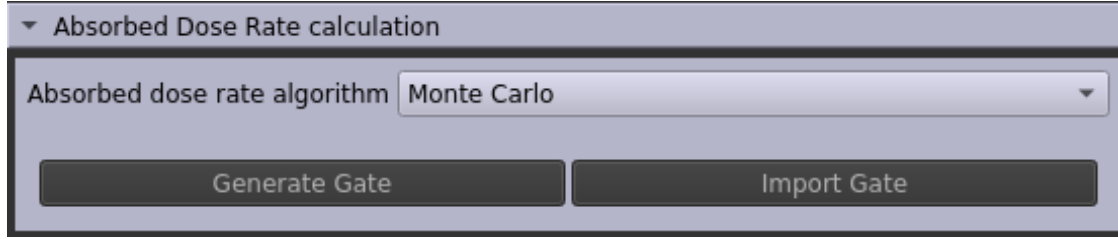


Figure 3.14: Implementation of the absorbed dose rate calculation by Monte Carlo Simulation (MC) in GATE

for compatibility with the rest of the workflow. This process also handles incomplete simulations correcting by real number of histories simulated. The importation process also places each volume in the respective time folder and rename it accordingly to the pre-established convention.

3.2.4 Time Data Extraction

Before integration in time, the time dependent data needs to be extracted from the respective images. OD3D expects a segmentation already performed at this point. All subsequent calculations were based in the VOI definition provided.

For activity workflow, the activity per segmented VOI per time point $A_{VOI}(t)$ are calculated. It is the simple sum of all voxels of the activity map inside each VOI.

$$A_{VOI}(t) = \sum_{\forall \text{voxel} \in VOI} A_{\text{voxel}}(t) \quad (3.4)$$

For absorbed dose rate workflow, the ADR per segmented VOI per time point $\dot{D}_{VOI}(t)$ are calculated. This is the mass-weighted average of all voxels of the ADR inside each VOI.

$$\dot{D}_{VOI}(t) = \frac{1}{M_{VOI}(t)} \cdot \sum_{\forall \text{voxel} \in VOI} m_{\text{voxel}}(t) \cdot \dot{D}_{\text{voxel}}(t) \quad (3.5)$$

The VOI mass per time point is calculated in both cases.

$$M_{VOI}(t) = \sum_{\forall \text{voxel} \in VOI} m_{\text{voxel}}(t) \quad (3.6)$$

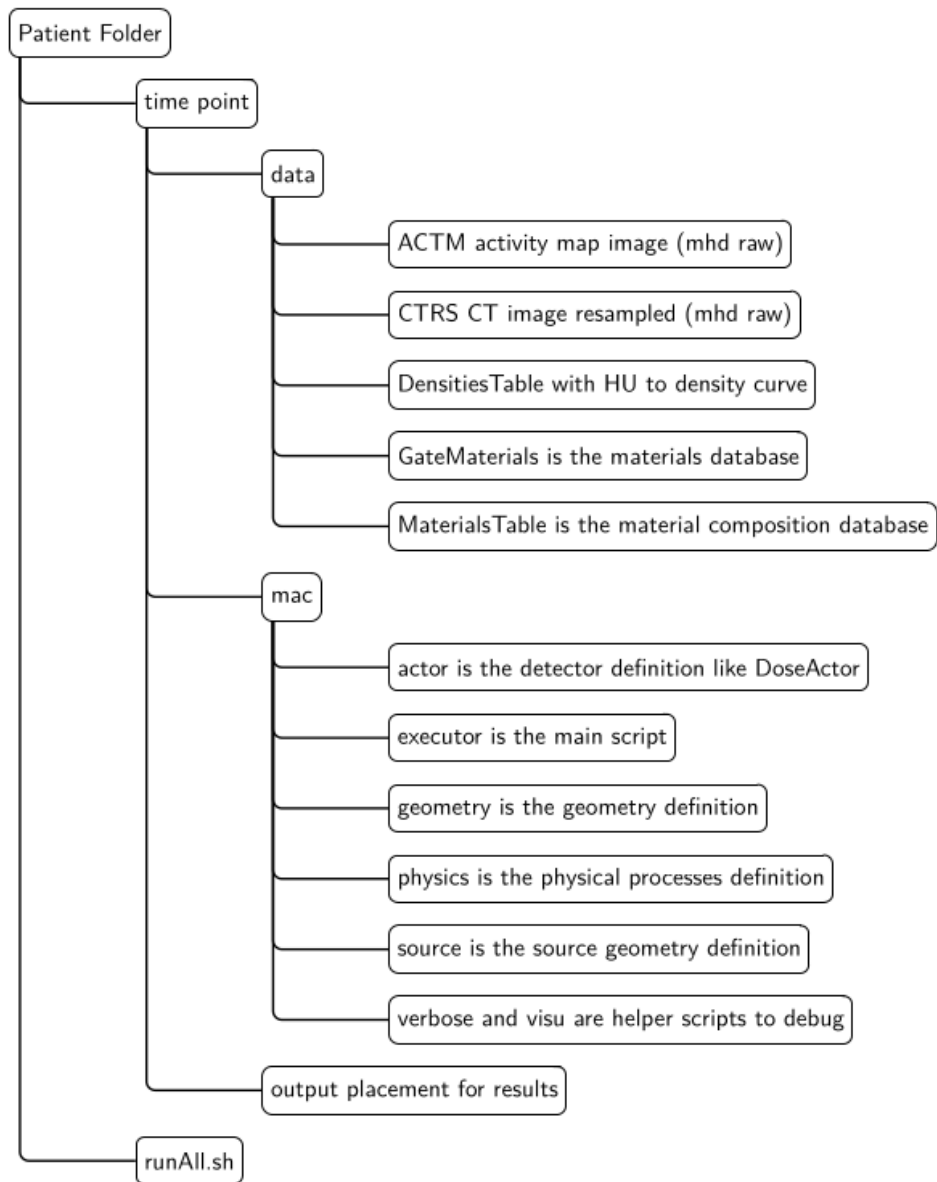


Figure 3.15: Structure of the files created for GATE input

3.2.5 Time Integration

Figure 3.16 show the typical pharmacokinetics of a radiopharmaceutical. It can be split in three main sections: uptake, data, tail.

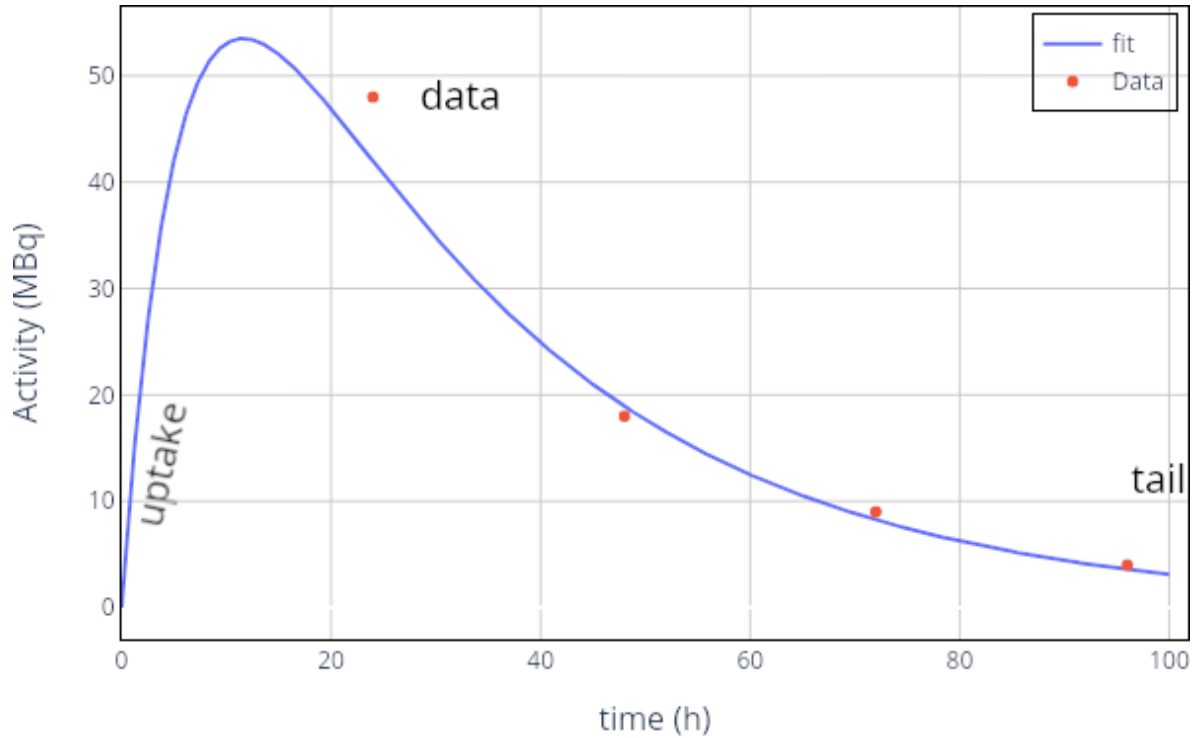


Figure 3.16: Sections in the pharmacokinetics of a radiopharmaceutical: uptake section $[T_0, T_1]$, Data section $(T_1, T_f]$, Tail section (T_f, ∞)

The fitting function usually reflects the pharmacokinetics main characteristics. However, for the uptake and tail sections, a hypothesis must be done.

Uptake section: from administration time to first measurement point. In the general case there is a need to wait until the equipment is able to measure due to restrictions like dead time. It is usually considered that the radiopharmaceutical distribution in the target organ needs to be modeled with some assumption.

The different possibilities are:

- **Linear:** assumes a fast administration. Activity at administration time T_0 is assumed to be $A(T_0) = 0$, and then increases linearly to the first time point T_1 . A measurement in the uptake section is mandatory for this assumption. Figure 3.17 resumes the main aspect of this assumption.

- Constant: assumes a slow administration and a slow uptake. It is considered that activity is constant between administration and the first time point. Figure 3.18 resumes the main aspect of this assumption.
- Exponential: assumes a fast uptake. The activity is rapidly incorporated to the VOI, and the first measurement time point is very late after administration. Figure 3.19 resumes the main aspect of this assumption.
- Free: assumed an unknown behavior. The activity is modeled using the fitting curve.

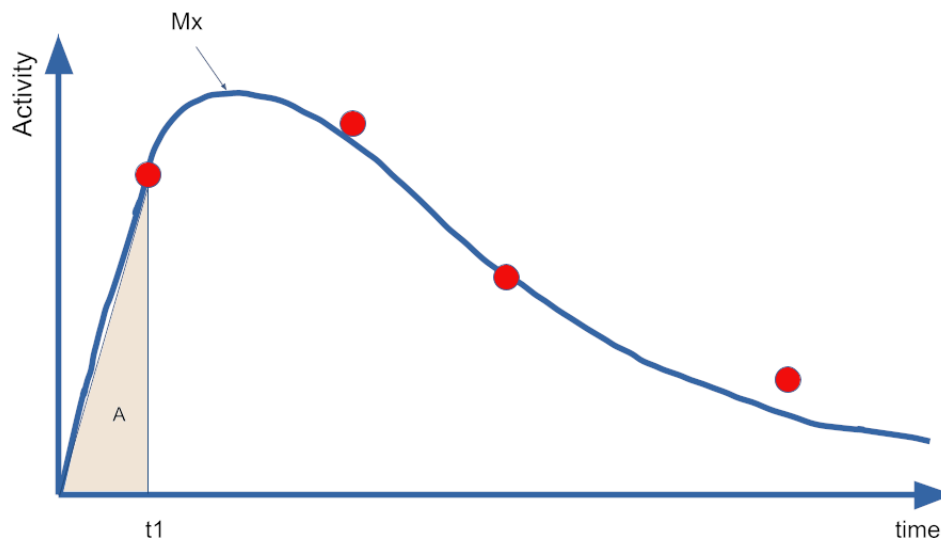


Figure 3.17: Linear uptake assumption. M_x is the theoretical maximum activity (or absorbed dose rate), t_1 is the first time point. The integration from 0 to t_1 is equal to triangle area A . Therefore a linear behavior can replace the unknown uptake section.

Data section: This is the actual data measured in the images. The integration in this step can be done using trapezoidal methods or just using numerical integration on a fitted function. Some fitting function usually considered are:

- *Mono-exponential:* $A(t) = A \cdot e^{-B \cdot t}$
- *Bi-exponential:* $A(t) = A \cdot e^{-B \cdot t} + C \cdot e^{-D \cdot t}$
- *Tri-exponential:* $A(t) = \sum_{i=1}^3 A_i \cdot e^{-B_i \cdot t}$
- *X-exponential:* $A(t) = A \cdot t^B \cdot e^{-C \cdot t}$

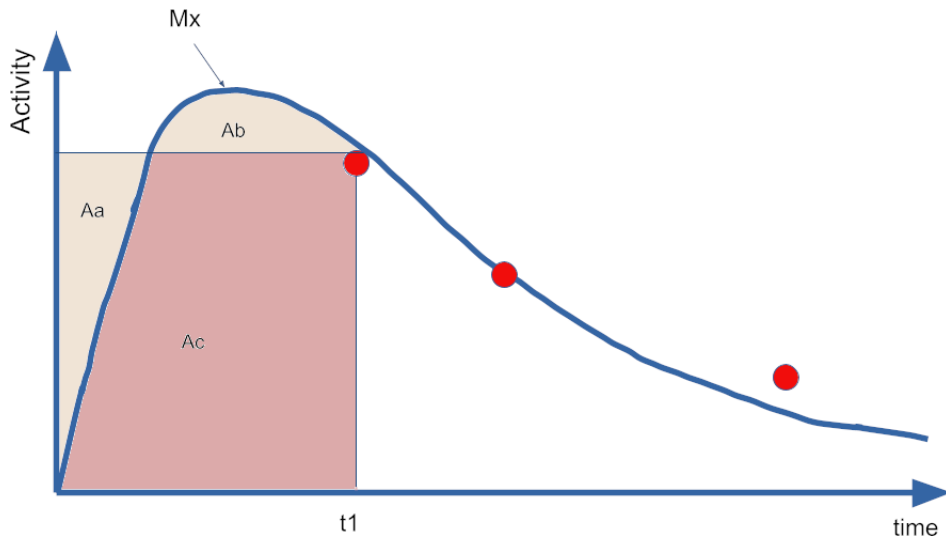


Figure 3.18: Constant uptake assumption. M_x is the theoretical maximum activity (or absorbed dose rate), t_1 is the first time point. The integration from 0 to t_1 is equal to areas $A_c + A_b$. The assumption establishes $A_a = A_b$, therefore a constant behavior can replace the unknown uptake section.

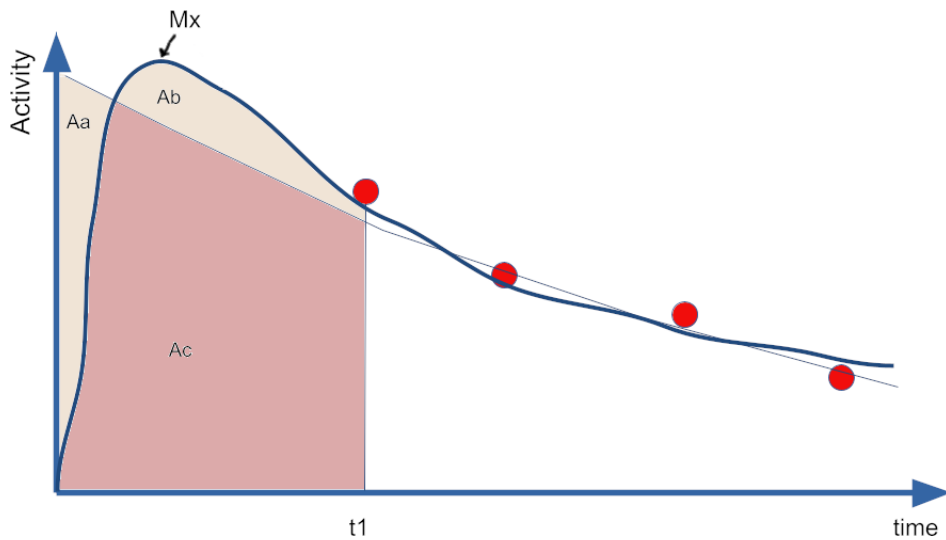


Figure 3.19: Exponential uptake assumption. M_x is the theoretical maximum activity (or absorbed dose rate), t_1 is the first time point. The integration from 0 to t_1 is equal to areas $A_c + A_b$. The assumption establishes $A_a = A_b$, therefore an exponential behavior can replace the unknown uptake section.

Tail section: after the last data point T_f the radionuclide is still in patient's body; therefore the integration must cover all decay up to infinity. The main assumptions are:

- *Physical decay:* no data about metabolism is present, the physical decay is just $A(t) = A_f \cdot e^{-\lambda \cdot t}$, where A_f is the activity in the last time point, $\lambda = \frac{\ln(2)}{T_{1/2}}$ and $T_{1/2}$ is the physical half life of selected isotope.
- *Effective decay:* Some knowledge about the biological decay is available, therefore a population-based effective decay factor is being used instead $A(t) = A_f \cdot e^{-\lambda_{eff} \cdot t}$. $T_{eff} = \frac{\ln(2)}{\lambda_{eff}}$ is the effective half life, accounting for both physical and biological decay.
- *Fitting decay:* the fitting function obtained in the data section is being used. This is not possible if the trapezoid integration was used in the data section.

The extracted time data variables need to be integrated in time. This was implemented in the OD3D module as a section that offers the election of each part of the fitting process as seen in Figure 3.16.

Figure 3.20 shows the graphical interface for data time integration in OD3D.

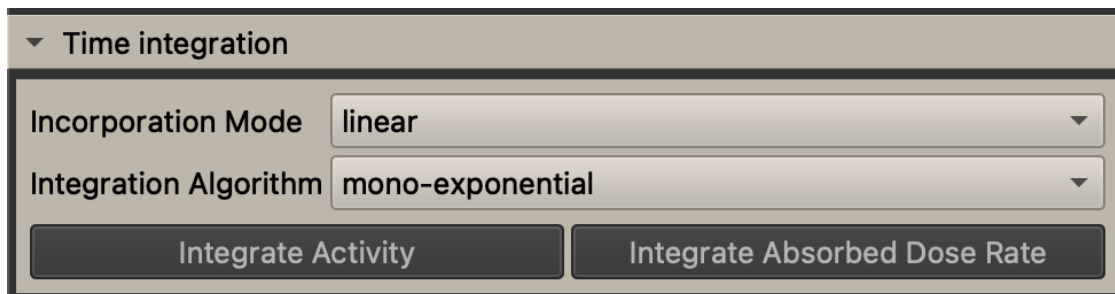


Figure 3.20: Implementation of the time integration of the data in OD3D

3.2.6 Reporting

The reporting tools were an original goal of this work, but the current implementation only includes data exportation to the IRDBB database [GIBAUD 2020]. Further developments will handle the exportation of a PDF file with all relevant data to be reported.

OpenDose3D module benchmarking

Contents

4.1	Evaluation of the generated kernels for convolution	91
4.1.1	Generation of DPK	92
4.1.2	Generation of VDK from DPK	96
4.2	Benchmarking of the Monte Carlo implementation	98
4.2.1	Materials and Methods	98
4.2.2	Results	100
4.2.3	Final Remarks	101
4.3	Comparison against commercial software	102
4.3.1	Segmentation and RTSTRUCT I/O	102
4.3.2	Comparison of the measured activities	108
4.3.3	Comparison of the time integration process	115
4.4	Absorbed dose rate algorithm comparison	115
4.4.1	Local Energy Deposition	116
4.4.2	Homogeneous Convolution	116
4.4.3	Heterogeneous Convolution	123
4.5	Conclusions	127

In this chapter we present the benchmarking steps for OpenDose3D (OD3D). We start by making an evaluation of the DPK and VDK generation for different isotopes. Then, a benchmark of the Monte Carlo algorithm is presented as a summary of our published article. Followed by a CDW comparison of OD3D against two commercial software in a clinical test case. Finally, a comparison of the implemented ADR algorithms is presented.

4.1 Evaluation of the generated kernels for convolution

To validate the convolution methods, the kernels must be generated and validated first. In this work, the kernels were generated by the use of DPK as explained in subsection 1.5.2.

4.1.1 Generation of DPK

The first step is to validate the generated DPK with those similarly reported in the literature. [PAPADIMITROULAS 2012] reported DPK generated in several media using GATE 6.1 and Geant4 4.9.4p02. Their simulations were made using concentric spherical shells and measuring the absorbed dose in a 3D voxel map as shown in Figure 4.1. The simulation also uses the ion source capabilities of geant4.

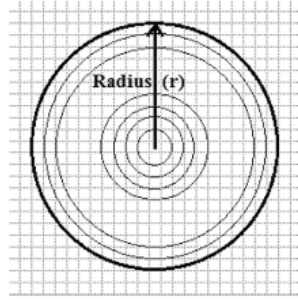


Figure 4.1: PPDT simulation schema.

We compared our calculation (using GATE 8.2, Geant4 4.10.5, ion source, [VERGARA GIL 2019a]) with the reported values. A priori, the differences in version of GATE should not induce differences in the results as the physics; lists and interaction processes, cross-sections, etc., remained the same. The main difference between approaches lies in energy scoring: [PAPADIMITROULAS 2012] scores the energy in voxels, whereas we score the energy deposited directly in each spherical shell (200 shells with logarithmic radius increase from $1 \mu\text{m}$ to 1m) and deriving the function of the absorbed dose to the radial distance by using the effective radius ($R_{D,i}$) of the shell, as described by [JANICKI 2004] and displayed in Equation 4.1:

$$R_{D,i} \cong \sqrt{\frac{1}{3} \frac{R_{i+1}^3 - R_i^3}{R_{i+1} - R_i}} \quad (4.1)$$

The energy deposited in each shell per disintegration ($E_{D,i}$) is divided by the shell mass ($M_{D,i}$), giving the function of the absorbed dose to the effective radius of the shell (Equation 4.2).

$$DPK(R_{D,i}) = \frac{E_{D,i}}{M_{D,i}} \quad (4.2)$$

Since the DPK is pre-calculated in water, it is possible to use other materials using the formalism proposed by [CROSS 1992] as shown in Equation 1.24.

Figure 4.2 shows our results for some selected isotopes, although more isotopes were simu-

lated. Figure 4.3 (^{131}I), Figure 4.4 (^{177}Lu), and Figure 4.5 (^{90}Y) present the comparison with literature in the reference domain as our calculations cover a broader distance range. Each isotope simulation took approximately one week in a workstation (10^8 primaries representing 100 MBq as per ion source definition to get less than 1% uncertainty in the outermost shell), although several isotopes can be processed at the same time.

The observed differences, especially in the ^{177}Lu case were consistent with the differences reported by [TRANEL 2019]. These derive from differences between geometry definition and energy scoring, and the non-ideal discretization of space in 3D voxels in ref [PAPADIMITROULAS 2012], which is more relevant at high gradient zones. The difference in the GATE version is not relevant in this case as the same ENDFVII disintegration library [ALLISON 2016] is used. In the case of [GRAVES 2019] data, the MNCP software was used and therefore a different disintegration library that explains the low energy discrepancies as reported by [MAIGNE 2011].

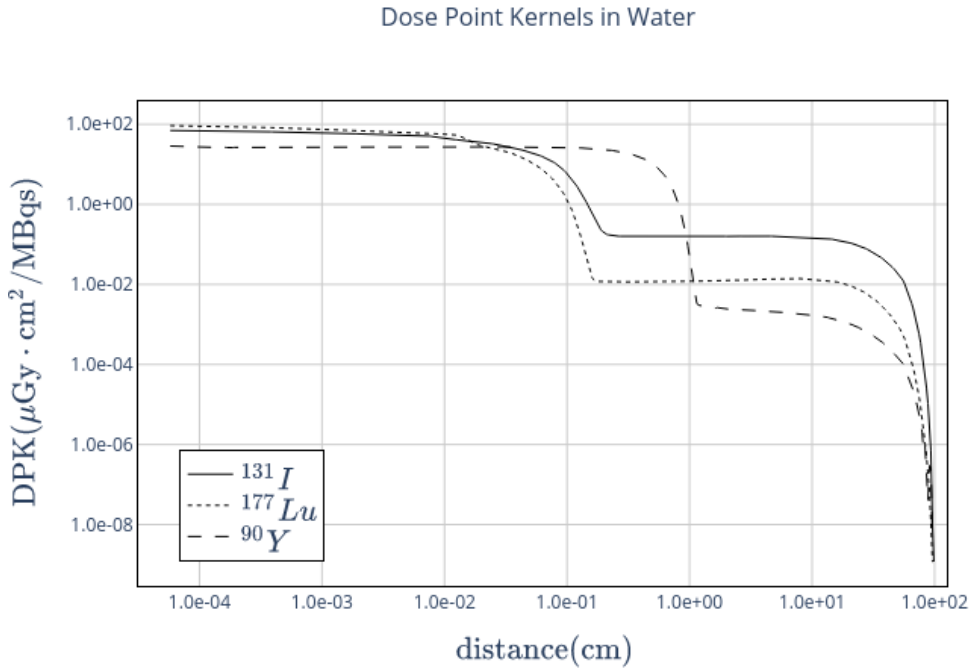


Figure 4.2: DPK generated by OD3D scripts

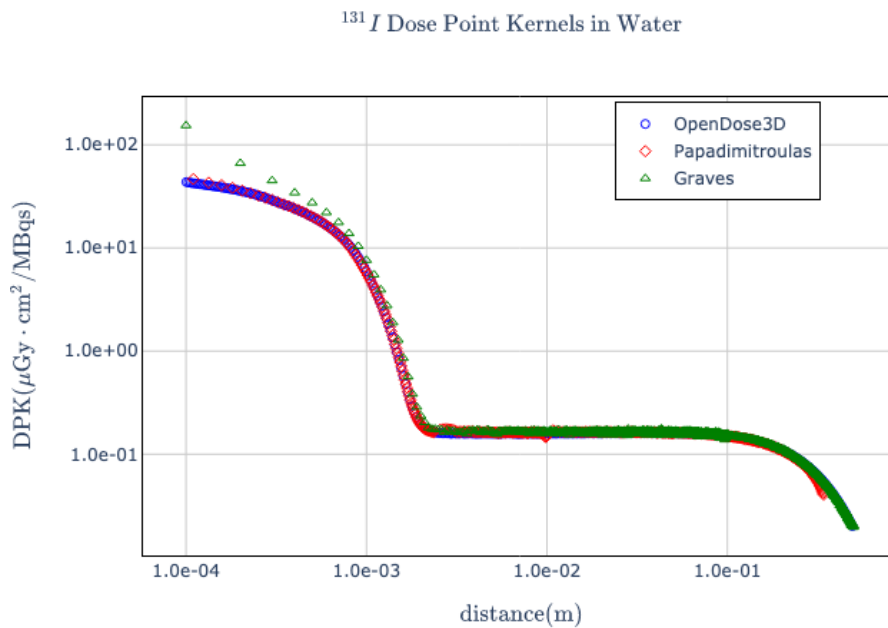


Figure 4.3: Comparison of ^{131}I -DPK in water from OD3D compared with references [PAPADIMITROULAS 2012] and [GRAVES 2019] in the domain of the reported values

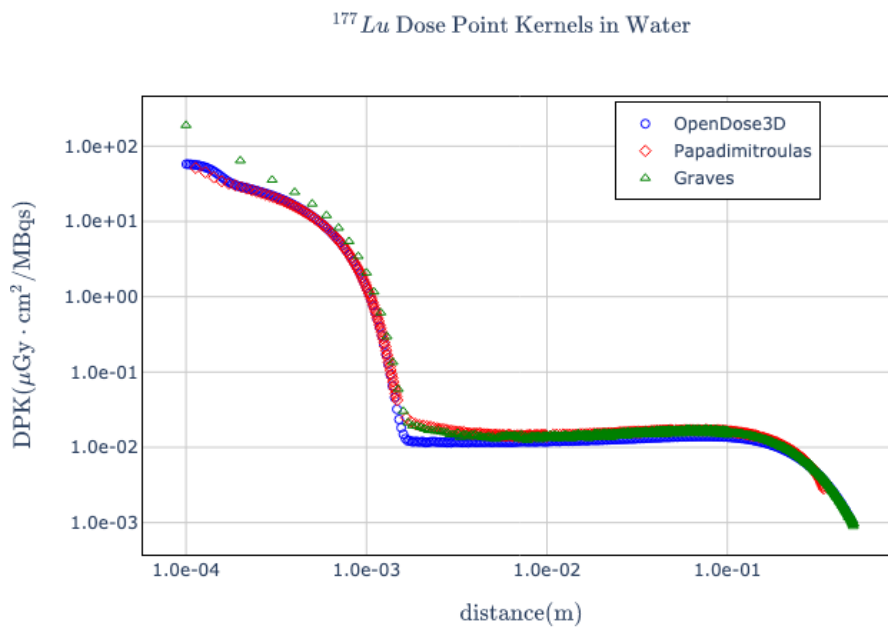


Figure 4.4: Comparison of ^{177}Lu -DPK in water from OD3D compared with references [PAPADIMITROULAS 2012] and [GRAVES 2019] in the domain of the reported values

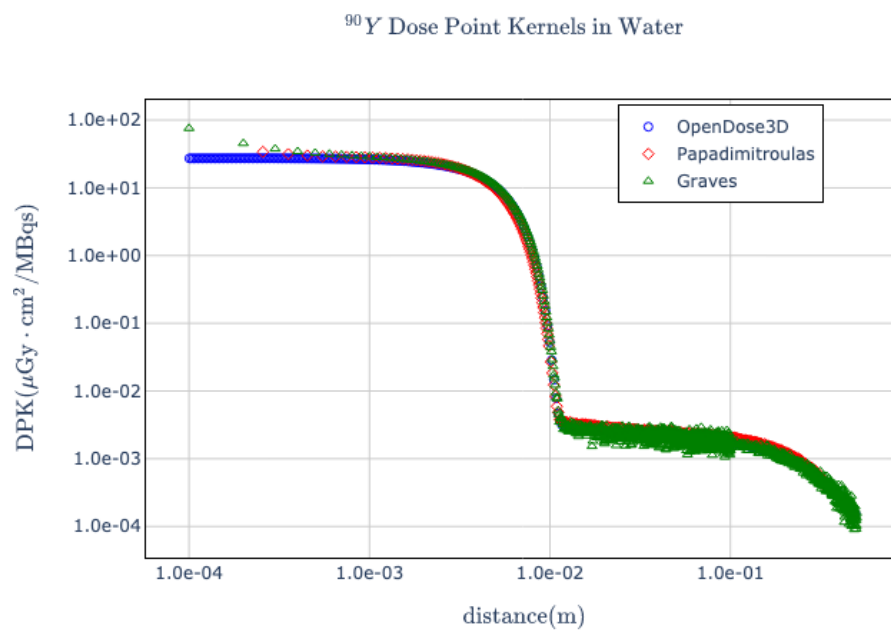


Figure 4.5: Comparison of ^{90}Y -DPK in water from OD3D compared with references [PAPADIMITROULAS 2012] and [GRAVES 2019] in the domain of the reported values

4.1.2 Generation of VDK from DPK

With the DPK validated, the VDK generation process must be validated at this point. With the theory described in subsection 1.5.2.1, a python script was produced to generate VDK in water for some isotopes (with pre-calculated DPK) and any voxel size. The results for ^{90}Y , ^{131}I and ^{177}Lu in soft tissue, using Equation 1.24 with $\eta_w = 0.976$ [CROSS 1992], are compared to the values published in MIRD Pamphlet 17 [BOLCH 1999] and to [LANCONELLI 2003]. The MIRD 17 values were generated for soft tissue only and calculated using EGS4, unfortunately there were no data for ^{177}Lu at that moment. Lanconelli report calculations for several isotopes and media, and for several voxel sizes. The MIRD 17 data was produced using EGS4 Monte Carlo code, therefore we expected some differences specially in the close vicinity where the mean free path of charged particles may vary because of old EGS vs modern GATE differences in the implementation of electron interactions.

Figure 4.6, Figure 4.7 and Figure 4.8 present the comparison of VDK for the selected isotopes in 3 mm voxel for soft tissue. The differences observed in the case of ^{90}Y can only be explained by differences in emission spectra, as our results were consistent with those reported by [LANCONELLI 2003].

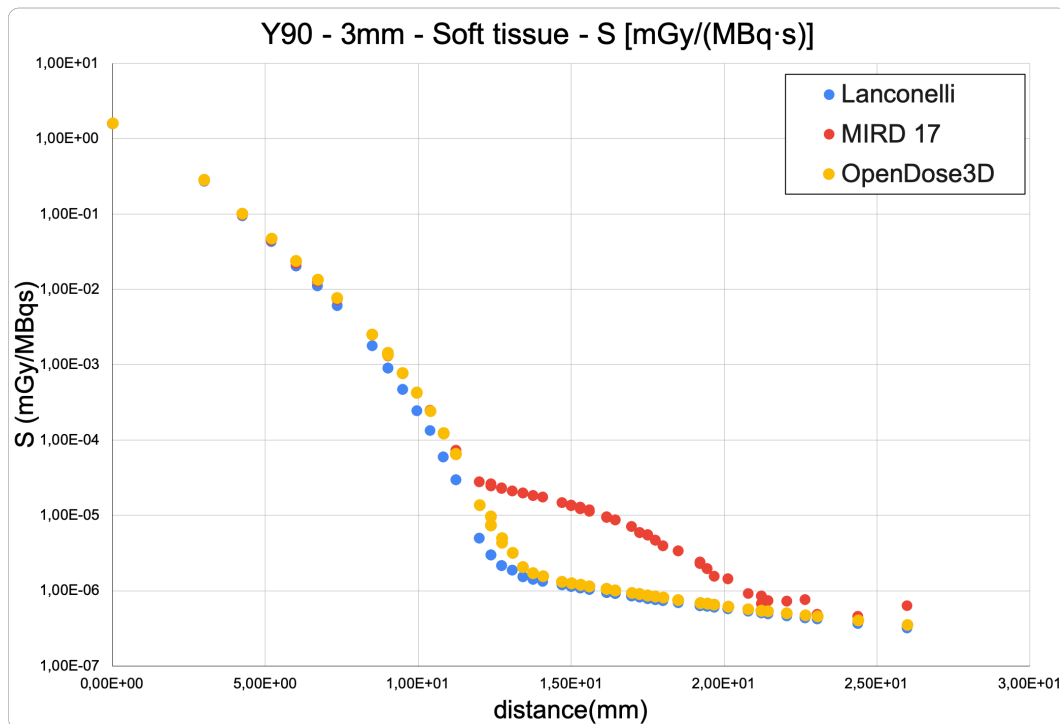
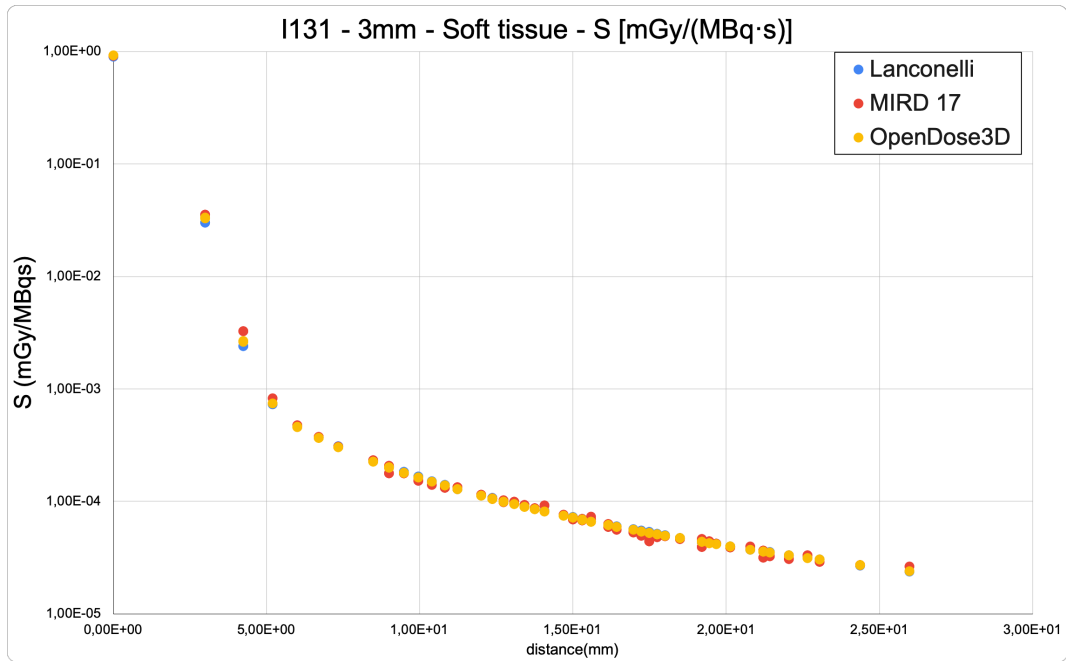
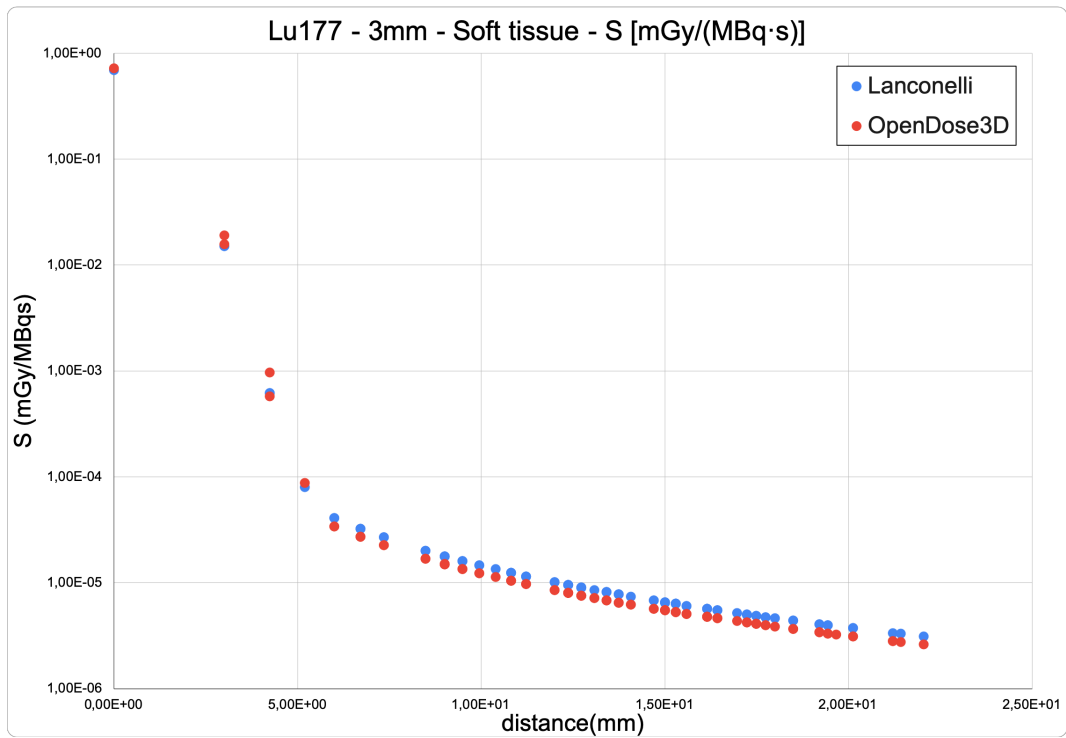


Figure 4.6: VDK comparison for ^{90}Y in soft tissue with cubic voxel size 3 mm side

Figure 4.7: VDK comparison for ^{131}I in soft tissue with cubic voxel size 3 mm sideFigure 4.8: VDK comparison for ^{177}Lu in soft tissue with cubic voxel size 3 mm side

4.2 Benchmarking of the Monte Carlo implementation

As presented in subsection 3.2.3.3, the Monte Carlo input file template has been already validated by [MILANO 2021] using the previous OD3D version named MCID. The main aspects of the benchmark presented in the article are summarized here.

4.2.1 Materials and Methods

For the algorithm evaluation, voxelized models were defined, starting from real patient images. The choice of using models was expressly made in order to set activity ground truth and to easily define different density/activity combinations by properly modifying the model. It is important to notice that the algorithm is strictly related to the validation process with computational models; no real patient images had been directly loaded on MCID.

The algorithm developed for the evaluation of the TPS can be summarized as follows:

- Model creation.
- Simulation of SPECT projections.
- Attenuation map generation and tomographic reconstruction.
- Creation of the input file for the MC simulation.
- Conversion of the GATE output file in absorbed dose images.
- Calculation of absorbed dose images by convolution of voxel S-values (performed in an independent homemade software for comparison and verification purposes).

The voxelized model used in this benchmark was constructed starting from a real patient CT (512×512 matrix with a pixel size of $1.367 \text{ mm} \times 1.367 \text{ mm}$ and a spacing between slices of 3.27 mm , high quality full diagnostic scan). Activity maps, with the same voxel and matrix size of the CT scan, were also constructed, which allows the definition of the activity concentration ratio among different regions.

^{99m}Tc -SPECT projections were simulated with the SIMIND MC code [LJUNGBERG 1989] using the contoured CT and the activity map created as input. The reconstruction was performed using the ordered-subset expectation maximization (OSEM) algorithm, with two iterations and 10 subsets. Corrections for the collimator-detector response (CDR), attenuation, and scatter were applied, the latter obtained through the *ESSE* algorithm [FREY 1996]. The reconstructed images had cubic voxels of 4.1 mm size and matrix size of 128×128 .

Voxelized models were designed, simulating three clinical cases with different activity and density maps.

The Uniform Liver (UL) case: has liver with homogeneous density, uniform activity inside the liver and no activity outside it. Liver homogeneity and uniform activity distribution were the hypotheses of the standard MIRD approach at the organ level, so this scenario was considered in order to compare the average absorbed dose calculated by the MC-based TPS with the average absorbed dose calculated by the classical AAPM (American Association of Physicists in Medicine) Equation 4.3 [DEZARN 2011]:

$$D(\text{Gy}) = 49.38 \text{ Gy}\cdot\text{kg}\cdot\text{GBq}^{-1} \cdot \frac{A_0(\text{GBq})}{m(\text{kg})} \quad (4.3)$$

Where A_0 is the ^{90}Y activity at the injection time and m is the liver mass. The multiplicative factor $49.38 \text{ Gy}\cdot\text{kg}\cdot\text{GBq}^{-1}$ accounts for the physical characteristics of ^{90}Y (half-life and average energy emitted per nuclear transition) and has a relative statistical uncertainty of 0.1 % [DEZARN 2011]. No production of bremsstrahlung and energy completely released inside the mass of interest were also assumed for the calculation of the multiplicative factor.

The Spherical Regions (SR) Case: has homogeneous liver and activity in three spherical regions only. These spheres, placed inside the liver, were named **SS** (Small Sphere), **MS** (Medium Sphere), and **BS** (Big Sphere) and their radii were 10 mm, 20 mm and 30 mm, respectively.

This scenario was created in order to compare the average absorbed dose for each sphere obtained from the GATE output with that obtained from OLINDA/EXM [STABIN 2005] S-factors for ^{90}Y and spheres of soft tissues with unit density.

From the table of S-factors associated to sphere masses included into OLINDA/EXM, the following relationship between S-factors (expressed in $\text{mGy}\cdot\text{MBq}\cdot\text{s}$) and sphere mass m (expressed in g) was obtained and used to derive the corresponding dosimetric factor for a sphere of arbitrary mass:

$$S[\text{mGy}\cdot\text{MBq}\cdot\text{s}] = 0.12456 \cdot m[\text{g}]^{-0.97267} \quad (4.4)$$

As S-factors were referred to spheres with unit density, the soft tissue density for this scenario was set to $1.00 \text{ g}\cdot\text{cm}^{-3}$.

The Non-Uniform Liver (NUL) Case: can be divided in two subcases:

- **NUL-a:** presenting a liver with homogeneous density and activity placed inside both spherical regions and liver with activity concentration ratio of 5:1, respectively. This

presents a non-uniform activity distribution and was built to evaluate the absorbed dose differences between the S-voxel convolution method and MC.

- **NUL-b:** presenting a liver with non-homogeneous density and activity placed inside the spherical regions (possible tumor lesions) and liver with activity concentration ratio of 5:1, respectively. This is a realistic scenario and was developed in order to quantify the absorbed dose distribution in tumor regions with different density as compared to the healthy parenchyma, using the S-voxel convolution method and MC.

4.2.2 Results

The computational time for each MC simulation was around 5 h. The relative statistical uncertainty on the absorbed dose value in a single voxel, due to the MC statistical processing, was below 1% for the range 150 Gy to 700 Gy, below 2% for the range 50 Gy to 150 Gy and below 10% for the range 1 Gy to 10 Gy.

Uniform Liver Case: The results for the mean absorbed dose calculation with the MIRD approach at the organ level and direct MC simulation were reported in Table 4.1.

D_{gate} (Gy)	D_{mird} (Gy)	$RD(\%)$
36.79	36.69	0.27

Table 4.1: Comparison between average absorbed dose values to the liver, calculated from the GATE image (D_{gate}) and from the MIRD approach (D_{mird}) at the organ level. The relative difference is defined as $RD(\%) = \frac{D_{gate}}{D_{mird}} - 1$

Spherical Regions Case: The comparison between average absorbed dose values for each sphere is reported in Table 4.2.

Sphere type	D_{gate} (Gy)	D_{olinda} (Gy)	$RD(\%)$
BS	666	625	6.57
MS	558	604	7.62
SS	176	571	69.2

Table 4.2: Mean absorbed dose values for each sphere, calculated from the GATE image (D_{gate}) and from the application of the OLINDA/EXM factors (D_{olinda}). The relative difference is defined as $RD(\%) = \frac{D_{gate}}{D_{olinda}} - 1$

In this case, differences were more visible, above all for SS, whose result is probably affected by partial volume effects (PVE). In order to verify this assumption and reduce these effects, the initial activity map was used as input for MC simulation, skipping SPECT simulation

and reconstruction. The obtained results were reported in Table 4.3, where the PVE becomes more evident as the spheres decrease in size.

Sphere type	D_{gate} (Gy)	D_{olinda} (Gy)	$RD(\%)$
BS	613	625	1.92
MS	588	604	2.65
SS	517	571	9.46

Table 4.3: Mean absorbed dose values for each sphere, calculated from the GATE image (D_{gate}) with a reduced workflow and from the application of the OLINDA/EXM factors (D_{olinda}). The relative difference is defined as $RD(\%) = \frac{D_{gate}}{D_{olinda}} - 1$

Non-Uniform Liver Case: Several absorbed dose profiles for each subcase were extracted from different transversal slices. All profiles selected for the NUL-a case showed a relative difference within 3% between the absorbed dose images calculated by MC simulation and convolution of voxel S-values. Relative differences for the entire liver confirmed that this result is valid for all liver slices, except for some boundary voxels, actually external to the liver and characterized by low dose values (less than few grays).

The relative differences (RD) between the absorbed dose images were up to 14% in the spherical regions. This is introduced by the spheres having a different density ($1.200 \text{ g}\cdot\text{cm}^{-3}$) as compared to the surrounding liver ($1.050 \text{ g}\cdot\text{cm}^{-3}$) which convolution does not take into account. The ratio of the densities 14.28% is in complete agreement with the observed relative differences.

4.2.3 Final Remarks

The benchmark of the MC algorithm is demonstrated at both organ and voxel level for the ^{90}Y case. Since the change of the isotope in the MC method is just a matter of changing the source definition, the rest of the algorithm remains unchanged. Therefore, given that the isotopes are a standard library already validated in GATE, we can conclude that the entire algorithm is validated.

In particular, for the Uniform Liver scenario, the comparison between mean absorbed doses to liver assessed with the MIRD approach at the organ level and with the MC-based TPS showed a very good agreement ($RD = 0.27\%$). It is interesting to point out that D_{mird} is a merely theoretical quantity, while D_{gate} depends on the image quality, e.g., partial volume effects (PVE), which in this first case appear negligible due to the big size of the observed object (i.e., the whole liver).

The effects due to image blurring become relevant when dealing with smaller objects, as in the Spherical Regions case. This scenario allowed a comparison between the average absorbed doses to each sphere. While the BS and the MS present a $RD < 8\%$ between the

two methods, the SS shows a dramatic $RD = -69.2\%$, caused by the PVE affecting the SPECT simulation with SIMIND.

4.3 Comparison against commercial software

We compared OD3D against two commercial software MIM and Planet Dose. The test case is a patient with advanced liver cancer, provided by the IAEA CRP E2.30.05 on Dosimetry in Radio-pharmaceutical therapy for personalized patient treatment. The imaging data consists of 5 SPECT/CT acquired after administration of 6848 MBq of ^{177}Lu -DOTATATE®. The calibration factor ($122.6 \text{ Bq}\cdot\text{counts}^{-1}$) was provided by the clinical department where acquisitions and reconstructions were performed.

The objective is to compare activities and time-activity curves. In order to split the problem in smaller steps, we first decided to investigate the consistency of RT Struct definition and import/export (in order to make sure that we indeed compared activities in the same volumes). Segmentation should be the same in all platforms. Organ mass/volume should be recorded.

The comparison was made against two commercial software:

1. MIM: Sureplan® MRT
2. Dosisoft: Planet Dose®

Timestamp extraction was tested in all three platforms (OD3D, Planet Dose, MIM). All platforms calculate the same timestamp, based on acquisition time after injection: 1.0h, 3.91h, 21.77h, 45.04h, 93.36h. These correspond to the planned scan times at 1h, 4h, 24h, 48h and 96h respectively.

4.3.1 Segmentation and RTSTRUCT I/O

To perform the segmentation comparison we shall use a unique software to create the VOI, then export it and finally import it in a different software. We have performed some test of interoperability using the three software OD3D, Planet Dose and MIM. Doing this we have encountered some issues:

- MIM software cannot read RTSTRUCT generated by OD3D.
- MIM software can read RTSTRUCT generated by Planet Dose, but only allocate in one time point.
- Planet Dose cannot insert RTSTRUCT generated by OD3D at the right time point.

- OD3D can read RTSTRUCT generated by Planet Dose, but only allocate in one time point.

We can therefore draw a summary of possible structure exchange between platforms as seen in Figure 4.9. It is observed that by using the MIM platform to create the primary segmentation, we can successfully import it in the other software.

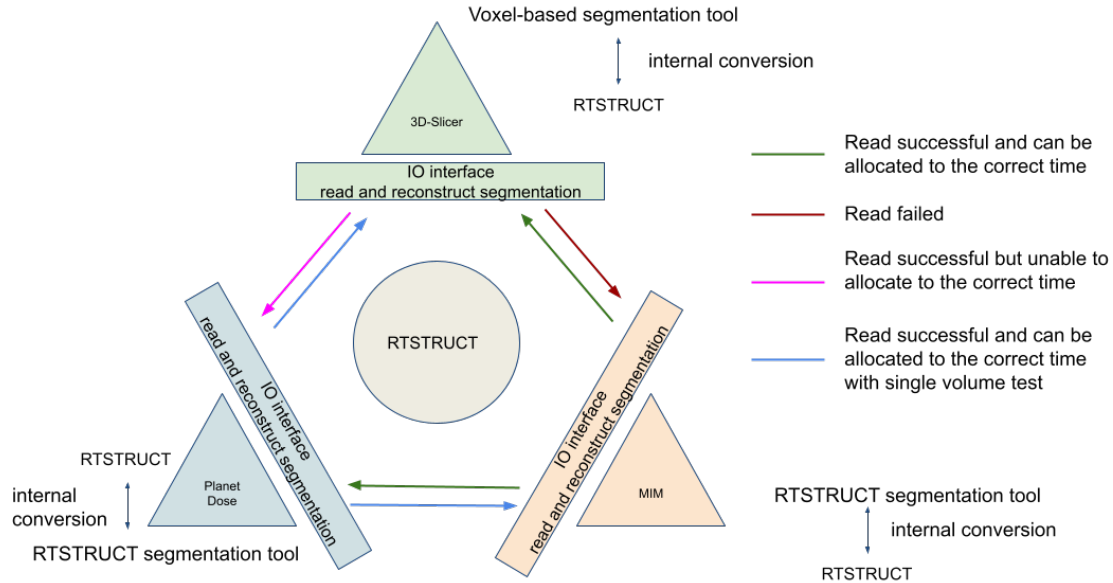


Figure 4.9: Interoperability with RTSTRUCT for the different workstations: OD3D, Planet Dose and MIM

We decided to use the MIM platform to draw the primary segmentation. Five time point RTSTRUCT files were generated in MIM. They were successfully imported into OD3D to generate the binary label maps that can be converted back into Voxel-based segmentation. RTSTRUCT files were also successfully imported to the Planet Dose.

The organ segmentation considered 6 organ/tissue VOI; (Left Lung (LL), Right Lung (RL), Left Kidney (LK), Right Kidney (RT), Liver and Spleen), plus the sum of remaining organs called remainder of the body (RB) making a total of 7 VOI.

When initially imported in Planet Dose, the RTSTRUCT contour for RB represented the whole body (without the cavities generated by included VOI). This in fact corresponds to preferences that can be setup within Planet Dose: by default, all VOI included in a large VOI are suppressed. The RB VOI for Planet Dose was regenerated using internal Boolean operations. The results are presented in Table 4.4.

Since the organ segmentation was initially performed in MIM, the volume information in the MIM platform was used as a reference to compare with the remaining two software. Table 4.5 shows some volume deviations between MIM and Planet Dose (around 9% relative difference). However, OD3D shows very good consistency with MIM.

MIM		Volume (cm ³)					
Time (h)	LL	RL	LK	RK	spleen	liver	RB
1.0	709	893	159	172	103	1666	21279
3.9	749	955	187	170	98	1502	22030
21.8	770	1057	155	135	100	1741	21197
45.0	667	811	135	156	105	1853	21000
93.4	854	1057	141	137	99	1832	21149

Planet Dose							
Time (h)	LL	RL	LK	RK	spleen	liver	RB
1.0	773	988	174	191	116	1747	21170
3.9	803	1051	204	187	111	1576	21911
21.8	842	1163	173	148	112	1828	20333
45.0	721	899	152	173	118	1947	20509
93.4	936	1212	159	152	112	1924	21000

OD3D							
Time (h)	LL	RL	LK	RK	spleen	liver	RB
1.0	698	891	161	172	103	1664	21329
3.9	749	953	188	171	98	1500	22049
21.8	749	1056	155	136	101	1740	21232
45.0	667	810	136	157	105	1849	21085
93.4	836	1054	143	138	99	1829	21199

Table 4.4: Volumes in MIM and corresponding values after export to Planet Dose and OD3D

Relative differences ($RD(\%) = \frac{A}{MIM} - 1$) in segmented volumes							
Planet Dose vs MIM (mean 7.4%)							
Time (h)	LL	RL	LK	RK	spleen	liver	RB
1.0	-8.3	-9.6	-8.6	-9.9	-11.2	-4.6	0.5
3.9	-6.7	-9.1	-8.3	-9.1	-11.7	-4.7	0.5
21.8	-8.6	-9.1	-10.4	-8.8	-10.7	-4.8	4.2
45.0	-7.5	-9.8	-11.2	-9.8	-11.0	-4.8	2.4
93.4	-8.8	-12.8	-11.3	-9.9	-11.6	-4.8	0.7
OD3D vs MIM (mean 0.02%)							
Time (h)	LL	RL	LK	RK	spleen	liver	RB
1.0	1.6	0.2	-1.2	0.0	0.0	0.1	-0.2
3.9	0.0	0.2	-0.5	-0.6	0.0	0.1	-0.1
21.8	2.8	0.1	0.0	-0.7	-1.0	0.1	-0.2
45.0	0.0	0.1	-0.7	-0.6	0.0	0.2	-0.0
93.4	2.2	0.3	-1.4	-0.7	0.0	0.2	-0.2

Table 4.5: Relative difference ($RD(\%) = \frac{A}{MIM} - 1$) of segmented volumes. "A" stands for either OD3D or Planet Dose.

Figure 4.10 show a simplified schema to explain the differences encountered. The RTSTRUCT file contains a lot of contour information registered for each slice of the tomographic image. Therefore, a simpler example was created.

We used a 10×10 pixels organ contour example to illustrate the segmentation process in clinical dosimetry software and the differences generated when converting RT structures into voxel-based contours. There are four steps in the re-pixelation when moving the VOI as a RTSTRUCT file to a different software:

1. Image acquisition with intrinsic machine resolution into voxel-based contour. Here is the machine converting process, the image saves pixel information in each slice, this information can be quantified to be some ROI.
2. Images refer to a some contour which is made by the operator. The principle is that if the organ edge touches this pixel, this pixel will become this part of ROI.
3. Voxel (Pixel) based contours convert into polygon which connects the center of the outermost pixel to form a polygon, after finishing this step the RTSTRUCT is generated.
4. The polygon is regenerated into a voxel (Pixel) based contour.

Different software may diverge here, there are two possibilities for the re-pixelation:

1. The polygonal line passing through the midpoint of the pixel will be re-identified as the corresponding ROI.
2. The polygonal line that touches the pixel will be re-identified as the corresponding ROI.

According to these assumptions, it is possible to analyze the re-pixelation process of Planet Dose and 3D-Slicer for the same RTSTRUCT file. Figure 4.10 show the re-pixelation influence in the import/export sequence. In the fourth subfigure, the red pixels that are touched by a polygonal line can be recognized as part of ROI if the second possibility is used. The re-pixelated voxel-based contour will contain more information than the first one based in the center of pixel recognition principle.

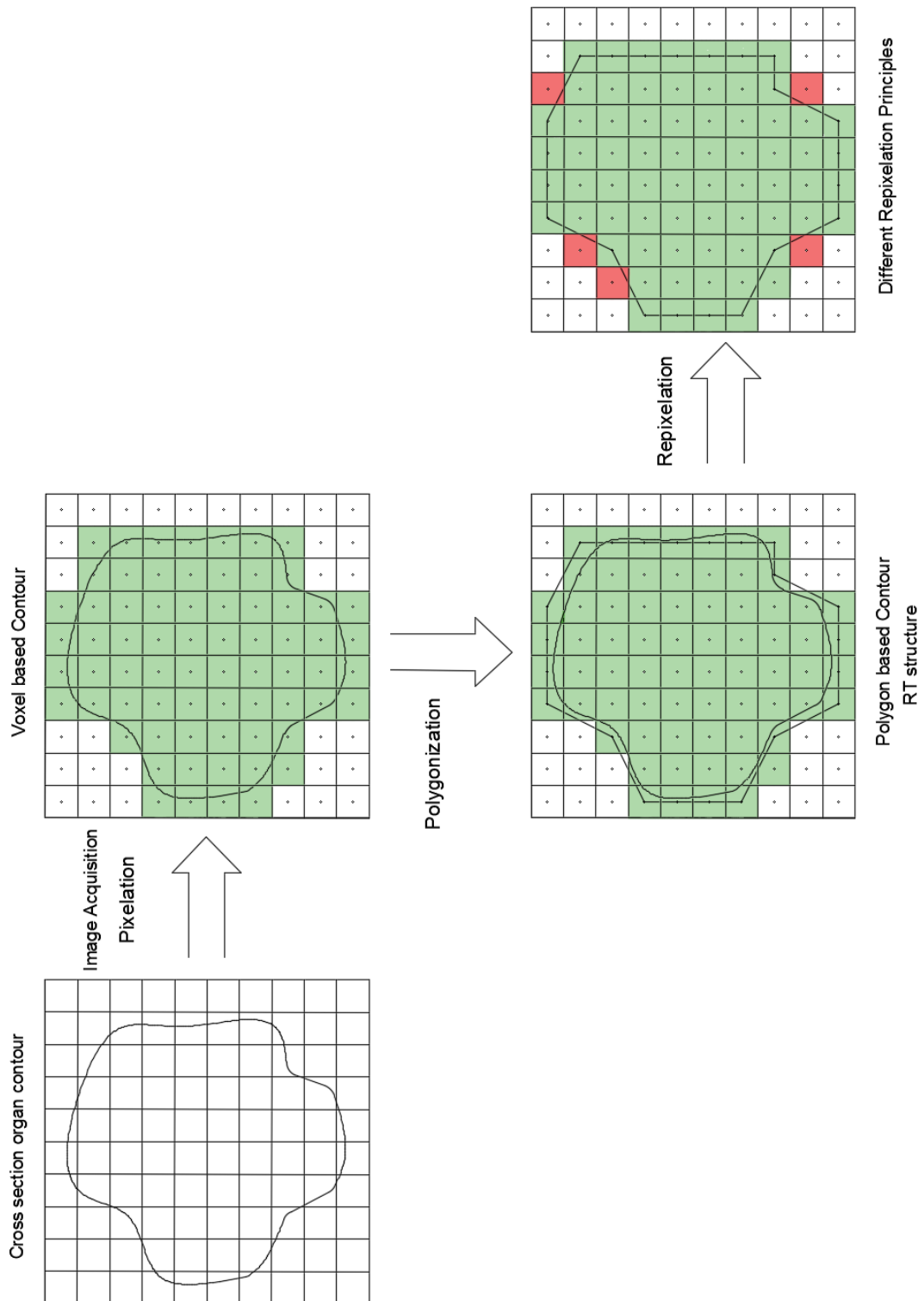


Figure 4.10: Inner conversion process from voxel-based contour to polygon-based contour with two different re-pixelation possibilities

4.3.2 Comparison of the measured activities

Activities in different VOI as extracted in all three software are presented in Table 4.6.

Given that the volumes were different between Planet Dose and the other workstations, the activity cant be compared directly. Therefore, the activity concentration was computed to remove the volume influence and allow the comparison. Activity concentration in the different VOI extracted in all three software are presented in Table 4.7.

Table 4.8 presents the relative differences in activity concentration extracted from OD3D compared with Planet Dose and with MIM. As can be seen in the comparison of OD3D vs Planet Dose, the relative differences were low ($RD < 4\%$) for homogeneous VOI (kidneys, spleen, liver) and can be large in the lungs and the RB. This can be explained by the exclusion in Planet Dose of low density voxels even when they belong to the segmented VOI. The relative differences between MIM and OD3D were consistently below 2%, as could be expected from volume segmentation results (Table 4.5). Figure 4.11 (lungs), Figure 4.12 (kidneys), and Figure 4.13 (liver and spleen), present the plots for the distribution of activity in time for the selected VOI for all platforms.

MIM		Activity (MBq)					
Time (h)	LL	RL	LK	RK	spleen	liver	RB
1.0	30.5	34.2	84.1	91.6	52.6	572	1085
3.9	22.5	25.7	80.2	76.0	49.2	525	903
21.8	15.6	11.5	63.2	54.1	50.1	460	538
45.0	10.8	8.4	42.7	44.4	40.1	405	382
93.4	7.2	5.3	23.5	22.5	24.2	267	264

Planet Dose							
Time (h)	LL	RL	LK	RK	spleen	liver	RB
1.0	34.5	40.6	91.4	100	57.7	591	993
3.9	25.5	31.3	86.1	83.2	54.6	549	841
21.8	16.5	14.1	68.7	59.4	57.2	482	492
45.0	11.9	10.1	46.3	48.5	45.3	422	350
93.4	7.4	9.1	26.0	25.1	26.7	280	239

OD3D							
Time (h)	LL	RL	LK	RK	spleen	liver	RB
1.0	30.6	34.1	85.4	91.6	52.7	572	1086
3.9	22.7	25.5	80.9	77.0	49.5	525	900
21.8	15.4	11.6	63.3	54.3	50.2	457	543
45.0	11.0	8.5	43.0	44.3	40.0	404	386
93.4	7.2	5.4	23.7	22.6	24.6	266	265

Table 4.6: Activity (MBq) present in segmented VOI in MIM, Planet Dose and OD3D

MIM		Activity Concentration (kBq·cm ⁻³)					
Time (h)	LL	RL	LK	RK	spleen	liver	RB
1.0	43.0	34.1	192	177	296	18.3	1.43
3.9	40.7	31.9	163	179	311	20.3	1.38
21.8	39.6	28.8	197	226	305	17.5	1.44
45.0	45.7	37.6	226	195	290	16.4	1.45
93.4	35.7	28.8	216	222	308	16.6	1.44

Planet Dose		Activity Concentration (kBq·cm ⁻³)					
Time (h)	LL	RL	LK	RK	spleen	liver	RB
1.0	39.4	30.8	175	159	263	17.4	1.44
3.9	37.9	29.0	149	163	274	19.3	1.39
21.8	36.2	26.2	176	206	272	16.7	1.50
45.0	42.3	33.9	200	176	258	15.6	1.49
93.4	32.5	25.1	192	200	272	15.8	1.45

OD3D		Activity Concentration (kBq·cm ⁻³)					
Time (h)	LL	RL	LK	RK	spleen	liver	RB
1.0	43.6	34.2	189	177	296	18.3	1.43
3.9	40.7	32.0	162	178	311	20.3	1.38
21.8	40.7	28.8	197	224	302	17.5	1.43
45.0	45.7	37.6	224	194	290	16.5	1.44
93.4	36.4	28.9	213	221	308	16.7	1.44

Table 4.7: Activity concentration (kBq·cm⁻³) present in segmented VOI in MIM, Planet Dose and OD3D

Relative differences in activity concentration ($RD(\%) = \frac{A}{OD3D} - 1$)							
Planet Dose vs OD3D							
Time (h)	LL	RL	LK	RK	spleen	liver	RB
1.0	-9.7	-9.8	-7.5	-10.0	-11.2	-4.8	0.8
3.9	-6.7	-9.3	-7.8	-8.6	-11.7	-4.8	0.6
21.8	-11.1	-9.2	-10.4	-8.1	-9.8	-4.8	4.4
45.0	-7.5	-9.9	-10.5	-9.3	-11.0	-5.0	2.8
93.4	-10.7	-13.0	-10.1	-9.2	-11.6	-4.9	1.0
MIM vs OD3D							
Time (h)	LL	RL	LK	RK	spleen	liver	RB
1.0	-1.6	-0.2	1.3	0.0	0.0	-0.1	0.2
3.9	0.0	-0.2	0.5	0.6	0.0	-0.1	0.1
21.8	-2.7	-0.1	0.0	0.7	1.0	-0.1	0.2
45.0	0.0	-0.1	0.7	0.6	0.0	-0.2	0.4
93.4	-2.1	-0.3	1.4	0.7	0.0	-0.2	0.2

Table 4.8: Relative differences ($RD(\%) = \frac{A}{OD3D} - 1$) in activity concentration at each time point. "A" stands for either Planet Dose or MIM.

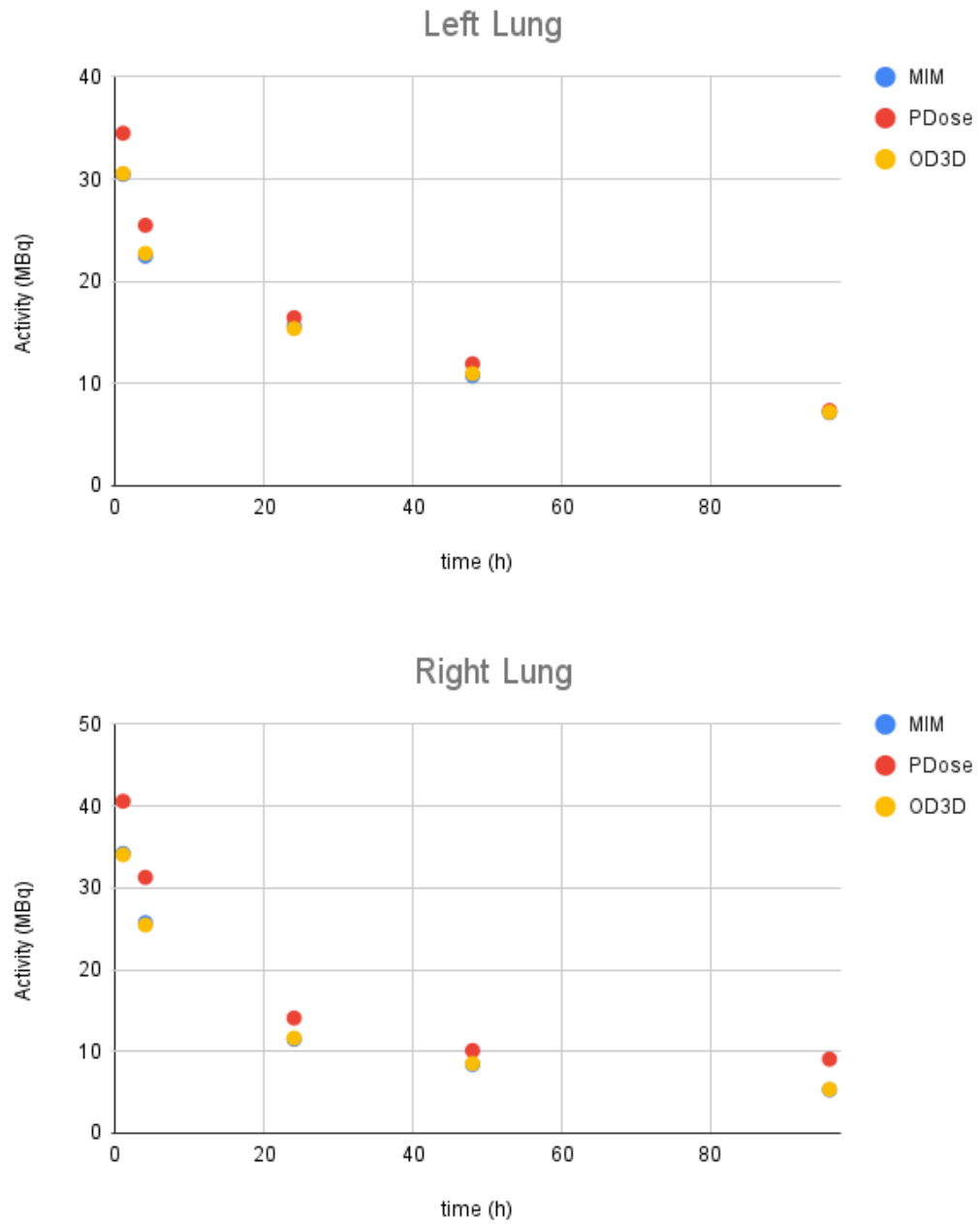


Figure 4.11: Activity plots for lungs, comparison among all platforms

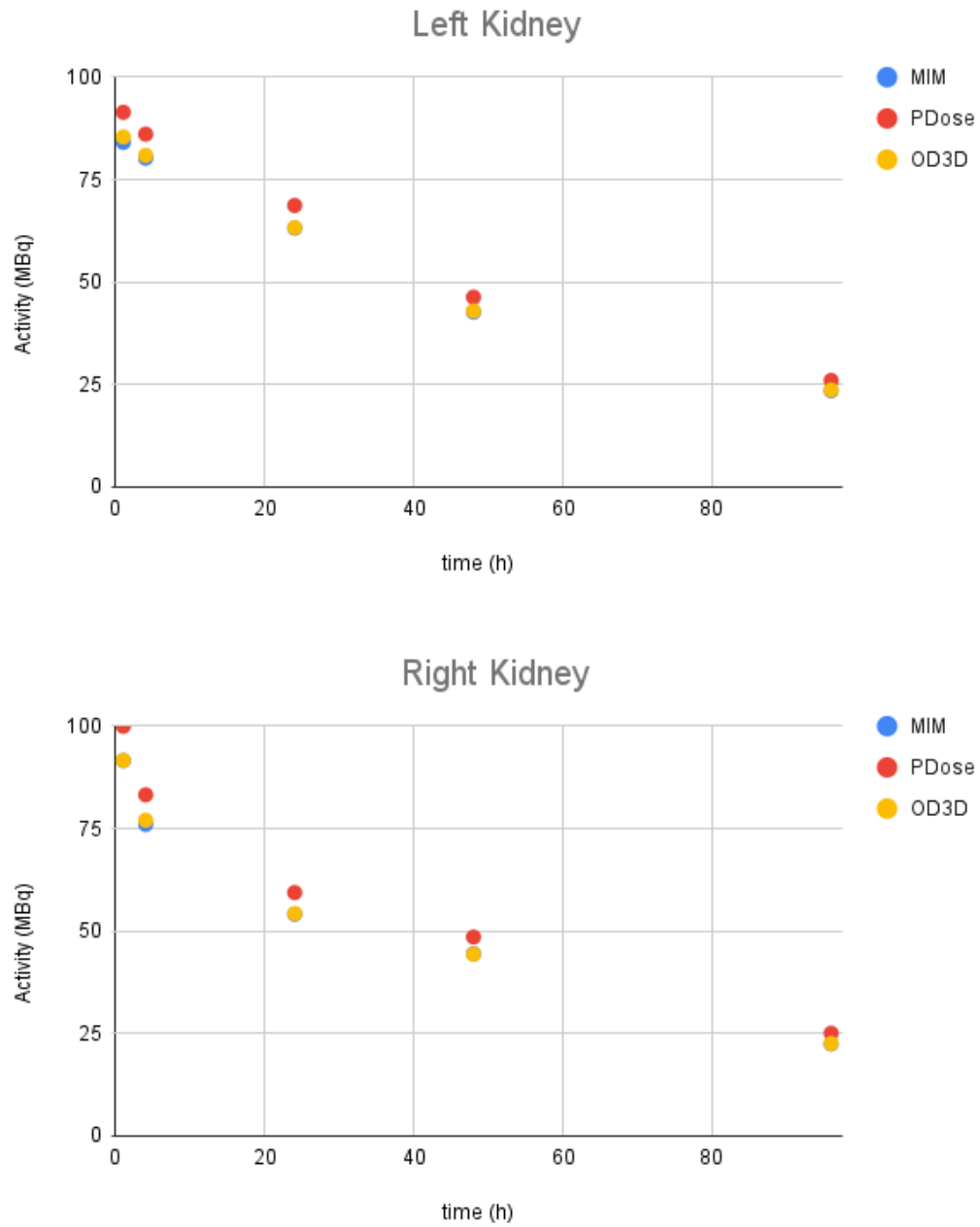


Figure 4.12: Activity plots for kidneys, comparison among all platforms

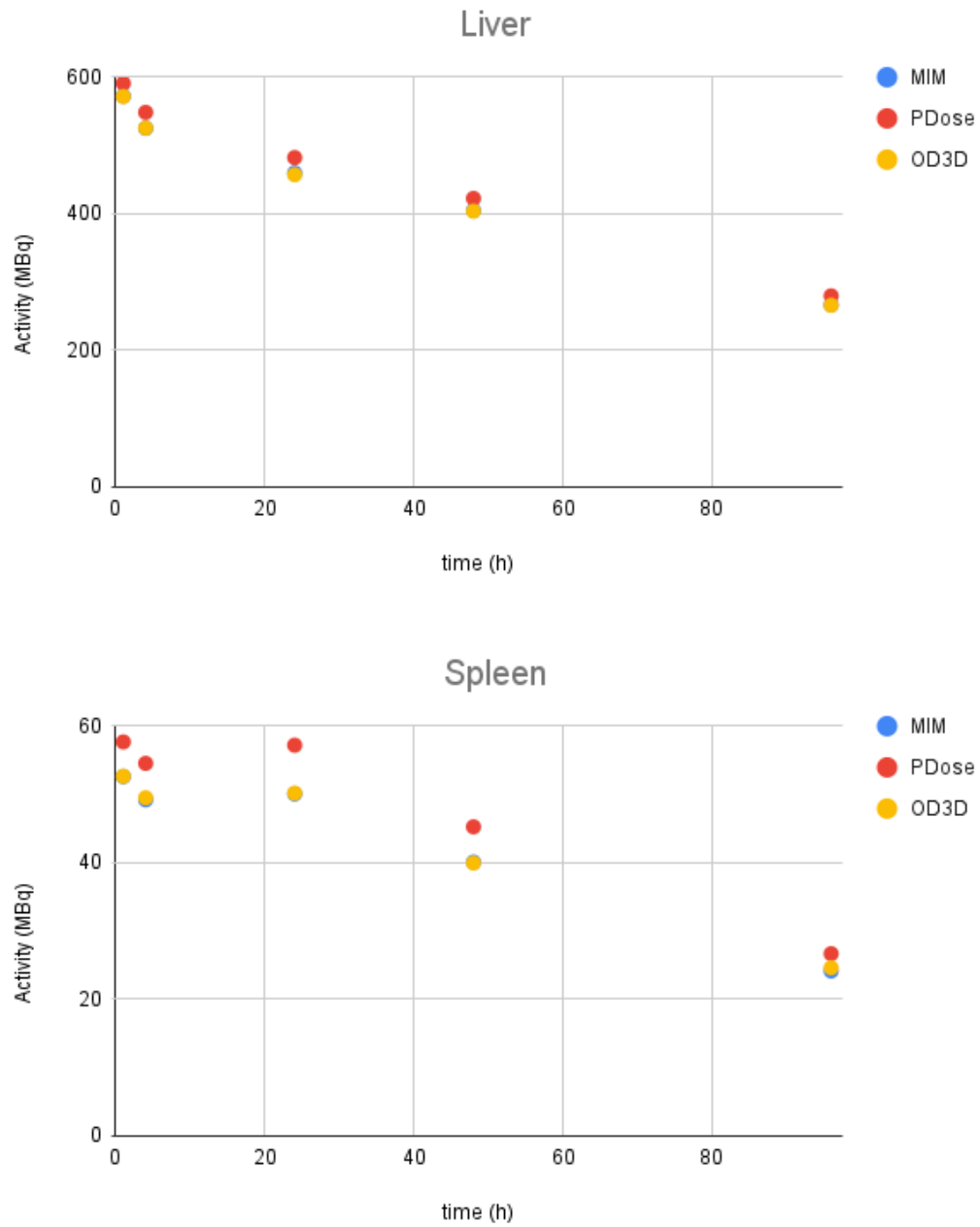


Figure 4.13: Activity plots for liver and spleen, comparison among all platforms

4.3.3 Comparison of the time integration process

A constant uptake mode, defined as repeat the value at T1 in T0, was chosen for the test case. This decision was taken based on the fact that ^{177}Lu -DOTATATE is administered very slowly to the patient, therefore we are in the presence of a slow administration.

The constant uptake mode is called line mode in Planet Dose. For data integration mode we have chosen the mono-exponential for all workstations to . Finally, for tail mode we have also chosen mono-exponential. Table 4.9 show the time-integrated activities (TIA) calculated by all three platforms Planet Dose, OD3D and MIM. The differences in lungs, observed in last section for Planet Dose, were propagated to this point. For the remaining VOI, the differences follow the same pattern as before.

Platform	Time integrated activity \tilde{A} (MBq·h)						
	LL	RL	LK	RK	spleen	liver	RB
Planet Dose	2295	1974	6899	6710	7684	77733	58145
OD3D	1778	1407	6321	6076	7010	73520	64276
MIM	1760	1386	6279	6055	6883	73768	63772

Table 4.9: Time integrated activity \tilde{A} (MBq·h) calculated by all three platforms

4.4 Absorbed dose rate algorithm comparison

The different absorbed dose rate (ADR) calculation algorithms are compared in this section. Table 4.10 presents the ADR algorithms implemented in each software with their respective density correction method.

ADR algorithms without density correction use default soft tissue density, except OD3D that allows the user to select the default density (between water, soft tissue, bone, lungs, adipose tissue).

ADR algorithms with density correction are divided into two categories: organ-density and voxel-density corrections.

- The organ averaged density correction methods (MIM) are driven by the organ segmentation, and generate averaged organ density.
- The density map correction methods (OD3D and Planet Dose) use the density map directly, and recalculate each target voxel mass.

Platform	Absorbed Dose Rate Algorithm				
	LED	LED+DC	HC	HC+DC	MC
Planet Dose	Tissue Density	Density Map	Tissue Density	Density Map	
MIM	Tissue Density	Organ averaged density	Tissue Density	Organ averaged Density	
OD3D	User selected Density	Density Map	User selected Density	Density Map	GATE

Table 4.10: Absorbed Dose Rate Algorithm and density correction methods implemented in each software. LED is local energy deposition, HC is homogeneous convolution, MC is Monte Carlo simulation and DC is density correction.

4.4.1 Local Energy Deposition

A full dosimetry using the local energy deposition algorithm is performed in the test case described in previous section. MIM doesn't support the LED approach for ^{177}Lu . Therefore, in this section, only OD3D and Planet Dose are compared.

The ADR obtained at 3.9 h are presented in Table 4.11 with and without density correction.

The results without density correction follow the behavior observed in previous section. The density correction introduces big relative differences for lungs, but were maintained for the rest of VOI. This can be explained by the Planet Dose filtering low density voxels in the calculation, as explained previously, that leads to decreased ADR.

4.4.2 Homogeneous Convolution

The same test made for LED is repeated, but this time using homogeneous convolution. The kernels were not similar between 3 platforms:

- MIM: the ^{177}Lu kernel data from [LANCONELLI 2003] are used.
- OD3D: the specific VDK generated for this work are used.
- Planet Dose: uses a 0.5 mm kernel that is rescaled to correct voxel dimensions using the algorithm of [FERNANDEZ 2013].

It is worth mentioning that, in terms of computational time, all three platforms complete

Absorbed dose rate (mGy·h ⁻¹) by LED							
No density correction							
Platform	LL	RL	LK	RK	spleen	liver	RB
OD3D	2.64	2.34	36.2	38.1	41.8	29.9	3.51
Planet Dose	2.52	2.45	35.2	36.9	40.8	28.8	3.28
<i>RD</i> (%)	-4.6	4.6	-2.6	-2.9	-2.5	-3.7	-6.8
With density correction							
Platform	LL	RL	LK	RK	spleen	liver	RB
OD3D	7.8	8.7	35.9	37.6	40.8	29.2	3.6
Planet Dose	5.1	5.0	35.5	36.9	40.6	28.2	3.4
<i>RD</i> (%)	-34.7	-42.2	-1.2	-1.7	-0.4	-3.5	-5.9

Table 4.11: Absorbed dose rate (mGy·h⁻¹) at 3.9 h calculated by local energy deposition algorithm, the relative difference ($RD(\%) = \frac{PlanetDose}{OD3D} - 1$) is also reported.

the homogeneous convolution (with and without density correction) in a few seconds. In order to avoid the influence of the density correction that was discussed previously, the results calculated in soft tissue without density correction were compared in Table 4.12. It is observed a higher difference in lungs (12.4% and 10.4%) due to the Planet Dose algorithm that removes voxel data below a specific density threshold.

It can be noted that OD3D results were in agreement with the results of MIM. For Planet Dose the differences observed were in agreement with the results reported in the previous section regarding the differences due to geometry at high gradient zones, Figure 4.4.

In order to further verify our convolution method, a Monte Carlo (GATE) simulation in water with the same activity distribution was performed to avoid any influence of the density and compare to the same results obtained by FFT convolution in water. The template described in subsection 3.2.3.3 was used, but the material was set to water in the whole geometry. Table 4.13 presents the comparison in all-time points and in all VOI. A consistent relative difference (mean 1.6%) is observed. This can be explained by GATE using a non-continuous conversion from HU number to density, even using the same calibration curve accordingly to GATE manual ¹:

"The parameter «DensityTolerance» allows the user to define the density tolerance. Even if it is possible to generate a new Geant4 material (atomic composition and density) for each different HU, it would lead to too much different materials, with a long initialization time. So we define a single material for a range of HU belonging to the same material range (in the

¹https://opengate.readthedocs.io/en/latest/voxelized_source_and_phantom.html#id17

Absorbed Dose Rate (mGy·h ⁻¹)							
Platform	LL	RL	LK	RK	spleen	liver	RB
Planet Dose	2.52	2.41	34.4	36.1	39.8	28.3	3.24
OD3D	2.88	2.69	35.4	37.4	40.7	29.7	3.75
MIM	2.86	2.68	34.9	36.9	40.1	29.4	3.73
Relative difference to OD3D ($RD(\%) = \frac{A}{OD3D} - 1$)							
Planet Dose	-12.4	-10.4	-2.8	-3.4	-2.1	-4.8	-13.7
MIM	-0.6	-0.3	-1.3	-1.2	-1.4	-1.1	-0.7

Table 4.12: ADR calculated by homogeneous FFT convolution in soft tissue at 3.9h without density correction. The relative difference ($RD(\%) = \frac{A}{OD3D} - 1$) is also provided. "A" stands for either Planet Dose or MIM

first calibration Table) and with densities differing for less than the tolerance value."

A final comparison was made with the FFT convolution against LED and MC. Figure 4.14 (lungs), Figure 4.15 (kidneys), and Figure 4.16 (spleen and liver) present the plots for every VOI. It can be noted the high difference in the lungs as already seen in previous sections.

Absorbed dose rate ($\text{mGy}\cdot\text{h}^{-1}$) in water							
Monte Carlo in full water model							
Time (h)	LL	RL	LK	RK	spleen	liver	RB
1.0	5.2	4.5	45.4	47.3	40.9	31.9	5.3
3.9	3.1	2.9	38.1	40.2	43.8	32.0	4.1
21.8	2.8	1.6	33.6	31.4	39.8	24.4	2.8
45.0	1.8	1.3	25.7	24.3	31.0	21.6	2.0
93.4	1.3	0.8	13.8	13.6	19.1	13.7	1.4
FFT Convolution in water without density correction							
Time (h)	LL	RL	LK	RK	spleen	liver	RB
1.0	5.2	4.5	44.7	46.6	40.3	31.4	5.2
3.9	3.0	2.9	37.5	39.6	43.1	31.5	4.0
21.8	2.8	1.6	33.1	30.9	39.2	24.0	2.7
45.0	1.8	1.3	25.2	23.9	30.5	21.3	2.0
93.4	1.3	0.8	13.6	13.4	18.8	13.5	1.3
Relative difference ($RD(\%) = \frac{FFT}{MC} - 1$)							
Time (h)	LL	RL	LK	RK	spleen	liver	RB
1.0	-1.62	-1.60	-1.59	-1.61	-1.61	-1.57	-1.66
3.9	-1.72	-1.60	-1.59	-1.57	-1.63	-1.58	-1.68
21.8	-1.58	-1.50	-1.60	-1.56	-1.60	-1.59	-1.63
45.0	-1.51	-1.46	-1.63	-1.60	-1.63	-1.58	-1.67
93.4	-1.56	-1.57	-1.58	-1.61	-1.61	-1.58	-1.63

Table 4.13: ADR ($\text{mGy}\cdot\text{h}^{-1}$) calculated in water by MC and by homogeneous FFT convolution

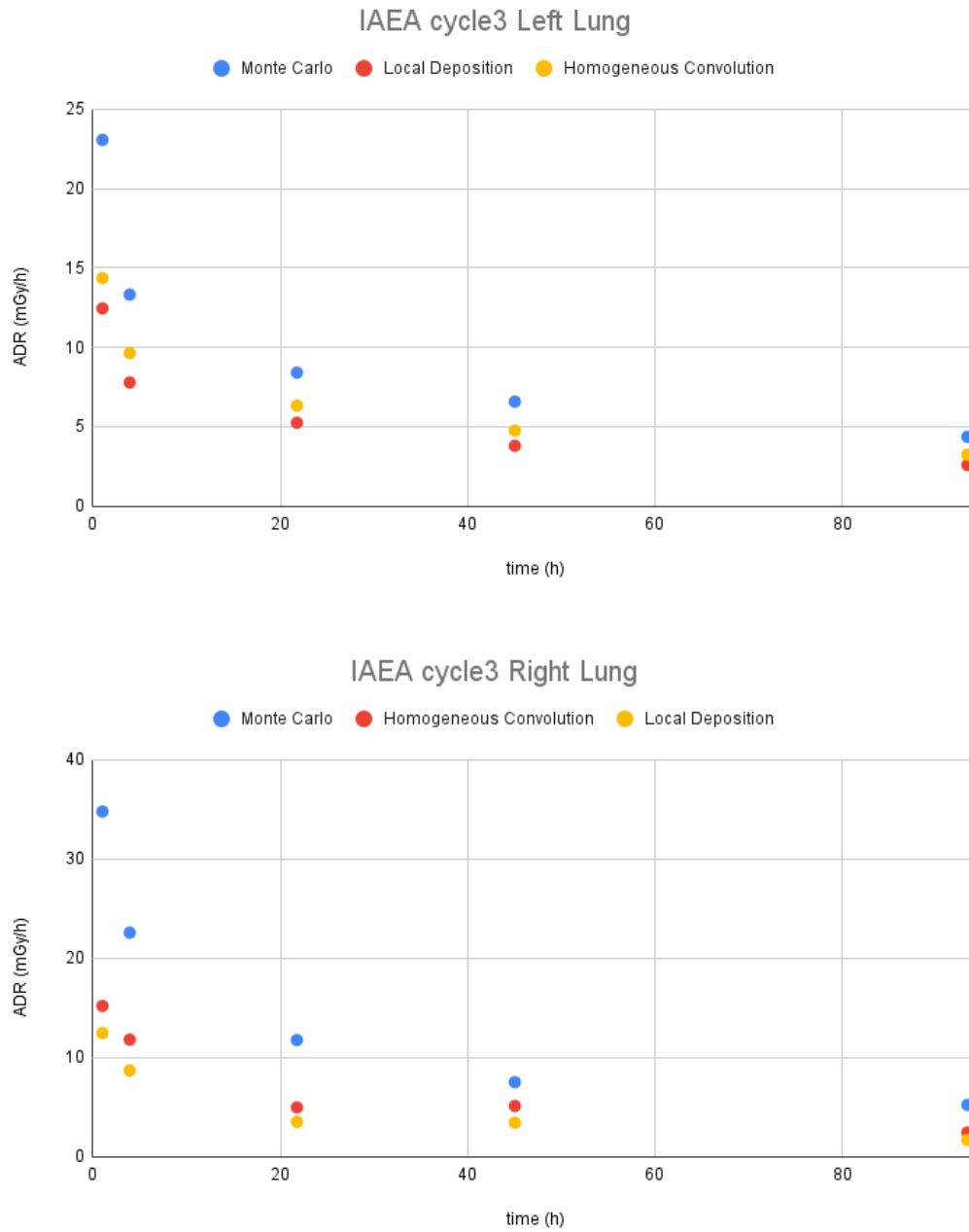


Figure 4.14: Comparison of the ADR calculated in lungs, with density correction, by OD3D using LED, FFT convolution and Monte Carlo.

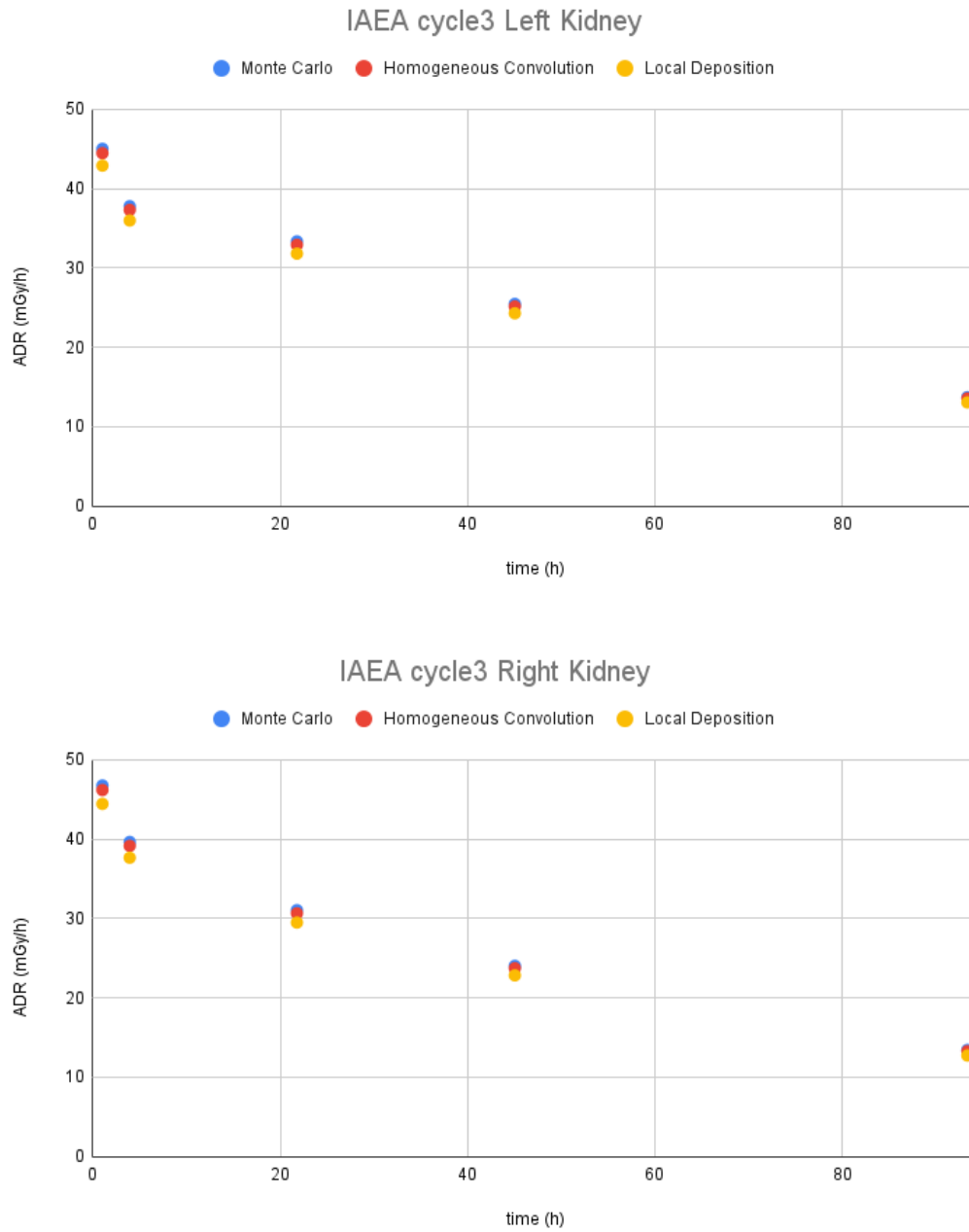


Figure 4.15: Comparison of the ADR calculated in kidneys, with density correction, by OD3D using LED, FFT convolution and Monte Carlo.

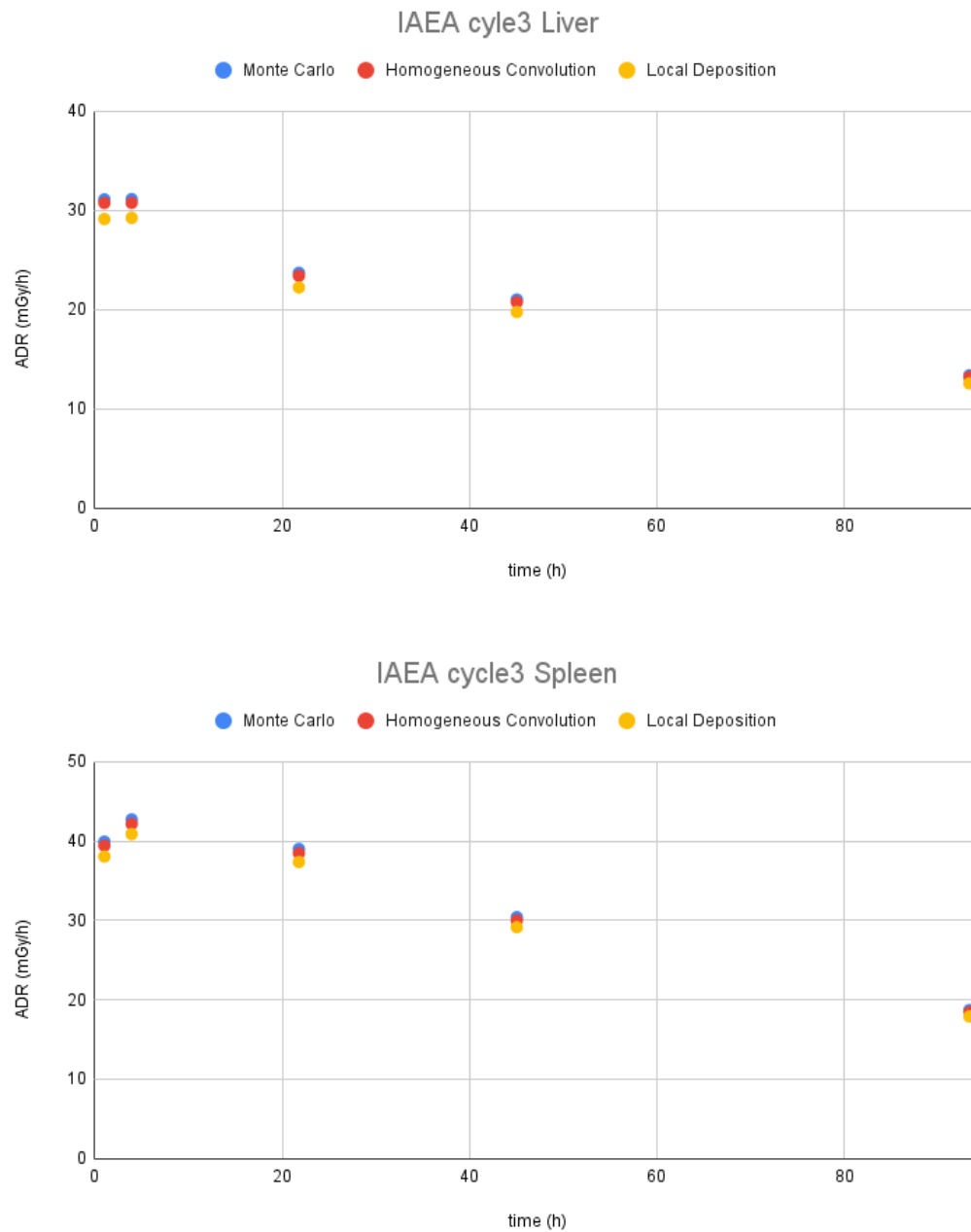


Figure 4.16: Comparison of the ADR calculated in liver and spleen, with density correction, by OD3D using LED, FFT convolution and Monte Carlo.

4.4.3 Heterogeneous Convolution

To validate the fast heterogeneous convolution algorithm (FHCA), a new segmentation was performed to focus more in the abdominal region, especially the tumors, and to include the bones and lungs to study the influence of heterogeneous regions. In this case the homogeneous regions were separated from the heterogeneous regions to ease the comparison.

Figure 4.17 (liver) and Figure 4.18 (tumors) present the results for homogeneous regions, where an agreement is observed for all methods.

Figure 4.19 presents the results for heterogeneous regions. In this case the LED method show a high discrepancy from the rest as it does not take into account cross irradiation nor photon contributions, and it is expected to be lower than the others. FHCA is closer than FFT to the behavior of Monte Carlo, although the increased complexity and increased simulation time does not justify its use in practice. While LED and FFT obtained results in less than a minute, FHCA needs some hours to finish (around 40 minutes per time point in a 16 core workstation) which is similar to the total time of Monte Carlo (around 6 hours total to obtain less than 10 % uncertainty in non-source VOI).

As a conclusion, it is not recommended implementing this algorithm in clinical practice as, being not superior to the Monte Carlo equivalent, it takes around the same calculation time to get the results.

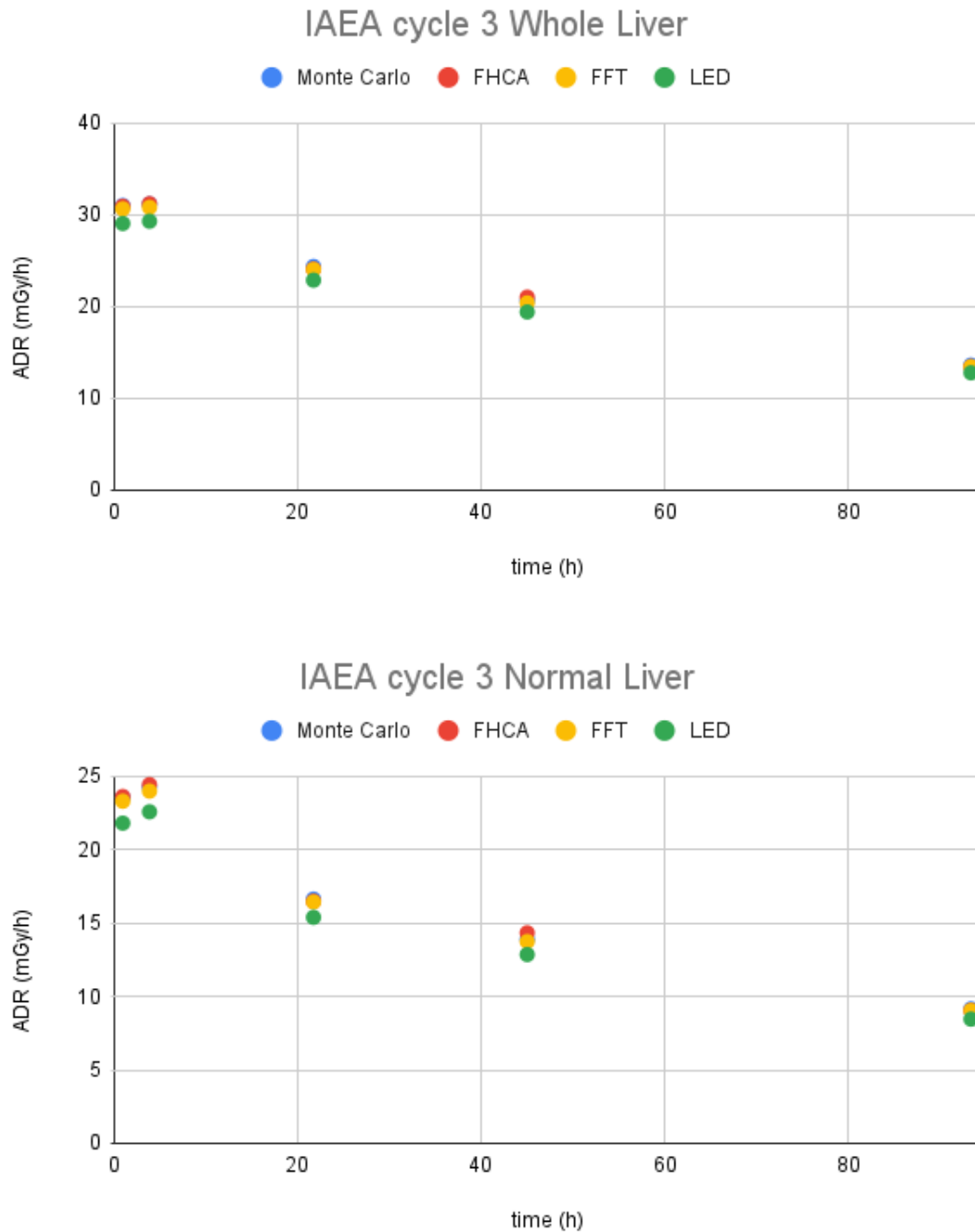


Figure 4.17: Comparison of the ADR calculated in liver (total and healthy), with density correction, by OD3D using LED, FFT, FHCA and Monte Carlo.

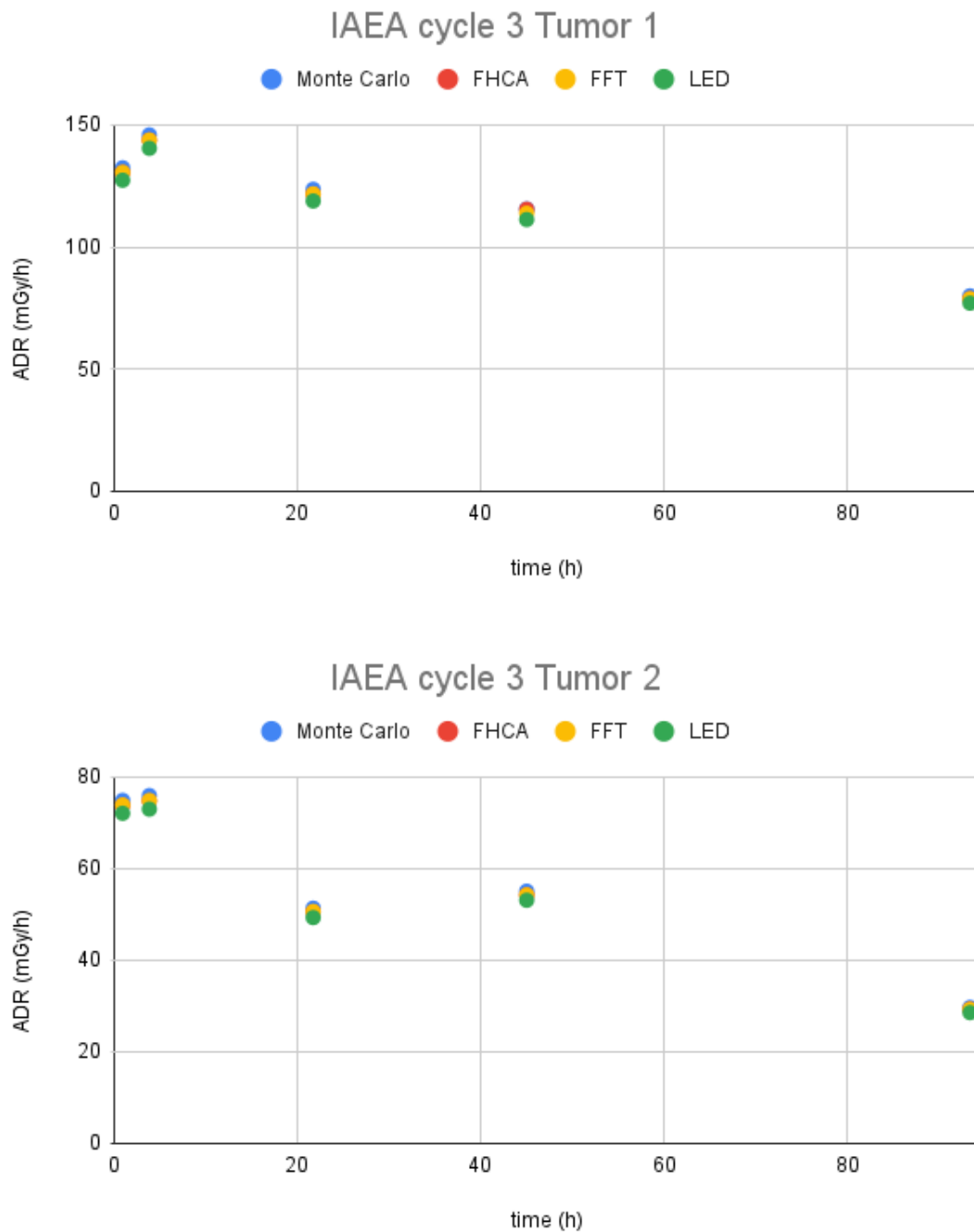


Figure 4.18: Comparison of the ADR calculated in tumors, with density correction, by OD3D using LED, FFT, FHCA and Monte Carlo.

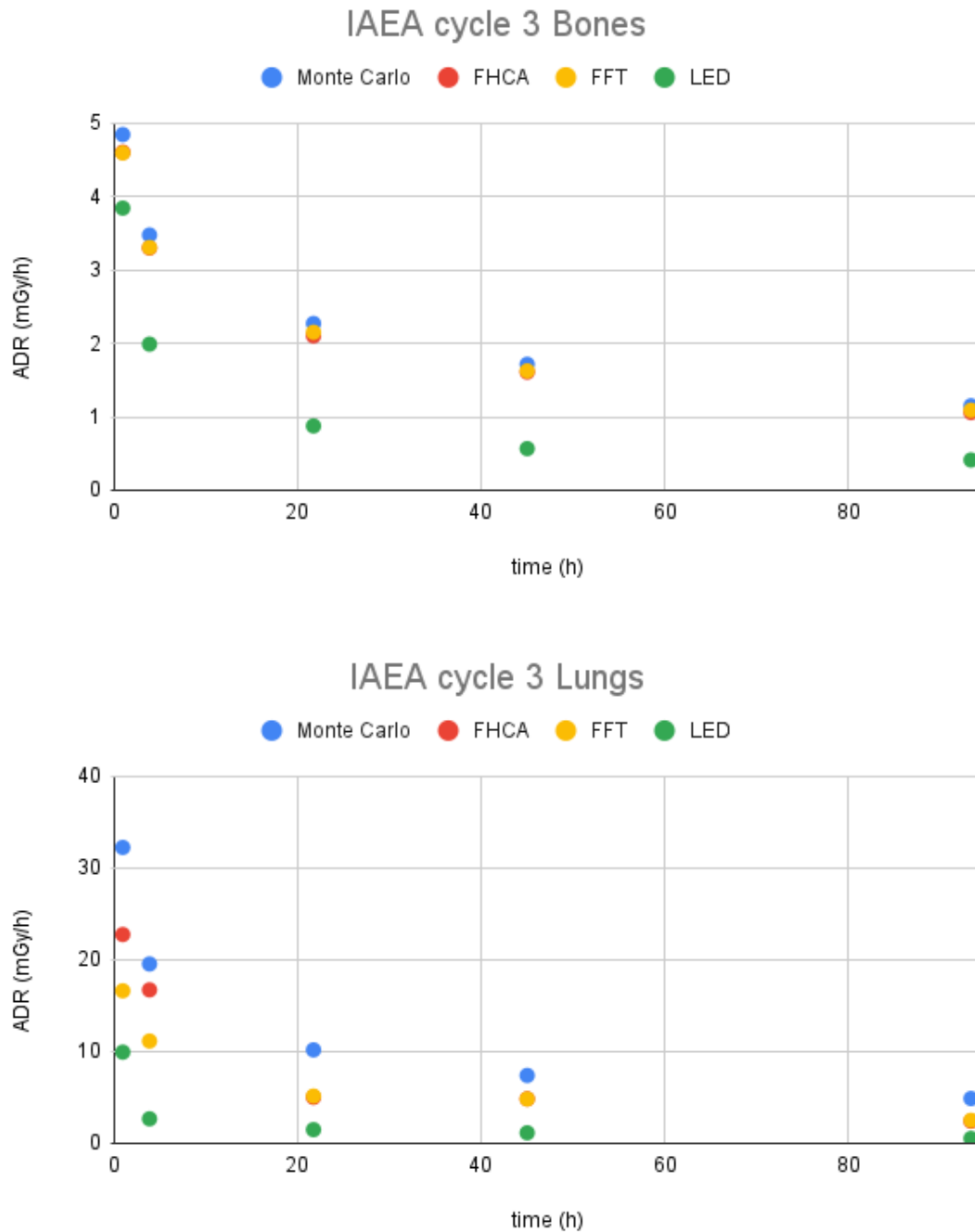


Figure 4.19: Comparison of the ADR calculated in heterogeneous regions with density correction by OD3D using LED, FFT, FHCA and Monte Carlo.

4.5 Conclusions

In this chapter we have performed several benchmarking on different sections of the implementation of OD3D.

The generated DPK and VDK matches with those reported in literature. Therefore, we can conclude that the algorithm used for its generation is accurate and can be extended to include more radionuclides.

The Monte Carlo workflow, together with the use of GATE, was validated and published. We can conclude that MC can be used as a reference dosimetry and any other approximation can use it for comparison.

The CDW implementation inside OD3D yields similar results when compared to commercial software. We can conclude that the CDW inside OD3D were correctly implemented.

The alternative ADR methods (LED, Homogeneous convolution and heterogeneous convolution), report similar values to the MC method in their range of applicability. Therefore, we can conclude that, when conditions are met, we can use the alternative methods to speed the CDW.

Implementation of patient specific clinical dosimetry

Contents

5.1	Dosimetry for IUCT	130
5.2	Dosimetry for RMH	140
5.3	Dosimetry for UKW	150
5.4	Discussion	164

In this chapter we will report results from the application of the developed dosimetry module OD3D in a clinical environment. The implementation was designed to be a comparison of in situ calculations and the present methodology.

The MEDIRAD project collected images and data from 4 clinical centers, each having their own acquisition protocol due to local resources and administrative constraints. As a consequence, a common dosimetry procedure was not possible, and the dosimetric processing was specifically adapted to each clinical center, thereby requiring further development. The data was acquired for thyroid cancer patients with thyroidectomy and post-therapy with ^{131}I .

Three centers were considered, with tag names RMH, IUCT and UKW. The fourth center, with no available CT was not considered for this study. Calculated data tables are all presented in Appendix C.

OD3D was adapted to cover the clinical situations encountered during the MEDIRAD project:

- For IUCT the images consist in a unique time point acquisition from neck to abdomen, with all corrections applied.
- For RMH the images could be one or multiple time points SPECT acquisitions, from neck to torso, corrected by attenuation using a single CT acquisition.
- For UKW the images consist in a single SPECT/CT acquisition with all corrections applied, plus multiple time point SPECT acquisitions without any correction.

5.1 Dosimetry for IUCT

Images consist of a unique SPECT/CT acquisition performed at late 96h time point. External whole body (WB) probe measurements were performed for WB pharmacokinetics. Patients were scanned from head to pelvis. The CT image was converted into a 3D density map and SPECT images were converted to 3D activity maps according to the calibration procedure. Calibration data was provided by the center. The CT was calibrated following Schneider curve [SCHNEIDER 1996]. The SPECT was calibrated for sensitivity resulting in a value of $92.2 \text{ counts} \cdot \text{MBq}^{-1} \cdot \text{s}^{-1}$. Table 5.1 shows the patient data. Figure 5.1 shows a sample patient where the FOV can be appreciated.

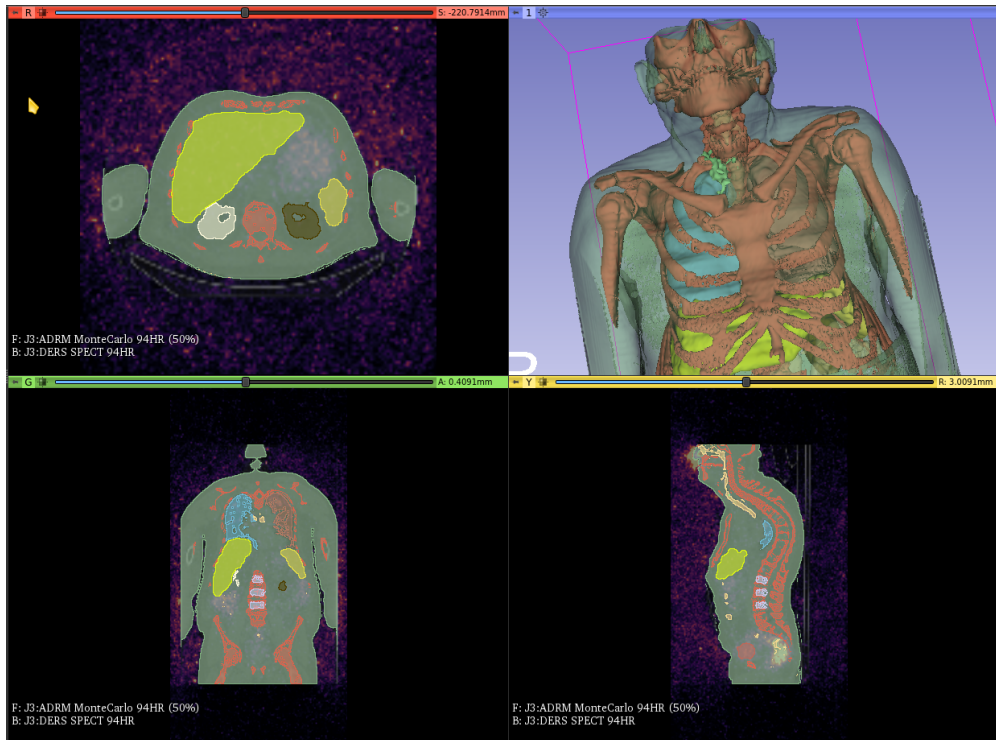


Figure 5.1: Sample patient of IUCT

Voxel-based absorbed dose rates were calculated for the whole FOV, using MC simulation with voxelized source and density map generated directly from patient data. Absorbed dose rates (ADR) were obtained using GATE 9.1. Simulations took 8 hours per patient in a workstation (AMD Ryzen2700X 16 cores, 32GB RAM) and taking over 1GB of RAM per patient. Several patients could be run simultaneously. The ADR were imported back to OD3D.

The patients were scanned from neck to pelvis, this allows different structures to be segmented. Segmented structures considered were the lungs (left/right), the salivary glands, the bones visible in the field of view, the neck region (even though the functional volume defined may hide high activity gradients in microscopic regions), the liver, kidneys (left/right), spleen, urinary bladder and L2-L4. The total body mass was documented for each patient

before the imaging sessions. The remainder was defined as the total body minus all defined regions of interest. Table C.7 show the patient mass measured for segmented VOI. Figure 5.2 show the patient mass variations for segmented VOI.

Since there was only one time point, the external whole body measurements were used as an approximation to calculate T_{eff} for each organ. Except the neck region where a fixed value of $T_{eff} = 68$ h was used, derived from experimental results obtained at RMH. To evaluate the accuracy of this approximation, a study of the T_{eff} for the neck region, with the RMH patients with more than one time point was made. Figure 5.3 show the variation of the T_{eff} for the neck region for all the patients considered. It can be noticed that the proposed $T_{eff} = 68$ h was contained in the dispersion. But also that the T_{eff} had a very large dispersion.

Time integration was performed using mono-exponential curves calculated with the defined T_{eff} and the measured point. ADR in VOI, Equation 2.2, were integrated into absorbed doses in VOI and in addition the cumulated activities were also integrated from the activities for comparison to the original study. Table C.8 show the absorbed doses calculated by OpenDose3D using Monte Carlo simulation and integrated in each VOI. Figure 5.5 show the absorbed dose variation for all patients. Table C.9 show the residence times calculated by OpenDose3D for segmented VOI. Figure 5.4 show the residence time variations for segmented VOI.

Equivalent doses were obtained based on the [ICRP60 1990] (Table C.10) and [ICRP103 2007] (Table C.11) recommendations, calculated on Excel using the absorbed doses calculated in identified VOI. Figure 5.6 and Figure 5.7 show the respective variations of equivalent doses for all patients. For target organs not segmented the absorbed dose in remainder of the body considered homogeneous was used and multiplied by the recommended tissue weighting factors (Wt). The equivalent dose per organ for all patients were averaged and then summed to obtain the effective dose.

In parallel, absorbed and effective doses were also calculated using IDAC 2.1 [ANDERSSON 2017]. The absorbed doses were calculated for each patient with mass correction. The effective doses were calculated based on patient-averaged residence times in VOI, with no mass corrections. Table C.12 show the absorbed doses calculated with IDAC 2.1. Figure 5.8 show the absorbed dose variation per patient. Table 5.2 present the comparison for effective dose comparison. It shall be noted the huge dispersion in patient data that yield an uncertainty in effective dose calculation near 100% that can only be appreciated by the use of OpenDose3D.

A range of absorbed doses was observed for all segmented organs, with the majority of thyroid remnants absorbed doses below 20 Gy (median 4 Gy). For the rest of the organs, the absorbed doses were consistently below 1.6 Gy (median 500 mGy) in the case of urinary bladder wall, below 800 mGy (median 360 mGy) for lungs and salivary glands and below 200 mGy (median 150 mGy) for the other organs.

Patient	Sex	Height (cm)	Weight (kg)	Injected Activity (MBq)	Acquisition Time (h)
ICR-001	Female	159	56	3787	90
ICR-003	Female	159	90	3780	93
ICR-004	Female	150	100	3787	93
ICR-005	Female	169	59	3700	95
ICR-006	Male	172	88	3700	96
ICR-008	Female	160	62	3700	93
ICR-009	Female	172	69	3700	94
ICR-010	Male	178	78	3700	100
ICR-013	Male	166	82	3630	95
ICR-014	Female	170	80	3740	94
ICR-015	Male	178	90	3710	93
ICR-016	Male	182	78	3660	95
ICR-017	Female	162	70	3700	95
ICR-018	Female	163	57	3700	97
ICR-019	Female	156	55	3700	92
ICR-020	Female	164	75	3700	97
ICR-021	Female	170	85	3700	95
ICR-022	Male	180	92	3700	95
ICR-023	Female	164	57	3700	95.6
ICR-024	Female	160	68	3700	98
ICR-025	Female	161	77	3700	97
ICR-026	Female	163	70	3720	96
ICR-027	Female	170	70	3620	95
ICR-028	Male	191	102	3680	93.2
ICR-029	Female	170	54	3630	93.7

Table 5.1: Patient data from IUCT.

Method	OpenDose3D [mSv·MBq ⁻¹]	IDAC 2.1 [mSv·MBq ⁻¹]
ICRP 60	$(1.34 \pm 1.09) \times 10^{-1}$	1.3×10^{-1}
ICRP 103	$(9.64 \pm 6.77) \times 10^{-2}$	1.1×10^{-1}

Table 5.2: Effective dose comparison between OpenDose3D and IDAC 2.1.

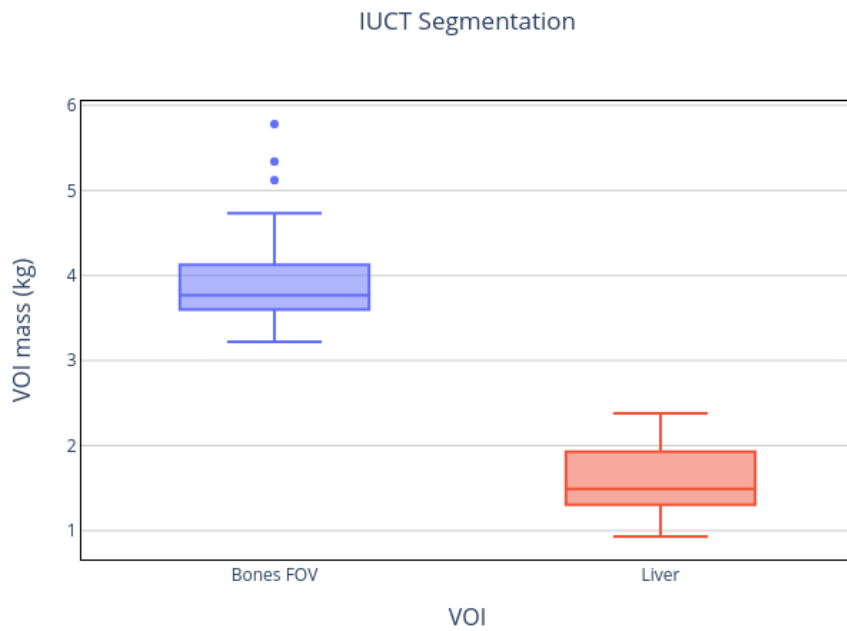
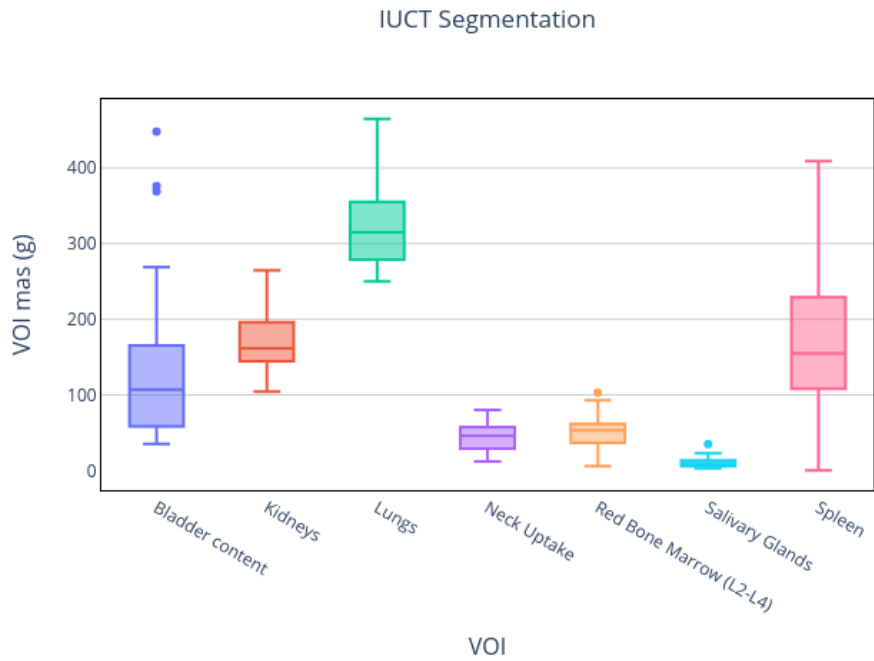


Figure 5.2: Mass statistics for segmented VOI

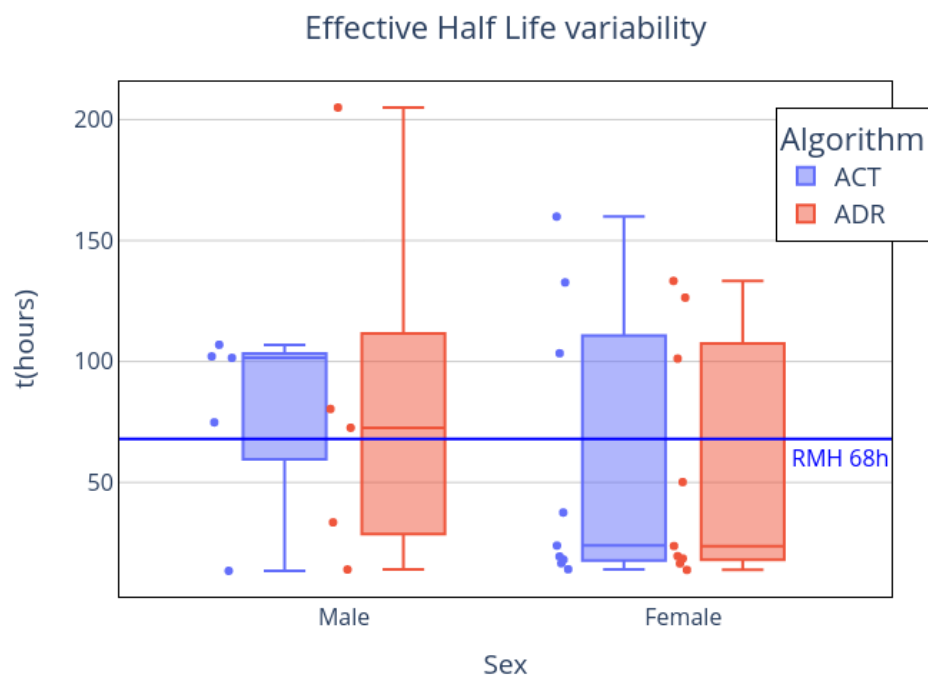


Figure 5.3: Effective half life (T_{eff}) for the neck region calculated for RMH patients with more than 1 time point acquisition. The fitting was performed in both Activity curve and Absorbed dose rate curve.

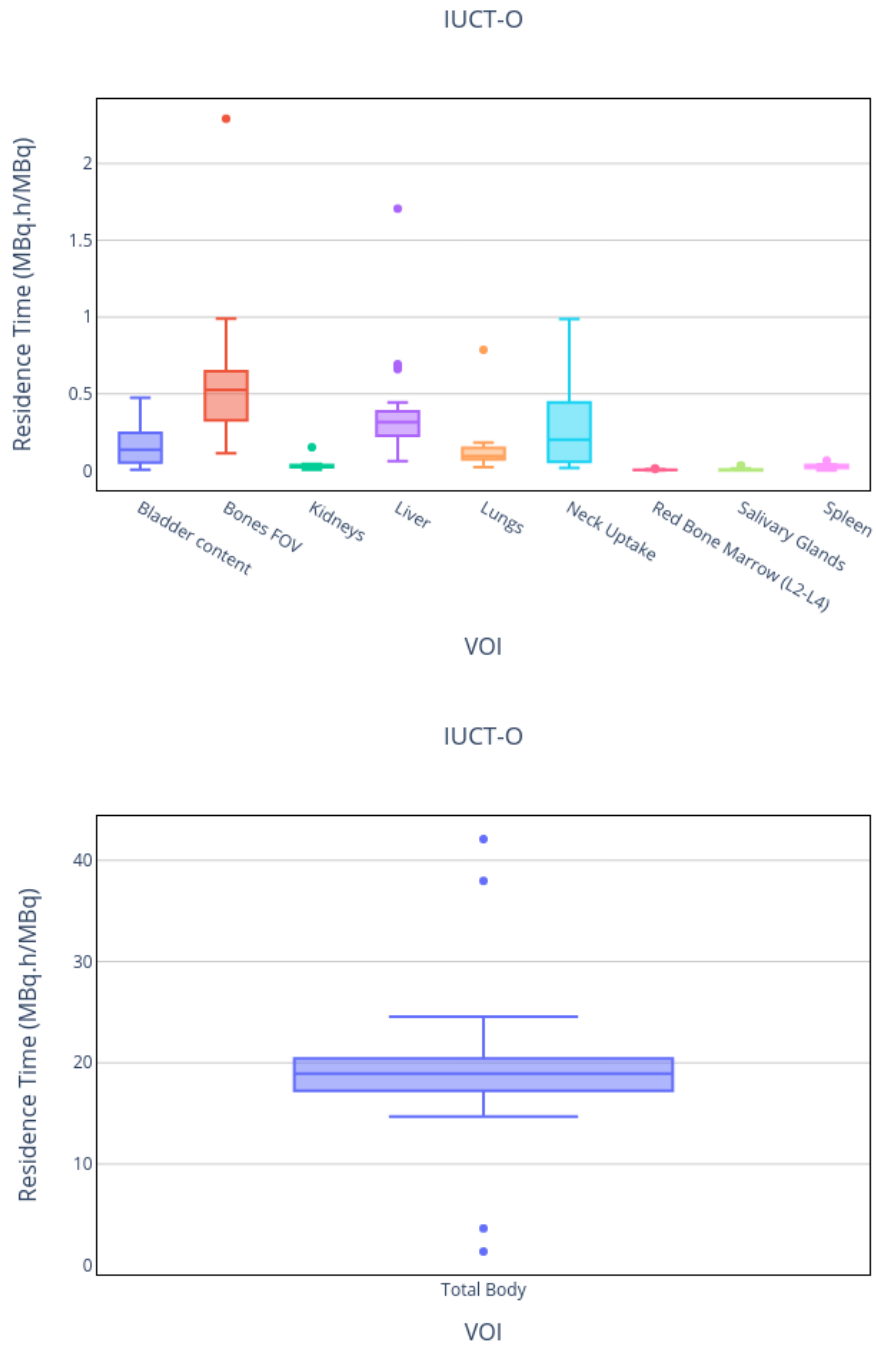


Figure 5.4: Residence time statistics for segmented VOI

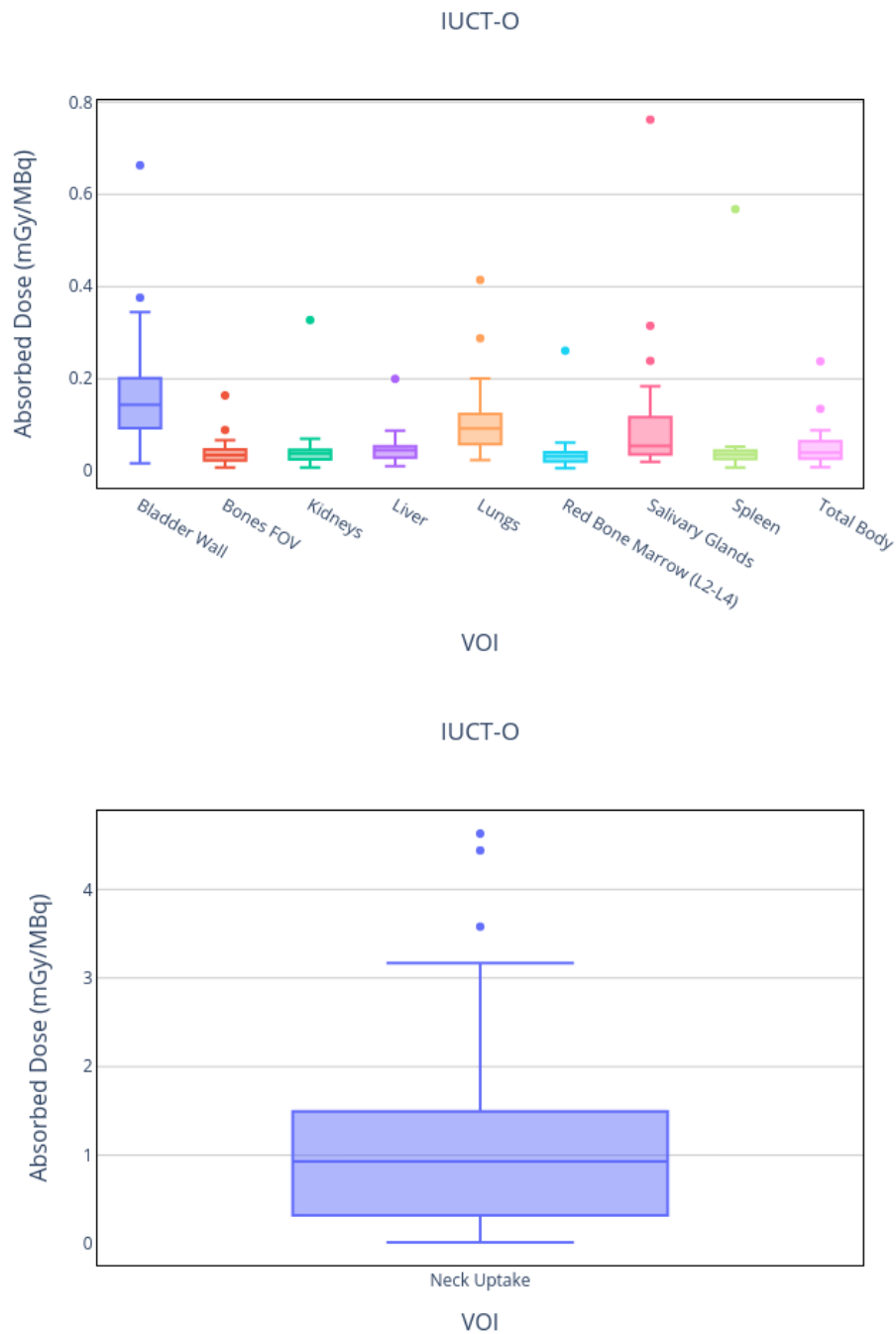


Figure 5.5: Absorbed dose statistics for segmented VOI, calculated by MC in OpenDose3D

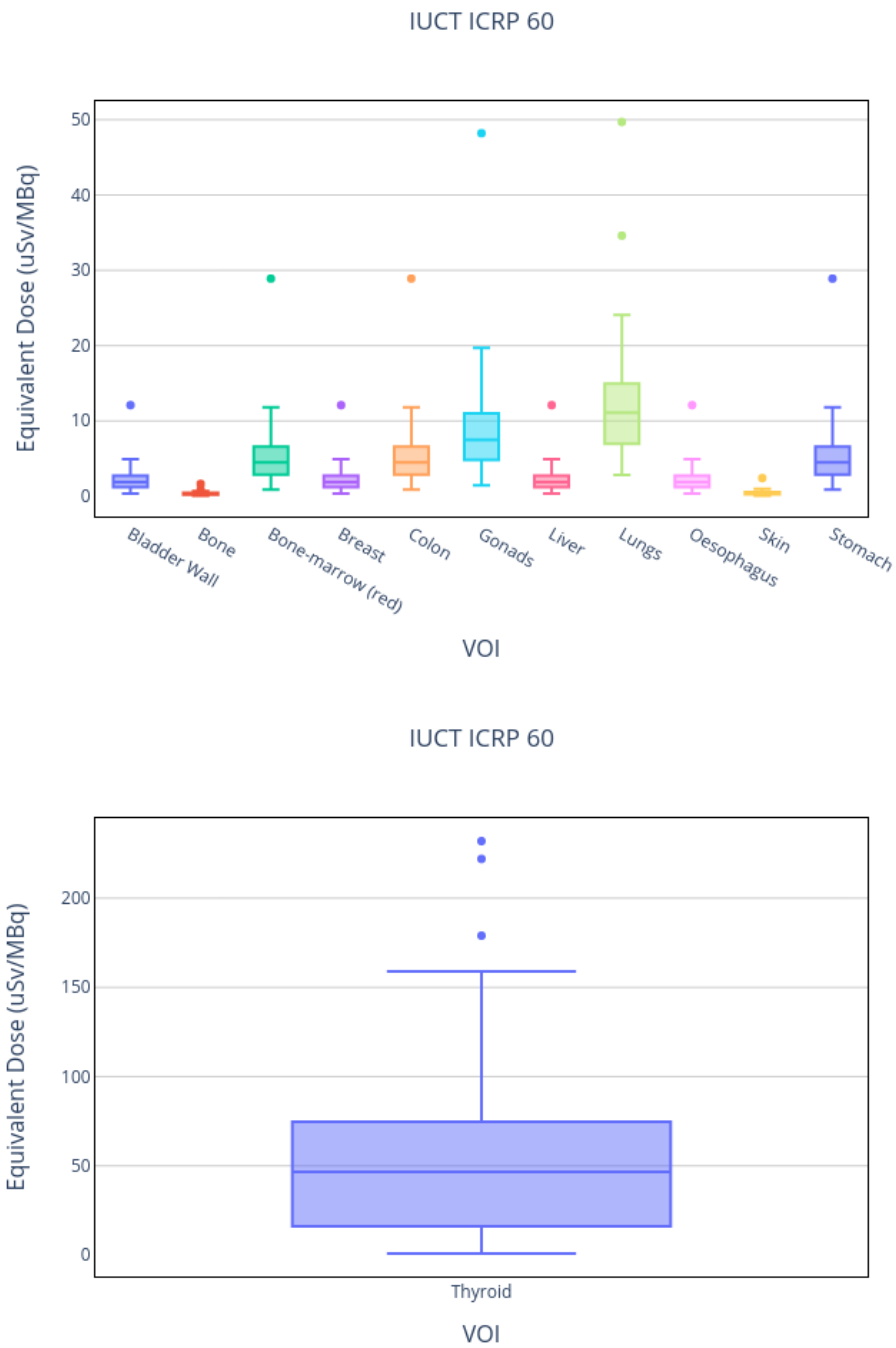


Figure 5.6: Equivalent Dose statistics calculated by ICRP 60 recommendations [ICRP60 1990]

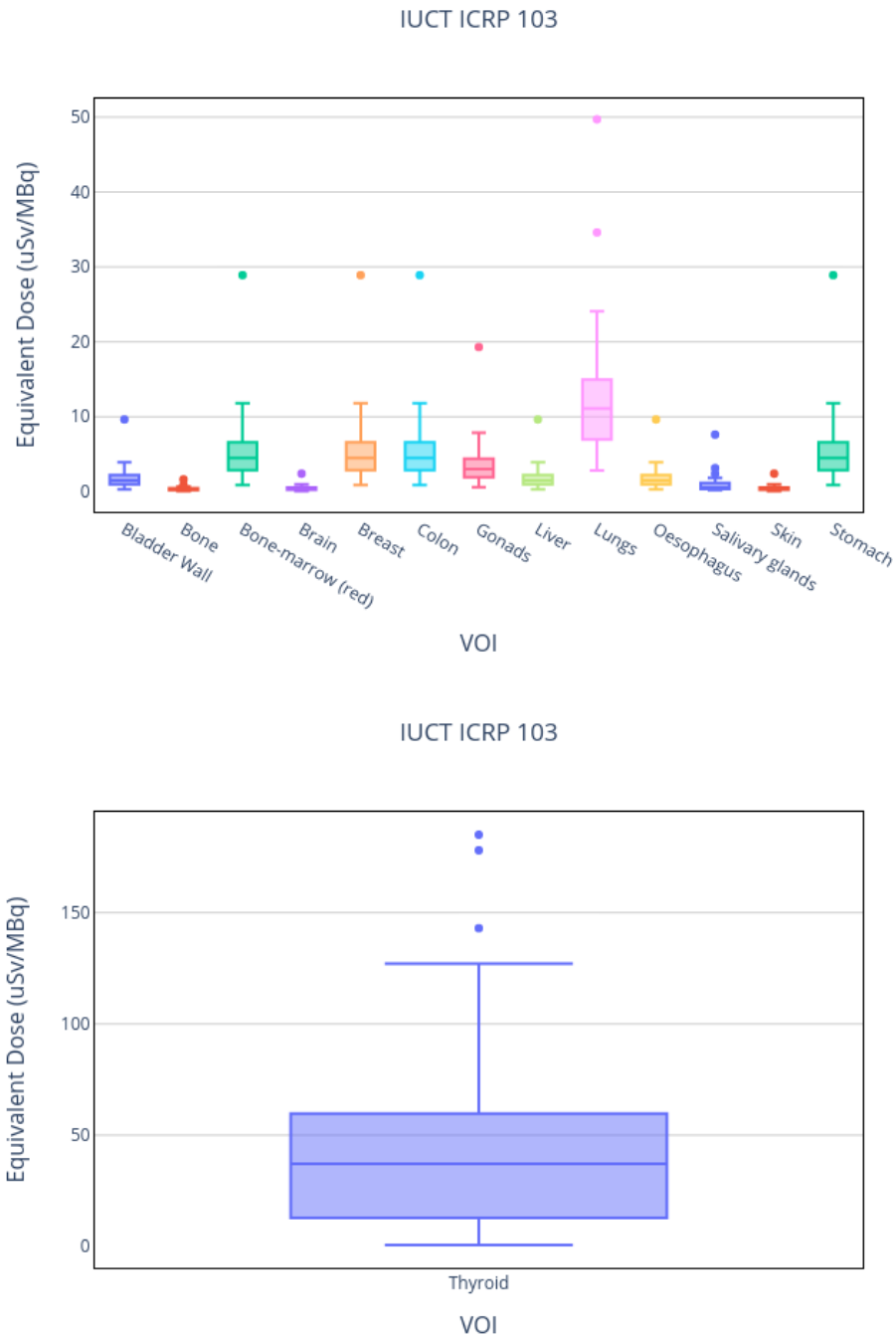


Figure 5.7: Equivalent Dose statistics calculated by ICRP 103 recommendations [ICRP103 2007]

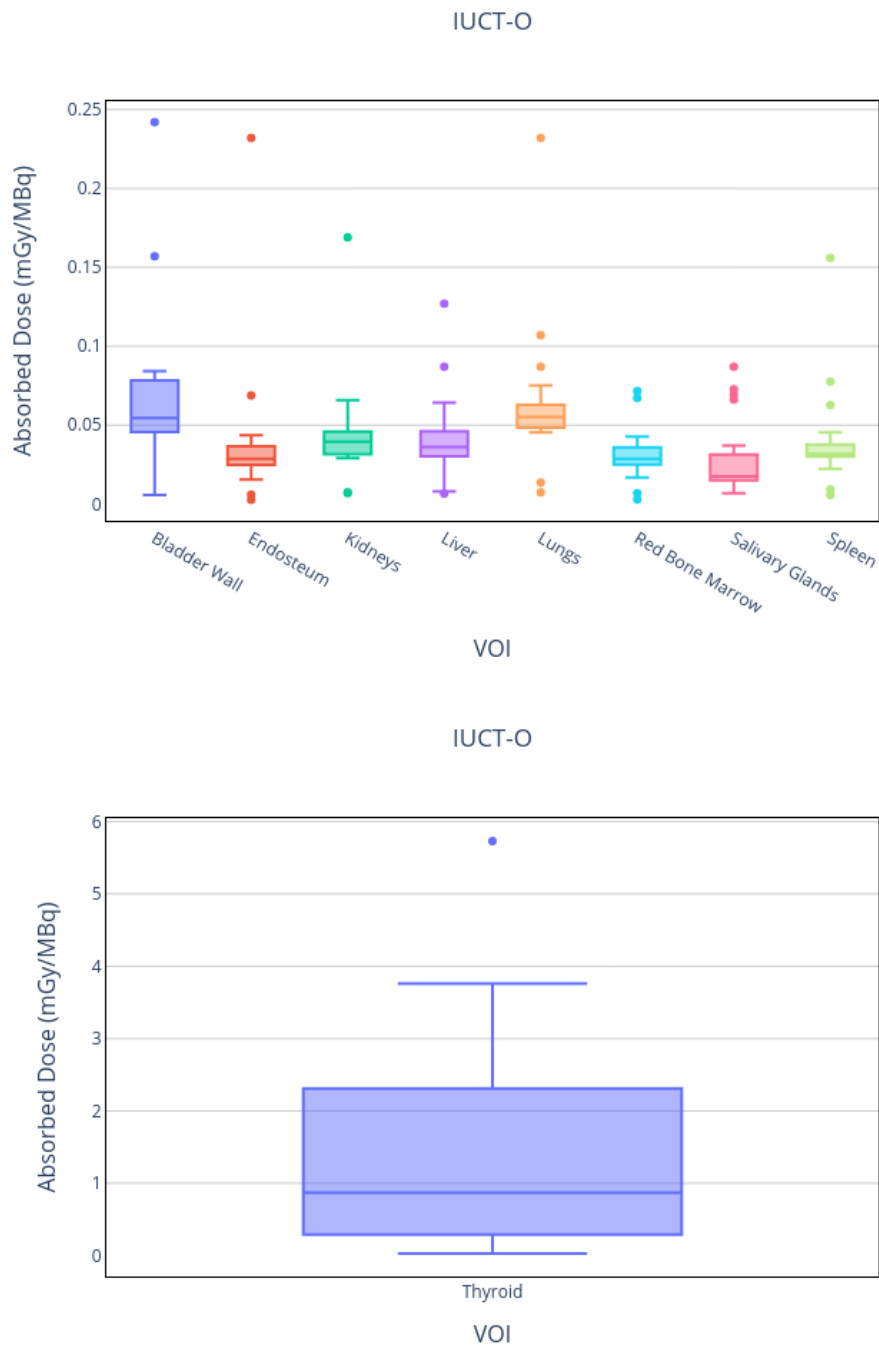


Figure 5.8: Absorbed Dose statistics calculated by IDAC 2.1 [ANDERSSON 2017]

5.2 Dosimetry for RMH

The selected images consist of one SPECT/CT acquired at 48h post administration. Two more optional SPECT at 24h and 96h, aligned with the 48h to use the CT for attenuation correction in every time point. A CT acquisition at each time point, even low dose, was not possible because of the ethical committee decision. External whole body (WB) probe measurements were performed for WB pharmacokinetics. Patients were scanned from head to torso, so no abdominal structures were visible. Only 13 patients with all 3 time points were selected for this study. Table 5.3 shows the patient data. Figure 5.9 shows a sample patient where the FOV can be appreciated.

Patient	Sex	Height (cm)	Weight (kg)	Injected Activity (MBq)
RMH-006	Male	171	61	3591
RMH-011	Female	167	60.2	3132
RMH-013	Male	174.7	106.3	3604
RMH-014	Female	164	59.2	3669
RMH-015	Male	189.5	133.6	3736
RMH-016	Male	175	65.1	3685
RMH-018	Male	188	181.6	3803
RMH-020	Female	163.5	55.6	3564
RMH-021	Female	160	93.5	1060
RMH-022	Female	157	90.7	3583
RMH-023	Female	166.5	122	3537
RMH-024	Female	158	102.8	3653
RMH-025	Female	161	59.7	3811

Table 5.3: Patient data from RMH.

Images were imported into 3D-Slicer and DICOM tags were extracted using the tools provided by the OpenDose3D module. The CT image was converted into a 3D density map and SPECT images were converted to 3D activity maps according to calibration data provided by the center. The CT was calibrated following Schneider curve [SCHNEIDER 1996]. The SPECT was calibrated for sensitivity resulting in a value of $62.4 \text{ counts} \cdot \text{MBq}^{-1} \cdot \text{s}^{-1}$.

Voxel-based absorbed dose rates for every time point were calculated for the whole FOV, using MC simulation with voxelized source and density map generated directly from patient data. The CT was propagated to each time point following the same procedure as for attenuation correction to remove the bias introduced. Absorbed dose rates (ADR) were obtained using GATE 9.1. Simulations took 8 hours per patient in a workstation (AMD Ryzen2700X 16 cores, 32GB RAM) as the number of time points was reasonable (3) and taking over 5GB

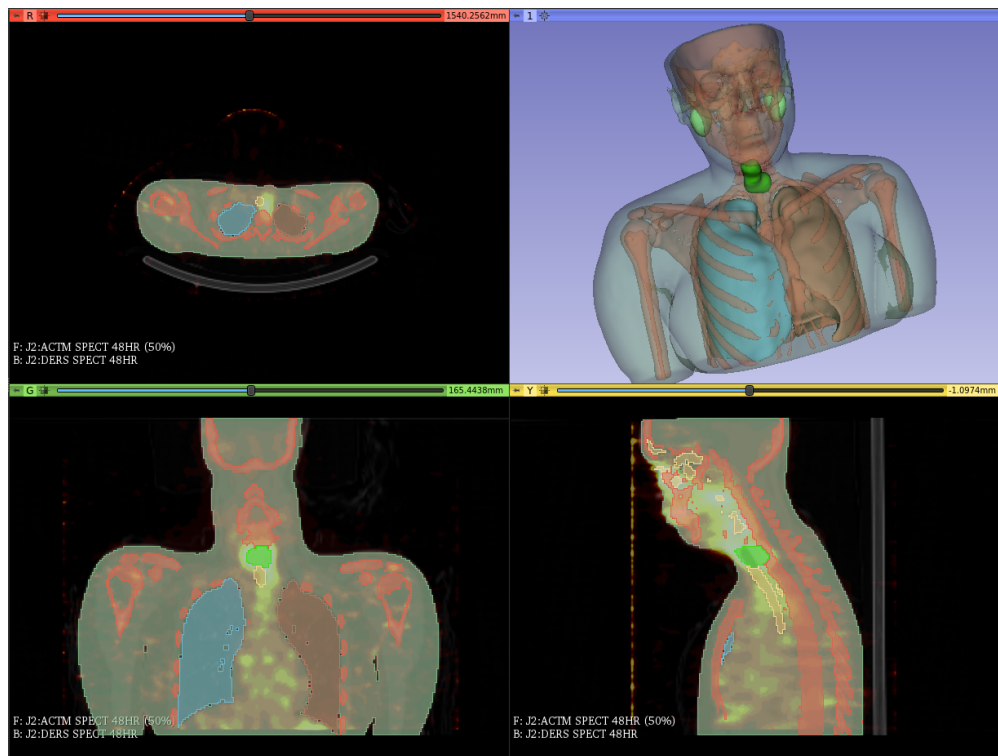


Figure 5.9: Sample patient of RMH

of RAM in total. The ADR were imported back to OD3D.

The segmentation was then performed using tools available in 3D-Slicer. Depending on the situation, manual or threshold-based segmentation was made on the density map (CT) or the activity map (SPECT). For high gradient regions (Whole Body, Lungs, Bones and neck region) the threshold-based segmentation is used. For the rest of cases, manual segmentation by using paint tools of 3D-Slicer is used. In the case of the neck region, it is segmented using the activity map, the other VOI are segmented in the density map. This provided both ADR and Activity in organs at different time points. Table C.1 report the masses of each segmented VOI for all patients. Figure 5.10 show the patient mass variations for segmented VOI.

Time integration was performed using mono-exponential fit function. ADR in VOI, Equation 2.2, were integrated into absorbed doses in VOI and in addition the cumulated activities were also integrated from the activities for comparison to the original study. Table C.2 show the absorbed doses calculated in OpenDose3D using MC simulation. Figure 5.12 show the absorbed dose variation between patients for segmented VOI. Table C.3 show the residence time per segmented VOI for all patients. Figure 5.11 show the residence time variations for segmented VOI.

Equivalent doses were obtained based on the [ICRP60 1990] (Table C.4) and [ICRP103 2007] (Table C.5) recommendations, calculated on Excel using the absorbed doses calculated in identified VOI. Figure 5.13 and Figure 5.14 show the respective variations of equivalent

doses for all patients. For target organs not segmented the absorbed dose in remainder of the body considered homogeneous was used and multiplied by the recommended tissue weighting factors (Wt). The neck regions was used as surrogate for the required thyroid VOI in the ICRP recommendations. The equivalent dose per organ for all patients were averaged and then summed to obtain the effective dose.

In parallel, absorbed and effective doses were also calculated using IDAC 2.1 [ANDERSSON 2017]. The absorbed doses were calculated for each patient with mass correction. Table C.6 show the absorbed doses calculated.

The effective doses were calculated based on patient-averaged residence times in VOI, with no mass corrections. Table C.6 show the absorbed doses calculated with IDAC 2.1. Figure 5.15 show the variation in the absorbed doses calculated with IDAC 2.1. Table 5.4 presents the effective dose comparison. It should be noted a large dispersion in patient data that yield an uncertainty in effective dose calculation near 100 % that can only be appreciated by the use of OpenDose3D.

Method	OpenDose3D [mSv·MBq ⁻¹]	IDAC 2.1 [mSv·MBq ⁻¹]
ICRP 60	$(8.60 \pm 8.47) \times 10^{-2}$	1.5×10^{-1}
ICRP 103	$(7.64 \pm 6.75) \times 10^{-2}$	1.2×10^{-1}

Table 5.4: Effective dose comparison between OpenDose3D and IDAC 2.1.

A range of absorbed doses was observed for all segmented organs with the majority of thyroid remnants absorbed doses below 24 Gy (median 4 Gy). For the rest of organs, the absorbed doses were consistently below 2 Gy (median 400 mGy) for lungs and salivary glands and below 400 mGy (median 150 mGy) for the rest of organs.

As a final benchmark, a comparison with RMH *in situ* dosimetry was performed. RMH dosimetry was made with an internal independent academic software, called Dodose [ABREU 2021a], which uses a dose point kernel for electrons only. Figure 5.16 show the comparison with the absorbed dose calculated by RMH. The values are comparable for bones and parotid glands, being OD3D persistently higher (50 %) than RMH as expected for considering also the gamma contribution. In the case of Neck region, the difference (80 %) is because of a segmentation by Dodose, that cuts the internal air regions, removing also the activity present by PVE, therefore reducing the total activity accounted for in the region.

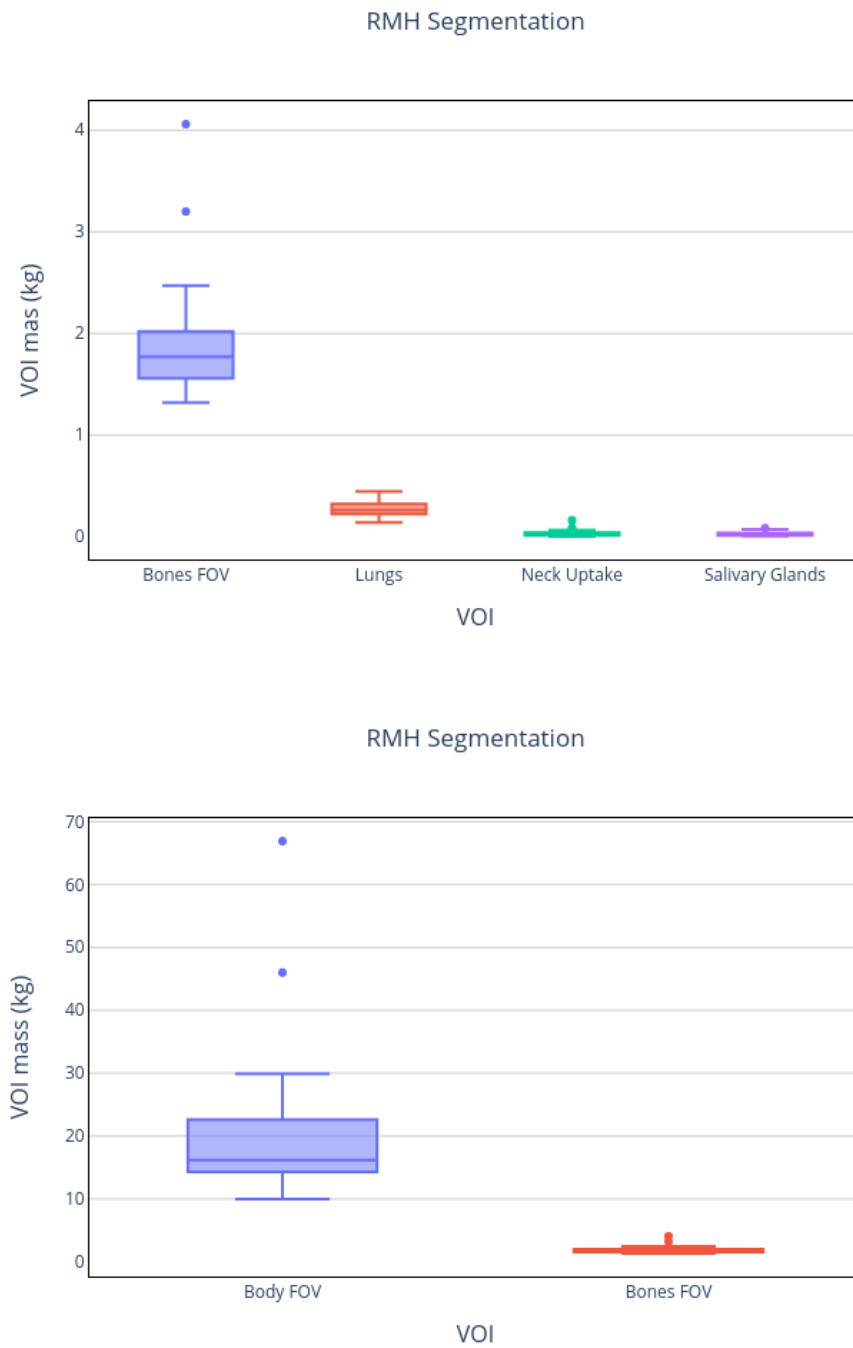


Figure 5.10: Mass statistics for segmented VOI

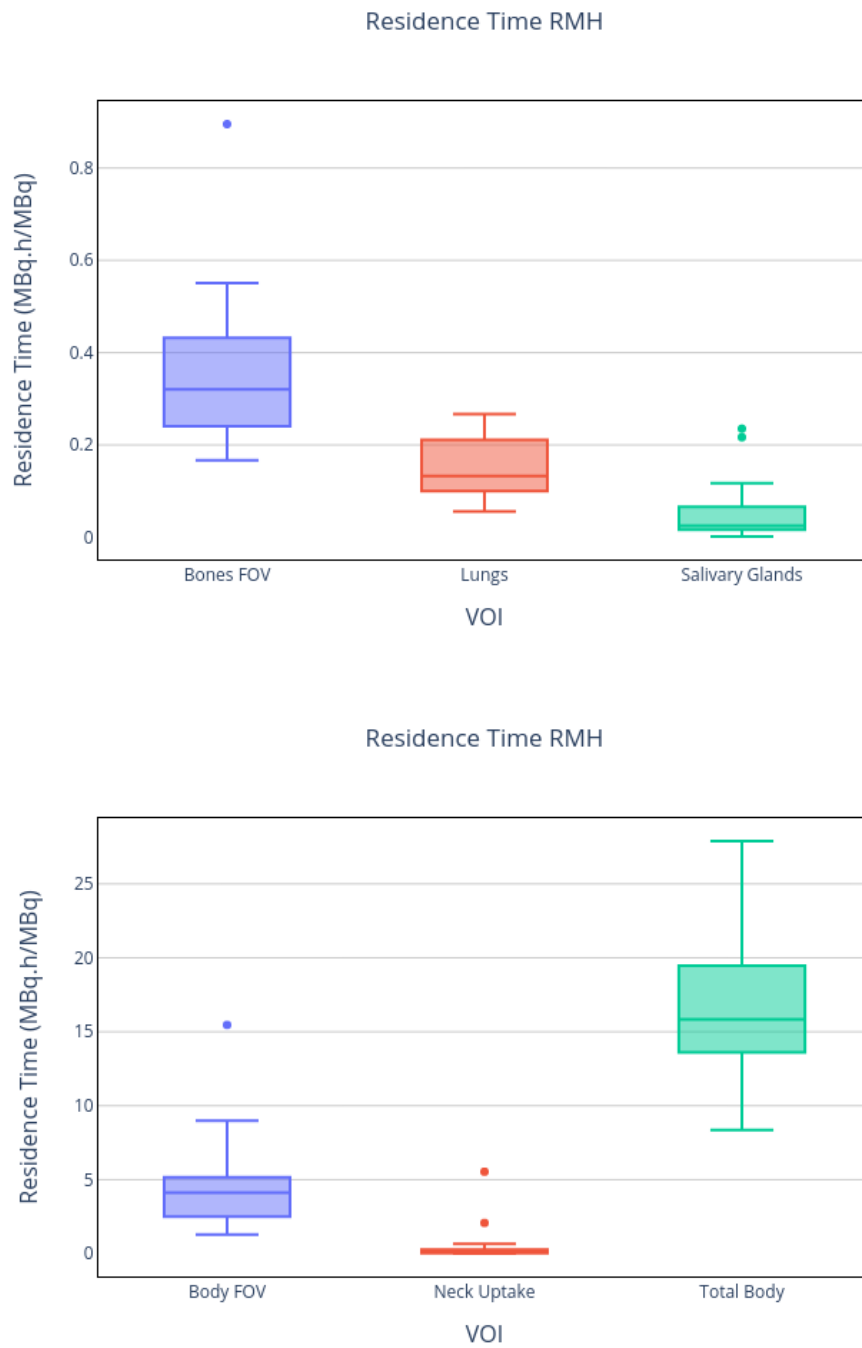


Figure 5.11: Residence time statistics for segmented VOI

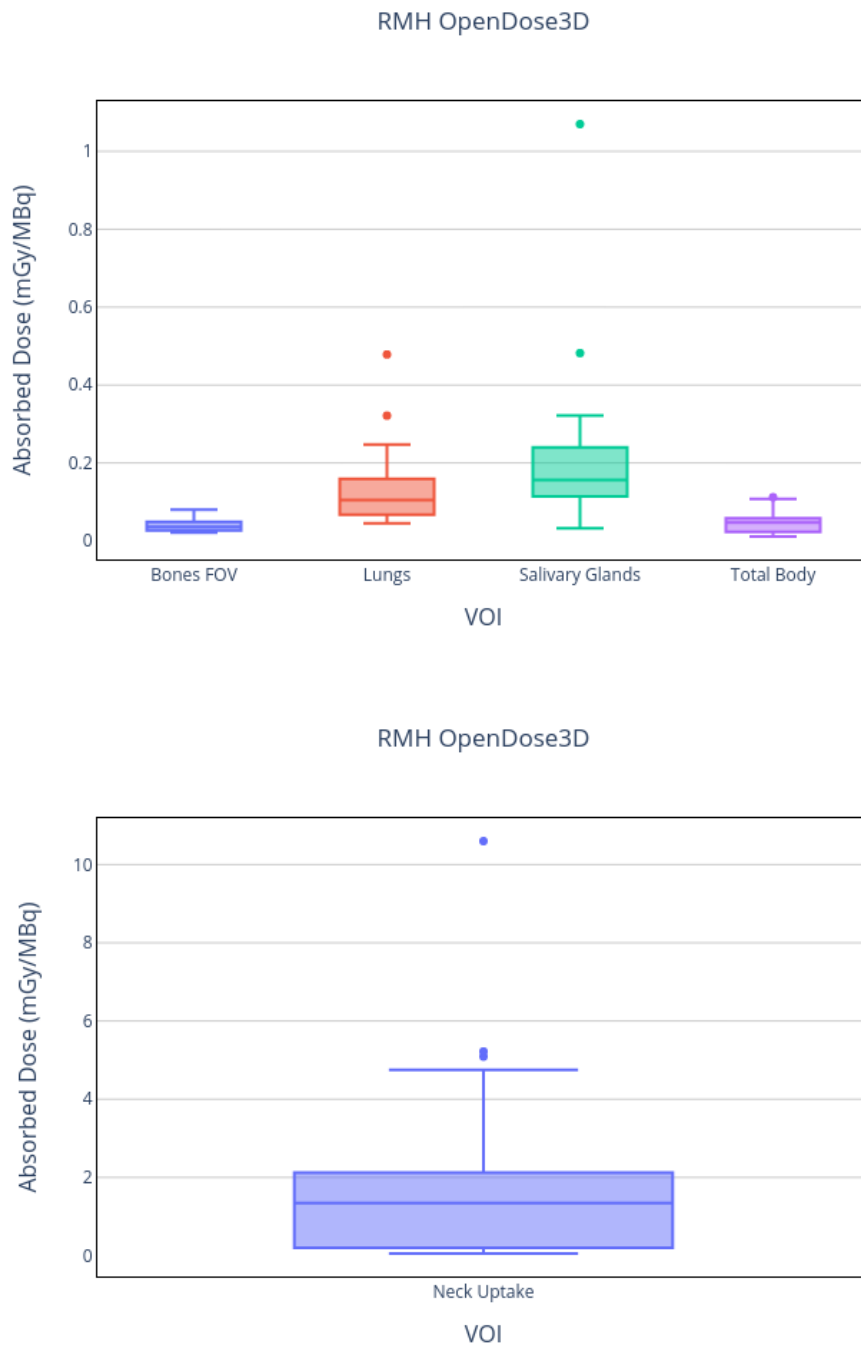


Figure 5.12: Absorbed dose statistics for segmented VOI, calculated by MC in OpenDose3D

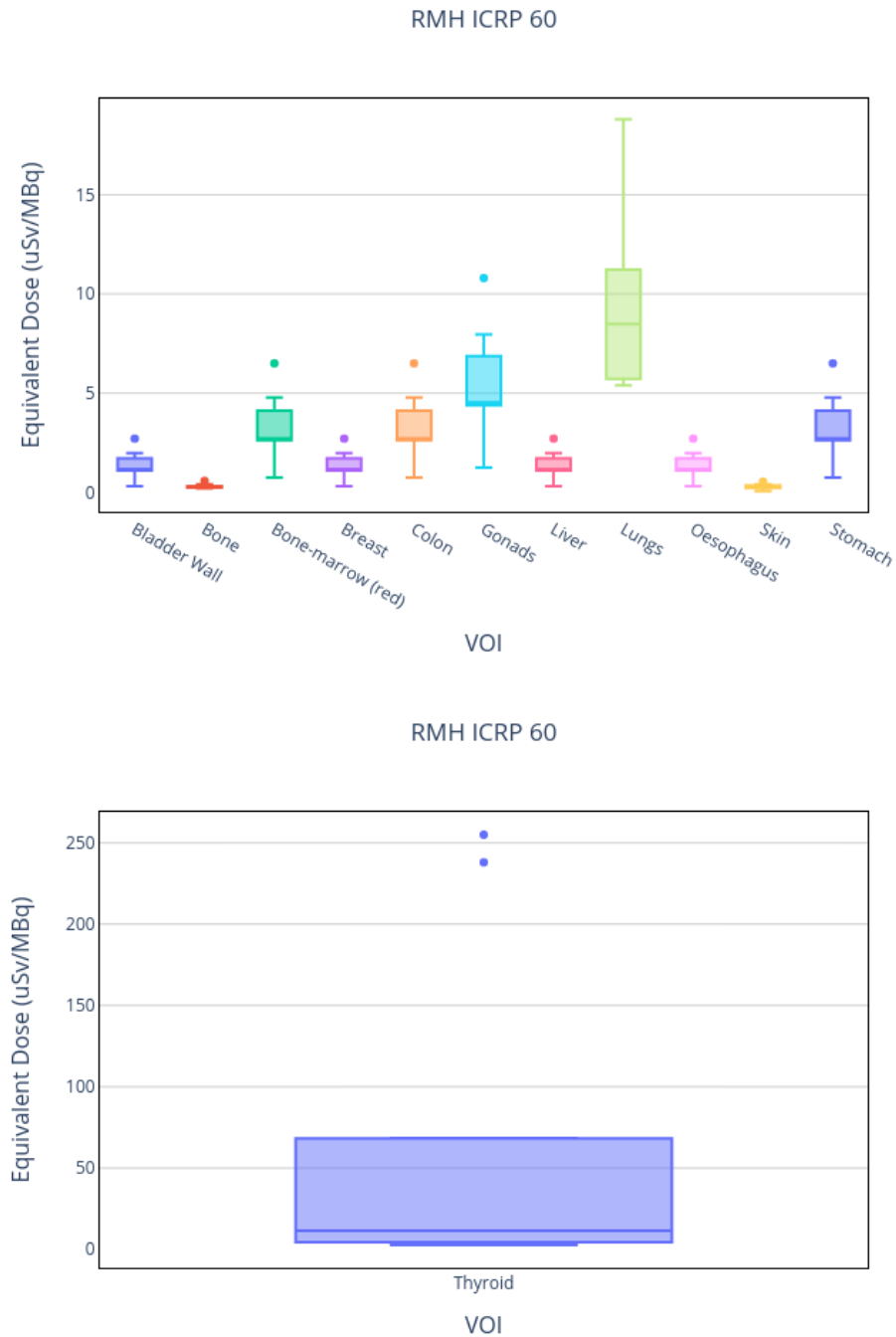


Figure 5.13: Equivalent Dose statistics calculated by ICRP 60 recommendations [ICRP60 1990]

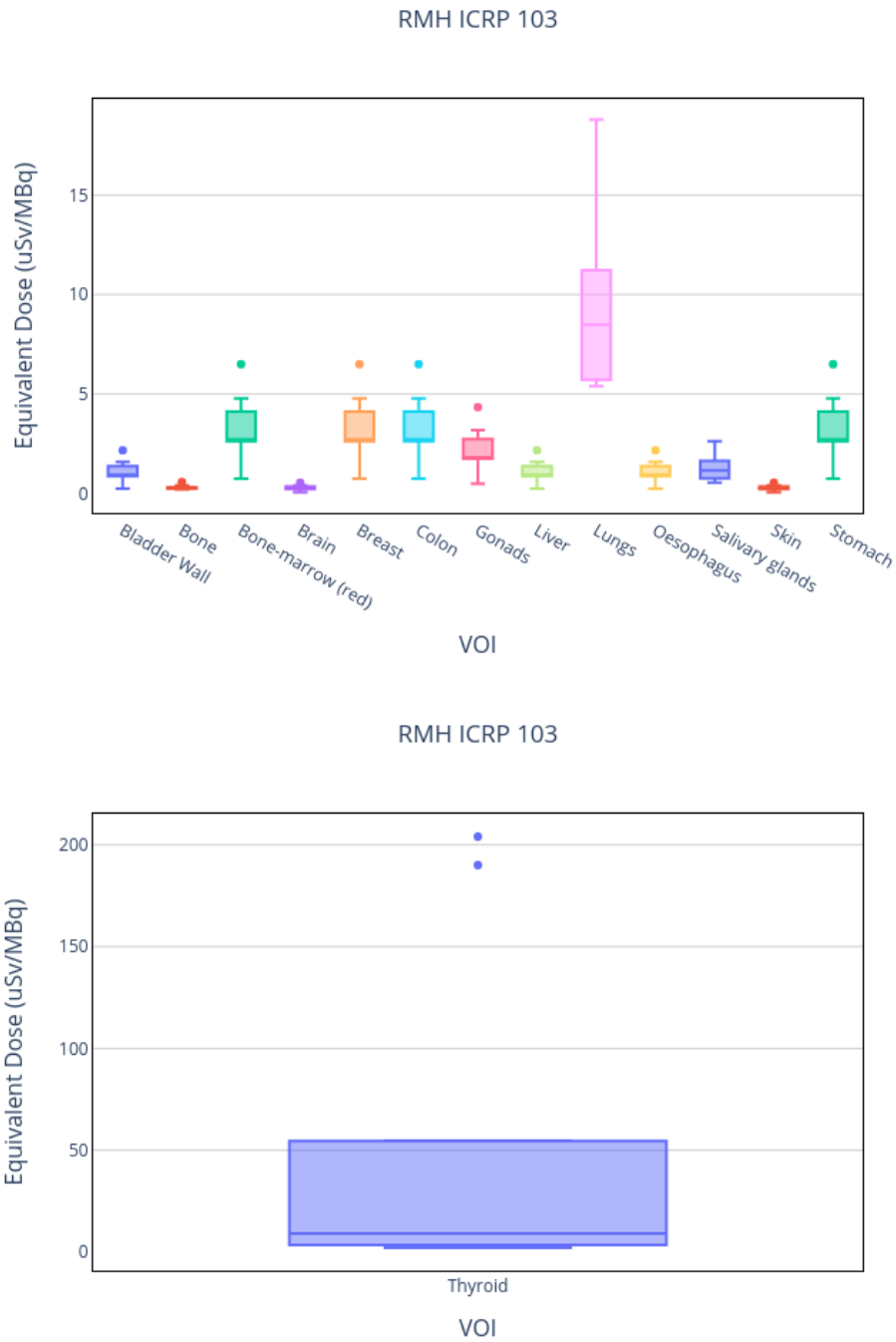


Figure 5.14: Equivalent Dose statistics calculated by ICRP 103 recommendations [ICRP103 2007]

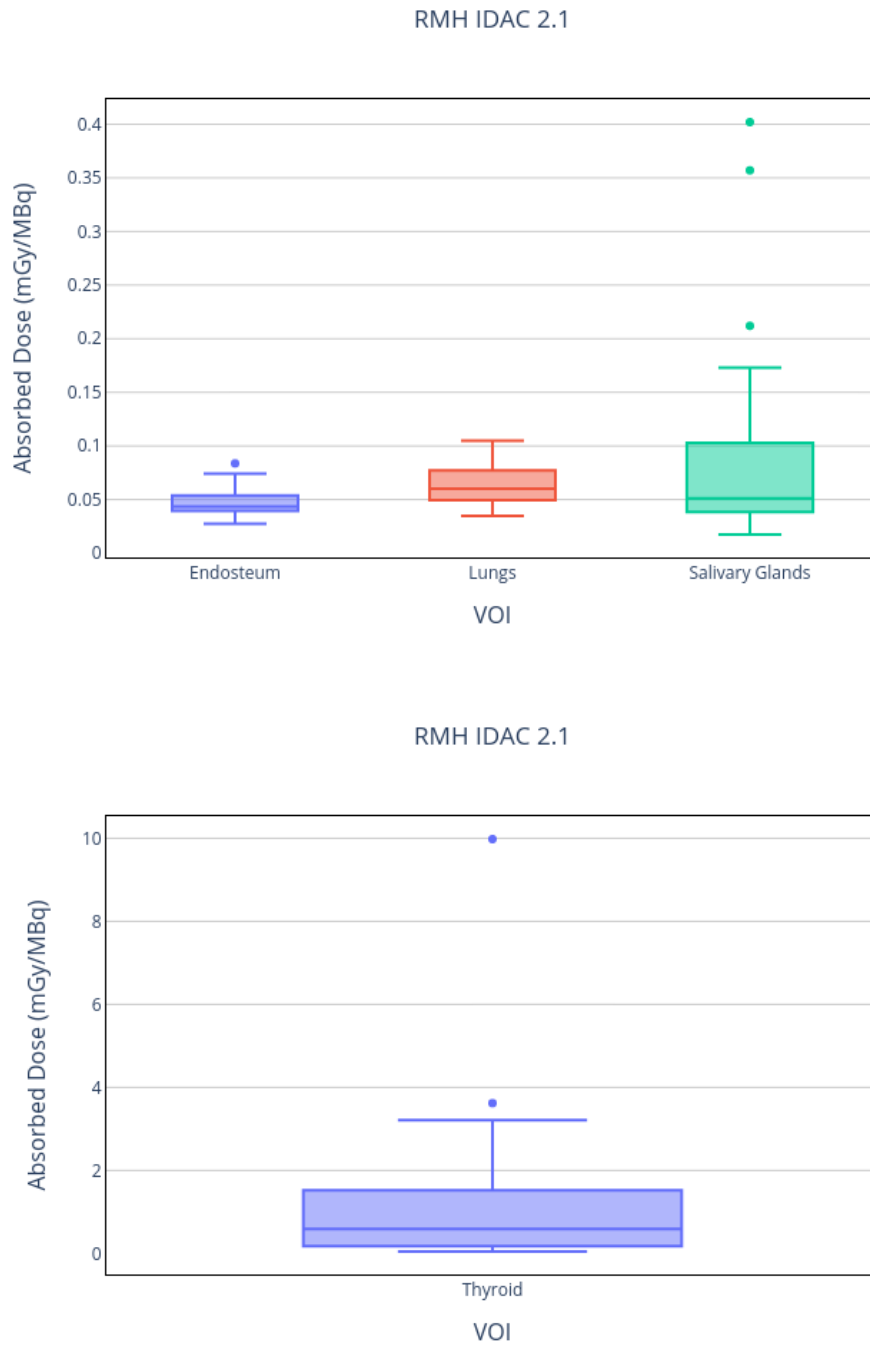


Figure 5.15: Absorbed Dose statistics calculated by IDAC 2.1 [ANDERSSON 2017]

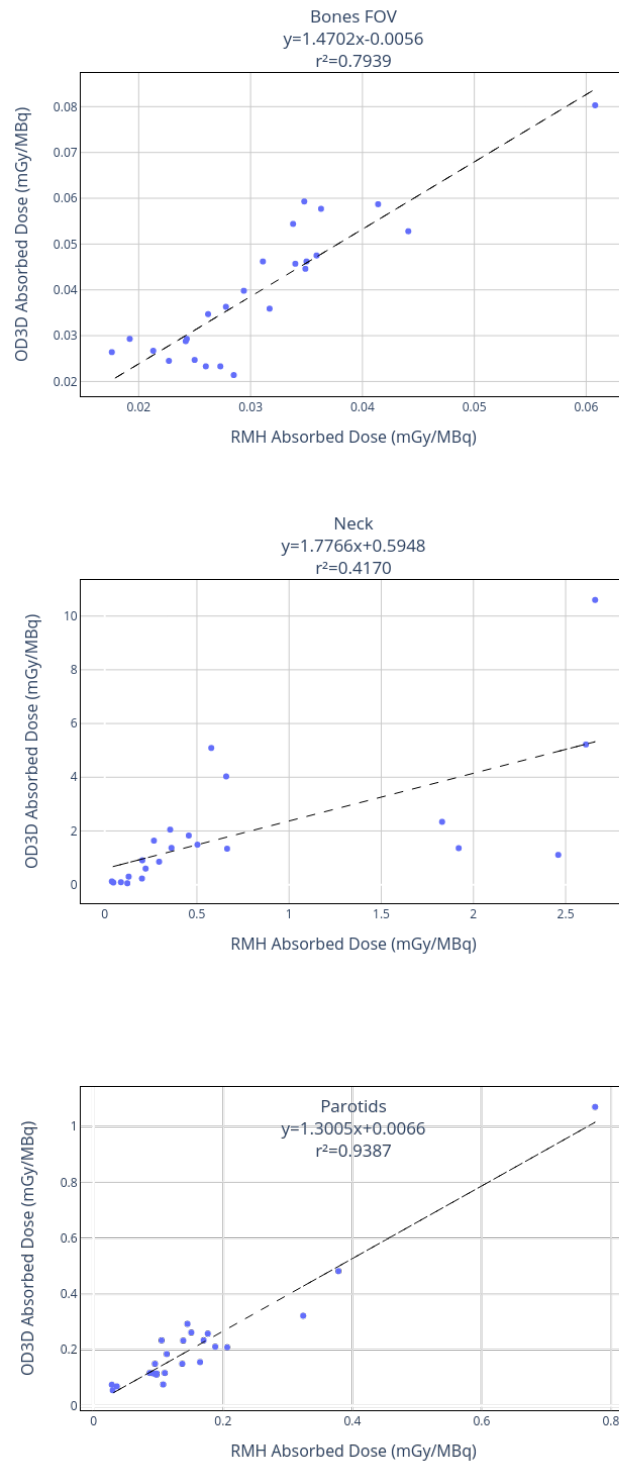


Figure 5.16: Comparison of Absorbed Dose calculated by RMH in situ and those calculated by this work

5.3 Dosimetry for UKW

The selected images consist of one SPECT/CT acquired at 48h post administration. More uncorrected SPECT at different time points were acquired to perform the pharmacokinetics, no external probe measurements were available. A CT in each time point was not possible because of the decision of the ethical committee. Patients were scanned from head to abdomen. Only patients with 2 or more time points were selected for this study. Blood dosimetry was also reported by UKW. Table 5.5 shows the patient data. Figure 5.17 shows a sample patient where the FOV can be appreciated.

Patient	Time points	Sex	Height (cm)	Weight (kg)	Injected Activity (MBq)	Absorbed Dose to Blood (mGy)
UKW-001	3	Female	85	170	3550	205
UKW-002	5	Female	72	172	3511	242
UKW-003	5	Female	64	156	3550	424
UKW-004	4	Female	78	162	3571	262
UKW-005	5	Female	46	167	3425	310
UKW-006	3	Female	115	170	3515	285
UKW-007	5	Female	70	158	3717	334
UKW-008	2	Female	70	173	3632	no
UKW-009	4	Female	117	170	3605	no
UKW-010	1	Female	60	162	3651	290
UKW-011	3	Female	108	173	3502	307
UKW-012	3	Female	77	164	3560	290
UKW-013	4	Male	80	168	3580	289
UKW-014	3	Female	85	166	3564	334
UKW-015	3	Male	96	180	3601	267
UKW-016	5	Female	68	193	3911	313
UKW-017	4	Male	94	185	3519	605
UKW-018	3	Female	85	156	3602	325
UKW-019	2	Female	62	158	3581	no
UKW-020	5	Male	82	187	3660	259
UKW-021	5	Female	96	173	3597	349

Table 5.5: Patient data from UKW. Blood dosimetry were not performed for patients 8, 9, and 19.

Voxel-based absorbed dose rates were calculated for the whole FOV, using MC simulation with voxelized source and density map generated directly from patient data in the SPECT/CT

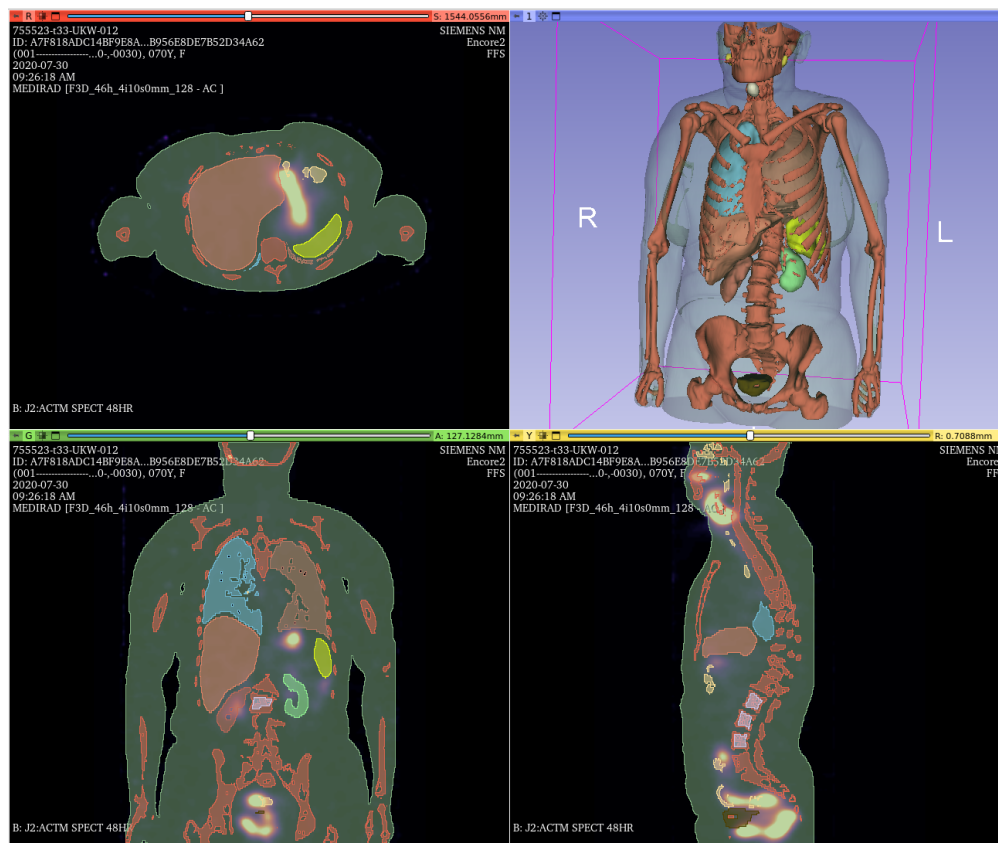


Figure 5.17: Sample patient of UKW

time point.

SPECT images registration process was implemented automatically in OpenDose3D, by using the rigid parameters in the Elastix module of 3D-Slicer. There were no anatomical references to allow for elastic registration. The 48hr SPECT/CT was expected to be already registered with the provided CT, therefore this point was taken as the reference. Then, the CT was used as density map for every time point.

Absorbed dose rates (ADR) were obtained using GATE 9.1. Simulations took 8 hours per patient in a workstation (AMD Ryzen2700X 16 cores, 32GB RAM) and taking over 1GB of RAM per patient. Several patients could be run simultaneously. The ADR were imported back to OD3D.

Patients were scanned from neck to pelvis, so different structures can be segmented. Segmented structures considered were the lungs (left/right), the salivary glands, the bones visible in the field of view, the neck region (even though the functional volume defined may hide high activity gradients in microscopic regions), the liver, kidneys (left/right), spleen, urinary bladder and L2-L4. The total body mass was documented for each patient before the imaging sessions. The remainder was defined as the total body minus all defined regions of interest. Figure 5.18 show the segmented VOI mass variations for all patients. Table C.13

show the mass of segmented VOI.

The uncorrected SPECT were used to calculate T_{eff} of each organ. Table C.14 show the calculated T_{eff} from the mono-exponential fitting process. Figure 5.19 show the T_{eff} variation for all patients. A huge dispersion in T_{eff} for every VOI can be noticed.

Time integration was performed using mono-exponential curves calculated with the calculated T_{eff} and the measured point at 48h for the SPECT/CT. ADR in VOI, Equation 2.2, were integrated into absorbed doses in VOI and in addition the cumulated activities were also integrated from the activities for comparison to the original study. Table C.15 show the absorbed doses calculated in OpenDose3D using MC simulation. Figure 5.21 show the absorbed dose variation per patient. Table C.16 show the residence times calculated by OpenDose3D. Figure 5.20 show the residence time variations for segmented VOI.

Equivalent doses were obtained based on the [ICRP60 1990] (Table C.17) and [ICRP103 2007] (Table C.18) recommendations, calculated on Excel using the absorbed doses calculated in identified VOI. Figure 5.22 and Figure 5.23 show the respective variations of equivalent doses for all patients. For target organs not segmented the absorbed dose in remainder of the body considered homogeneous was used and multiplied by the recommended tissue weighting factors (Wt). The equivalent dose per organ for all patients were averaged and then summed to obtain the effective dose.

In parallel, absorbed and effective doses were also calculated using IDAC 2.1 [ANDERSSON 2017]. The absorbed doses were calculated for each patient with mass correction. The effective doses were calculated based on patient-averaged residence times in VOI, with no mass corrections. Table C.19 show the absorbed doses calculated with IDAC 2.1. Figure 5.24 show the absorbed dose variation per patient. Table 5.6 present the comparison for effective dose comparison. It shall be noted the huge dispersion in patient data that yield an uncertainty in effective dose calculation near 100% that can only be appreciated by the use of OpenDose3D.

Method	OpenDose3D [mSv·MBq ⁻¹]	IDAC 2.1 [mSv·MBq ⁻¹]
ICRP 60	$(3.50 \pm 3.42) \times 10^{-1}$	3.8×10^{-1}
ICRP 103	$(2.89 \pm 2.75) \times 10^{-1}$	3.1×10^{-1}

Table 5.6: Effective dose comparison between OpenDose3D and IDAC 2.1.

A range of absorbed doses was observed for all segmented organs with the median of thyroid remnants absorbed doses 13.8 Gy (median 16.74 Gy for IDAC 2.1). For the rest of organs, the absorbed doses were consistently below 2 Gy (median 400 mGy) for lungs and salivary glands and below 400 mGy (median 200 mGy) for the rest of organs.

Two structures were selected to evaluate the relation of the calculated doses to the blood dosimetry performed by UKW. The structures selected (liver and L2-L4/red bone marrow) are only influenced by the activity present in the blood. In liver case due to high blood volume, and in L2-L4 case because it is one of the critical organs at risk. Figure 5.25 show

the relation between calculated absorbed dose to liver and the blood dosimetry performed at UKW. Figure 5.26 show the relation between calculated absorbed dose to L2-L4 and the blood dosimetry performed at UKW. These figures show no correlation between the methods, this may be explained by the fact that self-absorbed dose is only part of the equation and that cross irradiation is very important to consider.

Comparable results are observed if we compare population based values. Figure 5.27 show the variations for each dosimetry method. Due to the high dispersion in the data, the population mean for each method is contained in one standard deviation. It can be also seen that each box plot overlaps with the others, and with the high uncertainties present, there is no statistical difference in the absorbed dose calculated by each method.

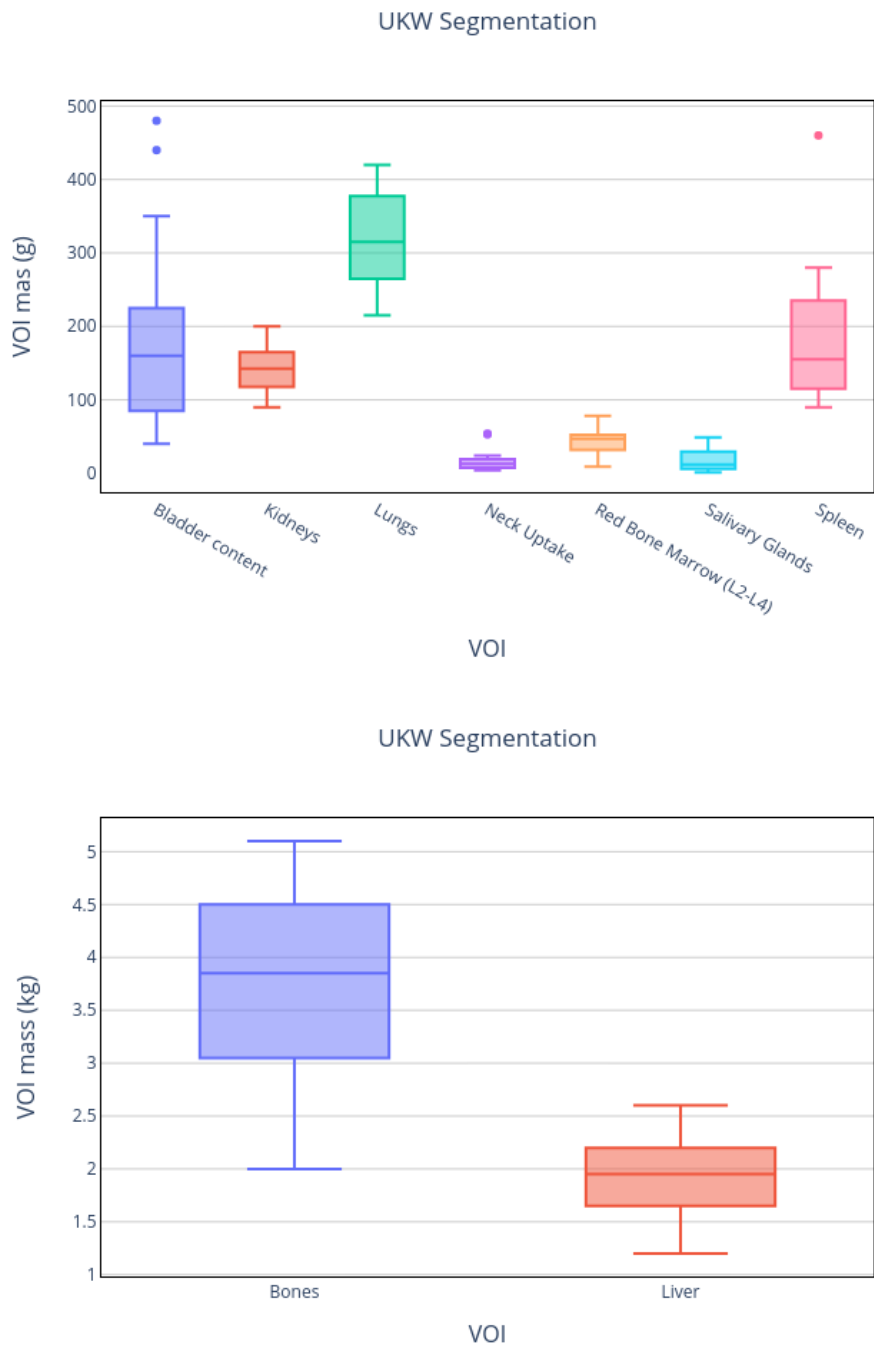
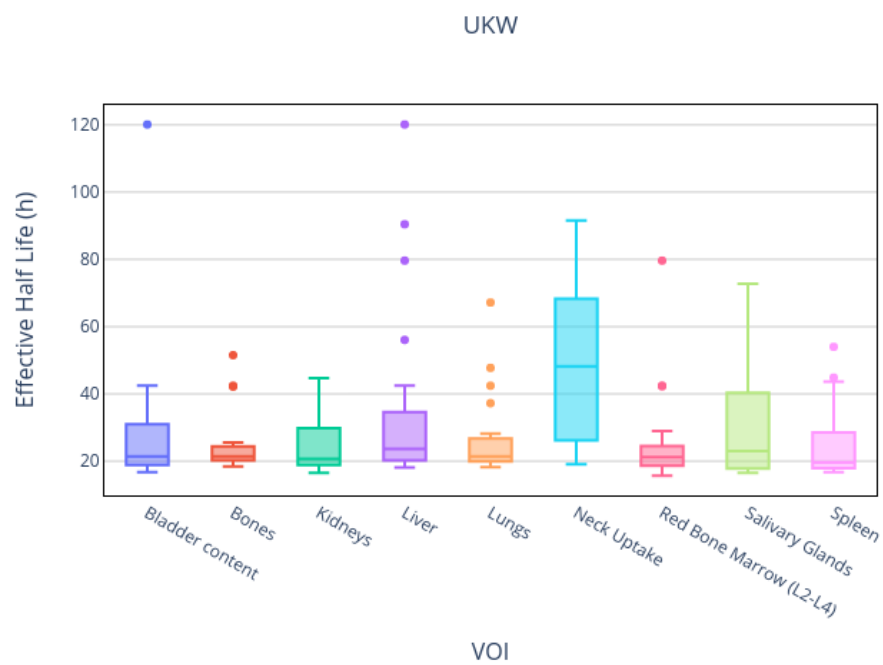


Figure 5.18: Mass statistics for segmented VOI

Figure 5.19: T_{eff} statistics for segmented VOI

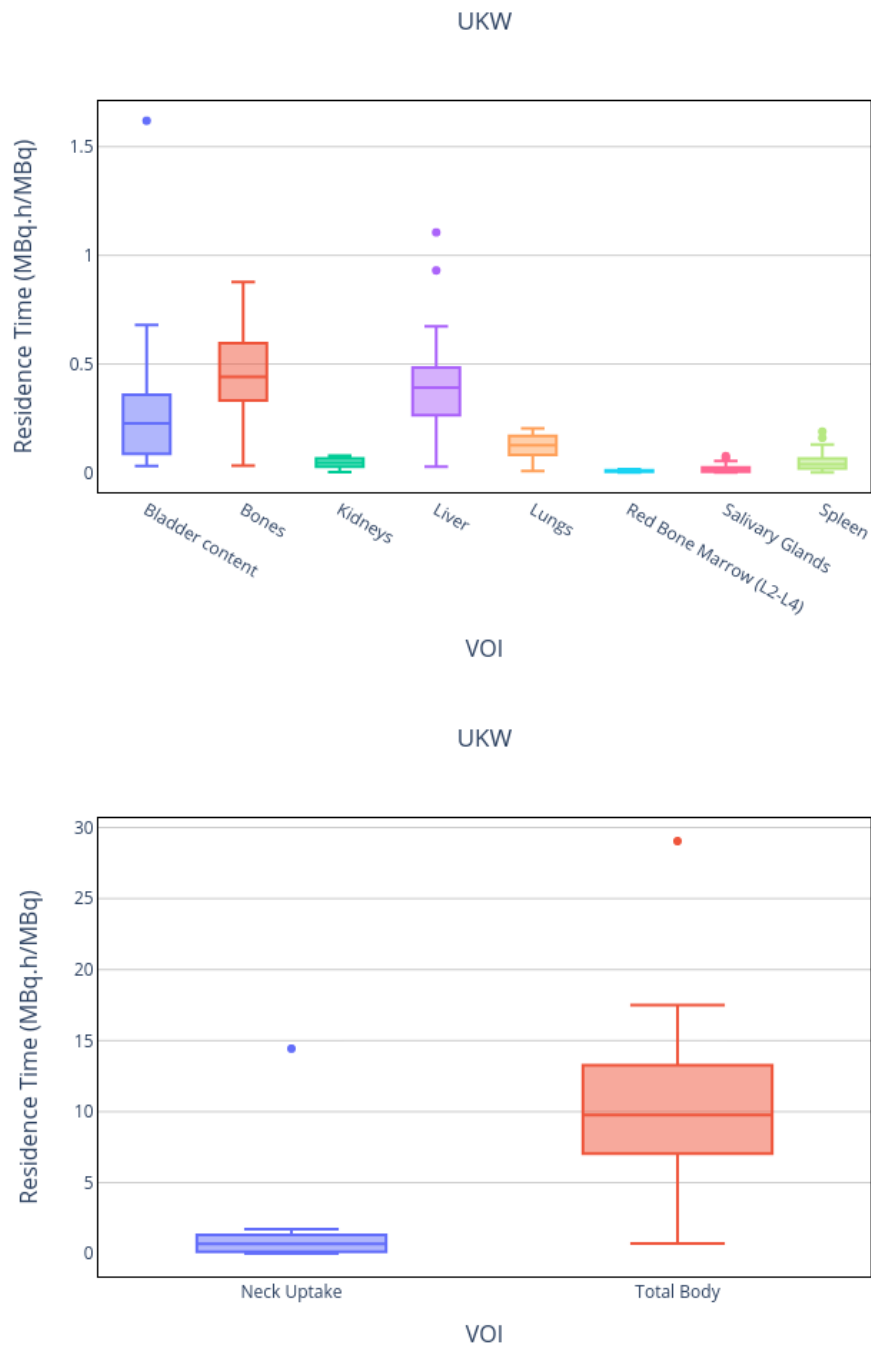


Figure 5.20: Residence time statistics for segmented VOI

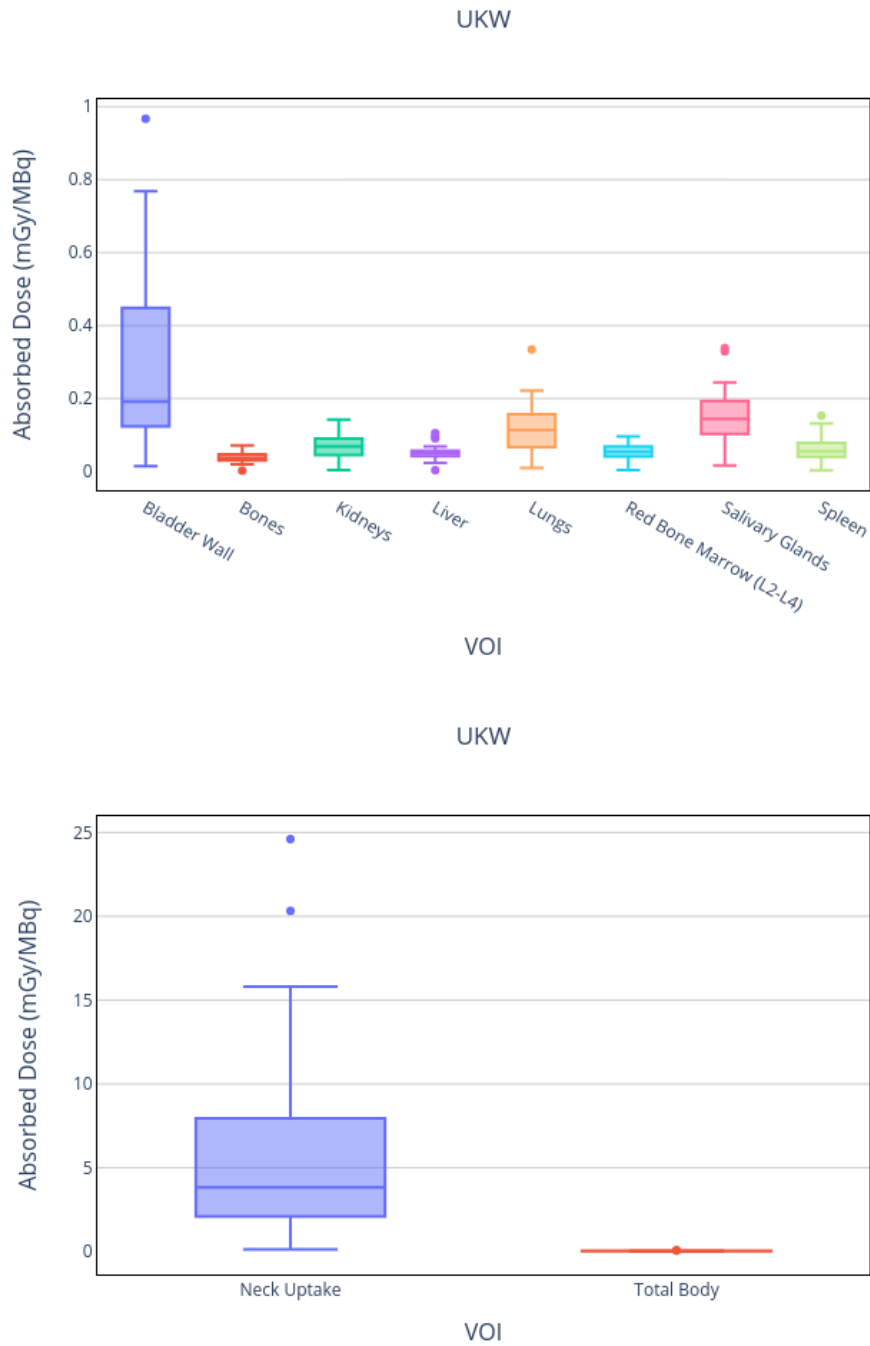


Figure 5.21: Absorbed dose statistics for segmented VOI, calculated by MC in OpenDose3D

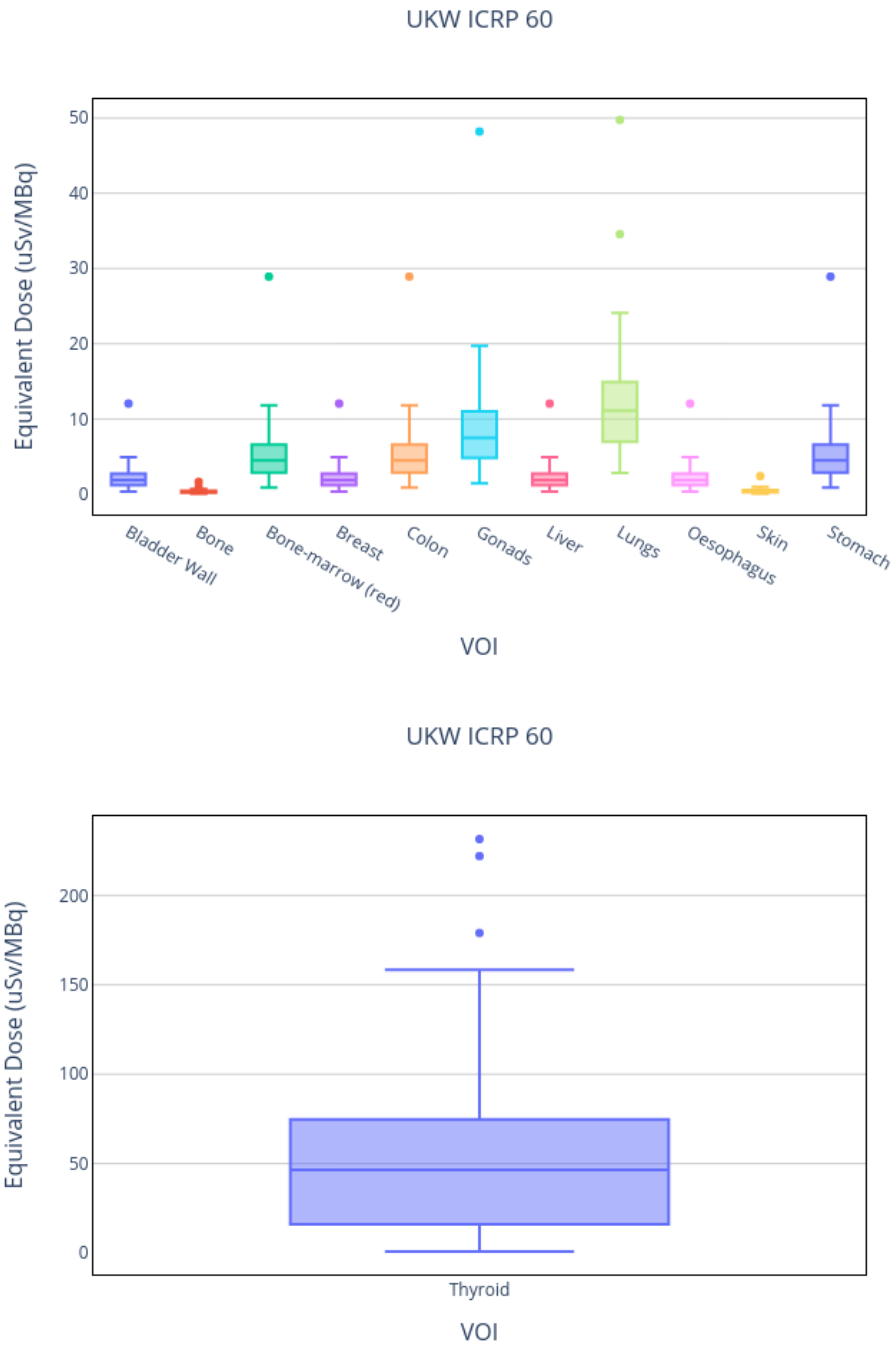


Figure 5.22: Equivalent Dose statistics calculated by ICRP 60 recommendations [ICRP60 1990]

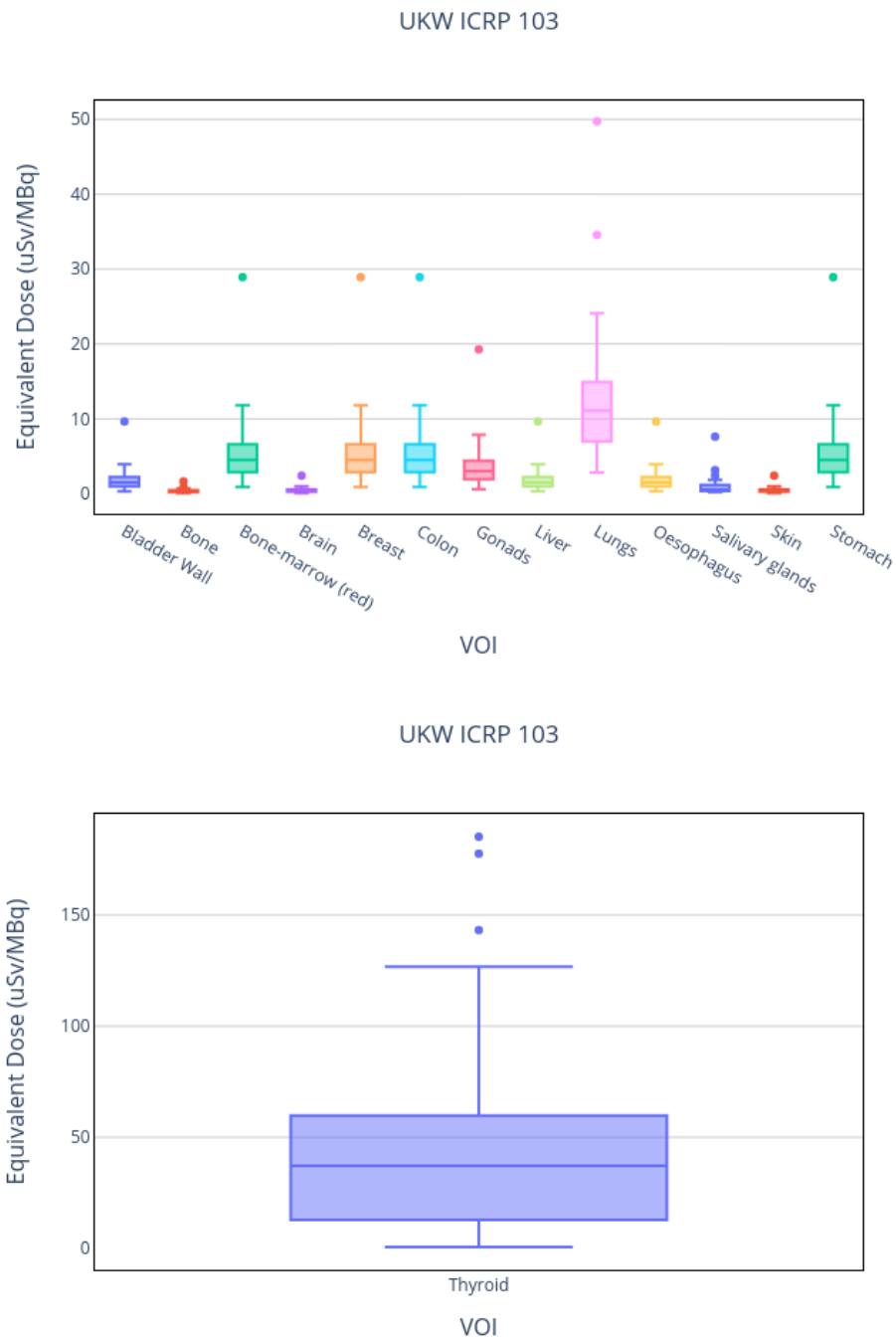


Figure 5.23: Equivalent Dose statistics calculated by ICRP 103 recommendations [ICRP103 2007]

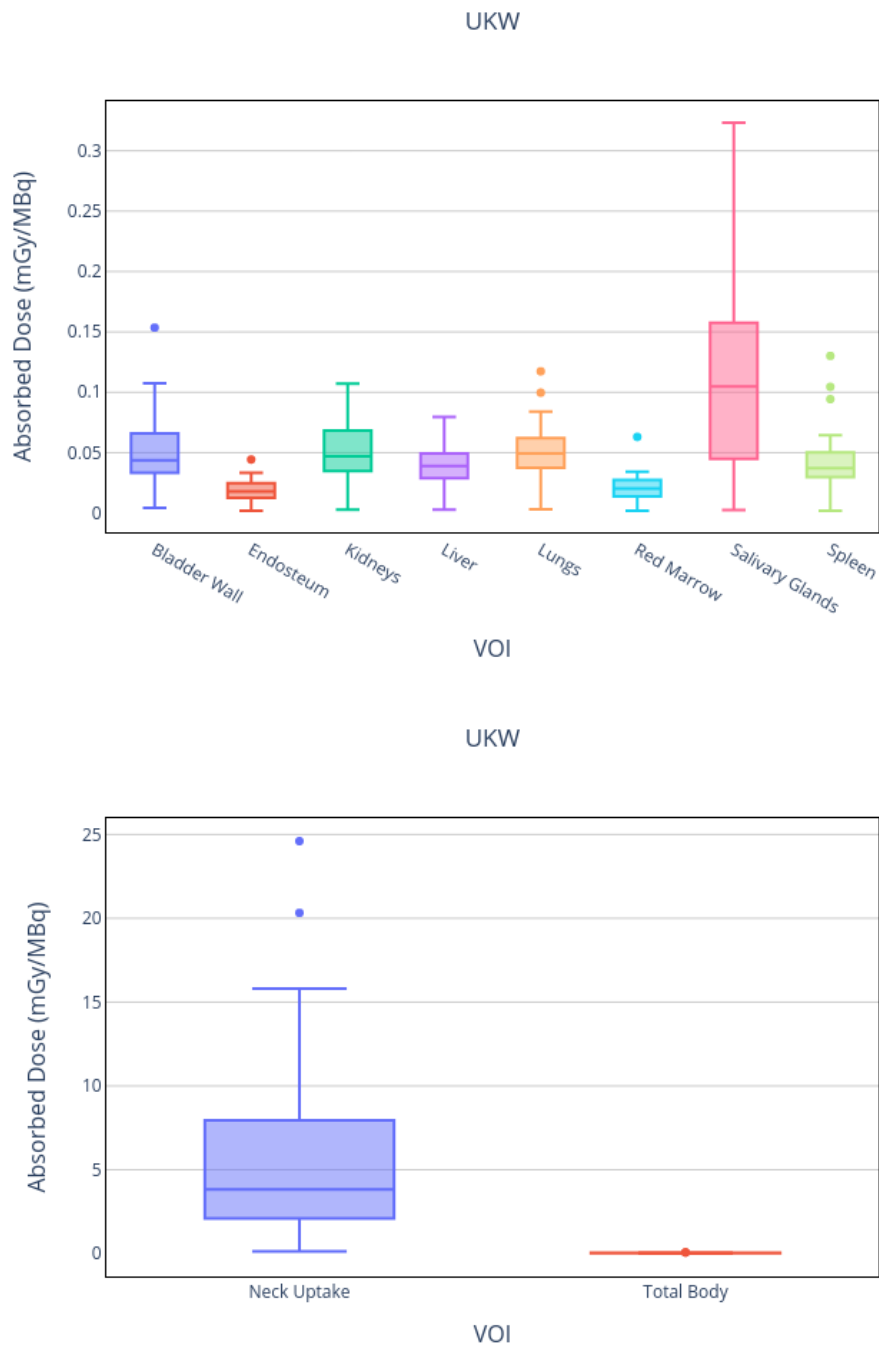


Figure 5.24: Absorbed Dose statistics calculated by IDAC 2.1 [ANDERSSON 2017]

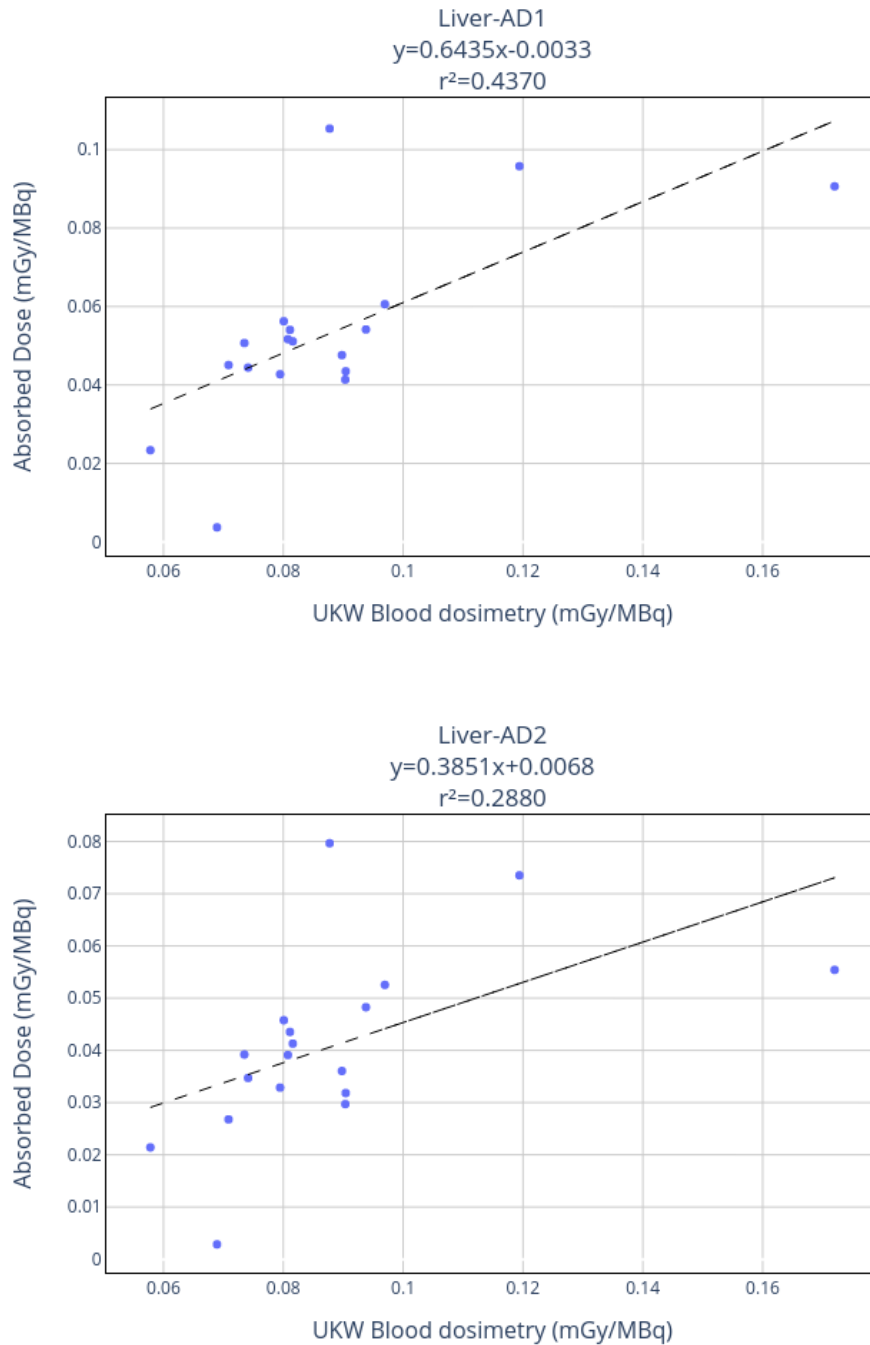


Figure 5.25: Comparison of presented results for liver with blood based dosimetry performed at UKW. AD1 is patient-specific Monte Carlo-based calculation. AD2 is model-based (IDAC 2.1) calculation.

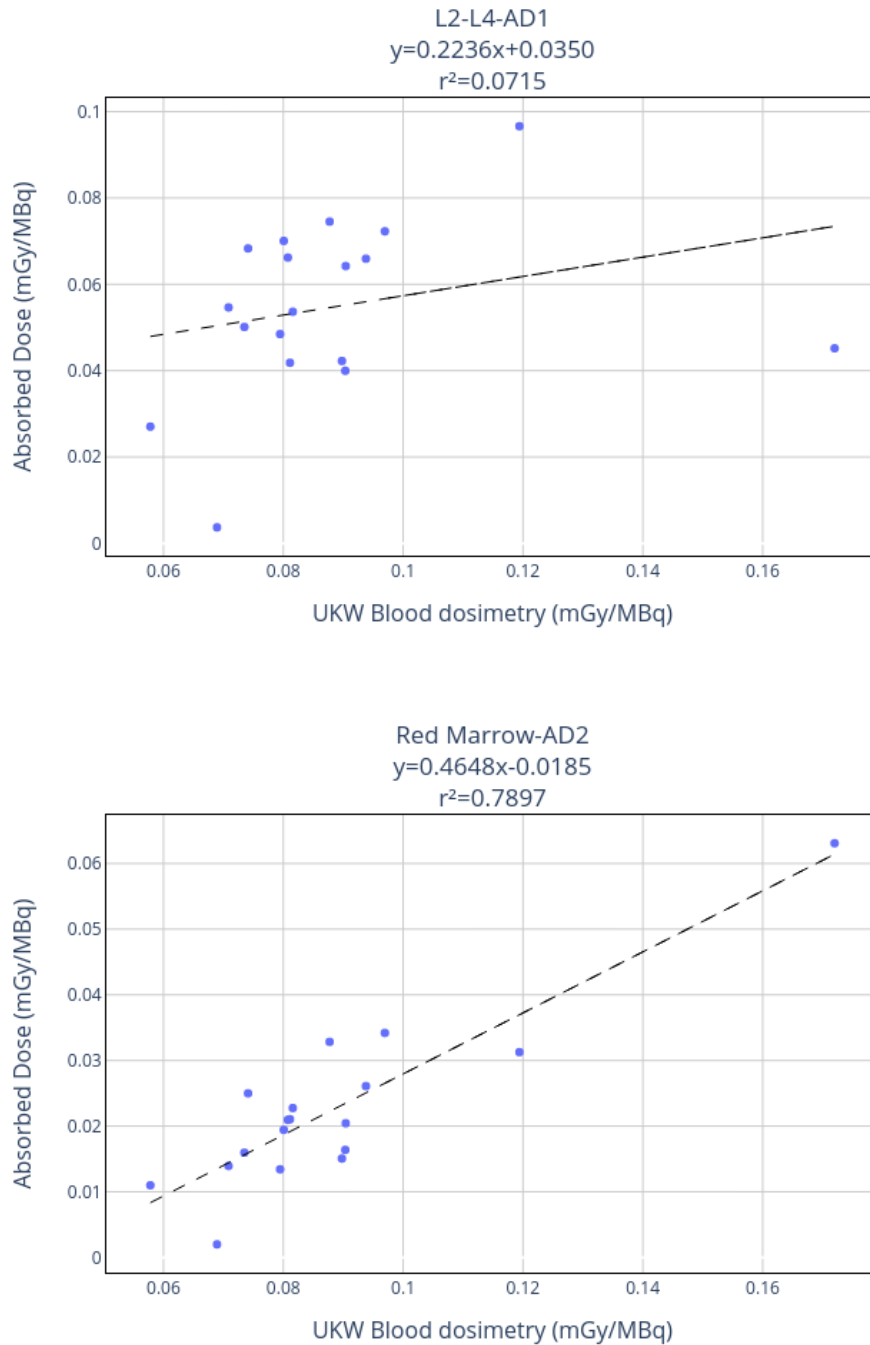


Figure 5.26: Comparison of presented results for L2-L4 with blood based dosimetry performed at UKW. AD1 is patient-specific Monte Carlo-based calculation. AD2 is model-based (IDAC 2.1) calculation.

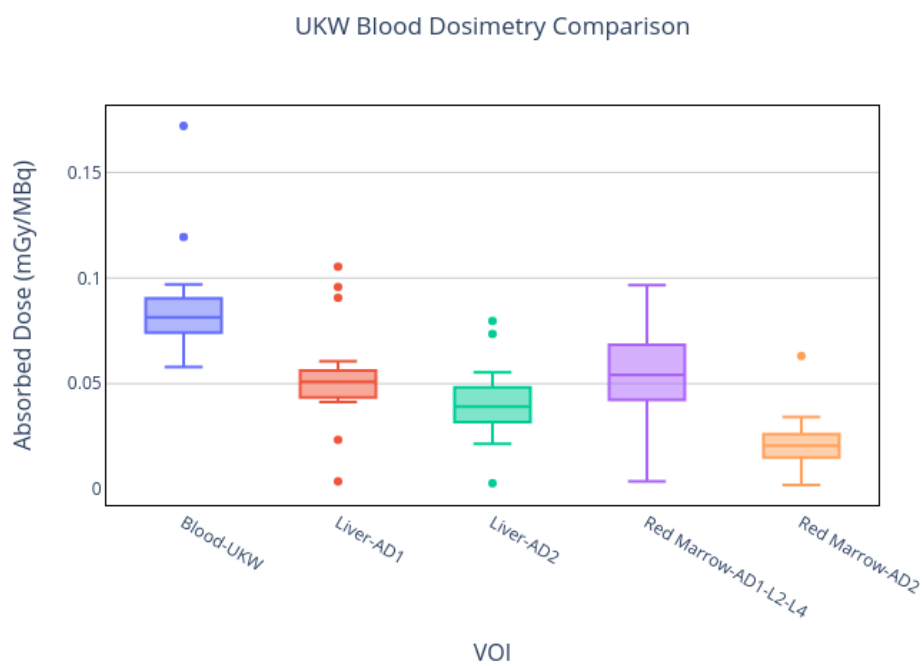


Figure 5.27: Comparison of presented results with blood based dosimetry performed at UKW. AD1 is patient-specific Monte Carlo-based calculation. AD2 is model-based (IDAC 2.1) calculation.

5.4 Discussion

The dosimetry of three centers was performed using the proposed methodologies and the provided 3D-Slicer module. The workflows were adapted to each specific case showing OD3D flexibility to different clinical scenarios:

- For RMH, only one CT was acquired, used for attenuation correction for every time point. This has the obvious drawback of omitting all geometry variations in the patient, by the repositioning, the organ (VOI) movement, and the organ change in volume and density. But historically, this approach was accepted. Also the SPECT scan was performed just to the thorax, therefore dosimetry could not be performed for abdominal structures.
- For IUCT, only one late time point was acquired. Pharmacokinetics was measured with an external whole body probe as a global parameter. This approach cannot give account of organ specific metabolism, reducing the value of the dosimetry results and increasing the overall uncertainty.
- For UKW, one SPECT/CT was acquired plus several other SPECT, without corrections, at different time points. This approach has some problems: the time registration must be done on the SPECT images without anatomical references; all geometry variations in the patient are omitted as described for RMH; big organs, as the liver for example, has different attenuation correction coefficients depending on the depth in the body, therefore summing the counts in the uncorrected SPECT, contains an implicit uncertainty that can't be measured at this point.
- For RMH and UKW, some patients contained only 1 acquisition. This forced the adoption of a methodology equivalent to that used for IUCT. This changes completely the data homogeneity.

For single time point patients, like IUCT and some RMH and UKW, the pharmacokinetics was assumed to be equal to those measured with external probes. Except the neck region where a fixed value of $T_{eff} = 68$ h was used. Figure 5.3 show that, even when the proposed T_{eff} was contained in the measured dispersion, this dispersion was very large ($RD > 100\%$). Therefore, the assumption of a fixed T_{eff} for all patients was very poor. However, without direct measurements in each patient (either by probes or SPECT), it is impossible to estimate a better value. This situation is the same for every organ (VOI) considered. Patient UKW-010 (Table C.14) with only one time point measured, is the best example of how a single T_{eff} used for all organs differ significantly ($RD > 100\%$ respect to median Figure 5.19) from the overall behavior of all the other patients from same group.

The proposed dosimetry workflow gives same order magnitude results as model-based dosimetry. This was expected for these cases, the ^{131}I has a very well-defined pharmacokinetics, extensively studied in literature. For patients with normal excretion systems (gastric and urinary), the ^{131}I metabolism is really fast and only the thyroid tissue and the salivary

glads have more extended metabolism. Model-based dosimetry in this case is considered a gold standard as the time curves behave like mono-exponential decay with a defined T_{eff} . However, we could see big variations in metabolism in different organs (VOI) for the studied patients. The facts that the involved activities are very low, and that there are big uncertainties in the acquisition protocols, are the main factors that leverage our results with model-based dosimetry.

The same software solution was used to perform all steps, except reconstruction, in the dosimetric workflow. The software was adapted to accept only one CT and to register functional images. This proves the high flexibility of the proposed solution to be adapted to different clinical situations.

Conclusion générale et perspectives futures

Dans ce travail, les flux de travail de la dosimétrie clinique ont été analysés. Il existe un protocole de dosimétrie standard décrit par MIRDO [BOLCH 2009], mais il ne spécifie pas tous les détails pour réaliser la dosimétrie. Par conséquent, chaque centre clinique met en œuvre les étapes spécifiques de manière indépendante.

Dans le chapitre 1, une description des méthodologies actuellement disponibles est présentée. Nous discutons de l'importance de la normalisation des flux de travail cliniques et des outils dosimétriques. Nous concluons que la normalisation des flux de travail dosimétriques cliniques permettrait aux différentes équipes cliniques de réaliser une dosimétrie spécifique au patient selon une approche commune.

Dans le chapitre 2, deux flux de travail dosimétriques ont été présentés.

- La première approche consiste à intégrer l'activité mesurée en les volumes d'intérêt (VOI) dans le temps. Bien qu'il s'agisse de l'approche classique, dans notre proposition, nous avons ajouté tous les détails pour parvenir à une approche commune, depuis l'étalonnage de l'équipement, l'acquisition des images du patient et tous les flux de données nécessaires pour obtenir un résultat.
- La deuxième approche consiste à intégrer les débits moyens de dose absorbée (DDA) calculé en les volumes d'intérêt (VOI) dans le temps. Cette approche n'a pas été suffisamment explorée dans la littérature car sa mise en œuvre est supposée être très difficile. Mais comme expliqué dans cette thèse, le flux de travail peut être facilement implémenté dans un logiciel. Certains logiciels commerciaux l'implémentent déjà mais pas de manière standardisée.

Les résultats peuvent être soumis à une base de données DICOM pour être stockés. Nous avons découvert que la norme DICOM manque de descripteurs obligatoires critiques pour la traçabilité des données dosimétriques. Par conséquent, une base de données DICOM modifiée a été mise en œuvre pour accepter les résultats, appelée IRDBB [GIBAUD 2020]. En conclusion, il est nécessaire de modifier la norme DICOM afin d'inclure tous les descripteurs manquants et les fournisseurs devraient apporter leur soutien à la mise en œuvre de ces descripteurs dans leurs bases de données DICOM. IRDBB peut être utilisé par des logiciels commerciaux comme preuve de concept sur la façon de mettre en œuvre cela.

Nous concluons qu'une approche standardisée dans les flux de travail cliniques permettra d'augmenter la précision de la dosimétrie clinique.

Dans le chapitre 3, un logiciel de dosimétrie à la communauté en tant qu'outil open source a été présenté. Le logiciel, nommé OpenDose3D (OD3D), a été construit comme un module

de 3D-Slicer, reprenant tous les avantages déjà présents. Tous les outils disponibles pour le traitement DICOM, la visualisation d'images, l'enregistrement et la segmentation d'images, ont été utilisés dans le flux de travail du logiciel. En plus de cela, le logiciel :

- Standardise la nomenclature.
- Organise les données.
- Met en œuvre des algorithmes (dépôt local, convolution, Monte Carlo) pour calculer le DDA.
- Extrait les données pertinentes des images (activité dans le VOI ou DDA dans le VOI).
- Implémente l'intégration temporelle avec certaines hypothèses pour l'incorporation (linéaire, constante, exponentielle); pour l'ajustement des données (mono ou multi-exponentielle); et pour le traitement de la queue (par ajustement ou par décroissance physique).
- Implémente le téléchargement des résultats pour la base de données IRDBB.

Par rapport à la dosimétrie standard, nos solutions présentent les avantages suivants :

- Prend en compte implicitement les variations spécifiques des patients sans avoir à corriger un modèle standard.
- Met en œuvre un flux de dosimétrie complet, en commençant par les images reconstruites. Idéalement, les images doivent également être quantitatives, mais cela affecterait également la dosimétrie standard.
- Toutes les étapes sont indépendantes, reproductibles et traçables. Les étapes intermédiaires sont toujours stockées et ne dépendent que des étapes précédentes. Le flux de travail doit être complété à partir de l'étape qui a été répétée/recalculée.
- Le code source est accessible et vérifiable.

Nous concluons que ce logiciel, étant open source et disponible pour la communauté, permet de tester la précision de la dosimétrie entre différents centres. La communauté dispose maintenant d'un outil à utiliser et peut proposer des modifications à l'équipe de développement (OpenDose). Ainsi, il ne sera plus nécessaire de recourir à d'autres solutions universitaires indépendantes et fermées qui ne sont validées que pour des scénarios cliniques spécifiques et ne peuvent être utilisées ailleurs.

Dans le chapitre 4, OD3D a été validé en profondeur. Chaque étape du flux de travail a été testée par rapport à des solutions commerciales dans une approche commune visant à éliminer toutes les variables externes possibles. Nous concluons que :

- La segmentation est mise en œuvre différemment selon les systèmes. Même en utilisant un fichier DICOMRT standardisé, le contenu diffère. Cependant, les fichiers de segmentation peuvent être échangés entre les systèmes avec un traitement supplémentaire. Par conséquent, une normalisation du traitement et du stockage de la segmentation est nécessaire.
- L'enregistrement d'images élimine la nécessité d'une segmentation à chaque point temporel. Cependant, il nécessite la réalisation de mesures anatomiques. Habituellement, le comité d'éthique interdit l'acquisition de plusieurs TDM sur le même patient. Mais, comme une acquisition TDM est nécessaire pour la correction de l'atténuation, elle peut également être utilisée pour le processus d'enregistrement. Il est nécessaire d'adopter une position politique commune, déclarant la nécessité d'une TEMP/TDM quantitative dans tous les cas où elle est requise. Cette étape est essentielle pour adapter la dosimétrie à la radiothérapie interne.
- La quantification de l'activité est fortement affectée par la segmentation et l'enregistrement. Cependant, l'objectif final étant la dose absorbée, l'impact est diminué par la mesure de la masse dans la même VOI.
- L'incertitude de l'activité est élevée pour d'autres raisons, telles que les effets de volume partiel, le temps mort, l'atténuation, la diffusion, la réponse du détecteur, la pénétration septale et les artefacts de mouvement.
- Le calcul de le DDA dans les voxels est en accord avec les solutions commerciales. Par conséquent, la mesure de le DDA présente le même problème d'activité, mais l'incertitude est moindre puisque le processus de convolution élimine la quantification des artefacts de mouvement et du PVE. Le flux de travail DDA a la valeur ajoutée de prendre implicitement en compte la variation de masse dans le VOI.

Nous concluons que le logiciel OD3D a été validé et qu'il est prêt à être utilisé par les utilisateurs pour tester leurs systèmes commerciaux. Fondamentalement, nous considérons OD3D comme un moyen d'étalonnage et de mise en service des logiciels de dosimétrie commerciaux. En comparaison avec la radiothérapie externe, un plan de traitement est réalisé à l'aide de deux logiciels parallèles indépendants. À cet égard, OD3D complète les produits commerciaux plutôt que de les concurrencer.

Dans le chapitre 5, une introduction réussie d'OD3D dans une étude clinique de recherche a été présentée. Un total de 71 patients atteints de cancer de la thyroïde et ayant subi une thyroïdectomie après une post-thérapie par ^{131}I ont été évalués. La dosimétrie a été réalisée et comparée à une solution commerciale. Les résultats sont en accord avec la solution commerciale. Nous concluons que OD3D peut être utilisé pour tester des solutions commerciales dans des environnements cliniques. Cependant, un certificat médical (FDA ou CE) est obligatoire pour rapporter les résultats en pratique clinique. En attendant, OD3D peut être largement utilisé comme outil de recherche.

Ce travail a également contribué à différentes approches comme celle décrite par [KAYAL

2021]. OD3D est utilisé pour créer un modèle de patient de référence afin de réaliser des intercomparaisons cliniques entre différentes équipes sur les mêmes données de patients.

Ce travail a également contribué au développement d'une autre thèse de doctorat à l'université de Messine, qui a été présentée en 2021¹. La thèse évalue OD3D dans le contexte de la radiothérapie interne sélective (SIRT) avec ^{90}Y [PISTONE 2021a].

Dans le cadre de ce travail de doctorat, certaines questions restent encore sans réponse. Nous espérons donc pouvoir y donner suite avec des études que nous développerons. Il s'agit notamment des questions suivantes :

- En raison de la variation de la position de certains organes, il peut parfois être nécessaire de considérer une variation du volume d'intérêt à chaque point de mesure. Le flux de travail d'intégration de le DDA peut gérer ce facteur de manière implicite, mais pour en évaluer les implications, des études supplémentaires doivent être réalisées.
- Des études supplémentaires sont nécessaires pour évaluer tous les avantages du flux de travail DDA par rapport au flux de travail d'activité.

¹https://iris.unime.it/bitstream/11570/3214160/1/Tesi_dottorato_Pistone.pdf

Conclusion and perspectives

In this work the clinical dosimetry workflows were analyzed. The MIRD committee provides a standard calculation framework [BOLCH 2009], but it does not specify all the details required to perform clinical dosimetry in practice. As a result, every clinical center implements each specific step independently.

chapter 1 presented a description of currently available methodologies. A discussion of why a standardization of the clinical workflows, and the dosimetric tools is important. We conclude that the standardization of clinical dosimetric workflows would allow a unique approach for different clinical teams to perform patient specific dosimetry in a common approach.

chapter 2 presented two dosimetric workflows.

- The first by doing integration of the activity in the volumes of interest (VOI). Although this is the classical approach, in our proposition we have added all the details to achieve a common approach starting from the calibration of the equipment, acquisition of the patient images and all required data flow in order to produce a result.
- The second by doing integration of the absorbed dose rates (ADR). This approach has not being explored enough in literature as its implementation is supposed to be very hard. But the workflow can be easily implemented in a software. Some commercial software already implement it but not in a standardized way.

The results can be submitted to a DICOM database to be stored. We discovered that DICOM standard lacks critical mandatory descriptors for dosimetric data traceability. Therefore, a modified DICOM database was implemented to accept the results, named IRDBB [GIBAUD 2020]. As conclusion there is a need for DICOM standard modification, to include all the missing descriptor and there should be a support by vendors to implement these descriptors in their DICOM databases. IRDBB can be used by commercial software as a proof of concept on how to implement this.

We conclude that a standardized approach in the clinical workflows should allow increasing the reproducibility and traceability of clinical dosimetry.

chapter 3 presented a dosimetry software to the community as an open source tool. The software, named OpenDose3D (OD3D) was built as a 3D-Slicer module, taking all the advantages already present. All available tools for DICOM processing, image visualization, image registration and segmentation, were utilized inside the software workflow. On top of that, the software:

- Standardize the nomenclature.

- Organizes the data.
- Implements algorithms (local deposition, convolution, Monte Carlo) to calculate the ADR.
- Extracts the relevant data from images (activity in VOI or ADR in VOI)
- Implements the time integration with some assumptions for incorporation (linear, constant, exponential); for data fit (mono or multi exponential); and for tail processing (by fit or by physical decay).
- Implements the result upload for the IRDBB database.

In respect to the model-based dosimetry, our solutions has the following advantages:

- Takes into account implicitly patient-specific variations without doing corrections to a standard model.
- Implements a full dosimetry workflow, starting with the reconstructed images. Ideally, the images should also be quantitative, but this is also the case for the model-based dosimetry.
- All steps are independent, reproducible and traceable. Intermediate steps are always stored and are dependent only on previous steps. The workflow must be completed starting from the step that was repeated/recalculated.
- The source code is accessible and verifiable.

We conclude that this software, being open source and available for the community, allows testing dosimetry accuracy between different centers/software. The community now has a tool to use and propose modifications to the centralized team (OpenDose). This will remove the need for further independent closed academic solutions that are only validated for specific clinical scenarios and can't be used elsewhere.

chapter 4 presented the benchmark of OD3D. Every workflow step was tested against commercial solutions in a common approach to remove all possible external variables. We conclude that:

- Segmentation is implemented differently in different systems. Even when using a standardized DICOMRT file, the translation by proprietary systems may yield different results. However, the segmentation files should be exchanged between systems, but currently this requires some further processing. Therefore, a standardization in segmentation processing and storage is need.
- Image registration eliminates the need of a segmentation at each time point. However, it requires anatomical measurements to be performed. The ethical committee may forbid

multiple CT acquisition on the same patient. But, since a CT acquisition is needed for attenuation correction, it can also be used for the registration process. There is a need of a common political position, declaring the need of quantitative SPECT/CT in all the cases where they are required. This step is critical to scale the dosimetry to internal radiotherapy.

- Activity quantification is highly affected by segmentation and registration. However, since the final goal is absorbed dose, the impact is diminished by the mass measurement in the same VOI.
- Activity uncertainty is high for other reasons, such as partial volume effects, dead time, attenuation, scatter, detector response, septal penetration and motion artifacts.
- ADR calculation in voxels are in agreement with commercial solutions. Therefore, the measurement of ADR has the same problem as activity, but the uncertainty is lower since the process of convolution eliminates quantification motion artifacts. ADR workflow has the added value of taking implicitly into account the mass variation in the VOI.

We conclude that the OD3D software has been validated, and is ready for users to try it to test their commercial systems. Basically, we consider OD3D as a means to benchmark and commissioning commercial dosimetry software. As comparing with external beam radiotherapy, a treatment plan is done using 2 independent parallel software. In that respect, OD3D complements rather than competes with commercial products.

chapter 5 presented a successful introduction of OD3D into a research clinical study. A total of 71 thyroid cancer patients with thyroidectomy following ^{131}I post-therapy were evaluated. The dosimetry was performed and compared to a model-based solution. Results are in agreement with the model-based solution. We conclude that OD3D can be used to test commercial solutions in clinical environments. However, a medical certificate (FDA or CE) is mandatory to report the results in clinical practice. Meanwhile, OD3D can be extensively used as a research tool.

This work has also contributed to different approaches like the one described by [KAYAL 2021]. OD3D was used to create a reference dataset to perform clinical intercomparisons between different teams on same patient data.

This work has also contributed to the development of another doctoral thesis in the university of Messina, that was presented in year 2021². The thesis evaluates OD3D in the context of selective internal radiotherapy (SIRT) with ^{90}Y [PISTONE 2021a].

In the context of this doctoral work, some questions still remain unanswered, so we hope to be able to follow them up with studies that we will develop. This includes the following:

- Due to the variation in the position of some organs, it may sometimes be necessary to consider a variation in the volume of interest at each measurement point. The ADR

²https://iris.unime.it/bitstream/11570/3214160/1/Tesi_dottorato_Pistone.pdf

integration workflow can handle this factor implicitly, but to assess the implications, further studies shall be performed.

- Further studies are need to assess all the advantages of ADR workflow over activity workflow.

Bibliography

- ABREU, C., L. CARNEGIE PEAKE, J. TAPROGGE, et al. (2021a). “Preliminary results of INSPIRE clinical dosimetry study.” In: *Eur J Nucl Med Mol Imaging* 48 (Suppl 1).1, S1–S648 (cit. on p. 142).
- ABREU, C., L. CARNEGIE-PEAKE, J. TAPROGGE, et al. (Dec. 2021b). “INSPIRE clinical dosimetry study: initial results.” In: *Physica Medica* 92, S88–S89. DOI: 10.1016/s1120-1797(22)00187-9 (cit. on p. 45).
- AGOSTINELLI, S., J. ALLISON, K. AMAKO, et al. (2003). “Geant4a simulation toolkit.” In: *Nuclear Instruments and Methods in Physics Research Section A: Accelerators, Spectrometers, Detectors and Associated Equipment* 506.3, pp. 250–303. DOI: [https://doi.org/10.1016/S0168-9002\(03\)01368-8](https://doi.org/10.1016/S0168-9002(03)01368-8) (cit. on p. 38).
- ALLISON, J., K. AMAKO, J. APOSTOLAKIS, et al. (2006). “Geant4 developments and applications.” In: *IEEE Transactions on Nuclear Science* 53.1, pp. 270–278. DOI: 10.1109/TNS.2006.869826 (cit. on p. 38).
- ALLISON, J., K. AMAKO, J. APOSTOLAKIS, et al. (2016). “Recent developments in Geant4.” In: *Nuclear Instruments and Methods in Physics Research Section A: Accelerators, Spectrometers, Detectors and Associated Equipment* 835, pp. 186–225. DOI: <https://doi.org/10.1016/j.nima.2016.06.125> (cit. on pp. 38, 93).
- ANDERSSON, M., L. JOHANSSON, K. ECKERMAN, et al. (2017). “IDAC-Dose 2.1: an internal dosimetry program for diagnostic nuclear medicine based on the ICRP adult reference voxel phantoms.” In: *European Journal of Nuclear Medicine and Molecular Imaging Research* (cit. on pp. 23, 45, 131, 139, 142, 148, 152, 160, 197, 204, 212).
- ANGER, H. (1958). “Scintillation camera.” In: *Review of scientific instruments* 29.1, pp. 27–33 (cit. on pp. 26, 27, 41).
- BARDIÈS, M. and J. GEAR (Feb. 2021). “Scientific Developments in Imaging and Dosimetry for Molecular Radiotherapy.” In: *Clinical Oncology* 33.2, pp. 117–124. DOI: 10.1016/j.clon.2020.11.005 (cit. on p. 43).
- BERGER, M. (1978). “MIRD Pamphlet No. 2: Energy deposition in water by photons from point isotopic sources.” In: *The Journal of Nuclear Medicine* (cit. on p. 35).
- BIDGOOD, W., S. HORII, F. PRIOR, et al. (May 1997). “Understanding and Using DICOM, the Data Interchange Standard for Biomedical Imaging.” In: *Journal of the American Medical Informatics Association* 4.3, pp. 199–212. DOI: 10.1136/jamia.1997.0040199 (cit. on p. 25).
- BOLCH, W., L. BOUCHET, J. ROBERTSON, et al. (1999). “MIRD Pamphlet No. 17: The Dosimetry of Nonuniform Activity Distributions, Radionuclide S Values at the Voxel Level.” In: *The Journal of Nuclear Medicine* 40.1, 11S–36S (cit. on pp. 33, 34, 36, 37, 96).
- BOLCH, W., K. ECKERMAN, G. SGOUROS, et al. (2009). “MIRD Pamphlet No. 21: A Generalized Schema for Radiopharmaceutical Dosimetry Standardization of Nomenclature.” In: *The Journal of Nuclear Medicine* 50, pp. 477–484. DOI: 10.2967/jnumed.108.056036 (cit. on pp. 16, 18, 167, 171).

- BOTTA, F., A. MAIRANI, G. BATTISTONI, et al. (2012). “Customization of FLUKA Monte Carlo code for dosimetry on PET-CT and SPECT-CT images: Comparison with EGS-based 3D-RD and MCNP5.” In: *Journal of Nuclear Medicine* 53.supplement 1, pp. 1497–1497 (cit. on p. 83).
- BOTTA, F., A. MAIRANI, R. HOBBS, et al. (2013). “Use of the FLUKA Monte Carlo code for 3D patient-specific dosimetry on PET-CT and SPECT-CT images.” In: *Physics in Medicine and Biology* 58.22, pp. 8099–8120 (cit. on p. 83).
- BUSCOMBE, J. and S. NAVALKISSOOR (Aug. 2012). “Molecular radiotherapy.” In: *Clinical Medicine* 12.4, pp. 381–386. DOI: 10.7861/clinmedicine.12-4-381 (cit. on pp. 11, 13).
- CHAUVIN, M., D. BORYS, F. BOTTA, et al. (2020). “OpenDose: open access resources for nuclear medicine dosimetry.” In: *Journal of Nuclear Medicine* 61.7. DOI: 10.2967/jnumed.119.240366 (cit. on pp. 20, 23, 63, 73).
- CONSTANTINO, C. and J. HARRINGTON (1992). “An electron density calibration phantom for CT-based treatment planning computers.” In: *Medical Physics* 19.2, pp. 325–327 (cit. on p. 31).
- CRISTY, M. and K. ECKERMA (1987). “Specific Absorbed Fractions of Energy at Various Ages from Internal Photon Sources.” In: *Oak Ridge National Laboratory ORNL/TM-8381/V1* (cit. on pp. 19, 23).
- CROSS, W., N. FREEDMAN, and P. WONG (1992). *Tables of Beta-Ray dose distribution in water*. Vol. 10521. AECL Research (cit. on pp. 35, 92, 96).
- DAVIDSON, J. (1994). “The Central Limit Theorem, Stochastic Limit Theory.” In: *Oxford Scholarship Online Monographs* (cit. on p. 37).
- DELLA GALA, G., M. BARDIÈS, J. TIPPING, et al. (Dec. 2021). “Overview of commercial treatment planning systems for targeted radionuclide therapy.” In: *Physica Medica* 92, pp. 52–61. DOI: 10.1016/j.ejmp.2021.11.001 (cit. on pp. 46, 48).
- DESBORDES, P., C. PETITJEAN, and S. RUAN (2014). “3D automated lymphoma segmentation in PET images based on cellular automata.” In: *IEEE: Image Processing Theory, Tools and Applications*, pp. 1–6 (cit. on p. 47).
- DESBORDES, P., S. RUAN, R. MODZELEWSKI, et al. (2017). “Predictive value of initial FDG-PET features for treatment response and survival in esophageal cancer patients treated with chemo-radiation therapy using a random forest classifier.” In: *PloS One* 12.3 (cit. on p. 47).
- DEZARN, W., J. CESSNA, L. DEWERD, et al. (2011). “Recommendations of the American Association of Physicists in Medicine on dosimetry, imaging, and quality assurance procedures for ^{90}Y microsphere brachytherapy in the treatment of hepatic malignancies.” In: *Medical Physics* 38.8, pp. 4824–4845 (cit. on p. 99).
- DIEUDONNÉ, A., E. GARIN, S. LAFFONT, et al. (2011). “Clinical Feasibility of Fast 3-Dimensional Dosimetry of the Liver for Treatment Planning of Hepatocellular Carcinoma with ^{90}Y -Microspheres.” In: *The Journal of Nuclear Medicine* 52.12, pp. 1930–1937 (cit. on p. 47).
- DIEUDONNÉ, A., R. HOBBS, W. BOLCH, et al. (2010). “Fine-Resolution Voxel S Values for Constructing Absorbed Dose Distributions at Variable Voxel Size.” In: *The Journal of Nuclear Medicine* 51.10, pp. 1600–1607 (cit. on p. 47).
- DIEUDONNÉ, A., R. HOBBS, R. LEBTAHI, et al. (2013). “Study of the Impact of Tissue Density Heterogeneities on 3-Dimensional Abdominal Dosimetry: Comparison Between Dose Ker-

- nel Convolution and Direct Monte Carlo Methods.” In: *The Journal of Nuclear Medicine* 54.2, pp. 236–243 (cit. on p. 47).
- ECKERMAN, K. and A. ENDO (2008). *MIRD Radionuclide Data and Decay Scheme*. 2nd ed. SNM (cit. on pp. 12, 13, 80).
- FEDOROV, A., R. BEICHEL, J. KALPATHY CRAMER, et al. (2012). “3D-Slicer as an Image Computing Platform for the Quantitative Imaging Network.” In: *Magnetic Resonance Imaging* 30.9, pp. 1323–1341 (cit. on p. 64).
- FERNANDEZ, M., H. HÄNSCHEID, T. MAUXION, et al. (Aug. 2013). “A fast method for rescaling voxel S values for arbitrary voxel sizes in targeted radionuclide therapy from a single Monte Carlo calculation.” In: *Medical physics* 40, p. 082502. DOI: 10.1118/1.4812684 (cit. on p. 116).
- FERRARI, A., P. R. SALA, A. FASSO, et al. (Oct. 2005). “FLUKA: A multi-particle transport code (Program version 2005).” In: DOI: 10.2172/877507 (cit. on p. 38).
- FLEISCHMANN, D. and F. EDWARD BOAS (Jan. 2011). “Computed tomography old ideas and new technology.” In: *European Radiology* 21.3, pp. 510–517. DOI: 10.1007/s00330-011-2056-z (cit. on p. 28).
- FOWLER, J. F., D. K. BEWLEY, R. L. MORGAN, et al. (1963). “Dose-effect relationships for radiation damage to organized tissues.” In: *Nature* 199 (4890), pp. 253–255. DOI: 10.1038/199253A0 (cit. on p. 17).
- FOWLER, J. F. and B. E. STERN (Jan. 1960). “Dose-rate Effects: Some Theoretical and Practical Considerations.” In: <http://dx.doi.org/10.1259/0007-1285-33-390-389> 33, pp. 389–395. DOI: 10.1259/0007-1285-33-390-389 (cit. on p. 17).
- FRANQUIZ, J., S. CHIGURUPATI, and K. KANDAGATLA (2003). “Beta voxel S values for internal emitter dosimetry.” In: *Medical Physics* 30.6, pp. 1030–1032. DOI: 10.1118/1.1573204 (cit. on pp. 36, 37).
- FREY, E. and B. TSUI (1996). “A new method for modeling the spatially-variant, object-dependent scatter response function in SPECT.” In: *1996 IEEE Nuclear Science Symposium. Conference Record 2*, 1082–1086 vol.2 (cit. on p. 98).
- FRIEDLAND, G. and B. THURBER (Dec. 1996). “The birth of CT.” In: *American Journal of Roentgenology* 167.6, pp. 1365–1370. DOI: 10.2214/ajr.167.6.8956560 (cit. on p. 25).
- GARATTINI, S. (Jan. 2007). “Pharmacokinetics in cancer chemotherapy.” In: *European Journal of Cancer* 43 (2), pp. 271–282. DOI: 10.1016/J.EJCA.2006.10.015 (cit. on p. 13).
- GARAVENTA, A., B. DE BERNARDI, E. LANINO, et al. (Feb. 1991). “Treatment of advanced neuroblastoma with i-131 meta-iodobenzylguanidine.” In: *Cancer* 67.4, pp. 922–928. DOI: 10.1002/1097-0142(19910215)67:4<922::aid-cnrcr2820670411>3.0.co;2-d (cit. on p. 12).
- GARDIN, I., M. FDHILA, P. DESBORDES, et al. (2017). “Predictive value of dosimetry indices for treatment response in liver cancer patients treated with yttrium 90 microspheres using a random forest algorithm.” In: *The Journal of Nuclear Medicine* 58.1, p. 197 (cit. on p. 47).
- GARIN, E., X. PALARD, and Y. ROLLAND (June 2020). “Personalised Dosimetry in Radioembolisation for HCC: Impact on Clinical Outcome and on Trial Design.” In: 12.6, p. 1557. DOI: 10.3390/cancers12061557 (cit. on p. 25).

- GIAP, H., D. MACEY, J. BAYOUTH, et al. (1995). "Validation of a dose-point kernel convolution technique for internal dosimetry." In: *Phys. Med. Biol.* 40, pp. 365–381 (cit. on p. 35).
- GIBAUD, B. (2008). "The DICOM standard : a brief overview." In: *Molecular imaging: Computer reconstruction and practice*. Ed. by C. A. (LEMOIGNE YVES. NATO Science for Peace and Security Series. Springer, pp. 229–238 (cit. on p. 25).
- GIBAUD, B., M. BRENET, G. PASQUIER, et al. (2020). "A semantic database for integrated management of image and dosimetric data in low radiation dose research in medical imaging." In: *AMIA 2020 Annual Symposium* 3409134 (cit. on pp. 49, 50, 89, 167, 171).
- GLATTING, G., M. LANDMANN, T. KULL, et al. (Aug. 2005). "Internal radionuclide therapy: The ULMDOS software for treatment planning." In: *Medical physics* 32, pp. 2399–405. DOI: 10.1118/1.1945348 (cit. on p. 45).
- GLEISNER, K. S., E. SPEZI, P. SOLNY, et al. (Dec. 2017). "Variations in the practice of molecular radiotherapy and implementation of dosimetry: results from a European survey." In: *EJNMMI Physics* 4.1. DOI: 10.1186/s40658-017-0193-4 (cit. on p. 41).
- GOORLEY, T., M. JAMES, T. BOOTH, et al. (Dec. 2012). "Initial MCNP6 release overview. MCNP6 version 0.1." In: *Nuclear technology* 180, pp. 298–315. DOI: 10.13182/NT11-135 (cit. on p. 38).
- GORDON, R., R. BENDER, and G. HERMAN (Dec. 1970). "Algebraic Reconstruction Techniques (ART) for three-dimensional electron microscopy and X-ray photography." In: *Journal of Theoretical Biology* 29.3, pp. 471–481. DOI: 10.1016/0022-5193(70)90109-8 (cit. on p. 28).
- GRAVES, S., R. FLYNN, and D. HYER (2019). "Dose point kernels for 2,174 radionuclides." In: *Medical Physics* 46.11, pp. 5284–5293. DOI: <https://doi.org/10.1002/mp.13789>. eprint: <https://aapm.onlinelibrary.wiley.com/doi/pdf/10.1002/mp.13789> (cit. on pp. 93–95).
- HERTZ, S. and A. ROBERTS (1946). "Radioactive iodine in the study of thyroid physiology: VII The use of radioactive iodine therapy in hyperthyroidism." In: *Journal of american medical association* 131.2, pp. 81–86 (cit. on p. 12).
- HILL, R., B. HEALY, L. HOLLOWAY, et al. (Feb. 2014). "Advances in kilovoltage x-ray beam dosimetry." In: *Physics in Medicine and Biology* 59.6, R183–R231. DOI: 10.1088/0031-9155/59/6/r183 (cit. on p. 10).
- HIPPELÄINEN, E., M. TENHUNEN, H. MÄENPÄÄ, et al. (2016). "Quantitative accuracy of ¹⁷⁷Lu SPECT reconstruction using different compensation methods: phantom and patient studies." In: *European Journal of Nuclear Medicine and Molecular Imaging Research* 6, p. 16 (cit. on p. 46).
- HIPPELÄINEN, E., M. TENHUNEN, H. MÄENPÄÄ, et al. (Mar. 2017). "Dosimetry software Hermes Internal Radiation Dosimetry: From quantitative image reconstruction to voxel-level absorbed dose distribution." In: *Nuclear Medicine Communications* 38, p. 1. DOI: 10.1097/MNM.0000000000000662 (cit. on p. 46).
- HÖLLRIEGL, V., N. PETOUSSI-HENSS, K. HÜRKAMP, et al. (June 2021). "Radiopharmacokinetic modelling and radiation dose assessment of ²²³Ra used for treatment of metastatic castration-resistant prostate cancer." In: *EJNMMI Physics* 8.1. DOI: 10.1186/s40658-021-00388-1 (cit. on p. 12).

- HOUNSFIELD, G. (1980). “Computed Medical Imaging.” In: *Journal of Computer Assisted Tomography* 4.5, pp. 665–674. DOI: 10.1097/00004728-198010000-00017 (cit. on pp. 26, 31).
- HUDSON, H. and R. LARKIN (1994). “Accelerated image reconstruction using ordered subsets of projection data.” In: *IEEE Transactions on Medical Imaging* 13.4, pp. 601–609. DOI: 10.1109/42.363108 (cit. on p. 29).
- HWANG, A., B. FRANC, G. GULLBERG, et al. (2008). “Assessment of the sources of error affecting the quantitative accuracy of SPECT imaging in small animals.” In: *Physics in Medicine and Biology* 53.9, p. 2233 (cit. on p. 30).
- IAEA (2009). *Quality Assurance for SPECT Systems*. Human Health Series 6. Vienna: INTERNATIONAL ATOMIC ENERGY AGENCY (cit. on pp. 30, 32).
- (2015). *Nuclear Medicine Physics*. Non-serial Publications. Vienna: INTERNATIONAL ATOMIC ENERGY AGENCY (cit. on p. 11).
- ICRP10 (1968). “Recommendations of the International Commission on Radiological Protection. ICRP Publication 10.” In: *Ann. ICRP* (cit. on p. 16).
- ICRP103 (2007). “Recommendations of the International Commission on Radiological Protection. ICRP Publication 103.” In: *Ann. ICRP* 37.2-4 (cit. on pp. 23, 131, 138, 141, 147, 152, 159, 196, 203, 211).
- ICRP107 (2008). “Nuclear Decay Data for Dosimetric Calculations. ICRP Publication 107.” In: *Ann. ICRP* 38.3 (cit. on p. 23).
- ICRP110 (2009). “Adult Reference Computational Phantoms. ICRP Publication 110.” In: *Ann. ICRP* 39.2 (cit. on pp. 19, 23).
- ICRP133 (2016). “The ICRP Computational Framework for Internal Dose Assessment for Reference Adults: Specific Absorbed Fractions. ICRP Publication 133.” In: *Ann. ICRP* 45.2 (cit. on pp. 19, 23).
- ICRP145 (2020). “Adult mesh-type reference computational phantoms. ICRP Publication 145.” In: *Ann. ICRP* 49.3 (cit. on p. 20).
- ICRP17 (1969). “Protection of the Patient in Radionuclide Investigations. ICRP Publication 17.” In: *Ann. ICRP* (cit. on p. 16).
- ICRP2 (1959). “Recommendations of the International Commission on Radiological Protection. ICRP Publication 2.” In: *Ann. ICRP* (cit. on pp. 16, 19).
- ICRP23 (1975). “Report of the Task Group on Reference Man. ICRP Publication 23.” In: *Ann. ICRP* (cit. on p. 19).
- ICRP30 (1979). “Limits for Intakes of Radionuclides by Workers. ICRP Publication 30.” In: *Ann. ICRP* (cit. on pp. 13, 19).
- ICRP60 (1990). “Recommendations of the International Commission on Radiological Protection. ICRP Publication 60.” In: *Ann. ICRP* 21.1-3 (cit. on pp. 16, 23, 131, 137, 141, 146, 152, 158, 195, 202, 210).
- ICRP68 (1994). “Dose Coefficients for Intakes of Radionuclides by Workers. ICRP Publication 68.” In: *Ann. ICRP* 24.4 (cit. on pp. 13, 19).
- ICRU REPORT 10A (1962). *Radiation Quantities and Units*. National Bureau of Standards, USA: International Commission on Radiological Units and Measurements (ICRU) (cit. on p. 15).

- INTERNATIONAL ATOMIC ENERGY AGENCY (2018). *IAEA-NMQC Toolkit*. URL: <https://humanhealth.iaea.org/HHW/MedicalPhysics/NuclearMedicine/QualityAssurance/NMQC-Plugins/index.html> (visited on 07/10/2020) (cit. on p. 32).
- JAN, S., G. SANTIN, D. STRUL, et al. (Oct. 2004). “GATE: a simulation toolkit for PET and SPECT.” In: *Physics in medicine and biology* 49 (19), pp. 4543–4561. DOI: 10.1088/0031-9155/49/19/007 (cit. on p. 38).
- JANICKI, C. and J. SEUNTJENS (2004). “Determination of dose-point-kernel functions close to the source.” In: *Medical Physics* 31.4, pp. 814–818. DOI: 10.1118/1.1668393 (cit. on p. 92).
- KAO, Y., J. STEINBERG, Y. TAY, et al. (2013). “Post-radioembolization yttrium-90 PET/CT - part 1: diagnostic reporting.” In: *EJNMMI Res* 56.3. DOI: 10.1186/2191-219X-3-56 (cit. on p. 13).
- KAWRAKOW, I., D. ROGERS, E. MAINEGRA-HING, et al. (2020). *EGSnrc toolkit for Monte Carlo simulation of ionizing radiation transport*. doi:10.4224/40001303 [release v2020] (cit. on p. 38).
- KAYAL, G., M. CHAUVIN, A. VERGARA GIL, et al. (May 2021). “Generation of clinical ^{177}Lu SPECT/CT images based on Monte Carlo simulation with GATE.” In: *Physica Medica* 85, pp. 24–31. DOI: 10.1016/j.ejmp.2021.04.002 (cit. on pp. 169, 173).
- KESNER, A., E. OLGUIN, P. ZANZONICO, et al. (2018). “MIRDCalc V 1.0 - A community spreadsheet tool for organ-level radiopharmaceutical absorbed dose calculations.” In: *Journal of Nuclear Medicine* 59.supplement 1, pp. 473–473. eprint: <https://jnm.snmjournals.org/content> (cit. on pp. 23, 45).
- KHALIL, M., J. TREMOLEDA, T. BAYOMY, et al. (2011). “Molecular SPECT Imaging: An Overview.” In: *International Journal of Molecular Imaging* 2011, p. 15. DOI: 10.1155/2011/796025 (cit. on pp. 27, 30, 34).
- KIM, Y., Y. KIM, S. UM, et al. (2011). “Usefulness of Bremsstrahlung Images after Intra-arterial Y-90 Resin Microsphere Radioembolization for Hepatic Tumors.” In: *Nucl Med Mol Imaging* 45.1, pp. 59–67. DOI: 10.1007/s13139-010-0066-4 (cit. on p. 13).
- KLETTING, P., S. SCHIMMEL, H. HÄNSCHEID, et al. (Sept. 2015). “The NUKDOS software for treatment planning in molecular radiotherapy.” In: *Zeitschrift für Medizinische Physik* 25.3, pp. 264–274. DOI: 10.1016/j.zemedi.2015.01.001 (cit. on p. 46).
- KWEKKEBOOM, D., J. TEUNISSEN, W. BAKKER, et al. (2005). “Radiolabeled Somatostatin Analog [^{177}Lu -DOTA0,Tyr3]octreotate in Patients With Endocrine Gastroenteropancreatic Tumors.” In: *J Clin Oncol* 23.12, pp. 2754–2762. DOI: 10.1200/JCO.2005.08.066 (cit. on p. 12).
- KYKER, C., M. CHRISTOPHERSON, F. BERG, et al. (1956). “Selective irradiation of Lymph Nodes by radioluthetium (Lu-177).” In: *Cancer* 9, pp. 489–498 (cit. on p. 12).
- LANCONELLI, N., M. PACILIO, S. LO MEO, et al. (2003). “A free database of radionuclide voxel S values for the dosimetry of nonuniform activity distributions.” In: *Medical Physics* 30.6, pp. 1030–1032. DOI: 10.1118/1.1573204 (cit. on pp. 36, 96, 116).
- LANGE, K., M. BAHN, and R. LITTLE (June 1987). “A Theoretical Study of Some Maximum Likelihood Algorithms for Emission and Transmission Tomography.” In: *IEEE Transactions on Medical Imaging* 6.2, pp. 106–114. DOI: 10.1109/tmi.1987.4307810 (cit. on p. 29).

- LEEK, F., J. TAPROGGE, R. GREGORY, et al. (2019). “The MEDIRAD multi-national I-131 dosimetry study for thyroid ablation and adjuvant therapy: current status.” In: *European Journal of Nuclear Medicine and Molecular Imaging* 46.Suppl 1, S194–S195 (cit. on p. 50).
- LEVKOVILZ, R., D. FALIKMAN, M. ZIBULEVSKY, et al. (July 2001). “The design and implementation of COSEN, an iterative algorithm for fully 3-D listmode data.” In: *IEEE Transactions on Medical Imaging* 20.7, pp. 633–642. DOI: 10.1109/42.932747 (cit. on p. 29).
- LJUNGBERG, M. and S. STRAND (1989). “A Monte Carlo program for the simulation of scintillation camera characteristics.” In: *Computer Methods and Programs in Biomedicine* 29.4, pp. 257–272 (cit. on p. 98).
- LOEVINGER, R. and M. BERMAN (1976). “MIRD Pamphlet No. 1 Revised: A Revised Schema for Calculating the Absorbed Dose from Biologically Distributed Radionuclides.” In: *The Journal of Nuclear Medicine* (cit. on pp. 16, 24).
- MAIGNE, L., Y. PERROT, D. SCHAART, et al. (Feb. 2011). “Comparison of GATE/GEANT4 with EGSnrc and MCNP for electron dose calculations at energies between 15 keV and 20 MeV.” In: *Physics in medicine and biology* 56, pp. 811–27. DOI: 10.1088/0031-9155/56/3/017 (cit. on p. 93).
- MARCATILI, S. (Oct. 2015). “Multi-scale dosimetry for targeted radionuclide therapy optimisation.” PhD thesis. Universite de Toulouse 3 Paul Sabatier (cit. on p. 25).
- MARWAHA, G., R. MACKLIS, A. SINGH, et al. (2013). “Brachytherapy.” In: *Ophthalmic Radiation Therapy*. S. KARGER AG, pp. 29–35. DOI: 10.1159/000351053 (cit. on p. 11).
- MATSUNARI, I., G. BÖNING, S. ZIEGLER, et al. (1998). “Effects of Misalignment Between Transmission and Emission Scans on Attenuation-Corrected Cardiac SPECT.” In: *Journal of Nuclear Medicine* 39 (3) (cit. on p. 55).
- McKAY, E. and A. MALARODA (2018). “OpenDose: an extensible, open-source internal dosimetry calculator.” In: *Australasian Physical and Engineering Sciences in Medicine Engineering and Physical Sciences in Medicine*, p. 103 (cit. on pp. 24, 45).
- MEIJERING, E. H., W. J. NIESSEN, J. P. PLUIM, et al. (1999). “Quantitative Comparison of Sinc-Approximating Kernels for Medical Image Interpolation.” In: *Lecture Notes in Computer Science (including subseries Lecture Notes in Artificial Intelligence and Lecture Notes in Bioinformatics)* 1679, pp. 210–217. DOI: 10.1007/10704282_23 (cit. on pp. 67, 68).
- MILANO, A., A. VERGARA GIL, E. FABRIZI, et al. (Feb. 2021). “In Silico Validation of MCID Platform for Monte Carlo-Based Voxel Dosimetry Applied to ⁹⁰Y-Radioembolization of Liver Malignancies.” In: *Applied Sciences* 11.4, p. 1939. DOI: 10.3390/app11041939 (cit. on pp. 83, 98).
- MORA, E. (Mar. 2019). “Radiopharmaceutical dosimetry in targeted radionuclide therapy.” PhD thesis. Universite de Toulouse 3 Paul Sabatier (cit. on pp. 19, 46).
- PACILIO, M., E. AMATO, N. LANCONELLI, et al. (Mar. 2015). “Differences in 3D dose distributions due to calculation method of voxel S-values and the influence of image blurring in SPECT.” In: *Physics in medicine and biology*. DOI: 10.1088/0031-9155/60/5/1945 (cit. on p. 81).
- PAPADIMITROULAS, P., G. LOUDOS, G. NIKIFORIDIS, et al. (2012). “A dose point kernel database using GATE Monte Carlo simulation toolkit for nuclear medicine applications:

- Comparison with other Monte Carlo codes.” In: *Medical Physics* 39.8, pp. 5238–5247. DOI: 10.1118/1.4737096 (cit. on pp. 92–95).
- PASCIAK, A., A. BOURGEOIS, and Y. BRADLEY (2014). “A Comparison of Techniques for 90Y PET/CT Image-Based Dosimetry Following Radioembolization with Resin Microspheres.” In: *Frontiers in Oncology* 4.3, pp. 1–10 (cit. on p. 47).
- PETOUSSI HENSS, N., W. BOLCH, M. ZANKL, et al. (2007). “Patient-specific scaling of reference S-values for cross-organ radionuclide S-values: what is appropriate?” In: *Radiation Protection Dosimetry* 127.1-4, pp. 192–196. DOI: 10.1093/rpd/ncm270 (cit. on p. 24).
- PISTONE, D., A. CAMPENNI, A. ITALIANO, et al. (Dec. 2021a). “Internal dosimetry Monte Carlo study of TARE treatments: a comparison between GATE and GAMOS focused on lung dosimetry and background correction.” In: *Physica Medica* 92, S127. DOI: 10.1016/S1120-1797(22)00271-X (cit. on pp. 170, 173).
- PISTONE, D., A. ITALIANO, L. AUDITORE, et al. (2021b). “GATE Monte Carlo dosimetry in 90 Y TARE planning: influence of simulation parameters and image resampling on dosimetric accuracy and optimization of computational times.” In: *Atti della Accademia Peloritana dei Pericolanti - Classe di Scienze Fisiche, Matematiche e Naturali* 99.2, p. 4. DOI: 10.1478/AAPP.992A4 (cit. on p. 66).
- PÖPPERL, G., T. HELMBERGER, W. MÜNZING, et al. (2005). “Selective internal radiation therapy with sir-spheres in patients with nonresectable liver tumors.” In: *Cancer Biotherapy and Radiopharmaceuticals* 20.2, pp. 200–208 (cit. on pp. 11, 13).
- RIDIC (June 2000). “MIRDOSE 3 distribution suspended. Radiation Internal Dose Information Center.” en. In: *J. Nucl. Med.* 41.6, 13N–14N, 19N (cit. on p. 23).
- SANCHEZ-CRESPO, A., P. ANDREO, and S. LARSSON (2004). “Positron flight in human tissues and its influence on PET image spatial resolution.” In: *European journal of nuclear medicine and molecular imaging* 31.1, pp. 44–51 (cit. on p. 30).
- SARRUT, D., M. BARDIÈS, N. BOUSSION, et al. (2014). “A review of the use and potential of the GATE Monte Carlo simulation code for radiation therapy and dosimetry applications.” In: *Medical Physics* 41.6. DOI: 10.1118/1.4871617 (cit. on pp. 38, 81, 83).
- SAWIN, C. T. and D. V. BECKER (Apr. 1997). “Radioiodine and the Treatment of Hyperthyroidism: The Early History *.” In: *Thyroid* 7.2, pp. 163–176. DOI: 10.1089/thy.1997.7.163 (cit. on p. 16).
- SCHMIDT, M., B. HERO, and T. SIMON (Mar. 2016). “I-131-mIBG therapy in neuroblastoma: established role and prospective applications.” In: *Clinical and Translational Imaging* 4.2, pp. 87–101. DOI: 10.1007/s40336-016-0173-z (cit. on p. 12).
- SCHNEIDER, U., E. PEDRONI, and A. LOMAX (1996). “The calibration of CT Hounsfield units for radiotherapy treatment planning.” In: *Physics in Medicine and Biology* 41, pp. 111–124 (cit. on pp. 54, 55, 130, 140).
- SJOGREEN GLEISNER, K., M. LJUNGBERG, K. WINGÅRDH, et al. (Mar. 2005). “The LundA-Dose Method for Planar Image Activity Quantification and Absorbed-Dose Assessment in Radionuclide Therapy.” In: *Cancer biotherapy and radiopharmaceuticals* 20, pp. 92–7. DOI: 10.1089/cbr.2005.20.92 (cit. on p. 46).
- SONG, H., B. HE, A. PRIDEAUX, et al. (2006). “Lung Dosimetry for Radioiodine Treatment Planning in the Case of Diffuse Lung Metastases.” In: *Journal of Nuclear Medicine* 47.12,

- pp. 1985–1994. eprint: <https://jnm.snmjournals.org/content/47/12/1985.full.pdf> (cit. on p. 45).
- STABIN, M. (1996). “MIRDOSE: personal computer software for internal dose assessment in nuclear medicine.” In: *Journal of nuclear medicine : official publication, Society of Nuclear Medicine* 37 3, pp. 538–46 (cit. on pp. 23, 45).
- STABIN, M. and A. FARMER (2012). “OLINDA/EXM 2.0: The new generation dosimetry modeling code.” In: *The Journal of Nuclear Medicine* 53.1, p. 585 (cit. on p. 46).
- STABIN, M. and J. SIEGEL (2018). “RADAR dose estimate report: a compendium of radio-pharmaceutical dose estimates based on OLINDA/EXM version 2.0.” In: *The Journal of Nuclear Medicine* 59, pp. 154–160 (cit. on pp. 23, 45).
- STABIN, M., R. SPARKS, and E. CROWE (2005). “OLINDA/EXM: The second generation personal computer software for internal dose assessment in Nuclear Medicine.” In: *The Journal of Nuclear Medicine* 46.6, pp. 1023–1027 (cit. on pp. 23, 45, 99).
- STABIN, M. and X. XU (May 2014). “Basic Principles in the Radiation Dosimetry of Nuclear Medicine.” In: *Seminars in Nuclear Medicine* 44.3, pp. 162–171. DOI: 10.1053/j.semnuclmed.2014.03.008 (cit. on p. 24).
- STABIN, M. (2004). “New Internal Radiation Dose and Modeling Software; FDA Approves Commercial MIRDOSE Successor.” In: *Journal of Nuclear Medicine* 45 (11) (cit. on p. 23).
- STABIN, M. G., M. T. MADSEN, and H. ZAIDI (Nov. 2019). “Personalized dosimetry is a must for appropriate molecular radiotherapy.” In: *Med Phys* 46 (11), pp. 4713–4716. DOI: 10.1002/mp.13820 (cit. on p. 25).
- STELSON, A., E. WATSON, and R. CLOUTIER (Nov. 1995). “A History of Medical Internal Dosimetry.” In: *Health Physics* 69.5, pp. 766–782. DOI: 10.1097/00004032-199511000-00011 (cit. on p. 10).
- STILLER, W. (Dec. 2018). “Basics of iterative reconstruction methods in computed tomography: A vendor-independent overview.” In: *European Journal of Radiology* 109, pp. 147–154. DOI: 10.1016/j.ejrad.2018.10.025 (cit. on pp. 28, 29).
- STOKKE, C., P. M. GABIÑA, P. SOLNÝ, et al. (Nov. 2017). “Dosimetry-based treatment planning for molecular radiotherapy: a summary of the 2017 report from the Internal Dosimetry Task Force.” In: *EJNMMI Physics* 4.1. DOI: 10.1186/s40658-017-0194-3 (cit. on p. 16).
- STRIGARI, L., M. KONIJNENBERG, C. CHIESA, et al. (June 2014). “The evidence base for the use of internal dosimetry in the clinical practice of molecular radiotherapy.” In: 41.10, pp. 1976–1988. DOI: 10.1007/s00259-014-2824-5 (cit. on p. 17).
- TRANDEL, J. (Mar. 2019). “Apport de l’imagerie multimodale dans la caractérisation de la distribution de sources radioactives de ^{166}Ho dans un contexte de dosimétrie en microcuriethérapie.” PhD thesis. Université de Toulouse 3 Paul Sabatier (cit. on p. 93).
- URSO, R., P. BLARDI, and G. GIORGI (2002). “A short introduction to pharmacokinetics.” In: *Eur Rev Med Pharmacol Sci* 6.2, pp. 33–44 (cit. on pp. 13, 14).
- VAN GILS, C., C. BEIJST, R. VAN ROOIJ, et al. (2016). “Impact of reconstruction parameters on quantitative I-131 SPECT.” In: *Physics in Medicine and Biology* 61.14, pp. 5166–5182 (cit. on p. 30).
- VERA, P., R. MODZELEWSKI, S. HAPDEY, et al. (2013). “Does enhanced CT influence the biological GTV measurement on FDG-PET images?” In: *Radiotherapy and Oncology* 108.1, pp. 86–90 (cit. on p. 47).

- VERGARA GIL, A., E. AMATO, L. AUDITORE, et al. (2020). “OpenDose3D: A free, collaborative 3D-Slicer module for patient-specific dosimetry.” In: *European Journal of Nuclear Medicine and Molecular Imaging* 47.SUPPL 1, S314–S315 (cit. on p. 73).
- VERGARA GIL, A., M. CHAUVIN, G. KAYAL, et al. (2019a). “Geant4/GATE ion source implementation for internal dosimetry applications.” In: *European Journal of Nuclear Medicine and Molecular Imaging* 46.Suppl 1, S365 (cit. on pp. 83, 92).
- VERGARA GIL, A., E. MORA RAMIREZ, J. POUGET, et al. (2019b). “Fast heterogeneous convolution algorithm used in absorbed dose calculation for beta emitters.” In: *European Journal of Nuclear Medicine and Molecular Imaging* 46.Suppl 1, S473–S474 (cit. on p. 82).
- WARKENTIN, B., P. STAVREV, N. STAVREVA, et al. (2004). “A TCP-NTCP estimation module using DVHs and known radiobiological models and parameter sets.” In: *Journal of Applied Medical Physics* 5.1, pp. 50–63 (cit. on p. 17).
- WESSELS, B., M. KONIJNENBERG, R. DALE, et al. (Oct. 2008). “MIRD Pamphlet No. 20: The Effect of Model Assumptions on Kidney Dosimetry and Response Implications for Radionuclide Therapy.” In: *Journal of Nuclear Medicine* 49.11, pp. 1884–1899. DOI: 10.2967/jnumed.108.053173 (cit. on p. 17).
- WILLEMINK, M. and P. NOËL (Oct. 2018). “The evolution of image reconstruction for CT from filtered back projection to artificial intelligence.” In: *European Radiology* 29.5, pp. 2185–2195. DOI: 10.1007/s00330-018-5810-7 (cit. on p. 28).
- WISEMAN, G., C. WHITE, M. STABIN, et al. (2000). “Phase I/II 90Y-Zevalin (yttrium-90 Ibritumomab Tiuxetan, IDEC-Y2B8) Radioimmunotherapy Dosimetry Results in Relapsed or Refractory non-Hodgkin Lymphoma.” In: *Eur J Nucl Med* 27.7, pp. 766–777. DOI: 10.1007/s002590000276 (cit. on p. 13).
- WOLLNER, I., C. KNUITSEN, P. SMITH, et al. (1988). “Effects of hepatic arterial yttrium 90 glass microspheres in dogs.” In: *Cancer* 61.7, pp. 1336–1344 (cit. on pp. 11, 13).
- YANG, N., S. YAO, and D. LIU (2018). “Tumor necrosis factor-related apoptosis-induced ligand additive with iodine-131 of inhibits non-small cell lung cancer cells through promoting apoptosis.” In: *Oncology Letters* 16.1, pp. 276–284 (cit. on p. 12).
- ZUBAL, I., C. HARRELL, E. SMITH, et al. (2000). “1 Two dedicated software, voxel-based, anthropomorphic (torso and head) phantoms.” In: (cit. on p. 19).

Appendix to Chapter 2

A.1 DICOM header data required for CDW

In the case of DICOM management, the relevant data, extracted from headers and mandatory for CDW implementation, are presented in Table A.1

DICOM Tag	Description	Observations
(0020, 000d)	Study Instance UID	
(0020, 000e)	Series Instance UID	
(0010, 0010)	Patient Name	Must be anonymized
(0010, 0020)	Patient ID	
(0008, 0020)	Study Date	
(0008, 0060)	Modality	
(0008, 002A)	Acquisition Date Time	
(0008, 0022)	Acquisition Time	Alternative
(0008, 0032)	Acquisition Date	Alternative
(0018, 1242)	Actual Frame Duration (Tframe)	
(0054, 0053)	Number Of Frames In Rotation (Nframes)	Default 1 for PET
(0018, 1150)	Acquisition Duration T_{acq}	depending on vendor
(0043, 104E)	Acquisition Duration T_{acq}	depending on vendor
(0018, 1078)	Injection Date Time	
(0018, 107)	Injection Time	
(0018, 1074)	Injected Activity	
(0018, 0031)	Radiopharmaceutical	

Table A.1: List of mandatory DICOM tags extracted from image headers

The acquisition duration (T_{acq}) is derived from the extracted tags, and calculated depending on modality:

- For NM and PT: $T_{acq} = T_{frame} \cdot N_{frames}$

- For CT: Extracted directly from header.

There are also some more data, not mandatory for CDW, but used for traceability and reproducibility. Table A.2 presents the relevant tags extracted. In this case the traceability assures that the patient data is processed the same way as the calibration acquisitions.

DICOM Tag	Description
(0018,1077)	Radiopharmaceutical Specific Activity
(0018,1078)	Radiopharmaceutical Start DateTime
(0018,1079)	Radiopharmaceutical Stop DateTime
(0018,9314)	CT Reconstruction Sequence
(0018,9315)	Reconstruction Algorithm
(0018,9749)	PET Reconstruction Sequence
(0018,9755)	Time of Flight Information Used
(0018,9756)	Reconstruction Type
(0018,9758)	Decay Corrected
(0018,9759)	Attenuation Corrected
(0018,9760)	Scatter Corrected
(0018,9761)	Dead Time Corrected
(0018,9762)	Gantry Motion Corrected
(0018,9763)	Patient Motion Corrected
(0018,9764)	Count Loss Normalization Corrected
(0018,9765)	Randoms Corrected
(0018,9766)	Non-uniform Radial Sampling Corrected
(0018,9767)	Sensitivity Calibrated
(0018,9768)	Detector Normalization Correction
(0018,9769)	Iterative Reconstruction Method
(0018,9770)	Attenuation Correction Temporal Relationship
(0054,1101)	Attenuation Correction Method
(0054,1102)	Decay Correction
(0054,1103)	Reconstruction Method
(0054,1104)	Detector Lines of Response Used
(0054,1105)	Scatter Correction Method
(0033, 1038)	Siemens factor (fS)
(0040, 9224)	Hermes Intercept (AH)
(0040, 9225)	Hermes Slope (BH)

Table A.2: List of non-mandatory DICOM tags extracted from image headers. For Hermes images, the volume data (VD) of the respective volume must be converted to real data: $RWD = AH + BH \cdot VD$. For Siemens images, the volume data (VD) shall be divided by the Siemens factor fS: $RWD = \frac{VD}{fS}$

Appendix to Chapter 3

B.1 Required DICOM fields

The list of required DICOM fields is:

- (0x0020, 0x000d) - Study Instance UID
- (0x0020, 0x000e) - Series Instance UID
- (0x0010, 0x0010) - Patient Name
- (0x0010, 0x0020) - Patient ID
- (0x0008, 0x0020) - Study Date
- (0x0008, 0x0060) - Modality
- (0x0008, 0x002A) - Acquisition Date Time
 - Alternatives (the missing data must be added)
 - * (0x0008, 0x0022) - Acquisition Time
 - * (0x0008, 0x0032) - Acquisition Date
- Acquisition duration (T_{acq}), calculated depending on modality
 - For NM and PT: $T_{acq} = T_{frame} \cdot N_{frames}$
 - * (0x0018, 0x1242) - Actual Frame Duration (T_{frame}) in root tag or inside (0x0054, 0x0052) - Rotation Information Sequence
 - * (0x0054, 0x0053) - Number Of Frames In Rotation (N_{frames}) in root tag or inside (0x0054, 0x0052) - Rotation Information Sequence. This is 1 by default for PT.
 - for CT, depending on vendor:
 - * (0x0018, 0x1150) - Acquisition Duration
 - * (0x0043, 0x104e) - Acquisition Duration
- (0x0018, 0x1078) - Injection Date Time in root tag or inside (0x0054, 0x0016) - Radio-pharmaceutical Information Sequence

- Alternative (the missing data must be added)
 - * (0x0018, 0x107) - Injection Time in root tag or inside (0x0054, 0x0016) - Radiopharmaceutical Information Sequence
- (0x0018, 0x1074) - Injected Activity in root tag or inside (0x0054, 0x0016) - Radiopharmaceutical Information Sequence
- (0x0018, 0x1031) - Radiopharmaceutical in root tag or located inside one of these locations
 - (0x0054, 0x0016) - Radiopharmaceutical Information Sequence
 - (0x0054, 0x0300) - Radionuclide Code Sequence
 - (0x0054, 0x0304) - Radiopharmaceutical Code Sequence
- Other camera specific factors:
 - (0x0033, 0x1038) - Siemens factor, shall be divided by the corresponding volume
 - (0x0040, 0x9096) - Real World Value Mapping Sequence used by Hermes to store:
 - * (0x0040, 0x9224) - Hermes Intercept (A_H)
 - * (0x0040, 0x9225) - Hermes Slope (B_H)
 - * The volume data (V_D) of the respective volume must be converted to real data
 $RWD = A_H + B_H \cdot V_D$

Appendix to Chapter 5

C.1 RMH data tables

Patient	Mass (kg)							
	Body FOV	Left Lung	Right Lung	Bones FOV	Salivary Glands	Neck	Remainder	Total Body
RMH-001	2.03E+01	2.22E-01	3.62E-01	1.69E+00	4.26E-02	3.28E-02	7.36E+01	7.60E+01
RMH-002	1.54E+01	3.41E-01	3.81E-01	1.91E+00	3.33E-02	3.33E-02	6.06E+01	6.33E+01
RMH-003	1.79E+01	1.98E-01	2.84E-01	1.59E+00	9.27E-03	1.51E-02	7.09E+01	7.30E+01
RMH-004	1.38E+01	2.73E-01	2.95E-01	1.95E+00	1.24E-02	1.49E-02	5.57E+01	5.83E+01
RMH-005	2.13E+01	1.63E-01	2.09E-01	2.03E+00	7.12E-03	7.01E-03	8.74E+01	8.98E+01
RMH-006	1.40E+01	2.95E-01	3.54E-01	2.12E+00	4.08E-02	3.98E-02	5.81E+01	6.10E+01
RMH-007	1.32E+01	1.92E-01	2.29E-01	1.32E+00	1.87E-02	8.60E-03	5.26E+01	5.44E+01
RMH-008	1.51E+01	2.11E-01	2.60E-01	2.02E+00	6.82E-03	5.01E-02	5.62E+01	5.88E+01
RMH-009	1.54E+01	4.09E-01	4.84E-01	2.02E+00	3.26E-02	1.31E-02	6.99E+01	7.29E+01
RMH-010	1.81E+01	1.67E-01	2.13E-01	1.44E+00	2.76E-02	6.23E-03	5.90E+01	6.09E+01
RMH-011	9.98E+00	3.53E-01	2.89E-01	1.56E+00	8.57E-02	3.25E-02	5.72E+01	6.02E+01
RMH-012	1.54E+01	1.45E-01	1.97E-01	1.42E+00	5.69E-02	2.71E-03	4.57E+01	4.75E+01
RMH-013	1.58E+01	1.95E-01	2.38E-01	1.43E+00	3.28E-02	6.75E-02	1.04E+02	1.06E+02
RMH-014	1.28E+01	3.18E-01	3.33E-01	1.67E+00	1.94E-02	3.03E-02	5.68E+01	5.92E+01
RMH-015	2.67E+01	2.24E-01	3.05E-01	2.47E+00	7.17E-02	4.30E-02	1.30E+02	1.34E+02
RMH-016	1.44E+01	2.90E-01	3.21E-01	1.90E+00	3.71E-02	2.86E-02	6.25E+01	6.51E+01
RMH-017	2.01E+01	3.31E-01	3.84E-01	1.73E+00	6.25E-02	1.44E-02	8.00E+01	8.25E+01
RMH-018	4.60E+01	2.66E-01	3.07E-01	3.20E+00	3.03E-02	9.00E-02	1.78E+02	1.82E+02
RMH-019	6.69E+01	2.93E-01	3.95E-01	4.06E+00	8.92E-03	1.23E-02	6.34E+01	7.08E+01
RMH-020	1.22E+01	3.01E-01	3.25E-01	1.53E+00	1.15E-02	9.22E-03	5.34E+01	5.56E+01
RMH-021	2.11E+01	2.35E-01	2.88E-01	1.77E+00	1.41E-02	3.69E-02	9.12E+01	9.35E+01
RMH-022	2.66E+01	1.28E-01	1.53E-01	1.64E+00	8.67E-03	1.63E-01	8.86E+01	9.07E+01
RMH-023	2.88E+01	1.91E-01	2.69E-01	2.08E+00	1.65E-02	6.61E-02	1.19E+02	1.22E+02
RMH-024	2.99E+01	2.45E-01	2.06E-01	1.80E+00	2.14E-02	3.49E-02	1.00E+02	1.03E+02
RMH-025	1.62E+01	2.12E-01	2.54E-01	1.56E+00	3.21E-02	3.45E-02	5.55E+01	5.76E+01
Average	2.11E+01	2.48E-01	2.93E-01	1.92E+00	2.96E-02	3.55E-02	7.72E+01	7.99E+01
Standard Deviation	1.23E+01	7.12E-02	7.51E-02	5.95E-01	2.12E-02	3.42E-02	3.05E+01	3.07E+01

Table C.1: Segmented VOI mass for RMH patients. Total Body refers to total patient mass, documented before measurement.

Patient	Absorbed Dose (mGy·MBq ⁻¹)							Total Body
	Body FOV	Left Lung	Right Lung	Bones FOV	Salivary Glands	Neck	Remainder	
RMH-001	5.84E-02	9.78E-02	9.94E-02	5.93E-02	3.22E-01	1.11E+00	5.44E-02	5.55E-02
RMH-002	5.47E-02	1.17E-01	1.44E-01	3.59E-02	2.09E-01	8.54E-01	5.08E-02	5.17E-02
RMH-003	1.16E-01	4.67E-01	4.90E-01	5.87E-02	2.33E-01	1.34E+00	1.11E-01	1.12E-01
RMH-004	1.04E-01	3.29E-01	3.14E-01	5.28E-02	2.58E-01	2.34E+00	1.01E-01	1.01E-01
RMH-005	4.98E-02	1.18E-01	1.39E-01	4.62E-02	2.93E-01	1.49E+00	4.83E-02	4.86E-02
RMH-006	5.59E-02	1.59E-01	1.55E-01	2.93E-02	1.56E-01	2.29E-01	5.42E-02	5.46E-02
RMH-007	9.67E-02	1.40E-01	1.37E-01	4.62E-02	1.50E-01	4.03E+00	9.96E-02	9.89E-02
RMH-008	7.73E-02	1.76E-01	1.41E-01	4.57E-02	2.34E-01	5.22E+00	6.42E-02	6.76E-02
RMH-009	5.27E-02	1.10E-01	9.91E-02	3.63E-02	1.17E-01	1.06E+01	4.54E-02	4.70E-02
RMH-010	1.10E-01	2.38E-01	2.56E-01	8.03E-02	1.07E+00	1.83E+00	1.08E-01	1.08E-01
RMH-011	2.60E-02	6.34E-02	7.80E-02	2.93E-02	1.17E-01	9.20E-02	2.23E-02	2.29E-02
RMH-012	6.46E-02	2.21E-01	2.22E-01	4.46E-02	4.82E-01	9.07E-01	6.09E-02	6.21E-02
RMH-013	2.39E-02	4.45E-02	5.10E-02	2.47E-02	6.91E-02	8.10E-02	2.27E-02	2.29E-02
RMH-014	2.60E-02	8.31E-02	6.77E-02	2.88E-02	1.50E-01	1.21E-01	2.20E-02	2.28E-02
RMH-015	3.09E-02	4.29E-02	5.16E-02	2.45E-02	7.51E-02	5.09E+00	6.19E-03	1.11E-02
RMH-016	4.18E-02	1.02E-01	1.15E-01	2.14E-02	7.59E-02	1.36E+00	3.83E-02	3.91E-02
RMH-017	6.04E-02	1.64E-01	1.72E-01	4.75E-02	2.11E-01	2.05E+00	5.61E-02	5.71E-02
RMH-018	2.48E-02	5.00E-02	5.95E-02	2.64E-02	5.52E-02	3.00E-01	2.38E-02	2.41E-02
RMH-019	5.53E-02	1.43E-01	1.80E-01	5.44E-02	3.27E-02	1.64E+00	5.16E-02	5.51E-02
RMH-020	2.25E-02	4.77E-02	4.23E-02	2.33E-02	1.15E-01	5.37E-02	2.17E-02	2.19E-02
RMH-021	2.25E-02	4.77E-02	4.23E-02	2.33E-02	1.15E-01	5.37E-02	2.17E-02	2.19E-02
RMH-022	5.40E-02	9.10E-02	9.39E-02	5.77E-02	2.34E-01	4.75E+00	2.20E-02	3.14E-02
RMH-023	2.66E-02	4.89E-02	4.84E-02	2.67E-02	1.11E-01	1.37E+00	2.28E-02	2.37E-02
RMH-024	3.40E-02	7.60E-02	7.30E-02	3.47E-02	1.85E-01	1.24E-01	3.30E-02	3.33E-02
RMH-025	4.30E-02	1.14E-01	7.86E-02	3.98E-02	2.62E-01	5.99E-01	3.98E-02	4.07E-02
Average	5.33E-02	1.32E-01	1.34E-01	3.99E-02	2.13E-01	1.91E+00	4.81E-02	4.94E-02
Standard Deviation	2.84E-02	9.85E-02	1.02E-01	1.50E-02	2.05E-01	2.42E+00	2.96E-02	2.91E-02

Table C.2: Absorbed dose per VOI for RMH patients. Calculated using openDose3D by Monte Carlo simulation and integrated using the pharmacokinetics derived from SPECT images.

Patient	Residence Time (MBq \times h/MBq)							
	Body FOV	Left Lung	Right Lung	Bones FOV	Salivary Glands	Neck	Remainder	Total Body
RMH-001	6.25E+00	1.51E-01	2.40E-01	5.47E-01	1.17E-01	6.22E-01	2.18E+01	2.31E+01
RMH-002	2.79E+00	1.54E-01	1.75E-01	3.32E-01	5.21E-02	9.33E-02	1.33E+01	1.41E+01
RMH-003	5.96E+00	2.21E-01	2.70E-01	4.18E-01	1.70E-02	1.33E-01	2.43E+01	2.53E+01
RMH-004	4.40E+00	2.87E-01	2.47E-01	5.17E-01	2.45E-02	2.67E-01	1.42E+01	1.54E+01
RMH-005	4.73E+00	1.05E-01	1.28E-01	4.61E-01	1.68E-02	5.51E-02	1.35E+01	1.42E+01
RMH-006	2.20E+00	1.24E-01	1.43E-01	3.20E-01	6.71E-02	4.83E-02	7.66E+00	8.36E+00
RMH-007	4.89E+00	1.51E-01	1.30E-01	2.81E-01	2.11E-02	1.36E-01	1.34E+01	1.40E+01
RMH-008	7.56E+00	2.33E-01	2.01E-01	4.34E-01	3.27E-02	1.43E-01	1.05E+01	1.16E+01
RMH-009	3.33E+00	1.96E-01	2.33E-01	3.57E-01	2.76E-02	6.47E-01	1.34E+01	1.45E+01
RMH-010	8.99E+00	1.91E-01	2.29E-01	5.51E-01	2.35E-01	3.56E-02	2.67E+01	2.79E+01
RMH-011	1.28E+00	1.07E-01	1.12E-01	2.21E-01	7.03E-02	2.15E-02	1.19E+01	1.25E+01
RMH-012	4.11E+00	1.08E-01	1.07E-01	3.20E-01	2.17E-01	6.80E-03	1.07E+01	1.15E+01
RMH-013	1.59E+00	4.98E-02	6.42E-02	1.67E-01	1.72E-02	3.37E-02	1.55E+01	1.58E+01
RMH-014	1.66E+00	1.56E-01	1.11E-01	2.45E-01	2.16E-02	9.80E-03	1.13E+01	1.18E+01
RMH-015	3.12E+00	4.99E-02	6.19E-02	2.06E-01	8.50E-03	2.07E+00	1.71E+01	1.95E+01
RMH-016	1.90E+00	9.71E-02	1.19E-01	2.22E-01	2.49E-02	3.10E-01	1.69E+01	1.76E+01
RMH-017	4.46E+00	2.28E-01	2.52E-01	4.02E-01	9.76E-02	9.78E-02	1.68E+01	1.78E+01
RMH-018	4.64E+00	8.28E-02	9.93E-02	3.91E-01	1.11E-02	1.53E-01	1.91E+01	1.98E+01
RMH-019	1.55E+01	2.05E-01	2.88E-01	8.95E-01	1.60E-03	4.99E-02	1.57E+01	1.87E+01
RMH-020	2.05E+00	1.46E-01	1.19E-01	2.25E-01	1.35E-02	2.47E-02	1.56E+01	1.61E+01
RMH-021	2.59E+00	7.68E-02	8.12E-02	2.23E-01	1.26E-02	5.00E-03	1.18E+01	1.22E+01
RMH-022	7.61E+00	6.81E-02	6.88E-02	4.31E-01	1.96E-02	5.53E+00	1.50E+01	2.11E+01
RMH-023	3.21E+00	6.15E-02	8.19E-02	2.49E-01	1.47E-02	4.12E-01	1.39E+01	1.47E+01
RMH-024	4.70E+00	1.14E-01	9.22E-02	2.82E-01	3.10E-02	1.15E-02	1.90E+01	1.95E+01
RMH-025	3.27E+00	1.34E-01	9.64E-02	3.10E-01	6.51E-02	1.26E-01	1.78E+01	1.85E+01
Average	4.51E+00	1.40E-01	1.50E-01	3.60E-01	4.95E-02	4.42E-01	1.55E+01	1.66E+01
Standard Deviation	3.05E+00	6.33E-02	7.22E-02	1.57E-01	6.04E-02	1.14E+00	4.36E+00	4.61E+00

Table C.3: Residence time per VOI for RMH patients. Integrated using the pharmacokinetics derived from SPECT images.

Equivalent Dose ICRP 60 (mSv·MBq ⁻¹)														
Organ	Red Bone Marrow	Colon	Lung	Stomach	Breast	Remainder	Gonads	Bladder Wall	Oesophagus	Liver	Thyroid	Bone	Skin	Effective Dose
Wt	0.12	0.12	0.12	0.12	0.05	0.05	0.2	0.05	0.05	0.05	0.05	0.01	0.01	1
RMH-006	6.50E-03	6.50E-03	1.88E-02	6.50E-03	2.71E-03	2.71E-03	1.08E-02	2.71E-03	2.71E-03	2.71E-03	1.15E-02	2.93E-04	5.42E-04	7.50E-02
RMH-011	2.68E-03	2.68E-03	8.48E-03	2.68E-03	1.12E-03	1.12E-03	4.46E-03	1.12E-03	1.12E-03	1.12E-03	4.60E-03	2.93E-04	2.23E-04	3.17E-02
RMH-013	2.72E-03	2.72E-03	5.73E-03	2.72E-03	1.14E-03	1.14E-03	4.54E-03	1.14E-03	1.14E-03	1.14E-03	4.05E-03	2.47E-04	2.27E-04	2.86E-02
RMH-014	2.64E-03	2.64E-03	9.05E-03	2.64E-03	1.10E-03	1.10E-03	4.40E-03	1.10E-03	1.10E-03	1.10E-03	6.05E-03	2.88E-04	2.20E-04	3.34E-02
RMH-015	7.43E-04	7.43E-04	5.67E-03	7.43E-04	3.10E-04	3.10E-04	1.24E-03	3.10E-04	3.10E-04	3.10E-04	2.55E-01	2.45E-04	6.19E-05	2.65E-01
RMH-016	4.60E-03	4.60E-03	1.30E-02	4.60E-03	1.92E-03	1.92E-03	7.66E-03	1.92E-03	1.92E-03	1.92E-03	6.80E-02	2.14E-04	3.83E-04	1.13E-01
RMH-018	2.86E-03	2.86E-03	6.57E-03	2.86E-03	1.19E-03	1.19E-03	4.76E-03	1.19E-03	1.19E-03	1.19E-03	1.50E-02	2.64E-04	2.38E-04	4.14E-02
RMH-020	2.60E-03	2.60E-03	5.40E-03	2.60E-03	1.09E-03	1.09E-03	4.34E-03	1.09E-03	1.09E-03	1.09E-03	2.69E-03	2.33E-04	2.17E-04	2.61E-02
RMH-021	2.60E-03	2.60E-03	5.40E-03	2.60E-03	1.09E-03	1.09E-03	4.34E-03	1.09E-03	1.09E-03	1.09E-03	2.69E-03	2.33E-04	2.17E-04	2.61E-02
RMH-022	2.64E-03	2.64E-03	1.11E-02	2.64E-03	1.10E-03	1.10E-03	4.40E-03	1.10E-03	1.10E-03	1.10E-03	2.38E-01	5.77E-04	2.20E-04	2.67E-01
RMH-023	2.74E-03	2.74E-03	5.84E-03	2.74E-03	1.14E-03	1.14E-03	4.56E-03	1.14E-03	1.14E-03	1.14E-03	6.85E-02	2.67E-04	2.28E-04	9.33E-02
RMH-024	3.96E-03	3.96E-03	8.94E-03	3.96E-03	1.65E-03	1.65E-03	6.60E-03	1.65E-03	1.65E-03	1.65E-03	6.20E-03	3.47E-04	3.30E-04	4.25E-02
RMH-025	4.78E-03	4.78E-03	1.16E-02	4.78E-03	1.99E-03	1.99E-03	7.96E-03	1.99E-03	1.99E-03	1.99E-03	3.00E-02	3.98E-04	3.98E-04	7.45E-02
Average	3.24E-03	3.24E-03	8.89E-03	3.24E-03	1.35E-03	1.35E-03	5.39E-03	1.35E-03	1.35E-03	1.35E-03	5.47E-02	3.00E-04	2.70E-04	8.60E-02
Standard Deviation	1.42E-03	1.42E-03	3.95E-03	1.42E-03	5.91E-04	5.91E-04	2.36E-03	5.91E-04	5.91E-04	5.91E-04	8.80E-02	9.72E-05	1.18E-04	8.47E-02

Table C.4: Equivalent dose per VOI for RMH patients and Effective Dose calculated using ICRP60 [ICRP60 1990] algorithm.

Equivalent Dose ICRP 103 (mSv:MBq ⁻¹)																
Organ	Red Bone Marrow	Colon	Lung	Stomach	Breast	Re-mailer	Gonads	Bladder Wall	Oesophagus	Liver	Thyroid	Bone	Brain	Salivary glands	Skin	Effective Dose
Wt	0.12	0.12	0.12	0.12	0.12	0.12	0.08	0.04	0.04	0.04	0.04	0.01	0.01	0.01	0.01	1
RMH-006	6.50E-03	6.50E-03	1.88E-02	6.50E-03	6.50E-03	6.50E-03	4.34E-03	2.17E-03	2.17E-03	2.17E-03	9.16E-03	2.93E-04	5.42E-04	1.56E-03	5.42E-04	7.43E-02
RMH-011	2.68E-03	2.68E-03	8.48E-03	2.68E-03	2.68E-03	2.68E-03	1.78E-03	8.92E-04	8.92E-04	8.92E-04	3.68E-03	2.93E-04	2.23E-04	1.17E-03	2.23E-04	3.19E-02
RMH-013	2.72E-03	2.72E-03	5.73E-03	2.72E-03	2.72E-03	2.72E-03	1.82E-03	9.08E-04	9.08E-04	9.08E-04	3.24E-03	2.47E-04	2.27E-04	6.91E-04	2.27E-04	2.85E-02
RMH-014	2.64E-03	2.64E-03	9.05E-03	2.64E-03	2.64E-03	2.64E-03	1.76E-03	8.80E-04	8.80E-04	8.80E-04	4.84E-03	2.88E-04	2.20E-04	1.50E-03	2.20E-04	3.37E-02
RMH-015	7.43E-04	7.43E-04	5.67E-03	7.43E-04	7.43E-04	7.43E-04	4.95E-04	2.48E-04	2.48E-04	2.48E-04	2.04E-01	2.45E-04	6.19E-05	7.51E-04	6.19E-05	2.15E-01
RMH-016	4.60E-03	4.60E-03	1.30E-02	4.60E-03	4.60E-03	4.60E-03	3.06E-03	1.53E-03	1.53E-03	1.53E-03	5.44E-03	2.14E-04	3.83E-04	7.59E-03	3.83E-04	9.98E-02
RMH-020	2.86E-03	2.86E-03	6.57E-03	2.86E-03	2.86E-03	2.86E-03	1.90E-03	9.52E-04	9.52E-04	9.52E-04	1.20E-02	2.64E-04	2.38E-04	5.52E-04	2.38E-04	3.89E-02
RMH-018	2.60E-03	2.60E-03	5.40E-03	2.60E-03	2.60E-03	2.60E-03	1.74E-03	8.68E-04	8.68E-04	8.68E-04	2.15E-03	2.33E-04	2.17E-04	1.15E-03	2.17E-04	2.67E-02
RMH-020	2.60E-03	2.60E-03	5.40E-03	2.60E-03	2.60E-03	2.60E-03	1.74E-03	8.68E-04	8.68E-04	8.68E-04	2.15E-03	2.33E-04	2.17E-04	1.15E-03	2.17E-04	2.67E-02
RMH-021	2.60E-03	2.60E-03	5.40E-03	2.60E-03	2.60E-03	2.60E-03	1.74E-03	8.68E-04	8.68E-04	8.68E-04	2.15E-03	2.33E-04	2.17E-04	1.15E-03	2.17E-04	2.67E-02
RMH-022	2.64E-03	2.64E-03	1.11E-02	2.64E-03	2.64E-03	2.64E-03	1.76E-03	8.80E-04	8.80E-04	8.80E-04	1.90E-01	5.77E-04	2.20E-04	2.34E-03	2.20E-04	2.22E-01
RMH-023	2.74E-03	2.74E-03	5.84E-03	2.74E-03	2.74E-03	2.74E-03	1.82E-03	9.12E-04	9.12E-04	9.12E-04	5.48E-03	2.67E-04	2.28E-04	1.11E-03	2.28E-04	8.07E-02
RMH-024	3.96E-03	3.96E-03	8.94E-03	3.96E-03	3.96E-03	3.96E-03	2.64E-03	1.32E-03	1.32E-03	1.32E-03	4.96E-03	3.47E-04	3.30E-04	1.85E-03	3.30E-04	4.32E-02
RMH-025	4.78E-03	4.78E-03	1.16E-02	4.78E-03	4.78E-03	4.78E-03	3.18E-03	1.59E-03	1.59E-03	1.59E-03	2.40E-02	3.98E-04	3.98E-04	2.62E-03	3.98E-04	7.12E-02
Average	3.24E-03	3.24E-03	8.89E-03	3.24E-03	3.24E-03	3.24E-03	2.16E-03	1.08E-03	1.08E-03	1.08E-03	4.38E-02	3.00E-04	2.70E-04	1.32E-03	2.70E-04	7.64E-02
Standard Deviation	1.42E-03	1.42E-03	3.95E-03	1.42E-03	1.42E-03	1.42E-03	9.45E-04	4.73E-04	4.73E-04	4.73E-04	7.04E-02	9.72E-05	1.65E-03	6.36E-04	1.18E-04	6.75E-02

Table C.5: Equivalent dose per VOI for RMH patients and Effective Dose calculated using ICRP103 [ICRP103 2007] algorithm.

Absorbed Dose (mGy-MBq ⁻¹)				
Patient	Lungs	Endos- teum	Salivary Glands	Thyroid
RMH-001	9.08E-02	7.43E-02	2.12E-01	3.62E+00
RMH-002	6.32E-02	4.53E-02	9.66E-02	5.55E-01
RMH-003	1.05E-01	7.17E-02	5.12E-02	8.00E-01
RMH-004	8.48E-02	5.82E-02	5.44E-02	1.56E+00
RMH-005	5.50E-02	5.30E-02	4.03E-02	3.35E-01
RMH-006	3.48E-02	2.73E-02	9.25E-02	2.41E-01
RMH-007	5.90E-02	4.23E-02	4.73E-02	8.04E-01
RMH-008	6.63E-02	4.65E-02	6.33E-02	8.41E-01
RMH-009	6.03E-02	4.02E-02	4.77E-02	3.13E+00
RMH-010	1.04E-01	8.37E-02	4.02E-01	2.39E-01
RMH-011	4.98E-02	3.61E-02	1.24E-01	1.39E-01
RMH-012	4.61E-02	3.95E-02	3.57E-01	5.35E-02
RMH-013	4.11E-02	3.52E-02	3.44E-02	1.78E-01
RMH-014	7.50E-02	3.79E-02	4.61E-02	7.20E-02
RMH-015	4.66E-02	4.04E-02	2.94E-02	9.98E+00
RMH-016	5.16E-02	4.02E-02	4.61E-02	1.51E+00
RMH-017	8.57E-02	5.61E-02	1.73E-01	5.86E-01
RMH-018	5.34E-02	5.15E-02	2.95E-02	7.51E-01
RMH-019	8.43E-02	3.06E-02	1.74E-02	3.07E-01
RMH-020	6.31E-02	4.35E-02	3.68E-02	1.62E-01
RMH-021	4.78E-02	3.92E-02	3.44E-02	4.71E-02
RMH-022	5.67E-02	5.72E-02	7.42E-02	3.21E+00
RMH-023	4.81E-02	4.16E-02	3.90E-02	2.40E+00
RMH-024	6.60E-02	5.31E-02	6.79E-02	8.90E-02
RMH-025	6.53E-02	5.25E-02	1.22E-01	7.48E-01
Average	6.42E-02	4.79E-02	9.35E-02	1.29E+00
Standard Deviation	1.89E-02	1.36E-02	9.80E-02	2.10E+00

Table C.6: Absorbed dose per VOI for RMH patients. Calculated using IDAC 2.1 [ANDERSON 2017].

C.2 IUCT data tables

Patient	Mass (kg)													Remainder	Total Body
	Left Lung	Right Lung	Bones FOV	Salivary Glands	Neck	Bladder Content	Liver	Left Kidney	Right Kidney	Spleen	L2-L4				
ICR-001	2.30E-01	2.70E-01	3.22E+00	4.00E-03	5.10E-02	3.80E-02	1.22E+00	1.40E-01	1.07E-01	1.39E-01	3.10E-02	5.05E+01	5.60E+01		
ICR-003	2.60E-01	3.40E-01	3.65E+00	3.50E-02	6.50E-02	2.14E-01	1.49E+00	1.72E-01	1.65E-01	2.04E-01	6.00E-02	8.33E+01	9.00E+01		
ICR-004	2.90E-01	3.60E-01	3.91E+00	2.30E-02	5.70E-02	1.05E-01	2.36E+00	1.96E-01	1.90E-01	2.58E-01	6.70E-02	9.21E+01	1.00E+02		
ICR-005	2.80E-01	3.20E-01	3.51E+00	1.20E-02	5.70E-02	1.48E-01	1.47E+00	1.07E-01	1.23E-01	2.71E-01	5.30E-02	5.26E+01	5.90E+01		
ICR-006	2.20E-01	3.30E-01	5.78E+00	5.00E-03	5.90E-02	1.73E-01	1.79E+00	2.31E-01	2.31E-01	3.24E-01	8.50E-02	7.87E+01	8.80E+01		
ICR-008	2.40E-01	2.90E-01	3.23E+00	1.50E-02	3.10E-02	3.50E-02	1.51E+00	1.61E-01	1.31E-01	1.57E-01	6.10E-02	5.61E+01	6.20E+01		
ICR-009	2.60E-01	3.00E-01	3.60E+00	1.70E-02	2.80E-02	1.48E-01	1.75E+00	1.52E-01	1.38E-01	1.55E-01	3.20E-02	5.54E+01	6.20E+01		
ICR-010	2.70E-01	3.30E-01	4.11E+00	1.30E-02	4.60E-02	1.24E-01	1.31E+00	2.11E-01	1.83E-01	2.33E-01	7.60E-02	6.00E+01	6.70E+01		
ICR-013	3.10E-01	4.00E-01	3.65E+00	1.10E-02	5.00E-02	6.60E-02	1.92E+00	2.22E-01	1.89E-01	2.71E-01	1.03E-01	7.48E+01	8.20E+01		
ICR-014	2.90E-01	3.70E-01	3.63E+00	4.00E-03	5.50E-02	6.20E-02	1.63E+00	1.47E-01	1.40E-01	1.42E-01	6.30E-02	7.54E+01	8.20E+01		
ICR-015	3.40E-01	3.90E-01	4.73E+00	1.90E-02	1.80E-02	1.22E-01	2.32E+00	2.68E-01	2.61E-01	2.17E-01	9.30E-02	8.11E+01	9.00E+01		
ICR-016	4.30E-01	4.60E-01	5.34E+00	6.00E-03	2.50E-02	2.69E-01	1.53E+00	1.93E-01	1.43E-01	2.28E-01	5.30E-02	6.93E+01	7.80E+01		
ICR-017	2.70E-01	2.80E-01	3.77E+00	8.00E-03	4.00E-02	4.48E-01	1.96E+00	1.70E-01	1.68E-01	1.70E-01	3.00E-02	6.26E+01	7.00E+01		
ICR-018	2.30E-01	2.70E-01	3.44E+00	1.20E-02	2.70E-02	5.20E-02	1.29E+00	1.70E-01	1.94E-01	9.70E-02	6.00E-02	5.11E+01	5.70E+01		
ICR-019	2.40E-01	3.40E-01	4.20E+00	5.00E-03	3.40E-02	8.90E-02	9.31E-01	1.78E-01	1.52E-01	1.09E-01	3.80E-02	4.86E+01	5.50E+01		
ICR-020	3.20E-01	3.50E-01	3.71E+00	3.00E-03	8.00E-02	5.60E-02	1.32E+00	1.65E-01	1.52E-01	1.16E-01	6.00E-02	6.86E+01	7.50E+01		
ICR-021	3.20E-01	3.90E-01	4.11E+00	8.00E-03	5.80E-02	3.76E-01	2.38E+00	1.82E-01	1.41E-01	8.10E-02	4.80E-02	7.69E+01	8.50E+01		
ICR-022	3.30E-01	3.90E-01	4.17E+00	2.00E-02	4.80E-02	3.50E-02	1.36E+00	2.05E-01	2.39E-01	1.99E-01	5.00E-02	8.49E+01	9.20E+01		
ICR-023	2.90E-01	3.40E-01	3.85E+00	9.00E-03	2.90E-02	1.07E-01	1.24E+00	1.27E-01	1.33E-01	1.11E-01	4.20E-02	5.07E+01	5.70E+01		
ICR-024	2.90E-01	3.40E-01	3.85E+00	9.00E-03	2.90E-02	1.07E-01	1.24E+00	1.27E-01	1.33E-01	1.11E-01	4.20E-02	6.17E+01	6.80E+01		
ICR-025	2.30E-01	2.70E-01	3.60E+00	1.20E-02	4.10E-02	5.30E-02	1.37E+00	1.73E-01	1.45E-01	1.01E-01	2.30E-02	7.09E+01	7.70E+01		
ICR-026	3.30E-01	3.90E-01	3.53E+00	1.10E-02	6.70E-02	8.40E-02	1.34E+00	1.57E-01	1.41E-01	1.05E-01	4.50E-02	6.37E+01	7.00E+01		
ICR-027	2.70E-01	3.60E-01	3.86E+00	6.00E-03	3.90E-02	1.63E-01	1.23E+00	1.56E-01	1.48E-01	8.90E-02	1.20E-02	6.36E+01	7.00E+01		
ICR-028	4.50E-01	4.80E-01	5.12E+00	9.00E-03	7.10E-02	3.69E-01	2.21E+00	2.62E-01	2.22E-01	4.09E-01	5.30E-02	9.23E+01	1.02E+02		
ICR-029	3.00E-01	3.40E-01	3.63E+00	4.00E-03	1.20E-02	5.90E-02	2.03E+00	1.35E-01	7.40E-02	0.00E+00	6.00E-03	4.74E+01	5.40E+01		
Average	2.92E-01	3.48E-01	3.97E+00	1.12E-02	4.47E-02	1.40E-01	1.61E+00	1.76E-01	1.62E-01	1.72E-01	5.14E-02	6.69E+01	7.39E+01		
Standard Deviation	5.66E-02	5.43E-02	6.40E-01	7.32E-03	1.75E-02	1.14E-01	4.09E-01	4.03E-02	4.35E-02	8.99E-02	2.32E-02	1.37E+01	1.45E+01		

Table C.7: Segmented VOI mass for IUCT patients. Total Body refers to total patient mass, documented before measurement.

Patient	Absorbed Dose (mGy·MBq ⁻¹)													Total Body
	Left Lung	Right Lung	Bones FOV	Salivary Glands	Neck	Bladder Content	Liver	Left Kidney	Right Kidney	Spleen	L2-L4	Remainder		
ICR-001	8.35E-02	9.18E-02	2.43E-02	5.47E-02	3.27E-01	3.07E-02	5.32E-02	3.74E-02	3.73E-02	2.93E-02	3.45E-02	3.45E-02	3.80E-02	
ICR-003	9.75E-02	1.10E-01	3.47E-02	1.31E-01	6.41E-01	3.34E-01	5.38E-02	4.13E-02	5.41E-02	4.37E-02	3.68E-02	3.83E-02	4.04E-02	
ICR-004	3.72E-02	4.48E-02	2.96E-02	4.28E-02	1.43E+00	3.45E-01	3.01E-02	2.19E-02	2.68E-02	2.25E-02	1.89E-02	1.79E-02	2.36E-02	
ICR-005	1.68E-01	2.34E-01	8.91E-02	3.15E-01	4.63E+00	2.34E-01	8.80E-02	6.58E-02	7.41E-02	5.28E-02	6.15E-02	9.86E-02	1.35E-01	
ICR-006	8.02E-02	1.22E-01	2.88E-02	2.66E-02	1.35E+00	1.91E-01	4.58E-02	2.37E-02	2.94E-02	2.64E-02	2.03E-02	3.16E-02	4.13E-02	
ICR-008	2.23E-02	2.52E-02	7.60E-03	3.20E-02	2.45E-01	8.12E-02	1.05E-02	9.71E-03	9.69E-03	7.73E-03	7.42E-03	7.30E-03	8.31E-03	
ICR-009	3.51E-02	4.11E-02	2.12E-02	2.39E-01	3.80E-01	1.48E-01	2.95E-02	2.51E-02	2.94E-02	2.60E-02	2.75E-02	2.63E-02	2.80E-02	
ICR-010	6.68E-02	5.61E-02	1.29E-02	2.17E-02	4.44E+00	1.72E-02	1.13E-02	8.95E-03	6.15E-03	1.10E-02	5.91E-03	1.75E-02	2.28E-02	
ICR-013	1.36E-01	1.43E-01	6.70E-02	1.16E-01	3.17E+00	3.76E-01	5.41E-02	4.15E-02	3.80E-02	4.20E-02	2.95E-02	5.84E-02	8.86E-02	
ICR-014	5.43E-02	4.30E-02	2.33E-02	3.20E-02	1.22E-01	7.23E-02	2.53E-02	3.27E-02	1.96E-02	3.00E-02	2.24E-02	1.98E-02	2.13E-02	
ICR-015	8.13E-02	8.40E-02	2.54E-02	7.44E-02	1.67E-02	1.80E-01	4.47E-02	3.61E-02	3.43E-02	4.14E-02	3.59E-02	3.75E-02	3.76E-02	
ICR-016	1.45E-01	1.26E-01	4.49E-02	4.11E-02	2.15E+00	1.81E-01	5.00E-02	4.48E-02	4.01E-02	4.06E-02	3.74E-02	6.64E-02	7.31E-02	
ICR-017	8.15E-02	9.99E-02	3.80E-02	4.98E-02	1.33E-01	5.81E-02	6.60E-02	4.43E-02	4.79E-02	4.47E-02	4.37E-02	3.60E-02	4.04E-02	
ICR-018	2.43E-01	3.33E-01	4.39E-02	1.84E-01	6.77E-01	1.16E-01	5.60E-02	3.50E-02	5.00E-02	3.60E-02	3.21E-02	4.96E-02	5.84E-02	
ICR-019	8.69E-02	9.82E-02	4.72E-02	7.46E-02	1.18E+00	1.06E-01	5.20E-02	4.26E-02	5.65E-02	4.60E-02	5.49E-02	5.67E-02	6.63E-02	
ICR-020	8.69E-02	9.82E-02	4.72E-02	7.46E-02	3.69E-01	1.06E-01	5.20E-02	4.26E-02	5.65E-02	4.60E-02	5.49E-02	5.67E-02	6.63E-02	
ICR-021	5.07E-02	3.70E-02	1.92E-02	3.28E-02	6.79E-01	2.99E-02	2.45E-02	1.78E-02	1.73E-02	1.71E-02	1.88E-02	1.65E-02	2.12E-02	
ICR-022	7.58E-02	7.33E-02	3.91E-02	5.14E-02	1.40E+00	2.64E-01	3.30E-02	2.63E-02	2.23E-02	2.73E-02	2.12E-02	4.13E-02	4.73E-02	
ICR-023	8.73E-02	9.81E-02	5.05E-02	1.14E-01	3.58E+00	1.76E-01	4.40E-02	4.48E-02	3.86E-02	5.18E-02	3.37E-02	5.44E-02	7.48E-02	
ICR-024	1.10E-01	8.80E-02	2.76E-02	1.15E-01	1.68E+00	1.17E-01	2.80E-02	5.50E-02	2.20E-02	2.93E-02	2.42E-02	2.98E-02	3.43E-02	
ICR-025	1.18E-01	2.06E-01	5.07E-02	1.20E-01	9.63E-01	1.27E-01	4.88E-02	3.91E-02	4.59E-02	4.26E-02	3.97E-02	4.31E-02	5.16E-02	
ICR-026	9.70E-02	1.44E-01	4.33E-02	4.48E-02	2.05E-01	1.44E-01	8.80E-02	5.48E-02	6.48E-02	4.77E-02	5.00E-02	4.39E-02	5.14E-02	
ICR-027	6.82E-02	7.42E-02	2.09E-02	3.77E-02	9.29E-02	9.73E-02	4.53E-02	3.72E-02	3.53E-02	3.48E-02	2.30E-02	2.51E-02	2.81E-02	
ICR-028	3.35E-02	5.05E-02	1.82E-02	2.04E-02	3.03E-01	1.45E-01	1.87E-02	1.62E-02	1.63E-02	1.50E-02	1.59E-02	2.13E-02	2.34E-02	
ICR-029	5.02E-01	3.27E-01	1.64E-01	7.62E-01	9.71E-01	6.63E-01	2.00E-01	4.46E-01	2.09E-01	5.68E-01	2.61E-01	2.41E-01	2.38E-01	
Average	1.08E-01	1.14E-01	4.07E-02	1.12E-01	1.28E+00	1.74E-01	5.01E-02	5.16E-02	4.33E-02	5.52E-02	4.04E-02	4.68E-02	5.43E-02	
Standard Deviation	9.67E-02	8.18E-02	3.13E-02	1.53E-01	1.33E+00	1.40E-01	3.69E-02	8.33E-02	3.86E-02	1.08E-01	4.81E-02	4.50E-02	4.68E-02	

Table C.8: Absorbed dose per VOI for IUCT patients. Calculated using openDose3D by Monte Carlo simulation and integrated using the pharmacokinetics derived from SPECT images.

Patient	Residence Time (MBq × h/MBq)												
	Left Lung	Right Lung	Bones FOV	Salivary Glands	Neck	Bladder Content	Liver	Left Kidney	Right Kidney	Spleen	L2-L4	Remainder	Total Body
ICR-001	7.03E-02	8.59E-02	3.30E-01	3.30E-03	4.98E-02	6.30E-03	3.53E-01	2.46E-02	1.91E-02	1.82E-02	4.10E-03	1.64E+01	1.79E+01
ICR-003	8.23E-02	1.03E-01	4.58E-01	3.35E-02	2.56E-01	4.73E-01	3.36E-01	2.93E-02	3.81E-02	3.80E-02	7.70E-03	3.59E+01	3.80E+01
ICR-004	4.82E-02	7.50E-02	3.85E-01	3.90E-03	4.06E-01	2.81E-01	3.29E-01	2.00E-02	2.70E-02	2.58E-02	4.50E-03	1.92E+01	2.26E+01
ICR-005	1.65E-01	1.98E-01	9.90E-01	2.42E-02	9.88E-01	2.32E-01	6.93E-01	3.63E-02	4.68E-02	6.57E-02	1.46E-02	1.01E+01	2.05E+01
ICR-006	7.47E-02	1.50E-01	5.27E-01	3.00E-04	3.18E-01	2.40E-01	3.94E-01	2.55E-02	3.18E-02	3.25E-02	6.30E-03	1.50E+01	1.96E+01
ICR-008	1.90E-02	2.54E-02	1.12E-01	3.40E-03	1.97E-02	2.27E-02	8.57E-02	8.60E-03	7.00E-03	6.10E-03	1.90E-03	9.55E-01	1.36E+00
ICR-009	4.34E-02	4.96E-02	3.09E-01	3.98E-02	5.82E-02	1.53E-01	2.62E-01	1.64E-02	1.95E-02	1.90E-02	3.70E-03	1.86E+01	2.00E+01
ICR-010	3.48E-02	3.44E-02	1.74E-01	1.70E-03	7.83E-01	1.30E-02	6.27E-02	7.50E-03	4.40E-03	1.07E-02	1.40E-02	1.92E+00	3.64E+00
ICR-013	1.85E-01	1.79E-01	7.07E-01	6.20E-03	4.75E-01	1.84E-01	4.45E-01	4.21E-02	2.96E-02	3.95E-02	1.00E-02	8.76E+00	1.77E+01
ICR-014	6.13E-02	6.44E-02	3.22E-01	7.00E-04	4.11E-02	2.53E-02	2.03E-01	2.13E-02	1.16E-02	2.04E-02	5.00E-03	1.70E+01	1.83E+01
ICR-015	1.59E-01	1.39E-01	7.20E-01	8.00E-04	5.32E-01	3.16E-01	3.64E-01	3.81E-02	2.64E-02	3.90E-02	6.10E-03	1.12E+01	1.89E+01
ICR-016	1.59E-01	1.39E-01	7.20E-01	8.00E-04	5.32E-01	3.16E-01	3.64E-01	3.81E-02	2.64E-02	3.90E-02	6.10E-03	1.12E+01	1.89E+01
ICR-017	1.11E-01	1.28E-01	5.99E-01	2.20E-03	1.79E-02	1.40E-01	6.79E-01	3.49E-02	3.84E-02	3.56E-02	5.10E-03	1.22E+01	1.47E+01
ICR-018	9.70E-02	1.32E-01	6.34E-01	1.54E-02	1.05E-01	4.26E-02	3.82E-01	2.80E-02	5.44E-02	1.65E-02	8.20E-03	1.27E+01	1.64E+01
ICR-019	7.79E-02	1.04E-01	6.42E-01	1.30E-03	2.17E-01	5.67E-02	2.32E-01	3.03E-02	3.94E-02	2.38E-02	6.30E-03	1.30E+01	1.73E+01
ICR-020	7.79E-02	1.04E-01	6.42E-01	1.30E-03	2.17E-01	5.67E-02	2.32E-01	3.03E-02	3.94E-02	2.38E-02	6.30E-03	1.30E+01	1.73E+01
ICR-021	9.29E-02	6.97E-02	2.66E-01	9.00E-04	2.01E-01	6.65E-02	2.90E-01	1.43E-02	3.94E-02	6.00E-03	4.00E-03	1.68E+01	1.94E+01
ICR-022	1.03E-01	1.05E-01	4.90E-01	4.00E-03	4.96E-01	7.00E-02	1.73E-01	2.36E-02	2.28E-02	2.03E-02	4.40E-03	1.53E+01	2.04E+01
ICR-023	1.24E-01	1.28E-01	6.11E-01	4.40E-03	4.35E-01	1.36E-01	2.54E-01	2.41E-02	2.57E-02	2.61E-02	5.30E-03	1.29E+01	1.91E+01
ICR-024	8.62E-02	8.92E-02	3.64E-01	7.00E-03	3.44E-01	1.37E-01	2.10E-01	6.69E-02	1.61E-02	3.46E-02	4.00E-03	2.11E+01	2.40E+01
ICR-025	1.06E-01	1.88E-01	6.62E-01	1.04E-02	1.41E-01	4.20E-02	3.16E-01	2.94E-02	3.28E-02	2.03E-02	3.30E-03	1.47E+01	1.82E+01
ICR-026	1.35E-01	2.08E-01	6.15E-01	2.70E-03	3.81E-02	7.88E-02	6.60E-01	3.96E-02	4.73E-02	2.44E-02	9.30E-03	1.26E+01	1.55E+01
ICR-027	8.41E-02	1.06E-01	2.93E-01	1.30E-03	1.45E-01	1.05E-01	3.04E-01	2.86E-02	2.66E-02	1.51E-02	8.00E-04	2.29E+01	2.46E+01
ICR-028	5.51E-02	6.36E-02	3.50E-01	1.10E-03	7.86E-02	3.58E-01	1.97E-01	1.78E-02	1.53E-02	2.60E-02	3.20E-03	1.83E+01	2.00E+01
ICR-029	1.04E+00	5.33E-01	2.29E+00	2.16E-02	3.43E-02	2.62E-01	1.71E+00	2.40E-01	6.40E-02	0.00E+00	5.00E-03	3.59E+01	4.21E+01
Average	1.32E-01	1.28E-01	5.69E-01	7.25E-03	2.74E-01	1.53E-01	3.81E-01	3.66E-02	2.89E-02	2.51E-02	5.46E-03	1.55E+01	1.95E+01
Standard Deviation	1.94E-01	9.74E-02	4.13E-01	9.85E-03	2.55E-01	1.26E-01	3.19E-01	4.41E-02	1.48E-02	1.38E-02	2.94E-03	7.93E+00	8.06E+00

Table C.9: Residence time per VOI for IUCT patients. Integrated using the pharmacokinetics derived from SPECT images.

Equivalent Dose ICRP 60 (mSv:MBq ⁻¹)														
Organ	Red Bone Marrow	Colon	Lung	Stomach	Breast	Remainder	Gonads	Bladder Wall	Oesophagus	Liver	Thyroid	Bone	Skin	Effective Dose
Wt	0.12	0.12	0.12	0.12	0.05	0.05	0.2	0.05	0.05	0.05	0.05	0.01	0.01	1
ICR-001	4.14E-03	4.14E-03	1.05E-02	4.14E-03	1.73E-03	1.73E-03	6.90E-03	1.73E-03	1.73E-03	1.73E-03	1.64E-02	2.43E-04	3.45E-04	5.54E-02
ICR-003	4.60E-03	4.60E-03	1.25E-02	4.60E-03	1.92E-03	1.92E-03	7.66E-03	1.92E-03	1.92E-03	1.92E-03	3.21E-02	3.47E-04	3.83E-04	7.63E-02
ICR-004	2.15E-03	2.15E-03	4.92E-03	2.15E-03	8.95E-04	8.95E-04	3.58E-03	8.95E-04	8.95E-04	8.95E-04	7.15E-02	2.96E-04	1.79E-04	9.14E-02
ICR-005	1.18E-02	1.18E-02	2.41E-02	1.18E-02	4.93E-03	4.93E-03	1.97E-02	4.93E-03	4.93E-03	4.93E-03	2.32E-01	8.91E-04	9.86E-04	3.37E-01
ICR-006	3.79E-03	3.79E-03	1.21E-02	3.79E-03	1.58E-03	1.58E-03	6.32E-03	1.58E-03	1.58E-03	1.58E-03	6.75E-02	2.88E-04	3.16E-04	1.06E-01
ICR-008	8.76E-04	8.76E-04	2.85E-03	8.76E-04	3.65E-04	3.65E-04	1.46E-03	3.65E-04	3.65E-04	3.65E-04	1.23E-02	7.60E-05	7.30E-05	2.12E-02
ICR-009	3.16E-03	3.16E-03	4.57E-03	3.16E-03	1.32E-03	1.32E-03	5.26E-03	1.32E-03	1.32E-03	1.32E-03	1.90E-02	2.12E-04	2.63E-04	4.54E-02
ICR-010	2.10E-03	2.10E-03	7.37E-03	2.10E-03	8.75E-04	8.75E-04	3.50E-03	8.75E-04	8.75E-04	8.75E-04	2.22E-01	1.29E-04	1.75E-04	2.44E-01
ICR-013	7.01E-03	7.01E-03	2.03E-02	7.01E-03	2.92E-03	2.92E-03	1.17E-02	2.92E-03	2.92E-03	2.92E-03	1.59E-01	6.70E-04	5.84E-04	2.27E-01
ICR-014	2.38E-03	2.38E-03	5.84E-03	2.38E-03	9.90E-04	9.90E-04	3.96E-03	9.90E-04	9.90E-04	9.90E-04	6.10E-03	2.33E-04	1.98E-04	2.84E-02
ICR-015	4.50E-03	4.50E-03	9.92E-03	4.50E-03	1.88E-03	1.88E-03	7.50E-03	1.88E-03	1.88E-03	1.88E-03	8.35E-04	2.54E-04	3.75E-04	4.18E-02
ICR-016	7.97E-03	7.97E-03	1.63E-02	7.97E-03	3.32E-03	3.32E-03	1.33E-02	3.32E-03	3.32E-03	3.32E-03	1.08E-01	4.49E-04	6.64E-04	1.79E-01
ICR-017	4.32E-03	4.32E-03	1.09E-02	4.32E-03	1.80E-03	1.80E-03	7.20E-03	1.80E-03	1.80E-03	1.80E-03	6.65E-03	3.80E-04	3.60E-04	4.74E-02
ICR-018	5.95E-03	5.95E-03	3.46E-02	5.95E-03	2.48E-03	2.48E-03	9.92E-03	2.48E-03	2.48E-03	2.48E-03	3.39E-02	4.39E-04	4.96E-04	1.10E-01
ICR-019	6.80E-03	6.80E-03	1.11E-02	6.80E-03	2.84E-03	2.84E-03	1.13E-02	2.84E-03	2.84E-03	2.84E-03	5.90E-02	4.72E-04	5.67E-04	1.17E-01
ICR-020	6.80E-03	6.80E-03	1.11E-02	6.80E-03	2.84E-03	2.84E-03	1.13E-02	2.84E-03	2.84E-03	2.84E-03	1.85E-02	4.72E-04	5.67E-04	7.65E-02
ICR-021	1.98E-03	1.98E-03	5.26E-03	1.98E-03	8.25E-04	8.25E-04	3.30E-03	8.25E-04	8.25E-04	8.25E-04	3.40E-02	1.92E-04	1.65E-04	5.29E-02
ICR-022	4.96E-03	4.96E-03	8.95E-03	4.96E-03	2.07E-03	2.07E-03	8.26E-03	2.07E-03	2.07E-03	2.07E-03	7.00E-02	3.91E-04	4.13E-04	1.13E-01
ICR-023	6.53E-03	6.53E-03	1.11E-02	6.53E-03	2.72E-03	2.72E-03	1.09E-02	2.72E-03	2.72E-03	2.72E-03	1.79E-01	5.05E-04	5.44E-04	2.35E-01
ICR-024	3.58E-03	3.58E-03	1.19E-02	3.58E-03	1.49E-03	1.49E-03	5.96E-03	1.49E-03	1.49E-03	1.49E-03	8.40E-02	2.76E-04	2.98E-04	1.21E-01
ICR-025	5.17E-03	5.17E-03	1.94E-02	5.17E-03	2.16E-03	2.16E-03	8.62E-03	2.16E-03	2.16E-03	2.16E-03	4.82E-02	5.07E-04	4.31E-04	1.03E-01
ICR-026	5.27E-03	5.27E-03	1.45E-02	5.27E-03	2.20E-03	2.20E-03	8.78E-03	2.20E-03	2.20E-03	2.20E-03	1.03E-02	4.33E-04	4.39E-04	6.11E-02
ICR-027	3.01E-03	3.01E-03	8.54E-03	3.01E-03	1.26E-03	1.26E-03	5.02E-03	1.26E-03	1.26E-03	1.26E-03	4.65E-02	2.09E-04	2.51E-04	7.58E-02
ICR-028	2.56E-03	2.56E-03	5.04E-03	2.56E-03	1.07E-03	1.07E-03	4.26E-03	1.07E-03	1.07E-03	1.07E-03	1.52E-02	1.82E-04	2.13E-04	3.78E-02
ICR-029	2.89E-02	2.89E-02	4.97E-02	2.89E-02	1.21E-02	1.21E-02	4.82E-02	1.21E-02	1.21E-02	1.21E-02	4.86E-02	1.64E-03	2.41E-03	2.98E-01
Average	4.41E-03	4.41E-03	1.10E-02	4.41E-03	1.84E-03	1.84E-03	7.34E-03	1.84E-03	1.84E-03	1.84E-03	9.23E-02	3.50E-04	3.67E-04	1.34E-01
Standard Deviation	3.29E-03	3.29E-03	7.25E-03	3.29E-03	1.37E-03	1.37E-03	5.49E-03	1.37E-03	1.37E-03	1.37E-03	8.86E-02	2.64E-04	2.75E-04	1.09E-01

Table C.10: Equivalent dose per VOI for IUCT patients and Effective Dose calculated using ICRP60 [ICRP60 1990] algorithm.

Equivalent Dose ICRP 103 (mSv·MBq ⁻¹)																
Organ	Red Bone Marrow	Colon	Lung	Stomach	Breast	Re-mainder	Gonads	Bladder Wall	Oesophagus	Liver	Thyroid	Bone	Brain	Salivary glands	Skin	Effective Dose
Wt	0.12	0.12	0.12	0.12	0.12	0.12	0.08	0.04	0.04	0.04	0.04	0.01	0.01	0.01	0.01	1
ICR-001	4.14E-03	4.14E-03	1.05E-02	4.14E-03	4.14E-03	4.14E-03	2.76E-03	1.38E-03	1.38E-03	1.38E-03	1.31E-02	2.43E-04	3.45E-04	5.47E-04	3.45E-04	5.27E-02
ICR-003	4.60E-03	4.60E-03	1.25E-02	4.60E-03	4.60E-03	4.60E-03	3.06E-03	1.53E-03	1.53E-03	1.53E-03	2.56E-02	3.47E-04	3.83E-04	1.31E-03	3.83E-04	7.12E-02
ICR-004	2.15E-03	2.15E-03	4.92E-03	2.15E-03	2.15E-03	2.15E-03	1.43E-03	7.16E-04	7.16E-04	7.16E-04	5.72E-02	2.96E-04	1.79E-04	4.28E-04	1.79E-04	7.75E-02
ICR-005	1.18E-02	1.18E-02	2.41E-02	1.18E-02	1.18E-02	1.18E-02	7.89E-03	3.94E-03	3.94E-03	3.94E-03	1.85E-01	8.91E-04	9.86E-04	3.15E-03	9.86E-04	2.94E-01
ICR-006	3.79E-03	3.79E-03	1.21E-02	3.79E-03	3.79E-03	3.79E-03	2.53E-03	1.26E-03	1.26E-03	1.26E-03	5.40E-02	2.88E-04	3.16E-04	2.66E-04	3.16E-04	9.26E-02
ICR-008	8.76E-04	8.76E-04	2.85E-03	8.76E-04	8.76E-04	8.76E-04	5.84E-04	2.92E-04	2.92E-04	2.92E-04	9.80E-03	7.60E-05	7.30E-05	3.20E-04	7.30E-05	1.90E-02
ICR-009	3.16E-03	3.16E-03	4.57E-03	3.16E-03	3.16E-03	3.16E-03	2.10E-03	1.05E-03	1.05E-03	1.05E-03	1.52E-02	2.12E-04	2.63E-04	2.39E-04	2.63E-04	4.39E-02
ICR-010	2.10E-03	2.10E-03	7.37E-03	2.10E-03	2.10E-03	2.10E-03	1.40E-03	7.00E-04	7.00E-04	7.00E-04	1.78E-02	1.29E-04	1.75E-04	2.17E-04	1.75E-04	2.00E-02
ICR-013	7.01E-03	7.01E-03	2.03E-02	7.01E-03	7.01E-03	7.01E-03	4.67E-03	2.34E-03	2.34E-03	2.34E-03	1.27E-01	6.70E-04	5.84E-04	1.16E-03	5.84E-04	1.97E-01
ICR-014	2.38E-03	2.38E-03	5.84E-03	2.38E-03	2.38E-03	2.38E-03	1.58E-03	7.92E-04	7.92E-04	7.92E-04	4.88E-02	2.33E-04	1.98E-04	3.20E-04	1.98E-04	2.75E-02
ICR-015	4.50E-03	4.50E-03	9.92E-03	4.50E-03	4.50E-03	4.50E-03	3.00E-03	1.50E-03	1.50E-03	1.50E-03	6.68E-02	2.54E-04	3.75E-04	7.44E-04	3.75E-04	4.23E-02
ICR-016	7.97E-03	7.97E-03	1.63E-02	7.97E-03	7.97E-03	7.97E-03	5.31E-03	2.66E-03	2.66E-03	2.66E-03	8.60E-02	4.49E-04	6.64E-04	4.11E-04	6.64E-04	1.58E-01
ICR-017	4.32E-03	4.32E-03	1.09E-02	4.32E-03	4.32E-03	4.32E-03	2.88E-03	1.44E-03	1.44E-03	1.44E-03	5.32E-02	3.80E-04	3.60E-04	4.98E-04	3.60E-04	4.66E-02
ICR-018	5.95E-03	5.95E-03	3.46E-02	5.95E-03	5.95E-03	5.95E-03	3.97E-03	1.98E-03	1.98E-03	1.98E-03	2.71E-02	4.39E-04	4.96E-04	1.84E-03	4.96E-04	1.05E-01
ICR-019	6.80E-03	6.80E-03	1.11E-02	6.80E-03	6.80E-03	6.80E-03	4.54E-03	2.27E-03	2.27E-03	2.27E-03	4.72E-02	4.72E-04	5.67E-04	7.46E-04	5.67E-04	1.06E-01
ICR-020	6.80E-03	6.80E-03	1.11E-02	6.80E-03	6.80E-03	6.80E-03	4.54E-03	2.27E-03	2.27E-03	2.27E-03	1.48E-02	4.72E-04	5.67E-04	7.46E-04	5.67E-04	7.36E-01
ICR-021	1.98E-03	1.98E-03	5.26E-03	1.98E-03	1.98E-03	1.98E-03	1.32E-03	6.60E-04	6.60E-04	6.60E-04	2.72E-02	1.92E-04	1.65E-04	3.28E-04	1.65E-04	4.65E-02
ICR-022	4.96E-03	4.96E-03	8.95E-03	4.96E-03	4.96E-03	4.96E-03	3.30E-03	1.65E-03	1.65E-03	1.65E-03	5.60E-02	3.91E-04	4.13E-04	5.14E-04	4.13E-04	9.97E-02
ICR-023	6.53E-03	6.53E-03	1.11E-02	6.53E-03	6.53E-03	6.53E-03	4.35E-03	2.18E-03	2.18E-03	2.18E-03	1.43E-01	5.05E-04	5.44E-04	1.14E-03	5.44E-04	2.01E-01
ICR-024	3.58E-03	3.58E-03	1.19E-02	3.58E-03	3.58E-03	3.58E-03	2.38E-03	1.19E-03	1.19E-03	1.19E-03	6.72E-02	2.76E-04	2.98E-04	1.15E-03	2.98E-04	1.05E-01
ICR-025	5.17E-03	5.17E-03	1.94E-02	5.17E-03	5.17E-03	5.17E-03	3.45E-03	1.72E-03	1.72E-03	1.72E-03	3.85E-02	5.07E-04	4.31E-04	1.20E-03	4.31E-04	9.50E-02
ICR-026	5.27E-03	5.27E-03	1.45E-02	5.27E-03	5.27E-03	5.27E-03	3.51E-03	1.76E-03	1.76E-03	1.76E-03	8.20E-02	4.33E-04	4.39E-04	4.48E-04	4.39E-04	5.95E-02
ICR-027	3.01E-03	3.01E-03	8.54E-03	3.01E-03	3.01E-03	3.01E-03	2.01E-03	1.00E-03	1.00E-03	1.00E-03	3.72E-02	2.09E-04	2.51E-04	3.77E-04	2.51E-04	6.69E-02
ICR-028	2.56E-03	2.56E-03	5.04E-03	2.56E-03	2.56E-03	2.56E-03	1.70E-03	8.52E-04	8.52E-04	8.52E-04	1.21E-02	1.82E-04	2.13E-04	2.04E-04	2.13E-04	3.50E-02
ICR-029	2.89E-02	2.89E-02	2.89E-02	2.89E-02	2.89E-02	2.89E-02	1.93E-02	9.64E-03	9.64E-03	9.64E-03	3.88E-02	1.64E-03	2.41E-03	7.62E-03	2.41E-03	2.95E-01
Average	4.64E-03	4.64E-03	1.18E-02	4.64E-03	4.64E-03	4.64E-03	3.10E-03	1.55E-03	1.55E-03	1.55E-03	5.17E-02	3.56E-04	3.87E-04	8.52E-04	3.87E-04	9.64E-02
Standard Deviation	2.42E-03	2.42E-03	7.16E-03	2.42E-03	2.42E-03	2.42E-03	1.61E-03	8.05E-04	8.05E-04	8.05E-04	5.43E-02	1.82E-04	2.01E-04	7.33E-04	2.01E-04	6.77E-02

Table C.11: Equivalent dose per VOI for IUCT patients and Effective Dose calculated using ICRP103 [ICRP103 2007] algorithm.

Patient	Absorbed Dose (mGy·MBq ⁻¹)									
	Lungs	Endos- teum	Salivary Glands	Thyroid	Bladder Wall	Liver	Kidneys	Spleen	Red Bone Marrow	
ICR-001	5.57E-02	3.14E-02	1.72E-02	3.06E-01	5.44E-02	4.20E-02	3.59E-02	3.01E-02	3.09E-02	
ICR-003	1.07E-01	6.88E-02	8.70E-02	1.52E+00	1.57E-01	5.66E-02	6.59E-02	6.27E-02	6.72E-02	
ICR-004	5.94E-02	3.67E-02	2.56E-02	2.37E+00	8.42E-02	4.20E-02	3.96E-02	3.75E-02	3.64E-02	
ICR-005	8.70E-02	3.70E-02	7.27E-02	5.73E+00	7.78E-02	8.70E-02	6.30E-02	7.76E-02	3.95E-02	
ICR-006	4.84E-02	2.66E-02	1.22E-02	1.55E+00	5.95E-02	3.59E-02	3.35E-02	3.30E-02	2.69E-02	
ICR-008	7.38E-03	2.68E-03	6.81E-03	1.15E-01	5.62E-03	8.03E-03	7.43E-03	5.73E-03	2.86E-03	
ICR-009	5.51E-02	3.57E-02	6.62E-02	3.57E-01	7.38E-02	3.62E-02	3.51E-02	3.22E-02	3.49E-02	
ICR-010	1.36E-02	5.95E-03	6.97E-03	3.76E+00	8.97E-03	6.62E-03	6.89E-03	9.32E-03	6.86E-03	
ICR-013	4.55E-02	1.54E-02	1.58E-02	2.29E+00	3.50E-02	3.50E-02	3.17E-02	3.14E-02	1.69E-02	
ICR-014	5.43E-02	3.29E-02	1.68E-02	2.57E-01	5.86E-02	3.05E-02	3.21E-02	3.18E-02	3.21E-02	
ICR-015	5.69E-02	3.64E-02	2.83E-02	2.94E-02	7.06E-02	4.50E-02	4.56E-02	4.18E-02	3.56E-02	
ICR-016	4.56E-02	1.97E-02	1.07E-02	2.57E+00	5.22E-02	3.14E-02	3.14E-02	3.31E-02	2.09E-02	
ICR-017	5.22E-02	2.35E-02	1.46E-02	1.18E-01	4.84E-02	6.43E-02	4.32E-02	3.81E-02	2.41E-02	
ICR-018	5.24E-02	2.49E-02	3.70E-02	6.24E-01	4.30E-02	4.14E-02	4.51E-02	2.56E-02	2.51E-02	
ICR-019	4.89E-02	2.55E-02	1.54E-02	1.27E+00	4.54E-02	2.97E-02	4.03E-02	3.00E-02	2.55E-02	
ICR-020	4.89E-02	2.56E-02	1.50E-02	8.70E-01	4.57E-02	2.97E-02	4.03E-02	3.03E-02	2.55E-02	
ICR-021	5.73E-02	3.22E-02	1.76E-02	1.18E+00	6.03E-02	3.70E-02	2.95E-02	2.22E-02	3.16E-02	
ICR-022	4.81E-02	2.73E-02	1.79E-02	2.41E+00	4.86E-02	2.41E-02	2.97E-02	2.65E-02	2.73E-02	
ICR-023	5.57E-02	2.52E-02	2.14E-02	2.53E+00	5.05E-02	3.14E-02	3.32E-02	3.16E-02	2.56E-02	
ICR-024	6.89E-02	4.03E-02	3.19E-02	2.01E+00	7.97E-02	3.46E-02	5.38E-02	4.54E-02	3.97E-02	
ICR-025	6.35E-02	2.86E-02	3.11E-02	8.30E-01	4.97E-02	3.81E-02	4.00E-02	3.00E-02	2.86E-02	
ICR-026	6.26E-02	2.43E-02	1.59E-02	2.35E-01	4.44E-02	6.34E-02	4.81E-02	3.15E-02	2.51E-02	
ICR-027	7.51E-02	4.36E-02	2.34E-02	8.67E-01	8.43E-02	4.92E-02	4.70E-02	3.48E-02	4.28E-02	
ICR-028	4.70E-02	3.26E-02	1.50E-02	3.97E-01	8.02E-02	2.60E-02	2.91E-02	3.21E-02	3.21E-02	
ICR-029	2.32E-01	6.94E-02	6.78E-02	2.42E-01	1.27E-01	1.69E-01	1.56E-01	7.16E-02	7.16E-02	
Average	6.19E-02	3.09E-02	2.76E-02	1.38E+00	6.18E-02	4.38E-02	4.25E-02	3.35E-02	3.10E-02	
Standard Deviation	4.03E-02	1.49E-02	2.19E-02	1.36E+00	3.17E-02	3.11E-02	2.72E-02	1.43E-02	1.48E-02	

Table C.12: Absorbed dose per VOI for IUCT patients. Calculated using IDAC 2.1 [ANDERSSON 2017].

C.3 UKW data tables

Patient	Mass (kg)													Total Body
	Left Lung	Right Lung	Bones	Liver	Left Kidney	Right Kidney	Spleen	Bladder Content	Neck	Parotid glands	L2-L4	Remainder		
UKW-001	2.16E-01	2.51E-01	5.13E+00	2.13E+00	1.78E-01	1.66E-01	1.85E-01	1.56E-01	9.46E-03	4.66E-02	3.20E-02	7.65E+01	8.50E+01	
UKW-002	2.30E-01	3.00E-01	3.87E+00	1.59E+00	1.84E-01	1.32E-01	1.29E-01	3.49E-01	9.46E-03	7.73E-03	3.61E-02	6.51E+01	7.20E+01	
UKW-003	2.17E-01	2.67E-01	3.62E+00	2.25E+00	8.43E-02	9.97E-02	1.11E-01	1.07E-01	1.03E-02	1.21E-02	4.79E-02	5.71E+01	6.40E+01	
UKW-004	2.61E-01	3.15E-01	2.92E+00	1.69E+00	1.15E-01	1.04E-01	1.03E-01	1.92E-01	1.87E-02	1.22E-03	4.40E-02	7.22E+01	7.80E+01	
UKW-005	3.03E-01	3.29E-01	3.21E+00	1.31E+00	1.03E-01	1.20E-01	9.38E-02	1.33E-01	9.63E-03	1.61E-03	5.10E-02	4.03E+01	4.60E+01	
UKW-006	2.38E-01	3.15E-01	2.40E+00	2.37E+00	1.52E-01	1.44E-01	1.62E-01	5.34E-02	2.36E-02	4.14E-03	5.31E-02	1.09E+02	1.15E+02	
UKW-007	2.80E-01	3.74E-01	2.47E+00	1.22E+00	1.17E-01	1.08E-01	1.15E-01	4.79E-01	4.14E-03	5.42E-03	5.72E-02	6.47E+01	7.00E+01	
UKW-008	3.37E-01	3.94E-01	4.02E+00	1.91E+00	1.04E-01	1.17E-01	1.48E-01	1.64E-01	5.74E-03	1.25E-02	7.81E-02	6.27E+01	7.00E+01	
UKW-009	3.99E-01	3.68E-01	1.96E+00	2.60E+00	1.85E-01	1.01E-01	2.76E-01	1.62E-01	1.56E-02	1.24E-02	5.14E-02	1.11E+02	1.17E+02	
UKW-011	3.90E-01	4.50E-01	2.04E+00	2.48E+00	1.56E-01	1.33E-01	4.56E-01	3.01E-01	5.21E-03	7.18E-03	4.77E-02	1.02E+02	1.08E+02	
UKW-012	3.85E-01	3.95E-01	4.42E+00	1.76E+00	1.20E-01	1.19E-01	2.33E-01	8.13E-02	9.02E-03	7.46E-03	6.57E-02	6.93E+01	7.70E+01	
UKW-013	3.42E-01	3.96E-01	4.13E+00	2.25E+00	2.11E-01	1.88E-01	1.75E-01	2.05E-01	5.88E-03	2.55E-02	3.43E-02	7.20E+01	8.00E+01	
UKW-014	2.16E-01	2.53E-01	4.56E+00	2.11E+00	1.51E-01	1.56E-01	1.09E-01	2.45E-01	5.35E-02	3.22E-02	2.26E-02	7.71E+01	8.50E+01	
UKW-015	2.90E-01	3.43E-01	4.49E+00	2.23E+00	1.76E-01	1.82E-01	2.43E-01	4.43E-01	2.26E-02	5.30E-03	3.17E-02	7.65E+01	8.50E+01	
UKW-016	3.53E-01	4.36E-01	4.65E+00	1.83E+00	1.44E-01	1.32E-01	1.31E-01	1.13E-01	6.30E-03	4.85E-02	8.81E-03	6.01E+01	6.80E+01	
UKW-017	3.01E-01	3.57E-01	4.52E+00	2.00E+00	2.08E-01	1.80E-01	1.84E-01	2.01E-01	1.88E-02	4.91E-02	5.15E-02	8.58E+01	9.40E+01	
UKW-018	1.90E-01	2.40E-01	3.85E+00	1.76E+00	1.33E-01	1.52E-01	1.27E-01	5.13E-02	5.35E-02	1.43E-02	1.13E-02	7.84E+01	8.50E+01	
UKW-019	2.46E-01	2.77E-01	3.63E+00	1.40E+00	1.16E-01	1.20E-01	1.01E-01	4.83E-02	1.75E-02	9.44E-03	1.59E-02	5.60E+01	6.20E+01	
UKW-020	3.51E-01	4.19E-01	4.56E+00	1.59E+00	1.39E-01	1.37E-01	2.61E-01	4.08E-02	1.60E-02	2.66E-02	4.59E-02	7.44E+01	8.20E+01	
UKW-021	2.86E-01	3.13E-01	3.60E+00	2.09E+00	2.07E-01	1.52E-01	2.83E-01	9.04E-02	1.62E-02	3.38E-02	6.81E-02	8.88E+01	9.60E+01	
Average	2.94E-01	3.43E-01	3.69E+00	1.90E+00	1.48E-01	1.35E-01	1.76E-01	1.79E-01	1.63E-02	1.76E-02	4.35E-02	7.39E+01	8.09E+01	
Standard Deviation	6.37E-02	6.37E-02	9.08E-01	4.02E-01	3.76E-02	2.79E-02	9.07E-02	1.24E-01	1.37E-02	1.58E-02	1.86E-02	1.79E+01	1.80E+01	

Table C.13: Segmented VOI mass for UKW patients. Total Body refers to total patient mass, documented before measurement.

Patient	FOV Body	T_{eff} (h)													
		Left Lung	Right Lung	Bones	Liver	Left Kidney	Right Kidney	Spleen	Bladder Content	Neck	Parotid glands	L2-L4	Remainder		
UKW-001	18.5	18.4	18.5	18.5	19.2	18.4	18.1	17.8	18.9	75.9	17.8	18.0	18.5		
UKW-002	19.3	19.8	20.2	20.6	23.5	19.3	19.4	17.0	16.8	23.3	16.5	19.0	19.1		
UKW-003	25.4	27.6	28.8	25.6	25.4	25.1	26.5	22.3	25.9	75.4	23.2	25.5	24.8		
UKW-004	19.9	19.8	20.1	21.6	19.3	18.2	17.9	18.3	18.4	51.2	71.3	18.5	19.3		
UKW-005	21.6	19.2	20.4	20.9	25.6	20.9	19.4	18.2	21.7	91.6	45.1	20.8	21.4		
UKW-006	49.4	66.4	67.9	51.5	79.6	43.6	45.8	54.0	30.3	42.9	33.2	79.6	53.0		
UKW-007	21.1	26.9	19.0	21.0	18.2	36.1	31.6	30.3	18.4	68.7	72.7	18.7	21.1		
UKW-008	22.5	20.9	21.3	21.5	21.0	24.4	21.5	21.0	21.1	25.6	25.6	22.3	22.5		
UKW-009	19.8	20.3	21.1	19.9	19.6	20.3	15.8	26.9	31.2	19.1	26.9	22.3	22.9		
UKW-010	68.0	68.0	68.0	68.0	68.0	68.0	68.0	68.0	68.0	68.0	68.0	68.0	68.0		
UKW-011	30.9	24.8	49.7	25.0	90.4	23.7	44.5	19.6	20.3	85.4	50.2	29.0	27.3		
UKW-012	24.1	23.6	23.2	23.9	25.0	21.6	21.6	24.1	20.0	26.8	22.9	23.4	23.7		
UKW-013	19.3	19.8	20.2	20.6	23.5	19.3	19.4	17.0	16.8	23.3	16.5	19.0	18.5		
UKW-014	23.3	20.1	25.0	21.4	26.7	21.4	17.6	16.8	24.5	47.8	21.3	21.6	21.7		
UKW-015	19.1	17.8	18.6	18.6	19.9	19.8	19.0	16.7	20.3	67.8	16.9	18.4	19.0		
UKW-016	23.1	22.0	21.3	21.6	23.8	20.0	24.5	43.6	31.1	43.7	20.2	21.9	23.2		
UKW-017	44.1	19.5	31.1	23.0	120.1	15.7	17.3	19.3	120.1	48.9	20.5	15.6	38.0		
UKW-018	43.0	46.8	48.7	42.2	56.1	43.0	41.6	44.9	36.0	48.6	39.3	42.3	41.8		
UKW-019	42.4	42.4	42.4	42.4	42.4	42.4	42.4	42.4	42.4	35.8	41.4	42.4	42.4		
UKW-020	18.6	18.6	18.6	18.5	20.7	18.2	18.7	18.2	30.9	62.9	17.9	18.7	18.5		
UKW-021	21.1	18.0	18.5	19.3	21.4	21.6	20.9	19.7	19.0	19.4	17.5	19.4	21.3		
Average	26.3	25.6	27.7	24.9	36.1	24.6	25.2	25.4	29.2	49.2	30.8	25.8	25.9		
Standard Deviation	9.9	12.4	13.7	9.2	28.4	8.9	10.1	11.4	22.5	22.8	17.4	14.6	9.8		

Table C.14: T_{eff} per segmented VOI for UKW patients.

Patient	Absorbed Dose (mGy·MBq ⁻¹)												Total Body
	Left Lung	Right Lung	Bones FOV	Salivary Glands	Neck	Bladder Wall	Liver	Left Kidney	Right Kidney	Spleen	L2-L4	Remainder	
UKW-001	4.43E-02	4.31E-02	2.01E-02	2.35E-02	3.06E-02	2.92E-02	1.53E-01	1.86E-01	3.73E-01	9.58E-02	2.70E-02	1.26E-02	1.44E-02
UKW-002	8.44E-03	1.16E-02	2.50E-03	3.57E-03	3.83E-03	4.19E-03	2.93E-03	1.42E-02	1.11E+00	1.63E-02	3.63E-03	2.11E-03	2.52E-03
UKW-003	1.19E-01	1.52E-01	6.56E-02	9.59E-02	1.27E-01	1.57E-01	1.32E-01	5.07E-01	8.21E+00	1.68E-01	9.67E-02	5.89E-02	6.67E-02
UKW-004	5.94E-02	4.94E-02	3.09E-02	5.06E-02	5.91E-02	4.92E-02	5.90E-02	2.53E-01	3.83E+00	1.86E-01	5.01E-02	1.94E-02	2.26E-02
UKW-005	1.73E-01	1.26E-01	3.56E-02	4.34E-02	4.64E-02	2.14E-01	4.14E-02	2.46E-01	2.03E+01	1.24E-01	6.44E-02	6.35E-02	6.90E-02
UKW-006	6.46E-02	7.80E-02	3.79E-02	5.41E-02	5.07E-02	5.42E-02	4.22E-02	7.69E-01	7.86E+00	1.44E-01	4.19E-02	1.74E-02	2.10E-02
UKW-007	1.19E-01	1.61E-01	3.12E-02	4.75E-02	4.55E-02	4.68E-02	3.55E-02	1.07E-01	1.58E+01	1.88E-01	4.21E-02	2.50E-02	2.87E-02
UKW-008	5.53E-02	5.24E-02	1.95E-02	3.21E-02	3.28E-02	3.90E-02	3.82E-02	2.20E-01	4.84E+00	1.21E-01	2.83E-02	1.55E-02	1.80E-02
UKW-009	1.04E-01	1.23E-01	5.33E-02	6.82E-02	8.11E-02	1.15E-01	7.72E-02	1.42E-01	1.29E-01	1.16E-01	7.16E-02	3.52E-02	3.76E-02
UKW-010	1.80E-01	1.84E-01	2.93E-02	4.27E-02	6.19E-02	5.40E-02	5.30E-02	1.91E-01	1.51E+00	3.29E-01	4.85E-02	2.58E-02	2.94E-02
UKW-011	1.07E-01	1.37E-01	6.19E-02	1.05E-01	7.12E-02	1.05E-01	8.17E-02	1.42E-01	2.46E+01	1.06E-01	7.46E-02	3.27E-02	3.64E-02
UKW-012	8.67E-02	7.30E-02	4.45E-02	5.10E-02	6.97E-02	9.51E-02	4.72E-02	1.24E-01	1.22E+01	3.38E-01	5.36E-02	2.90E-02	3.36E-02
UKW-013	1.53E-01	2.04E-01	3.76E-02	5.16E-02	7.63E-02	7.99E-02	6.13E-02	4.48E-01	2.82E+00	1.62E-01	6.61E-02	3.35E-02	3.79E-02
UKW-014	9.90E-02	9.70E-02	4.72E-02	5.41E-02	9.36E-02	1.01E-01	1.13E-01	2.46E-01	4.07E+00	2.20E-01	6.58E-02	2.71E-02	3.34E-02
UKW-015	8.00E-02	7.32E-02	3.80E-02	4.45E-02	6.89E-02	6.83E-02	6.20E-02	5.22E-01	2.30E+00	1.51E-01	6.83E-02	2.84E-02	3.35E-02
UKW-016	1.80E-01	2.63E-01	4.21E-02	5.63E-02	8.45E-02	5.75E-02	6.80E-02	9.91E-02	3.79E+00	2.10E-01	7.02E-02	3.65E-02	4.11E-02
UKW-017	2.32E-01	4.37E-01	7.13E-02	9.07E-02	5.44E-02	5.30E-02	5.53E-02	7.69E-02	3.92E+00	2.45E-01	4.51E-02	5.17E-02	5.63E-02
UKW-018	1.03E-01	1.21E-01	3.07E-02	4.14E-02	4.09E-02	4.51E-02	3.23E-02	4.50E-01	2.29E+00	9.81E-02	3.99E-02	2.00E-02	2.35E-02
UKW-019	4.26E-02	4.44E-02	2.25E-02	2.61E-02	3.44E-02	4.02E-02	2.54E-02	1.23E-01	7.83E+00	7.07E-02	3.25E-02	1.50E-02	1.86E-02
UKW-020	1.42E-01	1.75E-01	3.11E-02	4.51E-02	7.80E-02	9.93E-02	5.55E-02	1.65E-01	2.76E+00	1.05E-01	5.47E-02	2.25E-02	2.63E-02
UKW-021	1.63E-01	1.49E-01	4.72E-02	6.06E-02	9.14E-02	9.60E-02	1.08E-01	9.67E-01	1.38E-01	8.85E-02	7.22E-02	4.24E-02	4.57E-02
Average	1.10E-01	1.31E-01	3.81E-02	5.18E-02	6.20E-02	7.63E-02	6.40E-02	2.85E-01	6.22E+00	1.56E-01	5.32E-02	2.92E-02	3.31E-02
Standard Deviation	5.61E-02	9.39E-02	1.64E-02	2.37E-02	2.72E-02	4.71E-02	3.65E-02	2.42E-01	6.74E+00	7.99E-02	2.09E-02	1.53E-02	1.64E-02

Table C.15: Absorbed dose per VOI for UKW patients. Calculated using openDose3D by Monte Carlo simulation and integrated using the pharmacokinetics derived from SPECT images.

Patient	Residence Time (MBq × h/MBq)													Total Body
	Left Lung	Right Lung	Bones	Liver	Left Kidney	Right Kidney	Spleen	Bladder Content	Neck	Parotid glands	L2-L4	Remainder		
UKW-001	0.05	0.05	0.41	0.21	0.02	0.02	0.19	0.21	0.02	0.034	0.003	4.1	5.4	
UKW-002	0.01	0.01	0.03	0.03	0.00	0.00	0.00	0.03	0.08	0.001	0.000	0.5	0.7	
UKW-003	0.14	0.21	0.88	0.93	0.05	0.08	0.07	0.40	0.71	0.015	0.015	11.2	15.3	
UKW-004	0.08	0.08	0.34	0.39	0.03	0.03	0.03	0.35	0.70	0.002	0.008	5.6	7.7	
UKW-005	0.13	0.10	0.35	0.22	0.02	0.14	0.02	0.23	1.73	0.001	0.009	6.7	9.8	
UKW-006	0.08	0.13	0.30	0.57	0.04	0.04	0.03	0.32	1.68	0.004	0.007	6.9	10.2	
UKW-007	0.09	0.15	0.31	0.27	0.03	0.03	0.02	0.32	0.88	0.007	0.009	5.3	7.3	
UKW-008	0.08	0.08	0.27	0.28	0.02	0.02	0.02	0.26	0.25	0.012	0.007	3.6	5.0	
UKW-009	0.17	0.17	0.38	0.67	0.06	0.04	0.09	0.15	0.01	0.011	0.012	15.6	17.5	
UKW-010	0.12	0.13	0.41	0.25	0.03	0.03	0.02	0.20	0.13	0.020	0.011	4.9	6.3	
UKW-011	0.19	0.22	0.46	1.11	0.05	0.07	0.16	0.26	1.22	0.005	0.012	13.3	16.3	
UKW-012	0.14	0.14	0.74	0.39	0.04	0.06	0.05	0.05	0.87	0.019	0.012	8.1	10.9	
UKW-013	0.16	0.18	0.58	0.48	0.07	0.07	0.04	0.65	0.14	0.031	0.008	8.8	11.4	
UKW-014	0.11	0.12	0.70	0.48	0.06	0.08	0.05	0.41	1.70	0.053	0.005	8.6	12.6	
UKW-015	0.12	0.14	0.59	0.40	0.05	0.06	0.06	1.62	0.19	0.006	0.007	9.0	12.4	
UKW-016	0.17	0.21	0.78	0.46	0.05	0.04	0.04	0.06	0.17	0.076	0.002	7.4	9.6	
UKW-017	0.13	0.24	0.60	0.49	0.04	0.03	0.03	0.10	14.43	0.066	0.006	12.9	29.0	
UKW-018	0.07	0.09	0.44	0.29	0.03	0.03	0.02	0.18	0.87	0.010	0.002	6.0	8.1	
UKW-019	0.06	0.06	0.28	0.15	0.02	0.02	0.01	0.04	1.60	0.004	0.002	3.1	5.5	
UKW-020	0.14	0.17	0.57	0.33	0.06	0.08	0.06	0.05	0.12	0.022	0.010	5.5	7.3	
UKW-021	0.16	0.16	0.59	0.47	0.08	0.06	0.13	0.68	0.02	0.021	0.015	14.8	17.4	
Average	0.11	0.14	0.48	0.42	0.04	0.05	0.05	0.31	1.31	0.020	0.008	7.7	10.7	
Standard Deviation	0.05	0.06	0.20	0.25	0.02	0.03	0.05	0.35	3.07	0.021	0.004	4.0	6.1	

Table C.16: Residence time per VOI for UKW patients. Integrated using the pharmacokinetics derived from SPECT images.

Equivalent Dose ICRP 60 (mSv:MBq ⁻¹)														
Organ	Red Bone Marrow	Colon	Lung	Stomach	Breast	Remainder	Gonads	Bladder Wall	Oesophagus	Liver	Thyroid	Bone	Skin	Effective Dose
Wt	0.12	0.12	0.12	0.12	0.05	0.05	0.2	0.05	0.05	0.05	0.05	0.01	0.01	1
ICR-001	4.14E-03	4.14E-03	1.05E-02	4.14E-03	1.73E-03	1.73E-03	6.90E-03	1.73E-03	1.73E-03	1.73E-03	1.64E-02	2.43E-04	3.45E-04	5.54E-02
ICR-003	4.60E-03	4.60E-03	1.25E-02	4.60E-03	1.92E-03	1.92E-03	7.66E-03	1.92E-03	1.92E-03	1.92E-03	3.21E-02	3.47E-04	3.83E-04	7.63E-02
ICR-004	2.15E-03	2.15E-03	4.92E-03	2.15E-03	8.95E-04	8.95E-04	3.58E-03	8.95E-04	8.95E-04	8.95E-04	7.15E-02	2.96E-04	1.79E-04	9.14E-02
ICR-005	1.18E-02	1.18E-02	2.41E-02	1.18E-02	4.93E-03	4.93E-03	1.97E-02	4.93E-03	4.93E-03	4.93E-03	2.32E-01	8.91E-04	9.86E-04	3.37E-01
ICR-006	3.79E-03	3.79E-03	1.21E-02	3.79E-03	1.58E-03	1.58E-03	6.32E-03	1.58E-03	1.58E-03	1.58E-03	6.75E-02	2.88E-04	3.16E-04	1.06E-01
ICR-008	8.76E-04	8.76E-04	2.85E-03	8.76E-04	3.65E-04	3.65E-04	1.46E-03	3.65E-04	3.65E-04	3.65E-04	1.23E-02	7.60E-05	7.30E-05	2.12E-02
ICR-009	3.16E-03	3.16E-03	4.57E-03	3.16E-03	1.32E-03	1.32E-03	5.26E-03	1.32E-03	1.32E-03	1.32E-03	1.90E-02	2.12E-04	2.63E-04	4.54E-02
ICR-010	2.10E-03	2.10E-03	7.37E-03	2.10E-03	8.75E-04	8.75E-04	3.50E-03	8.75E-04	8.75E-04	8.75E-04	2.22E-01	1.29E-04	1.75E-04	2.44E-01
ICR-013	7.01E-03	7.01E-03	2.03E-02	7.01E-03	2.92E-03	2.92E-03	1.17E-02	2.92E-03	2.92E-03	2.92E-03	1.59E-01	6.70E-04	5.84E-04	2.27E-01
ICR-014	2.38E-03	2.38E-03	5.84E-03	2.38E-03	9.90E-04	9.90E-04	3.96E-03	9.90E-04	9.90E-04	9.90E-04	6.10E-03	2.33E-04	1.98E-04	2.84E-02
ICR-015	4.50E-03	4.50E-03	9.92E-03	4.50E-03	1.88E-03	1.88E-03	7.50E-03	1.88E-03	1.88E-03	1.88E-03	8.35E-04	2.54E-04	3.75E-04	4.18E-02
ICR-016	7.97E-03	7.97E-03	1.63E-02	7.97E-03	3.32E-03	3.32E-03	1.33E-02	3.32E-03	3.32E-03	3.32E-03	1.08E-01	4.49E-04	6.64E-04	1.79E-01
ICR-017	4.32E-03	4.32E-03	1.09E-02	4.32E-03	1.80E-03	1.80E-03	7.20E-03	1.80E-03	1.80E-03	1.80E-03	6.65E-03	3.80E-04	3.60E-04	4.74E-02
ICR-018	5.95E-03	5.95E-03	3.46E-02	5.95E-03	2.48E-03	2.48E-03	9.92E-03	2.48E-03	2.48E-03	2.48E-03	3.39E-02	4.39E-04	4.96E-04	1.10E-01
ICR-019	6.80E-03	6.80E-03	1.11E-02	6.80E-03	2.84E-03	2.84E-03	1.13E-02	2.84E-03	2.84E-03	2.84E-03	5.90E-02	4.72E-04	5.67E-04	1.17E-01
ICR-020	6.80E-03	6.80E-03	1.11E-02	6.80E-03	2.84E-03	2.84E-03	1.13E-02	2.84E-03	2.84E-03	2.84E-03	1.85E-02	4.72E-04	5.67E-04	7.65E-02
ICR-021	1.98E-03	1.98E-03	5.26E-03	1.98E-03	8.25E-04	8.25E-04	3.30E-03	8.25E-04	8.25E-04	8.25E-04	3.40E-02	1.92E-04	1.65E-04	5.29E-02
ICR-022	4.96E-03	4.96E-03	8.95E-03	4.96E-03	2.07E-03	2.07E-03	8.26E-03	2.07E-03	2.07E-03	2.07E-03	7.00E-02	3.91E-04	4.13E-04	1.13E-01
ICR-023	6.53E-03	6.53E-03	1.11E-02	6.53E-03	2.72E-03	2.72E-03	1.09E-02	2.72E-03	2.72E-03	2.72E-03	1.79E-01	5.05E-04	5.44E-04	2.35E-01
ICR-024	3.58E-03	3.58E-03	1.19E-02	3.58E-03	1.49E-03	1.49E-03	5.96E-03	1.49E-03	1.49E-03	1.49E-03	8.40E-02	2.76E-04	2.98E-04	1.21E-01
ICR-025	5.17E-03	5.17E-03	1.94E-02	5.17E-03	2.16E-03	2.16E-03	8.62E-03	2.16E-03	2.16E-03	2.16E-03	4.82E-02	5.07E-04	4.31E-04	1.03E-01
ICR-026	5.27E-03	5.27E-03	1.45E-02	5.27E-03	2.20E-03	2.20E-03	8.78E-03	2.20E-03	2.20E-03	2.20E-03	1.03E-02	4.33E-04	4.39E-04	6.11E-02
ICR-027	3.01E-03	3.01E-03	8.54E-03	3.01E-03	1.26E-03	1.26E-03	5.02E-03	1.26E-03	1.26E-03	1.26E-03	4.65E-02	2.09E-04	2.51E-04	7.58E-02
ICR-028	2.56E-03	2.56E-03	5.04E-03	2.56E-03	1.07E-03	1.07E-03	4.26E-03	1.07E-03	1.07E-03	1.07E-03	1.52E-02	1.82E-04	2.13E-04	3.78E-02
ICR-029	2.89E-02	2.89E-02	4.97E-02	2.89E-02	1.21E-02	1.21E-02	4.82E-02	1.21E-02	1.21E-02	1.21E-02	4.86E-02	1.64E-03	2.41E-03	2.98E-01
Average	4.41E-03	4.41E-03	1.10E-02	4.41E-03	1.84E-03	1.84E-03	7.34E-03	1.84E-03	1.84E-03	1.84E-03	9.23E-02	3.50E-04	3.67E-04	1.34E-01
Standard Deviation	3.29E-03	3.29E-03	7.25E-03	3.29E-03	1.37E-03	1.37E-03	5.49E-03	1.37E-03	1.37E-03	1.37E-03	8.86E-02	2.64E-04	2.75E-04	1.09E-01

Table C.17: Equivalent dose per VOI for UKW patients and Effective Dose calculated using ICRP60 [ICRP60 1990] algorithm.

Equivalent Dose ICRP 103 (mSv·MBq ⁻¹)																
Organ	Red Bone Marrow	Colon	Lung	Stomach	Breast	Re-mainder	Gonads	Bladder Wall	Oesophagus	Liver	Thyroid	Bone	Brain	Salivary glands	Skin	Effective Dose
Wt	0.12	0.12	0.12	0.12	0.12	0.12	0.08	0.04	0.04	0.04	0.04	0.01	0.01	0.01	0.01	1
ICR-001	4.14E-03	4.14E-03	1.05E-02	4.14E-03	4.14E-03	4.14E-03	2.76E-03	1.38E-03	1.38E-03	1.38E-03	1.31E-02	2.43E-04	3.45E-04	5.47E-04	3.45E-04	5.27E-02
ICR-003	4.60E-03	4.60E-03	1.25E-02	4.60E-03	4.60E-03	4.60E-03	3.06E-03	1.53E-03	1.53E-03	1.53E-03	2.56E-02	3.47E-04	3.83E-04	1.31E-03	3.83E-04	7.12E-02
ICR-004	2.15E-03	2.15E-03	4.92E-03	2.15E-03	2.15E-03	2.15E-03	1.43E-03	7.16E-04	7.16E-04	7.16E-04	5.72E-02	2.96E-04	1.79E-04	4.28E-04	1.79E-04	7.75E-02
ICR-005	1.18E-02	1.18E-02	2.41E-02	1.18E-02	1.18E-02	1.18E-02	7.89E-03	3.94E-03	3.94E-03	3.94E-03	1.85E-02	8.91E-04	9.86E-04	3.15E-03	9.86E-04	2.94E-01
ICR-006	3.79E-03	3.79E-03	1.21E-02	3.79E-03	3.79E-03	3.79E-03	2.53E-03	1.26E-03	1.26E-03	1.26E-03	5.40E-02	2.88E-04	3.16E-04	2.66E-04	3.16E-04	9.26E-02
ICR-008	8.76E-04	8.76E-04	2.85E-03	8.76E-04	8.76E-04	8.76E-04	5.84E-04	2.92E-04	2.92E-04	2.92E-04	9.80E-02	7.60E-05	7.30E-05	3.20E-04	7.30E-05	1.90E-02
ICR-009	3.16E-03	3.16E-03	4.57E-03	3.16E-03	3.16E-03	3.16E-03	2.10E-03	1.05E-03	1.05E-03	1.05E-03	1.52E-02	2.12E-04	2.63E-04	2.39E-04	2.63E-04	4.39E-02
ICR-010	2.10E-03	2.10E-03	7.37E-03	2.10E-03	2.10E-03	2.10E-03	1.40E-03	7.00E-04	7.00E-04	7.00E-04	1.78E-02	1.29E-04	1.75E-04	2.17E-04	1.75E-04	2.00E-02
ICR-013	7.01E-03	7.01E-03	2.03E-02	7.01E-03	7.01E-03	7.01E-03	4.67E-03	2.34E-03	2.34E-03	2.34E-03	1.27E-02	6.70E-04	5.84E-04	1.16E-03	5.84E-04	1.97E-02
ICR-014	2.38E-03	2.38E-03	5.84E-03	2.38E-03	2.38E-03	2.38E-03	1.58E-03	7.92E-04	7.92E-04	7.92E-04	4.88E-02	2.33E-04	1.98E-04	3.20E-04	1.98E-04	2.75E-02
ICR-015	4.50E-03	4.50E-03	9.92E-03	4.50E-03	4.50E-03	4.50E-03	3.00E-03	1.50E-03	1.50E-03	1.50E-03	6.68E-02	2.54E-04	3.75E-04	7.44E-04	3.75E-04	4.23E-02
ICR-016	7.97E-03	7.97E-03	1.63E-02	7.97E-03	7.97E-03	7.97E-03	5.31E-03	2.66E-03	2.66E-03	2.66E-03	8.60E-02	4.49E-04	6.64E-04	4.11E-04	6.64E-04	1.58E-02
ICR-017	4.32E-03	4.32E-03	1.09E-02	4.32E-03	4.32E-03	4.32E-03	2.88E-03	1.44E-03	1.44E-03	1.44E-03	5.32E-02	3.80E-04	3.60E-04	4.98E-04	3.60E-04	4.66E-02
ICR-018	5.95E-03	5.95E-03	3.46E-02	5.95E-03	5.95E-03	5.95E-03	3.97E-03	1.98E-03	1.98E-03	1.98E-03	2.71E-02	4.39E-04	4.96E-04	1.84E-03	4.96E-04	1.05E-02
ICR-019	6.80E-03	6.80E-03	1.11E-02	6.80E-03	6.80E-03	6.80E-03	4.54E-03	2.27E-03	2.27E-03	2.27E-03	4.72E-02	4.72E-04	5.67E-04	7.46E-04	5.67E-04	1.06E-02
ICR-020	6.80E-03	6.80E-03	1.11E-02	6.80E-03	6.80E-03	6.80E-03	4.54E-03	2.27E-03	2.27E-03	2.27E-03	1.48E-02	4.72E-04	5.67E-04	7.46E-04	5.67E-04	7.36E-02
ICR-021	1.98E-03	1.98E-03	5.26E-03	1.98E-03	1.98E-03	1.98E-03	1.32E-03	6.60E-04	6.60E-04	6.60E-04	2.72E-02	1.92E-04	1.65E-04	3.28E-04	1.65E-04	4.65E-02
ICR-022	4.96E-03	4.96E-03	8.95E-03	4.96E-03	4.96E-03	4.96E-03	3.30E-03	1.65E-03	1.65E-03	1.65E-03	5.60E-02	3.91E-04	4.13E-04	5.14E-04	4.13E-04	9.97E-02
ICR-023	6.53E-03	6.53E-03	1.11E-02	6.53E-03	6.53E-03	6.53E-03	4.35E-03	2.18E-03	2.18E-03	2.18E-03	1.43E-02	5.05E-04	5.44E-04	1.14E-03	5.44E-04	2.01E-02
ICR-024	3.58E-03	3.58E-03	1.19E-02	3.58E-03	3.58E-03	3.58E-03	2.38E-03	1.19E-03	1.19E-03	1.19E-03	6.72E-02	2.76E-04	2.98E-04	1.15E-03	2.98E-04	1.05E-02
ICR-025	5.17E-03	5.17E-03	1.94E-02	5.17E-03	5.17E-03	5.17E-03	3.45E-03	1.72E-03	1.72E-03	1.72E-03	3.85E-02	5.07E-04	4.31E-04	1.20E-03	4.31E-04	9.50E-02
ICR-026	5.27E-03	5.27E-03	1.45E-02	5.27E-03	5.27E-03	5.27E-03	3.51E-03	1.76E-03	1.76E-03	1.76E-03	8.20E-02	4.33E-04	4.39E-04	4.48E-04	4.39E-04	5.95E-02
ICR-027	3.01E-03	3.01E-03	8.54E-03	3.01E-03	3.01E-03	3.01E-03	2.01E-03	1.00E-03	1.00E-03	1.00E-03	3.72E-02	2.09E-04	2.51E-04	3.77E-04	2.51E-04	6.69E-02
ICR-028	2.56E-03	2.56E-03	5.04E-03	2.56E-03	2.56E-03	2.56E-03	1.70E-03	8.52E-04	8.52E-04	8.52E-04	1.21E-02	1.82E-04	2.13E-04	2.04E-04	2.13E-04	3.50E-02
ICR-029	2.89E-02	2.89E-02	2.89E-02	2.89E-02	2.89E-02	2.89E-02	1.93E-02	9.64E-03	9.64E-03	9.64E-03	3.88E-02	1.64E-03	2.41E-03	7.62E-03	2.41E-03	2.95E-01
Average	4.64E-03	4.64E-03	1.18E-02	4.64E-03	4.64E-03	4.64E-03	3.10E-03	1.55E-03	1.55E-03	1.55E-03	5.17E-02	3.56E-04	3.87E-04	8.52E-04	3.87E-04	9.64E-02
Standard Deviation	2.42E-03	2.42E-03	7.16E-03	2.42E-03	2.42E-03	2.42E-03	1.61E-03	8.05E-04	8.05E-04	8.05E-04	5.43E-02	1.82E-04	2.01E-04	7.33E-04	2.01E-04	6.77E-02

Table C.18: Equivalent dose per VOI for UKW patients and Effective Dose calculated using ICRP103 [ICRP103 2007] algorithm.

Patient	Absorbed Dose (mGy·MBq ⁻¹)										
	Lungs	Endosteum	Liver	Kidneys	Spleen	Bladder Wall	Thyroid	Salivary Glands	Red Bone Marrow		
UKW-001	2.25E-02	1.04E-02	2.14E-02	2.51E-02	1.30E-01	3.18E-02	9.86E-02	5.92E-02	1.09E-02		
UKW-002	3.05E-03	2.01E-03	2.81E-03	2.96E-03	2.10E-03	4.30E-03	4.59E-01	2.64E-03	2.13E-03		
UKW-003	9.97E-02	2.90E-02	7.35E-02	1.07E-01	9.44E-02	7.44E-02	7.86E+00	1.57E-01	3.13E-02		
UKW-004	4.34E-02	1.42E-02	3.92E-02	4.14E-02	3.78E-02	4.79E-02	4.14E+00	2.28E-01	1.59E-02		
UKW-005	5.64E-02	1.76E-02	3.18E-02	9.81E-02	3.01E-02	4.26E-02	1.92E+01	7.24E-02	2.05E-02		
UKW-006	5.92E-02	1.80E-02	4.35E-02	4.69E-02	3.39E-02	5.06E-02	7.94E+00	1.28E-01	2.11E-02		
UKW-007	4.92E-02	1.32E-02	3.61E-02	3.69E-02	2.85E-02	4.36E-02	2.35E+01	1.62E-01	1.51E-02		
UKW-008	3.11E-02	9.33E-03	2.54E-02	2.73E-02	2.57E-02	3.41E-02	4.60E+00	1.09E-01	1.04E-02		
UKW-009	8.18E-02	3.33E-02	5.38E-02	6.91E-02	6.02E-02	6.69E-02	1.18E-01	1.18E-01	3.38E-02		
UKW-010	4.46E-02	1.23E-02	3.29E-02	4.27E-02	3.62E-02	3.37E-02	1.49E+00	3.23E-01	1.33E-02		
UKW-011	8.40E-02	2.94E-02	7.97E-02	7.25E-02	6.45E-02	6.57E-02	2.68E+01	9.94E-02	3.28E-02		
UKW-012	5.87E-02	2.10E-02	4.13E-02	6.83E-02	3.71E-02	3.40E-02	1.08E+01	3.15E-01	2.27E-02		
UKW-013	4.83E-02	1.97E-02	3.91E-02	5.59E-02	3.55E-02	7.71E-02	6.84E-01	4.83E-02	2.11E-02		
UKW-014	5.36E-02	2.32E-02	4.83E-02	6.31E-02	4.66E-02	6.43E-02	9.85E+00	1.05E-01	2.61E-02		
UKW-015	4.44E-02	2.29E-02	3.47E-02	4.75E-02	4.64E-02	1.54E-01	9.36E-01	1.70E-02	2.49E-02		
UKW-016	5.83E-02	1.87E-02	4.58E-02	4.55E-02	3.71E-02	3.20E-02	9.95E-01	1.32E-01	1.95E-02		
UKW-017	1.17E-01	4.43E-02	5.54E-02	4.49E-02	4.69E-02	5.34E-02	7.70E+00	1.60E-01	6.31E-02		
UKW-018	3.53E-02	1.50E-02	2.97E-02	2.86E-02	2.00E-02	3.55E-02	5.05E+00	2.78E-02	1.63E-02		
UKW-019	2.66E-02	9.61E-03	1.63E-02	2.09E-02	1.27E-02	1.50E-02	9.27E+00	1.98E-02	1.18E-02		
UKW-020	3.83E-02	1.29E-02	2.67E-02	4.81E-02	4.32E-02	2.20E-02	6.09E-01	3.42E-02	1.38E-02		
UKW-021	7.09E-02	3.34E-02	5.25E-02	7.09E-02	1.05E-01	1.08E-01	1.12E-01	4.89E-02	3.42E-02		
Average	5.37E-02	1.95E-02	3.95E-02	5.07E-02	4.63E-02	5.19E-02	6.77E+00	1.13E-01	2.19E-02		
Standard Deviation	2.64E-02	9.99E-03	1.78E-02	2.49E-02	3.05E-02	3.31E-02	7.84E+00	9.01E-02	1.27E-02		

Table C.19: Absorbed dose per VOI for UKW patients. Calculated using IDAC 2.1 [ANDERSSON 2017].

Scientific Production

D.1 Original papers

- Kayal G., Chauvin M., Mora Ramirez E., Clayton N., Vergara Gil A., Tran-Gia J., Lassmann M., Calvert N., Tipping J., Struelens L., Bardiès M. (2022). Modelling SPECT auto-contouring acquisitions for ^{177}Lu & ^{131}I molecular radiotherapy using new developments in Geant4/GATE, *Physica Medica*, Volume 96, Pages 101-113
- Kayal G., Clayton N., Vergara-Gil A., Struelens L., Bardiès M. (2022). Proof-of-concept of DosiTest: A virtual multicentric clinical trial for assessing uncertainties in molecular radiotherapy dosimetry. *Physica Medica*, Volume 97, Pages 25-35.
- Milano A., Vergara Gil A., Fabrizi E., Cremonesi M., Veronese I., Gallo S., Lanconelli N., Faccini R., Pacilio M. (2021). In silico validation of MCID platform for monte carlo-based voxel dosimetry applied to ^{90}Y -radioembolization of liver malignancies. *Applied Sciences*, Volume 11(4), Page 1939.
- Kayal G., Chauvin M., Vergara Gil A., Clayton N., Ferrer L., Moalosi T., Knoll P., Struelens L., Bardiès M. (2021). Generation of clinical ^{177}Lu SPECT/CT images based on monte carlo simulation with GATE. *Physica Medica*, Volume 85, Pages 24-31.
- Chauvin M., Borys D., Botta F., Bzowski P., Dabin J., Denis-Bacelar A. M., Desbrée A., Falzone N., Lee B. Q., Mairani A., Malaroda A., Mathieu G., McKa, E., Mora Ramirez E., Robinson A. P., Sarrut D., Struelens L., Vergara Gil A., and Bardiès M. (2020). OpenDose: open access resources for nuclear medicine dosimetry. *Journal of Nuclear Medicine*, Volume 61(7).
- Taprogge J., Leek F., Schurrat T., Tran-Gia J., Vallot D., Bardiès M., Eberlein U., Lassmann M., Schlögl S., Vergara Gil A., Team M. W. I., and Flux G. (2020). Setting up a quantitative spect imaging network for a european multi-centre dosimetry study of radioiodine treatment for thyroid cancer as part of the medirad project. *EJNMMI physics*, Vol. 7 (1), pp. 61.

D.2 Abstracts

- A. Vergara Gil, E. Amato, L. Auditore, M. Brenet, M. Chauvin, (2020). OpenDose3D: A free, collaborative 3D Slicer module for patient-specific dosimetry. *European Jour-*

nal of Nuclear Medicine and Molecular Imaging, Springer Verlag (Germany), 2020, 47 (SUPPL 1), pp.S314-S315.

- Leek F., Taprogge J., Gregory R., Newbold K., Verburg F., Luster M., Schurrat T., Trans-Gia J., Eberlein U., Lapa C., Buck A. K., Lassmann M., Mora Ramirez E., Vergara Gil A., Bardiès M., Vallot D., Courbon F., Vija L., Flux G. (2019). The MEDIRAD multinational ^{131}I dosimetry study for thyroid ablation and adjuvant therapy: current status. *European Journal of Nuclear Medicine and Molecular Imaging*, 46(Suppl 1), S194-S195.
- Maxime Chauvin, Damian Borys, Francesca Botta, Pawel Bzowski, Marco A.Coca Pérez, Marta Cremonesi, Jérémie Dabin, Ana M. Denis-Bacelar, Aurélie Desbrée, Ziad El Bitar, Nadia Falzone, Ludovic Ferrer, Didier Franck, Nico Lanconelli, Andrea Mairani, Alessandr Malaroda, Kamil Matusik, Erin McKay, Massimiliano Pacilio, Justyna Pieter, Andrew P. Robinson, José L. Rodríguez, Lara Struelens, Leonel A. Torres Aroche, Alex Vergara Gil, Manuel Bardiès. (2017). Abstract ID: 155 OpenDose: A collaborative effort to produce reference dosimetric data with Monte Carlo simulation software. *Physica Medica*, Volume 42, Pages 32-33.

D.3 Books

- Manuel Bardiès, Naomi Clayton, Gunjan Kayal, and Alex Vergara Gil, Patient-specific Dosimetry Calculations, in Ljungberg, Michael. *Handbook of Nuclear Medicine and Molecular Imaging for Physicists. Volume II*. Available from: VitalSource Bookshelf, Taylor & Francis, 2022.
- M Bardiès and A Vergara Gil, Absorbed dose calculation, in Lassman, Michael, *Dosimetry for Radiopharmaceutical Therapy IAEA Tech Series*, in Press, 2022.

D.4 International conferences

- Gibaud B., Brenet M., Pasquier G., Vergara Gil A., Bardiès M., Stratakis J., Damiak J., Van Dooren N., Spaltenstein J., Ratib O. (2020). A semantic database for integrated management of image and dosimetric data in low radiation dose research in medical imaging. *AMIA 2020 Annual Symposium*, (3409134). (Oral presentation).
- A. Vergara Gil, E. Amato, L. Auditore, M. Brenet, M. Chauvin, (2020). OpenDose3D: A free, collaborative 3D Slicer module for patient-specific dosimetry. *European Journal of Nuclear Medicine and Molecular Imaging*, Springer Verlag (Germany), 2020, 47 (SUPPL 1), pp.S314-S315.
- Vergara Gil A., Mora Ramirez E., Pouget J., Kotzki P., Santoro L., Deshayes E., Bardiès M. (2019a). Fast heterogeneous convolution algorithm used in absorbed dose calculation for beta emitters. *European Journal of Nuclear Medicine and Molecular Imaging*, 46(Suppl 1), S473-S474. (E-poster)

-
- Mora Ramirez E., Vergara Gil A., Ramos J. C. O., Pouget J., Kotzki P., Santoro L., Deshayes E., Bardies M. (2019). Absorbed dose calculation considering organ mass variation for patients treated with Luthatera. *European Journal of Nuclear Medicine and Molecular Imaging*, Volume 46(Suppl 1), S86. (Oral presentation).
 - Vergara Gil A., Chauvin M., Kayal G., Ocampo Ramos J. C., Bardiès M. (2019b). Geant4/GATE ion source implementation for internal dosimetry applications. *European Journal of Nuclear Medicine and Molecular Imaging*, 46(Suppl 1), S365 (Oral presentation).

List of Figures

1.1	Change in the top 25 causes of years of life lost (YLL) due to premature mortality in France from 1990 to 2010. http://www.healthdata.org/sites/default/files/files/country_profiles/GBD/ihme_gbd_country_report_france.pdf	10
1.2	Typical processes in the pharmacokinetics of a radiopharmaceutical inside an organ: Uptake and washout	14
1.3	Main characteristics of the PK curve: (T_{max}, C_{max}) is the coordinate of the peak, AUC is the area under the curve that obtained by integration to infinity, and $T_{1/2}$ is the terminal half-life obtained by assuming mono exponential behavior of the tail.	15
1.4	ORNL's age-specific mathematical anthropomorphic models.	20
1.5	ICRP 110 voxelized models.	21
1.6	ICRP 145 mesh models.	22
1.7	DICOM hierarchy: A DICOM folder contains 1 or several patients. A patient contains 1 or more studies that correspond to single imaging exam encounter. A study is made of 1 or more series that correspond to single image acquisitions, most often corresponding to a single image volume. A series consists of 1 or more instances with each instance corresponding to a single slice of the image	26
1.8	Back-projection technique. To calculate the four pixel values in the image from the measured ray sums, the original estimate starts with all pixel values at zero. Starting arbitrarily with the vertical rays, the ray sums in the estimated image are all zero, but the measured values are 11 and 9. These "errors" are divided equally between the two pixels along each ray (5.5 in the two left pixels, 4.5 in the two right pixels). Next, the horizontal ray sums in the estimated image (both 10) are compared with the measured values (12 and 8), and the resulting errors (+2 and -2) are added along the horizontal rays. Finally, the errors in the diagonal ray sums are all added in successive steps. In this simple case, the correct image is obtained in a single iteration, but typically, several iterations are required.	28
1.9	A 33 cm diameter electron density calibration phantom. The numbers represent EDW for each rod. Manufactured by RMI and explained in detail by [CONSTANTINOU 1992].	31
1.10	Integration of DPK over two voxels [FRANQUIZ 2003]	37

2.1	Simplified clinical dosimetric workflow, created by Manuel Bardiès [BARDIÈS 2021].	43
2.2	Commercial workstation comparison, how they implement the CDW steps and in which order [DELLA GALA 2021].	48
2.3	IRDBB import demonstration	51
2.4	IRDBB storage demonstration	52
2.5	IRDBB querying demonstration	52
2.6	Proposed clinical dosimetric workflow.	53
2.7	Calibration process workflow	54
2.8	Hounsfield Units to density calibration curve using data from [SCHNEIDER 1996].	55
2.9	Activity integration workflow	56
2.10	Activity integration workflow, full details. The blue dotted box means repeated in every time point, the green dotted box means repeated in every VOI. . . .	58
2.11	ADR integration workflow	59
2.12	ADR integration workflow, full details. The blue dotted box means repeated in every time point, the green dotted box means repeated in every VOI. . . .	60
3.1	3D-Slicer Extension Wizard	65
3.2	DICOM module of 3D-Slicer	66
3.3	General Registration module of 3D-Slicer	69
3.4	Elastic registration module of 3D-Slicer	70
3.5	View of a sample segmentation	71
3.6	Segment Editor module of 3D-Slicer	72
3.7	General overview of the OpenDose3D module	76
3.8	Data hierarchy: There is only one patient now for processing and one study corresponding to one administration. The time folders (1 or n) contains the respective images. Each image is now tagged with a unique identifier, more images will be added later during processing.	78
3.9	3D-Slicer Data Module. Adding/editing missing tags can be done under the MRML node information table	79

3.10	Implementation of the absorbed dose rate algorithm selector	80
3.11	Implementation of the absorbed dose rate calculation by local energy deposition (LED)	81
3.12	Implementation of the absorbed dose rate calculation by FFT homogeneous convolution (FFT)	82
3.13	Implementation of the absorbed dose rate calculation by fast heterogeneous convolution algorithm (FHCA)	83
3.14	Implementation of the absorbed dose rate calculation by Monte Carlo Simulation (MC) in GATE	84
3.15	Structure of the files created for GATE input	85
3.16	Sections in the pharmacokinetics of a radiopharmaceutical: uptake section $[T_0, T_1]$, Data section $(T_1, T_f]$, Tail section (T_f, ∞)	86
3.17	Linear uptake assumption. M_x is the theoretical maximum activity (or absorbed dose rate), t_1 is the first time point. The integration from 0 to t_1 is equal to triangle area A. Therefore a linear behavior can replace the unknown uptake section.	87
3.18	Constant uptake assumption. M_x is the theoretical maximum activity (or absorbed dose rate), t_1 is the first time point. The integration from 0 to t_1 is equal to areas $A_c + A_b$. The assumption establishes $A_a = A_b$, therefore a constant behavior can replace the unknown uptake section.	88
3.19	Exponential uptake assumption. M_x is the theoretical maximum activity (or absorbed dose rate), t_1 is the first time point. The integration from 0 to t_1 is equal to areas $A_c + A_b$. The assumption establishes $A_a = A_b$, therefore an exponential behavior can replace the unknown uptake section.	88
3.20	Implementation of the time integration of the data in OD3D	89
4.1	PPDT simulation schema.	92
4.2	DPK generated by OD3D scripts	93
4.3	Comparison of ^{131}I -DPK in water from OD3D compared with references [PAPADIMITROULAS 2012] and [GRAVES 2019] in the domain of the reported values	94
4.4	Comparison of ^{177}Lu -DPK in water from OD3D compared with references [PAPADIMITROULAS 2012] and [GRAVES 2019] in the domain of the reported values	94

4.5	Comparison of ^{90}Y -DPK in water from OD3D compared with references [PAPADIMITROULAS 2012] and [GRAVES 2019] in the domain of the reported values	95
4.6	VDK comparison for ^{90}Y in soft tissue with cubic voxel size 3 mm side	96
4.7	VDK comparison for ^{131}I in soft tissue with cubic voxel size 3 mm side	97
4.8	VDK comparison for ^{177}Lu in soft tissue with cubic voxel size 3 mm side	97
4.9	Interoperability with RTSTRUCT for the different workstations: OD3D, Planet Dose and MIM	103
4.10	Inner conversion process from voxel-based contour to polygon-based contour with two different re-pixelation possibilities	107
4.11	Activity plots for lungs, comparison among all platforms	112
4.12	Activity plots for kidneys, comparison among all platforms	113
4.13	Activity plots for liver and spleen, comparison among all platforms	114
4.14	Comparison of the ADR calculated in lungs, with density correction, by OD3D using LED, FFT convolution and Monte Carlo.	120
4.15	Comparison of the ADR calculated in kidneys, with density correction, by OD3D using LED, FFT convolution and Monte Carlo.	121
4.16	Comparison of the ADR calculated in liver and spleen, with density correction, by OD3D using LED, FFT convolution and Monte Carlo.	122
4.17	Comparison of the ADR calculated in liver (total and healthy), with density correction, by OD3D using LED, FFT, FHCA and Monte Carlo.	124
4.18	Comparison of the ADR calculated in tumors, with density correction, by OD3D using LED, FFT, FHCA and Monte Carlo.	125
4.19	Comparison of the ADR calculated in heterogeneous regions with density correction by OD3D using LED, FFT, FHCA and Monte Carlo.	126
5.1	Sample patient of IUCT	130
5.2	Mass statistics for segmented VOI	133
5.3	Effective half life (T_{eff}) for the neck region calculated for RMH patients with more than 1 time point acquisition. The fitting was performed in both Activity curve and Absorbed dose rate curve.	134
5.4	Residence time statistics for segmented VOI	135

5.5	Absorbed dose statistics for segmented VOI, calculated by MC in OpenDose3D	136
5.6	Equivalent Dose statistics calculated by ICRP 60 recommendations [ICRP60 1990]	137
5.7	Equivalent Dose statistics calculated by ICRP 103 recommendations [ICRP103 2007]	138
5.8	Absorbed Dose statistics calculated by IDAC 2.1 [ANDERSSON 2017]	139
5.9	Sample patient of RMH	141
5.10	Mass statistics for segmented VOI	143
5.11	Residence time statistics for segmented VOI	144
5.12	Absorbed dose statistics for segmented VOI, calculated by MC in OpenDose3D	145
5.13	Equivalent Dose statistics calculated by ICRP 60 recommendations [ICRP60 1990]	146
5.14	Equivalent Dose statistics calculated by ICRP 103 recommendations [ICRP103 2007]	147
5.15	Absorbed Dose statistics calculated by IDAC 2.1 [ANDERSSON 2017]	148
5.16	Comparison of Absorbed Dose calculated by RMH in situ and those calculated by this work	149
5.17	Sample patient of UKW	151
5.18	Mass statistics for segmented VOI	154
5.19	T_{eff} statistics for segmented VOI	155
5.20	Residence time statistics for segmented VOI	156
5.21	Absorbed dose statistics for segmented VOI, calculated by MC in OpenDose3D	157
5.22	Equivalent Dose statistics calculated by ICRP 60 recommendations [ICRP60 1990]	158
5.23	Equivalent Dose statistics calculated by ICRP 103 recommendations [ICRP103 2007]	159
5.24	Absorbed Dose statistics calculated by IDAC 2.1 [ANDERSSON 2017]	160
5.25	Comparison of presented results for liver with blood based dosimetry performed at UKW. AD1 is patient-specific Monte Carlo-based calculation. AD2 is model-based (IDAC 2.1) calculation.	161

5.26	Comparison of presented results for L2-L4 with blood based dosimetry performed at UKW. AD1 is patient-specific Monte Carlo-based calculation. AD2 is model-based (IDAC 2.1) calculation.	162
5.27	Comparison of presented results with blood based dosimetry performed at UKW. AD1 is patient-specific Monte Carlo-based calculation. AD2 is model-based (IDAC 2.1) calculation.	163

List of Tables

3.1	Average kinetic energy of emitted charged particles per disintegration for selected isotopes	81
4.1	Comparison between average absorbed dose values to the liver, calculated from the GATE image (D_{gate}) and from the MIRD approach (D_{mird}) at the organ level. The relative difference is defined as $RD(\%) = \frac{D_{gate}}{D_{mird}} - 1$	100
4.2	Mean absorbed dose values for each sphere, calculated from the GATE image (D_{gate}) and from the application of the OLINDA/EXM factors (D_{olinda}). The relative difference is defined as $RD(\%) = \frac{D_{gate}}{D_{olinda}} - 1$	100
4.3	Mean absorbed dose values for each sphere, calculated from the GATE image (D_{gate}) with a reduced workflow and from the application of the OLINDA/EXM factors (D_{olinda}). The relative difference is defined as $RD(\%) = \frac{D_{gate}}{D_{olinda}} - 1$	101
4.4	Volumes in MIM and corresponding values after export to Planet Dose and OD3D	104
4.5	Relative difference ($RD(\%) = \frac{A}{MITM} - 1$) of segmented volumes. "A" stands for either OD3D or Planet Dose.	105
4.6	Activity (MBq) present in segmented VOI in MIM, Planet Dose and OD3D	109
4.7	Activity concentration (kBq·cm ⁻³) present in segmented VOI in MIM, Planet Dose and OD3D	110
4.8	Relative differences ($RD(\%) = \frac{A}{OD3D} - 1$) in activity concentration at each time point. "A" stands for either Planet Dose or MIM.	111
4.9	Time integrated activity \tilde{A} (MBq·h) calculated by all three platforms	115
4.10	Absorbed Dose Rate Algorithm and density correction methods implemented in each software. LED is local energy deposition, HC is homogeneous convolution, MC is Monte Carlo simulation and DC is density correction.	116
4.11	Absorbed dose rate (mGy·h ⁻¹) at 3.9h calculated by local energy deposition algorithm, the relative difference ($RD(\%) = \frac{PlanetDose}{OD3D} - 1$) is also reported.	117
4.12	ADR calculated by homogeneous FFT convolution in soft tissue at 3.9h without density correction. The relative difference ($RD(\%) = \frac{A}{OD3D} - 1$) is also provided. "A" stands for either Planet Dose or MIM	118

4.13	ADR ($\text{mGy}\cdot\text{h}^{-1}$) calculated in water by MC and by homogeneous FFT convolution	119
5.1	Patient data from IUCT.	132
5.2	Effective dose comparison between OpenDose3D and IDAC 2.1.	132
5.3	Patient data from RMH.	140
5.4	Effective dose comparison between OpenDose3D and IDAC 2.1.	142
5.5	Patient data from UKW. Blood dosimetry were not performed for patients 8, 9, and 19.	150
5.6	Effective dose comparison between OpenDose3D and IDAC 2.1.	152
A.1	List of mandatory DICOM tags extracted from image headers	185
A.2	List of non-mandatory DICOM tags extracted from image headers. For Hermes images, the volume data (VD) of the respective volume must be converted to real data: $RWD = AH + BH \cdot VD$. For Siemens images, the volume data (VD) shall be divided by the Siemens factor fS: $RWD = \frac{VD}{fS}$	187
C.1	Segmented VOI mass for RMH patients. Total Body refers to total patient mass, documented before measurement.	192
C.2	Absorbed dose per VOI for RMH patients. Calculated using openDose3D by Monte Carlo simulation and integrated using the pharmacokinetics derived from SPECT images.	193
C.3	Residence time per VOI for RMH patients. Integrated using the pharmacokinetics derived from SPECT images.	194
C.4	Equivalent dose per VOI for RMH patients and Effective Dose calculated using ICRP60 [ICRP60 1990] algorithm.	195
C.5	Equivalent dose per VOI for RMH patients and Effective Dose calculated using ICRP103 [ICRP103 2007] algorithm.	196
C.6	Absorbed dose per VOI for RMH patients. Calculated using IDAC 2.1 [ANDERSSON 2017].	197
C.7	Segmented VOI mass for IUCT patients. Total Body refers to total patient mass, documented before measurement.	199

C.8	Absorbed dose per VOI for IUCT patients. Calculated using openDose3D by Monte Carlo simulation and integrated using the pharmacokinetics derived from SPECT images.	200
C.9	Residence time per VOI for IUCT patients. Integrated using the pharmacokinetics derived from SPECT images.	201
C.10	Equivalent dose per VOI for IUCT patients and Effective Dose calculated using ICRP60 [ICRP60 1990] algorithm.	202
C.11	Equivalent dose per VOI for IUCT patients and Effective Dose calculated using ICRP103 [ICRP103 2007] algorithm.	203
C.12	Absorbed dose per VOI for IUCT patients. Calculated using IDAC 2.1 [ANDERSSON 2017].	204
C.13	Segmented VOI mass for UKW patients. Total Body refers to total patient mass, documented before measurement.	206
C.14	T_{eff} per segmented VOI for UKW patients.	207
C.15	Absorbed dose per VOI for UKW patients. Calculated using openDose3D by Monte Carlo simulation and integrated using the pharmacokinetics derived from SPECT images.	208
C.16	Residence time per VOI for UKW patients. Integrated using the pharmacokinetics derived from SPECT images.	209
C.17	Equivalent dose per VOI for UKW patients and Effective Dose calculated using ICRP60 [ICRP60 1990] algorithm.	210
C.18	Equivalent dose per VOI for UKW patients and Effective Dose calculated using ICRP103 [ICRP103 2007] algorithm.	211
C.19	Absorbed dose per VOI for UKW patients. Calculated using IDAC 2.1 [ANDERSSON 2017].	212

Résumé — La médecine nucléaire est une spécialité médicale qui étudie la physiologie des organes et le métabolisme de divers types de tumeurs. La médecine nucléaire utilise des produits pharmaceutiques liés à un isotope radioactif. La radiothérapie interne vectorisée (RIV) est une spécialité de la médecine nucléaire où le vecteur est dirigé vers des cibles, généralement des tumeurs, et où l'action des rayonnements ionisants vise à détruire les tumeurs. Le suivi et l'optimisation de la RMT nécessitent l'évaluation de l'irradiation délivrée au patient (dosimétrie).

Il y a un manque de standardisation en dosimétrie interne. Cette thèse propose une approche standardisée avec des flux de travail descriptifs pour la dosimétrie clinique. Un logiciel appelé OpenDose3D, basé sur 3D-Slicer en tant que module open source mettant en œuvre les flux de travail proposés, est développé, validé et mis à la disposition du public. Le module a été utilisé en recherche clinique dans le projet MEDIRAD.

Mots clés : Dosimétrie interne, workflows cliniques, 3D-Slicer.

Abstract — Nuclear medicine is a medical specialty that studies the physiology of organs and the metabolism of various types of tumors. Nuclear medicine uses pharmaceuticals bound to a radioactive isotope. Molecular radiotherapy (MRT) is a specialty of nuclear medicine where the vector is directed to targets, usually tumors, and the action of ionizing radiation is aimed at destroying tumors. The follow-up and optimization of MRT requires the evaluation of the irradiation delivered to the patient (dosimetry).

There is a lack of standardization in internal dosimetry. This thesis provides a standardized approach with descriptive clinical dosimetry workflows. A software named OpenDose3D, based in 3D-Slicer and implementing the proposed workflows was developed, validated and was made publicly available as an open source module. The module was used in clinical research within the MEDIRAD project.

Keywords: Internal dosimetry, Clinical dosimetry workflows, 3D-Slicer.

Centre de Recherches de Cancérologie de Toulouse
UMR 1037, INSERM
Ecole Doctorale GEET
Université Toulouse III, Paul Sabatier
31000 Toulouse, France

